Dissertation

submitted to the

Combined Faculty of Natural Sciences and Mathematics

of Heidelberg University, Germany

for the degree of

Doctor of Natural Sciences

Put forward by

Niels Kurz

born in Herdecke

Oral examination: 12.01.2021

Kinematically complete multiphoton ionization studies on optically trapped $^6\mathrm{Li}$ and $^6\mathrm{Li}_2$ created by single-color photoassociation

Referees: Priv.-Doz. Alexander Dorn
Prof. Dr. Matthias Weidemüller

如果你沒有看過，只是因爲你站得不夠高。

"If you haven't seen it yet, it's because where you stand is not high enough."

Abstract

In this work, a reaction microscope with a magneto-optical trap for ^{6}Li atoms, was extended by an optical dipole trap in order to be able to investigate in detail laser-induced atomic and molecular ionization dynamics in a cold quantum gas.
The optical dipole trap was operated at a full trap depth of 2.3 mK for ^{6}Li atoms and about 1% of the atoms in the MOT could be transferred into the dipole trap, with $1/e$ storage times exceeding 5 s. The optically trapped ensemble of ^{6}Li atoms was used as a target for ionisation with intensive and broadband femtosecond laser pulses ($\lambda = 750-820$ nm, $P = 10^{11}-10^{14}$ $\frac{\mathrm{W}}{\mathrm{cm}^2}$, $\Delta t = 30$ fs) and allowed to perform kinematically complete experiments, in which $^6\mathrm{Li}^+$ ions as well as photoelectrons were measured coincidentically .
As a first application, in this work, a series of association- and ionization mechanisms, which led to production of molecular $^6\mathrm{Li}_2^+$ ions, were investigated with trapped lithium atoms.
In photoassociative ionization, two atoms collide, which were previously lifted into the asymptotic $2p-3s$ potential energy curve by ladder excitation. During the collision the atoms autoionize into the $1^2\Sigma_g^+(^6\mathrm{Li}_2^+)$ groundstate of the molecular ion, since these two potential energy curves exhibit an avoided crossing. This process was observed when magneto-optically trapped atoms were illuminated with the femtosecond laser.
In the dipole trap, using single-color photoassociation, excited state molecules were produced in high-lying vibrational states $1^1\Sigma_g^+(\nu = 65)$ and $1^3\Sigma_g^+(v = 57)$ and spectroscopically investigated. A fraction of the excited state molecules decay via fluorescence into the molecular ground state. The $1^1\Sigma_g^+(\nu = 38)(^6\mathrm{Li}_2)$ ground state molecules created via the singlet resonance $1^1\Sigma_u^+(\nu = 65)(\mathrm{Li}_2^*)$ were detected via direct 3 photon ionisation. The momentum spectra show very low kinetic energies for the photo electrons of below 100 meV. Therefore in the molecular ion only vibrational states of Li_2^+ are getting populated, which are directly below the 3-photon transition energy.
Finally, a stepwise ionization mechanism was identified, which leads into the continuum via an intermediate molecular state of $^6\mathrm{Li}_2^*$ after photoassociation. The starting point is a photoassociated excited state molecule $1^1\Sigma_u^+(\nu = 65)(^6\mathrm{Li}_2^*)$, which absorbs two photons of the dipole trap laser ($\lambda = 1070\,\mathrm{nm} \pm 2\,\mathrm{nm}$). This happens via an intermediate molecular state $3^1\Sigma_g^+(2s+3s)$, after which it leads into the $1^2\Sigma_g^+(^6\mathrm{Li}_2^+)$ potential.

Zusammenfassung

In dieser Arbeit wurde ein Reaktionsmikroskop mit einer magneto-optischen Falle für ^{6}Li Atome, um eine optische Dipolfalle erweitert um die laser-induzierte atomare und molekulare Ionisationsdynamik in einem kalten Quantengas detalliert untersuchen zu können.
Die optische Dipolfalle wurde bei der vollen Fallentiefe von 2,3 mK für ^{6}Li Atome betrieben und ca. 1% der Atome in der MOT konnten in die Dipolfalle geladen werden, wobei die Speicherzeit der Atome eine Halbwertszeit von 5 s überschritt. Das optisch gefangene Ensemble aus ^{6}Li Atomen wurde als Target genutzt für Multi-Photon Ionisation mit intensiven und breitbandigen Femtosekundenlaser-Pulsen ($\lambda = 750 - 820\,\mathrm{nm}$, $P = 10^{11} - 10^{14}\,\frac{\mathrm{W}}{\mathrm{cm}^2}$, $\Delta t = 30\,\mathrm{fs}$) und erlaubte es kinematische vollständige Experimente durchzuführen, in denen sowohl Ionen als auch Photoelektronen koinzident nachgewiesen wurden. Als erste Anwendung wurden in dieser Arbeit eine Reihe von Assoziations- und Ionisationsmechanismen an den gespeicherten Lithiumatomen untersucht, die zur Erzeugung von molekularen $^6Li_2^+$ Ionen führen.
Bei der photoassoziativen Ionisation kollidieren zwei Atome, die sich durch vorangegangene stufenweise Laseranregung auf einer asymptotischen $2p - 3s$ Potentialkurve befinden. Beim Stoß autoionisieren die Atome in den $^6Li_2^+$ $1^2\Sigma_g^+$ Grundzustand des molekularen Ions, da die beiden Potentialkurven eine vermiedene Kreuzung aufweisen. Dieser Prozess wurde in der MOT bei Einstrahlung der Femtosekunden-Laserpulse beobachtet.
Mittels Ein-Farben Photoassoziation wurden in der Dipolfalle angeregte Lithiummoleküle in den Zuständen $1^1\Sigma_u^+$ und $1^3\Sigma_g^+$ in hochliegenden Vibrationszuständen ($\nu = 65$ bzw. $\nu = 57$) erzeugt und spektroskopisch untersucht. Diese angeregten Moleküle zerfallen durch Fluoreszenzemission teilweise in den molekularen Grundzustand. Die über die Singulett-Resonanz $1^1\Sigma_u^+(\nu = 65)(Li_2^*)$ erzeugten Grundzustandsmoleküle $1^1\Sigma_g^+(\nu = 38)(^6Li_2)$ wurden durch direkte 3-Photonenionisation mit fs-Laserpulsen nachgewiesen. Die Impulsspektren zeigen, dass die Photoelektronen mit sehr niedrigen Energien unter 100 meV entsehen, d.h. im molekularen Ion werden nur Li_2^+- Vibrationszustände direkt unterhalb der 3-Photonen Übergangsenergie bevölkert.
Schließlich wurde ein stufenweiser Ionisationsmechanismus identifiziert, der nach der Photoassoziation von Li_2^* über höher angeregte molekulare Zwischenzustände ins Kontinuum führt. Ausgehend vom Zustand $1^1\Sigma_u^+(\nu = 65)(^6Li_2^*)$ führt die Absorption zweier Photonen des Dipolfallenlasers ($\lambda = 1070\,\mathrm{nm} \pm 10\,\mathrm{nm}$) über den Zwischenzustand $3^1\Sigma_g^+(2s + 3s)$ ins $1^2\Sigma_g^+(^6Li_2^+)$ Potential.

Contents

Part I

Introduction and motivation

The underlying mechanisms of a plenitude of exciting physics like high-temperature superconductivity, neutron stars or quark-gluon plasmas are in its core based on correlations in quantum many-body systems. More than 40 years passed from the discovery of low-temperature superconductivity in 1911 to the first correct microscopic theory by Bardeen and Cooper, which attributed this phenomenon to the formation of correlated electrons, so called Cooper pairs, that condense into a collective state because of an attractive interaction mediated by lattice vibrations. This is to say, that electrons in a superconductor were identified to be a strongly interacting Fermi gas. A common "divide-and-conquer" strategy for understanding strongly interacting Fermi gases is to look at its constituents, quantum few-body systems like molecules or trimers. Nowadays we are in the fortunate situation, that ultracold Fermi gases with tunable interactions can routinely be created in many quantum optics labs all over the world. A common starting point for these experiments are laser-cooled alkali atoms like ^{6}Li. These laser-cooled fermionic ^{6}Li atoms then can be made ultra-cold by adjusting their interactions to strongly attractive and continue cooling them by successively removing hot atoms from the ensemble and letting the rest of the atoms re-thermalize, a procedure called forced evaporative cooling. The ability to tune the (effective) interactions between these atoms is the basis to cause transitions in a quantum gas between a Bose-Einstein condensate (BEC) and a Bardeen-Cooper-Schrieffer (BCS) superfluid (see Fig. 1). The effective two-body interactions are characterized by the so-called scattering length, which can be tuned by applying an external magnetic field and diverges at a critical value of the magnetic field. If the scattering length is made large and positive, as the temperature of the atomic ensemble is lowered, weakly bound dimers will form, which eventually condense into a molecular Bose-Einstein condensate as the quantum degenerate regime is entered. The production of a bosonic molecular BEC from a fermionic ^{6}Li gas was first demonstrated in 2003 [1]. These weakly bound ^{6}Li dimers are vibrationally highly excited bound states and they become "halo dimers" in a universal range in the vincinity of the crossover. They are called halo dimers, because their probability distribution, like a halo, is mostly concentrated outside of the range of the molecular interaction potential. The range in which halo dimers form is called universal, because the binding energy as well as the extension of the dimers are universally related to the scattering length, independently of microscopic details of the interaction potential. In the universal range the binding energy of a halo dimer is $E_b = \frac{-\hbar^2}{2m_{eff}a^2}$, where a is the scattering length. An illustration of a halo state is shown in Fig. 1, which shows that the bound state wave function has an exponential decay $\Psi_b(r) \sim \frac{e^{-\sqrt{\frac{2m}{\hbar^2}E_{bind}}r}}{r}$, where the slope of the decay is related to its binding energy.

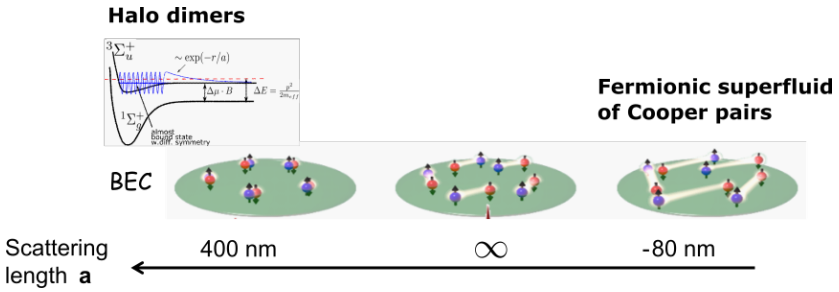

Figure 1: Illustration of a BEC-BCS cross over which exists in ^{6}Li at a magnetic field of $B_c = 834\,\mathrm{G}$.[2, 3]

In the present project it is planned as a mid-term goal to use a degenerate quantum gas like a molecular BEC of weakly bound $^6Li_2$ dimers as a target for ionization experiments. This means the ionization dynamics of the quantum gas induced, e.g. by ultra-short and intense laser pulses is studied in kinematically complete experiments with a multi-particle momentum spectrometer (reaction microscope). Though there have been experiments, including in this group, that investigated the laser induced ionization dynamics of (laser-cooled) and even ultra-cold (i.e. below the recoil temperature limit) alkali atoms in strong fields (see e.g. [4, 5, 6] and [7] respectively), reports about ionization of quantum degenerate matter are scarce up to day.

While in a dilute gas at densities of $10^{12}\,\mathrm{atoms/cm^3}$ with an average inter-particle distance of $10\,\mu$m, each particle's wavefunction reacts independently on the strong-field by a femtolaser pulse, in a BEC, in which all atoms or molecules are described by one collective wavefunction, the dynamics might be a different one. While ionization experiments of condensed Rb atoms with pulsed lasers of $10 - 16$ ns pulse length [8, 9] have been reported, a complete new aspect this experiment will add to the subject is the ionization of condensed weakly-bound dimers with ultra-short pulses of duration 30 fs or less. Typical vibrational periods of such molecules are on the order of several hundreds of femtoseconds, and therefore such short and intense pulses can "quasi-instantaneously" double ionize the molecule and lead to a reaction, called Coulomb explosion:

$$Li_2 + n\gamma_{fs} \rightarrow Li^+ + Li^+ + e_1 + e_2.$$

The KER of this reaction is given by the Coulomb repulsion energy, which directly depends on the internuclear distance at the time of double ionization, and it can be measured in our apparatus. This method is known as "Coulomb explosion imaging (CEI)", since, as can be seen from Fig. 2, the distribution of KERs maps the internuclear distance in the di-atomic dimer and therefore we can directly map the quantum mechanical wavefunction of the dimer. Therefore CEI of halo dimers can be seen as a direct way to measure the spatial size and the binding energy of halo dimers with high resolution. This technique excels any optical imaging method of measuring interparticle distances, since the released energy is large for small internuclear distances in the nanometer or sub-nanometer regime. While virtually all cold atoms experiments focus on indirect observations of microscopic molecule properties like binding energies by observing a change of macroscopic properties, like total atom number in an macroscopic ensemble of atoms, up to now, to the knowledge of the author, no cold atoms experiment directly tried to obtain a geometric picture of cold molecules which were associated from cold atoms. Femto-laser induced Coulomb explosion is typically achieved for peak intensities $> 4 \cdot 10^{15}\,\mathrm{W/cm^2}$. Such peak intensities require short pulses on the order of a

few tens of femtoseconds and pulse energies on the order of several hundred μJ. Such ultra-intense pulses are nowadays routinely created in laboratories around the world by a technique called "Chirped Pulse Amplification" (CPA).

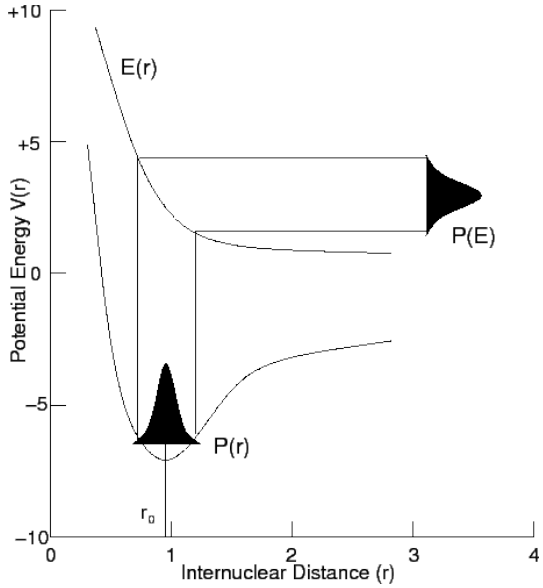

Figure 2: Schematic of how the KER distribution relates to the square of the nuclear wave-function in a Coulomb explosion of a di-atomic molecule.

While halo dimers are an interesting aspect of two-component fermionic spin mixtures, a three component fermionic spin mixture even would allow the creation of an exotic "Efimov state", which is a bound three body states, that forms even though a bound two-body state is not possible. While the association of ^{6}Li Efimov trimers in a three component spin mixture via radio-frequency spectroscopy has been demonstrated [10], in 2015 $^4He_3$ Efimov trimers have been detected in a reaction microscope [11].

The physics of ultra-cold spin mixtures is usually explored while confining them in a conservative optical dipole trap potential. Off-resonant all optical traps are the workhorses in cold atoms community. They allow for trapping of atoms and molecules by optical dipole forces with varying trap depths depending on the dynamical or static polarizability of the atom or molecule with relatively long storage times and they enable cooling of atoms to temperatures below the recoil limit. Optical dipole force traps not only play an important role in physics, but also in biological and medical research, where they can be used as "optical tweezers" to confine and hold even macroscopic objects like bacteria. The importance of the two essential experimental techniques in our project, optical dipole traps and chirped pulse amplification, is highlighted by the fact that the 2018 physics Nobel prize has been awarded to their respective inventors, Arthur Ashkin and Donna Strickland as well as Gérard Mourou.

Our recoil ion momentum spectrometer is a reaction microscope combined with a magneto-optical trap (magneto-optical trap recoil ion momentum spectrometer, MOTRIMS). The combined use of a weak electric extraction and a weak homogeneous, magnetic guiding field along the spectrometer axis allows to measure the three-dimensionl momentum vectors of recoiling ions and electrons emerging from the reaction volume. In order to create a molecular BEC within our reaction microscope, a high magnetic field on the order $700 - 1000\,\mathrm{Gauss}$ has to be applied, which controls the interactions of the atoms and therefore the scattering length of

the atoms, while ionization produces ions in the reaction volume. The question, the author of this thesis had to adress: How is such a high magnetic field of several hundreds of Gauss best implemented in a reaction microscope? Should it be homogeneous until the detector? And if it is not homogeneous until the detectors, how can the initial momenta of the charged fragments be properly reconstructed? When recoiling ions or electrons transverse an inhomogeneous magnetic field of that magnitude, superposed with an electric extraction field, the motion becomes more complicated and the equations of momentum reconstruction for a "conventional" reaction microscope do not necessarily apply. In this work, after careful consideration, it was opted for the path, in which ions and electrons will traverse a strong, axially symmetric (in good approximation), but longitudinally inhomogeneous magnetic field on their way to the detectors. The raised conceptual questions on the reconstruction of momenta or simply kinetic energies of charged fragments, had to be adressed by the author of this thesis. While some ideas are introduced, the solution of this problem cannot be given in an exact way, since the longitudinal and transversal motions of a charged particle in a combination of an electric field and an axisymmetric but inhomogeneous magnetic field are coupled and, to the knowledge of the author, do not have an analytical solution. While instrumentation, comprising a pair of intra-vacuum coils, an altered design of the vacuum chamber and beam geometries of the MOT, and the development of a fast polarity switching device, have been driven forward and completed by the end of this thesis, the creation of a BEC of weakly bound $^6Li_2$ dimers as a target for a reaction microscope remains a mid-term goal.

As a short-term goal, it was meant to demonstrate that, in a first step, atoms can be associated with cw light to form cold molecules which are stored in an optical dipole force trap. The molecules were detected and their ionization dynamics was studied using direct multi-photon ionization with broadband femtolaser pulses. The MOTRIMS apparatus was newly setup for ^{6}Li and extended by an optical dipole force trap, into which cold atoms are transferred from the magneto-optical trap. With this all-optical trap, we achieved trapping times on the order of several seconds. Therefore, after loading the dipole trap, there is sufficient time to ramp down the MOT magnetic field and to conduct measurements without severe degradation of the target. Multi-photon ionization of optically trapped atoms was investigated with intense fs laser pulses of duration 32 fs and pulse energies of up to $800\,\mu$J. This enabled us to coincidentally measure electrons and ions and to obtain high momentum resolutions of 0.055 a.u. and 0.03 a.u.for recoil ions and photoelectrons respectively. It was noted, that the IR laser participated in the ionization process, whenever single photon transitions via intermediate states can reach the continuum.

Single-color and two-color photo-association spectroscopy was performed on an optically trapped thermal sample of ^{6}Li atoms, and high lying vibrational levels of $a^3\Sigma_u^+$ and $1^1\Sigma_g^+$ could be adressed using a frequency-stabilized diode laser in the range of 675 nm. By exciting appropriate levels of $1^3\Sigma_g^+$ and $1^1\Sigma_u^+$, ground state molecules were created by spontaneous decay, in which mainly the highest lying vibrational levels $1^1\Sigma_g^+(\nu = 38)$ and $a^3\Sigma_u^+(\nu = 9)$ were populated. Because of the accessible wavelength range of the employed laser diode, the best choice of vibrational levels in these experiments were $1^3\Sigma_g^+(\nu = 57)$ and $1^1\Sigma_u^+(\nu = 65)$. While the molecule production rate and the detection efficiency in the triplet system were too low, in the singlet system it was possible to measure photoelectrons and recoiling molecular ions in coincidence after multi-photon ionization of $1^1\Sigma_g^+(\nu'' = 38)$ ground state molecules. In contrast to atomic ^{6}Li momentum spectra, where photo electrons showed at low intensity mainly, d- and g- wave character, with momenta distributed on a ring of radius $0.26-0.27$ a.u., the photo electrons from molecular ions show excess energies smaller than 100 meV. Therefore, in the molecular ion $1^2\Sigma_g^+(Li_2^+)$ only vibrational states directly below the three photon energy

are getting populated.

Two other molecular ion production mechanisms were established: Photoassociative ladder excitation and stepwise ionization after photoassociation. In the latter case, when the PA laser produces excited state molecules $1^1\Sigma_u^+(\nu = 65)(\mathrm{Li}_2^*)$, these can be directly ionized by absorption of two IR photons of our optical dipole force laser ($1070 \pm 2\,\mathrm{nm}$). By absorption of the first IR photon, the excited state molecule $1^1\Sigma_u^+(\nu = 65)(\mathrm{Li}_2^*)$ gets excited into an intermediate molecular state of the $3^1\Sigma_g^+(2S + 3S)$ potential energy from where the energy of another IR photon is sufficient to barely ionize it.

Photoassociative ladder excitation was found in experiments where our magneto-optical trap was used as a target for ionisation with broad band fs pulses from our femtolaser system. In a MOT, where a small fraction of atoms collide both in their first excited $2p$ state, the atoms can be excited by a photon of energy $1.52\,\mathrm{eV}$ within the low energy tail of the femtolaser spectrum into a scattering state on the $2p - 3s$ potential energy curve. This state autoionizes into a vibrational level $1^2\Sigma_g^+$ of the molecular ion with which it has a level crossing.

This thesis is structured as follows. The reader will be given an introduction to the field of recoil ion momentum spectroscopy and our reaction microscope in particular in part II. In part III about atom-light interactions, the reader will be given the necessary theoretical concepts of laser-cooling, dipole-force traps and photoionization of atoms. In part IV, after giving a necessary introduction to the spectroscopic notation of molecular potential energy curves in Sec. 7, the reader will be introduced to the technique of photoassociation, which was implemented in this thesis. Complementary information, about the magneto-association technique, which will be used in future experiments, is given in Sec. 9. After this, in Part V, all the instrumentation regarding the optical setup, which is necessary for operation of a magneto-optical trap, a dipole-force trap, optical diagnostics for both traps, and production of ultra-short pulses, that were implemented or operated in the course of this thesis, are described in Sec. 10. A few characterization measurements of MOT and optical dipole force trap, which make use of the optical diagnostics of Sec. 10.2 are presented to the reader in Sec. 11. In chapter 12 all experimental results regarding multi-photon ionization of an optically trapped target, molecular ion production mechanisms, and photoassociation are compiled. In chapter 13 a description of the future setup will be given, in which it will be possible to create a BEC: the design of the Feshbach coils, the polarity switching device, and a guide on reconstruction of momenta in an inhomogeneous axialsymmetric magnetic field is outlined. Finally a summary and outlook is given in Part VI.

Part II

The MOT Reaction Microscope (MOTRIMS)

In the following section, the reader will be acquainted with the field of recoil ion momentum spectroscopy and the basic principles of our particular apparatus, a "reaction microscope" combined with a magneto-optical trap, which serves as the starting point for investigations of ionization of cold atoms or molecules. In Sec. 1, it will be outlined that by measuring the flight times and positions of charged particles, the full three-dimensional momentum vector of charged fragments emerging from a reaction can be reconstructed. These equation for momentum reconstruction are conditional on the fact, that charged particles, like electrons or recoil ions, move in an antiparallel superposition of a homogeneous electric extraction and a magnetic guiding field along the spectrometer axis. The components which lie at the heart of each reaction microscope are their spectrometer and detector systems. The spectrometer refers to a tight arrangment of electrodes, that produce the homogeneous electric extraction field and screen the charged particles from external electric fields. The particular spectrometer of our reaction microscope will be shortly presented in Sec. 1.2. The experimental technique for measuring the flight times and simultaneously the hit position of charged particles on the detector, will be outlined in Sec. 1.3.

1 Recoil ion momentum spectroscopy (RIMS)

Most reactions involving collisions between a target (e.g. an atomic or molecular gas jet, a thin foil) and a projectile (e.g. an electron, ion or a photon) only yield a slight relative momentum change of the projectile, resulting in small maximum scattering angles, even for light projectiles, of sometimes only up ≈ 0.1 mrad which are hard to resolve experimentally. The idea behind the field of recoil ion momentum spectroscopy is to, instead, measure the momentum change of recoiled charged fragments emerging from the target, whose initial velocity, to a good approximation, is initially known in the laboratory system.

A Reaction Microscope (REMI) is a sophisticated machine in the field of recoil ion momentum spectroscopy, that has been developed to study the dynamic correlations of atomic and molecular reactions and allows a 4π-detection efficiency of all charged fragments emerging from the reaction under investigation ([12, 13], review article [14]). A scheme of a typical REMI is depicted in Fig. 3.

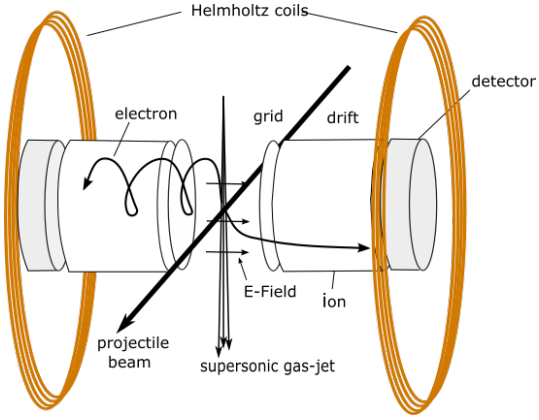

Figure 3: Scheme of a Reaction Microscope (ReMi) with a projectile beam crossing a stream of atoms and/or molecules produced by a supersonic gas-jet.

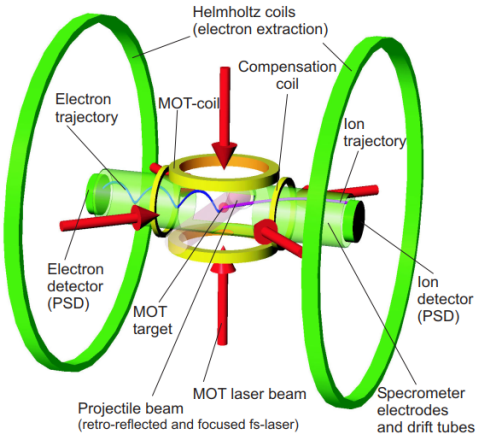

Figure 4: Scheme of a ReMi combined with a magneto-optical trap (MOTRemi), a combination that has been devised to investigate the dynamics of alkali and earth alkaline atoms in strong fields.Figure taken from [15]

The detectors in a Reaction Microscope remain at fixed positions and their area only cover a small fraction of the total solid angle of 4π. Nonetheless a 4π-detection efficiency is accomplished by the use of homogeneous electric and magnetic extraction fields, which guide the charged fragments to the respective detectors along the spectrometer axis. The electric extraction field is created by applying voltages to an arrangment of electrodes enclosing the reaction volume. The magnetic extraction field is particular important for the confinement of the trajectories of electrons, emerging from the reaction. Therefore the magnetic extraction field is created by a pair of large diameter Helmholtz coils, positioned with a slight preference to the side of the electron detector. A particular important component of the detectors of a Reaction Microscope are the multi-hit capable Multi-Channel-Plates (MCPs), which allow coincident detection of several particles at a time. The MCPs deliver information about the time of arrival of a charged fragment and through combination with a delay line anode allow simultaneously the detection of its hit position on the MCP (see Sect. 1.3). Given the precise knowledge of both, the electric and magnetic extraction field, this combination of position- and time-sensitive detection allows for the reconstruction of the vector momenta with very high momentum resolution (typically $\Delta p = 0.05$ a.u.) of all charged fragments emerging as products from a reaction (see Sec. 1.1). Consider e.g. the energy and momentum conservation relations in the laboratory frame for the collision of two particles from which N electrons and N' photons emerge as a product,

$$\begin{aligned} E_P^i + E_R^i &= E_P^f + E_R^f + \sum_{j=1}^{N} E_{ej}^f + Q \\ \mathbf{P}_P^i + \mathbf{P}_R^i &= \mathbf{P}_P^f + \mathbf{P}_R^f + \sum_{j=1}^{N} \mathbf{P}_{ej}^f + \sum_{l=1}^{N'} \mathbf{P}_{\gamma l}, \end{aligned}$$

where the sub-indices P and R stand for *projectile* and *recoil*, the upper indices i and f for *ini-*

tial and *final* respectively, and $Q = \sum_{j=1}^{N} E^f_{j,b} - E^i_{j,b}$ is the total inelasticity of the reaction, i.e. the change in total internal energy of the target, where $E^{f,i}_{j,b} < 0$ is the binding energy of the jth electron in the initial and final state respectively. Usually the initial momenta $\mathbf{P}^i_P$ and $\mathbf{P}^i_R$ are known to a good degree. For a process like single-ionization, see Sec. 6, the photon momentum $p_\gamma = E_\gamma/c$ is considered small compared to the momentum $p_e = \sqrt{2m_e\left(E_\gamma - Q - E^f_R\right)}$ of the photo-electron, as long as the inelasticity Q is small compared to the photon energy E_γ, where the recoil-energy is usually negligible because it is m_e/M_R smaller than the photo electron energy. Therefore in this approximation, in single ionization photo-electron and recoil ion emerge into opposite directions, balancing their momenta. If the inelasticity Q of the reaction is known, and $\mathcal{N}$ charged fragments with non-negligible momentum have been produced in the reaction, only $3\mathcal{N} - 4$ momenta components are independent and have to be determined experimentally. The experiment is then called *kinematically complete*. $E^{i/f}_b$ can refer to the electronic binding energy of initial and final state respectively in an atomic system, but for a di-atomic molecule it can also stand for the molecular binding energy $E(\nu, J)$, depending on the rovibrational quantum number ν and the rotational quantum number J.

If e.g. the inelasticity Q of the reaction is known and the momenta of all charged product fragments have been measured experimentally, the initial vector momenta can be reconstructed. Equally well, the knowledge of $\mathbf{P}^i_P$ and $\mathbf{P}^i_R$ in a *kinematically complete* experiment allows for the reconstruction of momentum of any undetected produced charged fragment. If $3\mathcal{N}-3$ momentum components of all charged fragments[1] have been measured, a *kinematically complete* experiment allows for the characterization of the inelasticity Q of the reaction.

The *momentum resolution* of a Reaction Microscope depends on, apart from the intrinsic time and spatial resolution of the spectrometer, various factors such as influence of electric (e.g. due to space charge effects) or magnetic stray fields (e.g. earth's magnetic field), the uncertainty with which $\mathbf{P}^i_R$ is known, and the extension of the reaction volume. The influence of electric stray fields usually can be compensated by choosing a higher extraction voltage. Also magnetic stray fields (e.g. earth magnetic field) are usually counteracted by external compensation coils. A rather large extension reaction volume can be compensated by choosing a special time-focusing geometry (see Sect. 1.1.1). The uncertainty of $\mathbf{P}^i_R$ is directly related to the temperature of the target. When the target is realized e.g. by a supersonic gas jet, the atoms or molecules move with a highly-directional momentum $p_{jet} = \sqrt{5k_BT_0M}$[2] in a specific direction (see. [16] p. 41), which can be substracted so that the analysis of the momentum balance takes place in the rest frame of the target. However, there always remains some random thermal spread $\Delta p_{thermal} = \sqrt{m_{ion}k_BT}$ due to the finite temperature of the target, which cannot be subtracted and corresponds to the uncertainty in our knowledge about $\mathbf{P}^i_R$. Depending on the reaction being studied, the thermal momentum spread can even be of the order or larger than the recoil ion momenta to be measured.

Therefore, a major motivation in connection with high momentum resolution RIMS is to produce a cold and well localized atomic or molecular target. For many atomic and molecular species (e.g. He, Ar, H_2) supersonic gas jets have established as a standard technique in the field of cold target recoil-ion momentum spectroscopy (COLTRIMS), allowing e.g. for He recoil ions an energy resolution of $\Delta E_R \approx \pm 30\,\mu eV$.

However for alkali and earth alkaline atoms, supersonic gas jets are hardly applicable. The starting point for the investigation of this reaction in recoil-ion momentum specstroscopy is a

[1] In the following we will limit ourselves to the special case of a recoil ion as a positively charged fragment

[2] where M is the mass of the atoms in the gas jet andT_0 their temperature, usually in the regime of a few K

magneto-optically trapped target (MOTRIMS), which yields high density atomic gas targets with temperatures in the sub-mK regime and therefore a significant reduction in thermal spread down to $\Delta p = 0.01$ a.u.. The use of a laser cooled target enables recoil ion energy measurements with a resolution in the range of 1 μeV , as first reported in [17] for ^{87}Rb. The working principle of a magneto-optical trap will be outlined in Sec. 4. A schematic of such a reaction microscope combined with a magneto-optical trap (MOTRemi) is shown in Fig. 4. It is important to note, that both the magnetic field of the MOT influences the measured distribution of momenta in the reaction microscope, but also the magnetic extraction field for the electrons has an influence on the operation of the MOT:

1. **Distortion of position spectrum:** Under otherwise field-free conditions, apart from the presence of the electric and magnetic extraction fields, the resulting spot of ion hit positions on the ion detector usually is circular. It was reported in [**?**, 18] that the presence of a magnetic field gradient of a MOT, deforms the circular spot into an elliptical shape, thereby reflecting larger transversal momenta than really present in the momentum distribution.

2. **Shift of trapping position:** In a standard 3D MOT the trapping potential has its minimum at the zero crossing of the magnetic field gradient. The static magnetic extraction field for the electrons however shifts the zero crossing of the magnetic field gradient, which is usually the geometric center of a pair of coils in Antihelmholtz configuration and consequently the position where the atoms are trapped.

In order to obtain position spectra, that are not changed by the magnetic field gradient of the MOT, the magnetic field has to be switched off prior to ionization. The off switching should happen as fast as possible, since as soon as the MOT is switched off, the atomic cloud can freely expand and the target density decreases. Experiments with fast switching of magnetic fields, e.g. by the use of a metal-oxide semiconductor field-effect transistor (MOSFET), have been reported in [19, 20, 21, 22]. With respect to pulsing the MOT magnetic field, the second point is of importance. On one hand, an amplitude change of the static magnetic extraction field, requires a readjustment of trapping beams, because of the shift in trapping position. On the other hand, everytime the MOT magnetic field is changed while the cooling beams are still on, the atomic cloud gets accelerated due to the position change of the trapping potential minimum. This effect can be avoided by switching off the cooling beams, before the MOT magnetic field is changed. Another solution was reported in [22], which made use of a so-called 2.5 MOT configuration, in which the trapping position is independent of the position of the zero crossing of the magnetic field gradient due to different beam polarizations.

1.1 Momentum reconstruction in a ReMi

As stated in the previous section, the detectors of a Reaction Microscope yield information about the time of flight (TOF) of a recoil ion, i.e. the time difference between the time when the ion impinges on the detector and its time of birth. Without going yet into detail about the detector system, which will be outlined in Sect. 1.3, in this section it will be explained how the initial momentum of the charged fragment, at time of birth, is reconstructed solely based on the knowledge of the electric and magnetic extraction field strength.

The homogeneous electric and magnetic field are applied antiparallelly and parallel to the spectrometer axis, given by the z- axis in Fig. 5, while the electric field is confined to an acceleration region around $z = 0$. The reconstruction of initial momenta of ions and electrons

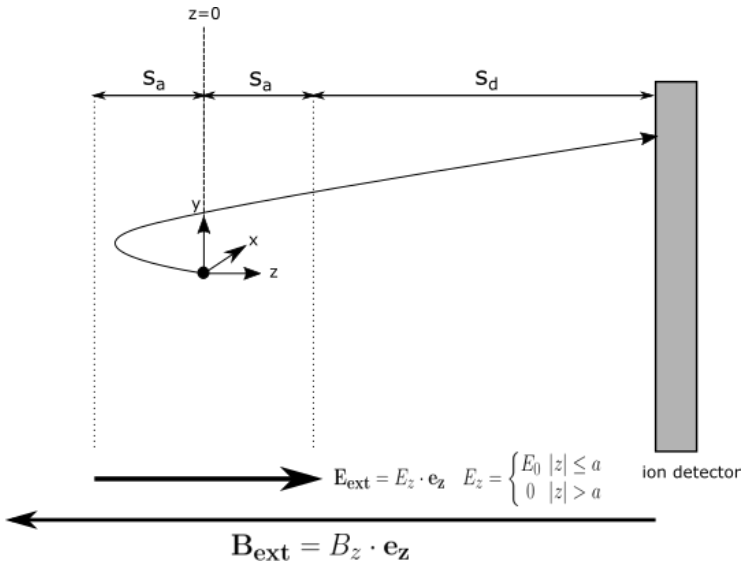

Figure 5: Principle of a REMI: An electric extraction field is applied along the spectrometer axis within an acceleration region and is zero within the drift region. Additionally a magnetic extraction field is applied antiparallel to the electric field to confine the electron trajectories and which is homogeneous across the acceleration and drifting region the whole distance between the reaction volume and the electron detector.

in a Reaction microscope, relies on the fact, that the motion of a charged particle in a such combination of a homogeneous magnetic and electric extraction field is decoupled and has analytical solutions, i.e. the equation of motion $m\frac{d\mathbf{v}}{dt} = q\left(\mathbf{E}(\mathbf{r}) + \mathbf{v} \times \mathbf{B}(\mathbf{r})\right)$ can be solved analytically for the longitudinal motion $\mathbf{r}_{\parallel}(t)$ along the spectrometer axis and the motion $\mathbf{r}_{\perp}(t)$ transversal to the spectrometer axis:

$$m\frac{d\mathbf{v}_{\parallel}}{dt} = q\mathbf{E_{ext}}, \tag{1}$$

$$m\frac{d\mathbf{v}_{\perp}}{dt} = q(\mathbf{v}_{\perp} \times \mathbf{B_{ext}}). \tag{2}$$

Therefore in the following discussion of the analytical solutions, physical quantities like kinetic energy and momentum will be split into their components parallel and perpendicular to the spectrometer axis.

1.1.1 Reconstruction of longitudinal momentum for ions and electrons

For a given acceleration potential U from $z = 0$ to the end of the acceleration region at $z = s_a$, the projection of the electric field on the spectrometer axis can be stated as

$$\mathbf{E_{ext}} \cdot \mathbf{e_z} = \begin{cases} \frac{U}{s_a} & |z| < s_a \\ 0 & |z| \geq s_a \end{cases}.$$

If an atom with mass m becomes ionized in the reaction volume, it might start with small amount of longitudinal kinetic energy $E_{kin,\parallel} = \frac{p_{\parallel}^2}{2M}$ due to the interaction, where $p_{\parallel} = m \cdot v_{\parallel}$ is the initial longitudinal momentum. The recoil ion might initially either move away $(-)$

or towards (+) the detector, its resulting time-of-flights would be $TOF_{\pm}(E_{kin,\parallel})$. The recoil ion first gets constantly accelerated within the acceleration region of extension s_a. The gain in kinetic energy amounts to $qU = q \cdot E_z \cdot s_a$, where q is the charge of the recoil ion. After leaving the acceleration region, the recoil ion drifts with constant velocity in the drift region of extension s_d until it impinges on the MCP. Let qU be be the potential by which the recoil ion gets accelerated towards the detector in the acceleration region and q its charge state, then the recoil-ion TOF as a function of their small initial kinetic energy $E_{kin,\parallel}$ is[3]

$$TOF_{\pm}(E_{kin,\parallel}) = \sqrt{m}\left[\frac{2a}{\sqrt{E_{kin,\parallel}+qU}\pm\sqrt{E_{kin,\parallel}}}+\frac{d}{\sqrt{E_{kin,\parallel}+qU}}\right] \tag{3}$$

$$= f\sqrt{\frac{m}{2qU}}\left[\frac{2a}{\sqrt{1+\epsilon}\pm\sqrt{\epsilon}}+\frac{d}{\sqrt{1+\epsilon}}\right], \tag{4}$$

where the dimensionless parameter $\epsilon = \frac{E_{kin,\parallel}}{qU}$ has been introduced, which is usually very small, so that an expansion of Eq. 4 around $\epsilon = 0$ to first order is a reasonable good approximation. The first term in Eq. 4 corresponds to the time the recoil ion spends in the acceleration region, while the second term corresponds to the flight time of the recoil ion in the drift region. The prefactor $f = 1018.05 \times \frac{ns}{cm}\sqrt{\mathrm{eV/amu}}$ has been introduced, so that Eq. 3 yields the TOF in ns, if the ion mass m is given in atomic mass units, the distances in cm, and the energies in eV. A typical TOF distribution showing backward and forward emission with almost equal probability is depicted in Fig. 6. The position of the symmetry center of the TOF distribution corresponds to recoil ions with $p_\parallel = 0$ and according to Eq. 3 it is given by

$$t_0 \equiv TOF(p_\parallel = 0) = f\sqrt{\frac{m}{2qU}}(2s_a + s_d) \tag{5}$$

In order to reconstruct $p_\parallel = \sqrt{2mE_\parallel}$, we need an inversion $E_\parallel(TOF)$ of Eq. 3. For a symmetric TOF distribution, we can define the time offset Δt with respect to t_0 via $2\Delta t = t_-(E_\parallel) - t_+(E_\parallel)$ and from Eq. 4 follows exactly without Taylor expansion

$$p_\parallel = f \cdot \frac{qU\Delta t}{s_a}, \tag{6}$$

which assigns, for every channel in the TOF spectrum, the longitudinal momentum of recoil ions or electrons in atomic momentum units, independent of the particle mass. Now f has the value $f = 8.04 \cdot 10^{-3}\frac{\hbar}{a_0} \cdot \frac{\mathrm{cm}}{\mathrm{ns\cdot eV}}$, so that the momentum is given in atomic units of momentum $\frac{\hbar}{a_0}$.

1.1.2 Time-focusing: McLaren configuration

The role of the drift zone becomes clear when we consider the influence of the finite extension of the reaction volume along the spectrometer axis. If the charged fragment was constantly accelerated until the detector, charged fragments which start with a little displacement from $z = \pm\delta z$ would correspondingly have shorter or longer flight times until the position of the detector at $z = z_d$. The ideal momentum resolution at an electric field strength of $\frac{U}{s_a} \approx 1\,\frac{\mathrm{V}}{\mathrm{cm}}$, a time resolution of $\delta t = 1\,\mathrm{ns}$ and the ideal assumption of a point-like reaction volume would amount to 0.01 a.u. from Eq. 6. However a realistic longitudinal, spatial extension of the

[3] here we implicitely assume that all recoil-ions start from the same point representing the reaction volume.

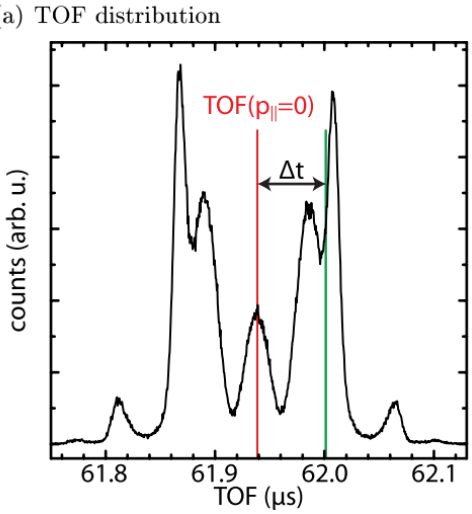

Figure 6: Illustration of a nearly symmetric TOF distribution of recoils ions (from [15]). Different channels of the reaction are reflected in several maxima around the symmetry center of the distribution.

reaction volume, causes a time jitter in arrival time for the recoil ions, since (a) they start at different potentials and (b) travel over different acceleration distances. If Δa is the longitudinal width of the extended reaction volume, from Eq. 3 follows

$$\frac{\delta t}{t} = \frac{2a-d}{4a+2d}\frac{\Delta a}{a}. \tag{7}$$

From Eq. 7 it becomes clear, that the time jitter can be eliminated to first order if the drift distance is chosen to be twice as long as the acceleration distance (so-called McLaren configuration): Charged fragments which start farther away from the detector at $z = -\delta z$ get accelerated by a higher acceleration potential and therefore have time to catch up with the charged fragments starting from $z = 0$. Moreover from Eq. 7, it becomes clear that the time jitter overall can be minimized by choosing large dimensions for acceleration and drift distance.

1.1.3 Reconstruction of transversal momentum for ions and electrons

For initial conditions $\mathbf{r}_\perp(t=0) = (0,0)$ and $\mathbf{v}_\perp(t=0) = \frac{1}{m}(p_{0x}, p_{0y})$ and an external magnetic field

$$\mathbf{B_{ext}} = B \cdot e_z$$

The set of Eqns. 2 in the acceleration and drift zone for ions and electrons can written out to be

$$\begin{aligned} m\frac{d^2x}{dt^2} &= qB\frac{dy}{dt} \\ m\frac{d^2y}{dt^2} &= -qB\frac{dx}{dt}, \end{aligned}$$

and for the initial conditions $\mathbf{r}(0) = 0$ and $\mathbf{v}(0) = \frac{1}{m}(p_{0x}, p_{0y})$ can be solved to give

$$\begin{aligned} x(t) &= \frac{1}{qB}\left(\sin(\omega_c t)p_{0x} + (1-\cos(\omega_c t))p_{0y}\right) \\ y(t) &= \frac{1}{qB}\left((\cos(\omega_c t)-1)p_{0x} + \sin(\omega_c t)p_{0y}\right). \end{aligned} \tag{8}$$

These solutions describe a helical trajectory on the way to the detector with its center being at $(x_0, y_0) = \frac{1}{qB}(p_{0y}, -p_{0x})$, $\omega_c = \frac{qB}{m}$ being the cycloton frequency of the charged fragment, and its radius $R = \sqrt{(x(t)-x_0)^2 + (y(t)-y_0)^2}$ being related to the total transversal momentum $p_\perp = \sqrt{p_{0x}^2 + p_{0y}^2}$ by

$$R = \frac{p_\perp}{q \cdot B}. \tag{9}$$

The solution Eq. 8 can be inversed for the detector hit points (x_d, y_d) to yield for the transversal momenta separately

$$\begin{aligned} p_{0x} &= \frac{qB}{2}\left(\cot\left(\frac{\omega_c T}{2}\right)x_d - y_d\right) \\ p_{0y} &= \frac{qB}{2}\left(x_d + \cot\left(\frac{\omega_c T}{2}\right)y_d\right). \end{aligned}$$

These equations are valid both for ions and electrons. An illustration of a recoil ion and electron distribution on a detector is given in Fig. 7 and 8 respectively. From both equations the total transversal momentum $p_\perp = \sqrt{p_{0x}^2 + p_{0y}^2}$ follows to be

$$p_\perp = \frac{qB}{2}\frac{r}{|\sin(\frac{\alpha}{2})|}, \tag{10}$$

where $r = \sqrt{x_d^2 + y_d^2}$ is the distance from the center of the point distribution (see Fig. 7), and $\alpha = \omega_c T$ is the phase swept by the charged fragment on the way to the detector (see Fig. 8). Additionally we can determine the emission angle φ_e of the charged fragment, by realizing that φ_e is given by $\theta_e(\alpha = 0)$ (compare Fig. 8) and that for$\alpha > 0$ the relationship is maintained by

$$\theta_e = \varphi_e + \mathrm{mod}(\frac{\alpha}{2}, 2\pi),$$

whereθ_e is the angle enclosed between $\mathbf{R_e} = (x_e, y_e)$ and the arbitrarly chosen x-axis.

In practice, for rotationally symmetric recoil ion and electron distributions on a detector, the origin of our coordinate system is usually determined as the "center of mass" of all data points. This "center of mass" point then corresponds to the arrival position of all charged fragments with vanishing transversal momentum $p_\perp$.

In experiment the magnetic extraction field can be measured by comparing the time difference between nodes of e.g. an r vs TOF distribution of electrons for low extraction voltage (see Fig. 9), which corresponds to the cycloton period

$$T = 2\pi\frac{m}{eB_z}.$$

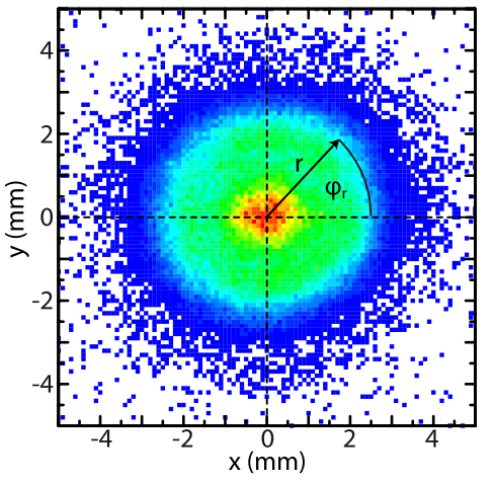

Figure 7: Illustration of the spatial distribution of recoil ions on a detector. From [15].

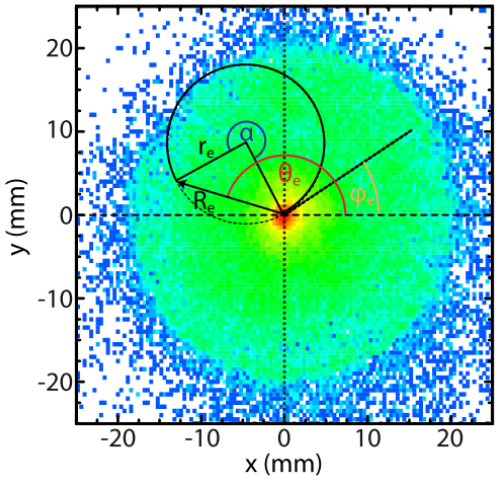

Figure 8: Illustration of the spatial distribution of electrons on a detector. From [15].

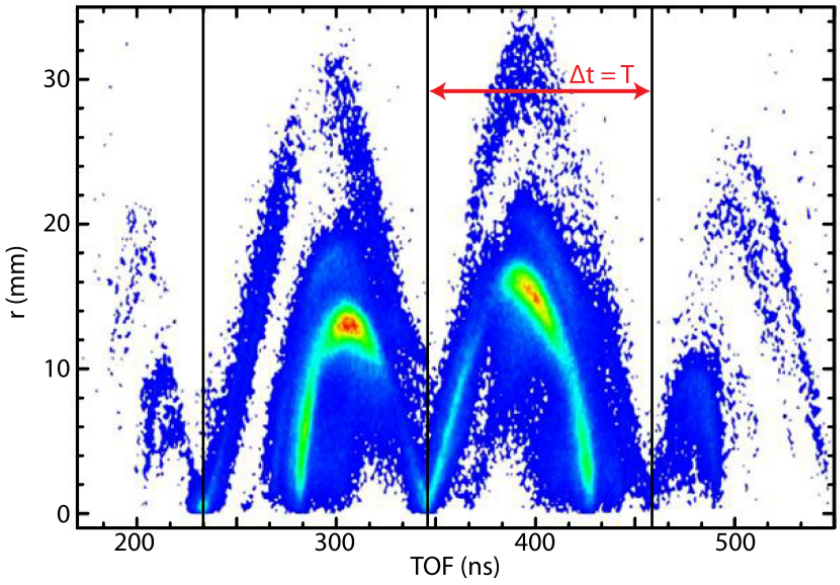

Figure 9: Distance from symmetry center versus time-of-flight (TOF) spectrum for electrons. . From [15].

Often for recoil ions, the approximation is made that their initial transversal velocity is barely influenced by the weak magnetic extraction field (usually < 10 G), and therefore its distance r from the origin [4] depends solely on its initial transversal kinetic energy $E_{kin,\perp} = \frac{p_{\perp,ion}^2}{2m}$. The displacement r of a recoil ion from the center of mass of the distribution on the detector therefore is given by

$$r = \sqrt{\frac{E_{kin,\perp}}{m}} \cdot TOF(E_{kin,\parallel}). \tag{11}$$

The distance r from the origin and therefore the initial transversal momentum $p_{r,\perp}$ clearly depends on the TOF of the recoil ion. If the ion has the initial transversal velocity $v_{r,\perp} = \sqrt{\frac{2E_{kin,\perp}}{m}}$, then the displacement r of the ion from the center of mass would be given by

$$\begin{aligned} r &= v_{r,\perp} \cdot TOF(E_{kin,\parallel}), \\ \Leftrightarrow p_{r,\perp} &= m \cdot \frac{r}{TOF(E_{kin,\parallel})} \end{aligned}$$

Therefore the initial transversal momentum depends on the initial longitudinal momentum. However for most TOF distributions, the magnitude of t_0 (Eq. 5) is on the order of tens of μs, while the width of the TOF distribution spans only a few hundred of ns. Therefore Eq. 5 in good approximation can be plugged into Eq. 11, which yields following expression for the transverse momentum of recoil ions

$$p_{r,\perp} = f\sqrt{mqU}\frac{r}{(2a+d)}, \tag{12}$$

where $f = 8.1847 \cdot \frac{\hbar}{a_0}/\sqrt{\text{amu} \cdot \text{eV}}$ in order for the transverse momentum to be in atomic units. For electrons the practical formula

$$p_{e,\perp} = f \cdot \frac{R_e}{T_e|\sin(\pi\frac{t_e}{T_e})|} \tag{13}$$

can be given where $f = 14.36\frac{\hbar}{a_0}\frac{\text{ns}}{\text{cm}}$ is the pre-factor in order for the momentum to be in atomic units, while the radial distance R_e is given in cm and the electron period T_e in ns.

1.2 The spectrometer

The spectrometer of our MOTRemi is a stacked assembly of gold coated electrodes of outer diameter of 11.2 cm and inner diameter of 8.45 cm which are mutually isolated with the gap between adjacent electrodes being about 1 mm (see Fig. 10) . In the MOT region 3 cm wide gap has been cut into the electrodes to allow for the trapping laser beam for the x and y direction to pass. Additionally and not visible in Fig. 10, for the z beam of the MOT to allow passing the spectrometer, a circular aperture is cut into three of the middle electrodes. The influence of this openings on the electric extraction field of the otherwise perfectly shielding spectrometer has been checked in a previous PhD thesis [18] by importing the CAD model of the spectrometer into the TOSCA electrostatic solver software. It was found that the openings did not have a critical effect on the extraction field, even when the boundaries on ground potential were placed only 1.5 cm away from the opening.

[4] again a transversal extension of the reaction volume is neglected first

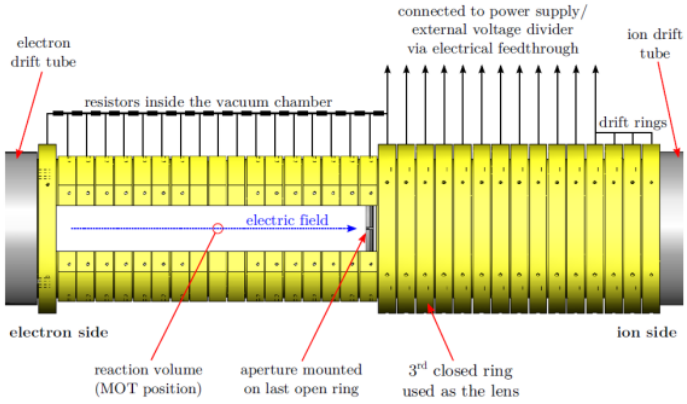

Figure 10: Detailed schematic of our spectrometer, consisting of 33 gold-plated electrodes, each having a width of 11.5 mm, stacked together and mutually isolated by 1 mm thick ceramic spacers. 19 adjacent of the 33 electrodes are connected intra vacuum in series with 18 k thin film resistors (prior to installation tested to have deviations of less than 0.1%), while the rest is connected to external voltage dividers via electrical feedthroughs.

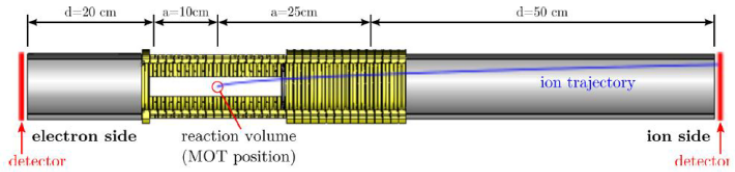

Figure 11: Schematic of spectrometer with drift tubes and detectors, showing the McLaren configuration of our Remi with respective ion and electron acceleration and drift distances. The extraction fields in our experiment typically were between 0.43 $\frac{\text{V}}{\text{cm}}$ to 0.86 $\frac{\text{V}}{\text{cm}}$.

1.3 The detector system

A particle detector in our reaction microscope is comprised of several components, among which the most important ones are (in the order of proximity to the drift tube): two stacked micro-channel-plates (MCP) and a delay line anode on the ion side and a delay line hexanode on the electron side (see Fig. 12).

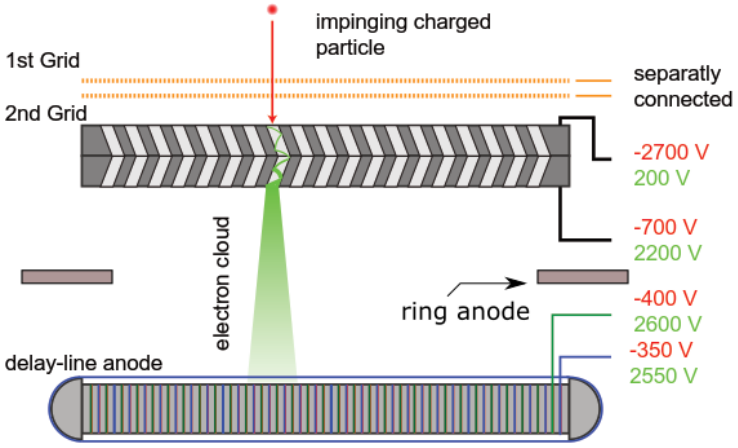

Figure 12: Schematic cross section of detector assembly: Grids, MCP stack, ring anode and delay-line anode are eletrically insulated from each other by ceramic spacers, not shown in the cross section. Typically applied voltages for ions (red) and electrons (green) to the MCPs and the delay line anode are shown on the right. (slightly adapted from [15])

A single MCP basically is a plate equipped with a narrow grid of miniature electron multipliers (see following section 1.3.1) which produce electron clouds on the plate's back side at the hit position of the weakly charged particle on its front side. The electron clouds then are picked up by a delay line anode (see section 1.3.2) which produce voltage spikes that can be measured and used to calculate position information. The MCPs require high operation voltages on the order of $2 - 3\,\mathrm{keV}$, which is why strong voltage gradients close to and inside the detector volume occur. In order to screen the potential of the MCPs from the drift region, which must be field free, two high transmittivity grids are positioned next to the drift tubes and are set to the same potential as the drift tube[5]. In order to guaruantee a homogeneous electric field without any transversal component between MCP and delay-line anode, that might change the 1:1 imaging property of the detector, a ring anode, i.e. a conducting plate with a round hole of diameter corresponding to the outer diameter of the MCP, is positioned in between. The sign of the voltages inside the detector depends on the sign of the charge of the charged particles, i.e. negative voltages are used in case of ions and positive voltages for electrons. Since after the MCP only electrons are accelerated, ring potential must be higher than MCP potential and delay-line anode potential must be higher than ring anode potential.

Naturally, in a real-world reaction microscope, not all charged particles, that are created within the ionization volume, will be detected. The probability of detecting a charged particle depends on the acceptance of the spectrometer, the transmission T_{grid} of the grids and the absolute detection efficiency P_{abs}^{MCP} of the MCPs. Under the assumption of a full 4π collection efficiency, an absolute detection effieciency $P_{abs}^{MCP} = 58\,\%$ [23] and a throughput of$T_{grid} \approx 78\,\%$ for a single grid[6], a maximum detection efficiency can be estimated to be

$$P_{max}^{Det} = P_{abs}^{MCP} \cdot T_{grid}^2 \approx 35\,\%.$$

[5] Additionally, the second grid suppresses feedback between ion and electron detector.
[6] which can be calculated from geometrical properties of the grid

1.3.1 The micro-channel plate

A micro-channel plate (MCP) is a plate fabricated from a lead glass, which exhibits an array of parallel, round channels, typically with diameter of 10 μm and 15 μm center-to-center spacings ([24]). The inner wall of these channels are coated with a semiconductor, while parallel electric contact to both ends of each channel is provided by a metallic coating to the front and back-side of the MCP. Each channel then constitues a miniature electron multiplier, where the front and back side of the MCP serve as input and output electrode, and the total resistance between the electrodes is on the order of 10^9 Ohms. By application of a high voltage between both electrodes, weakly charged fragments with a minimum kinetic energy can trigger an avalanche of up to 10^7 secondary electrons, thereby producing a cloud of electrons at the end-electrode of a micro channel, whose "center-of-mass" represents the hit position of the charged fragment (see Fig. 13).

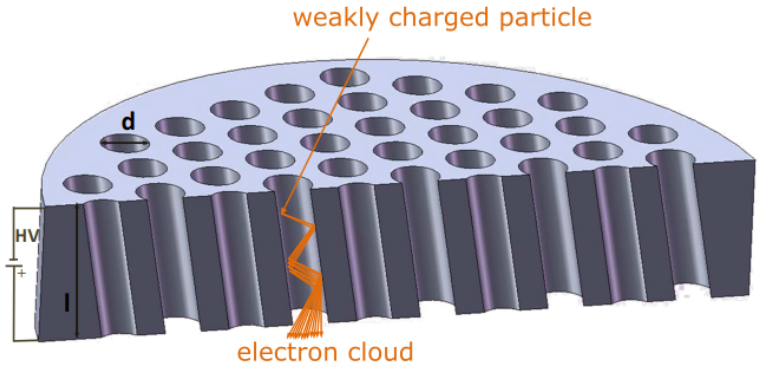

Figure 13: Schematic of a micro-channel plate: An array of micro-channels of diameter typically $d = 10$ μm in a plate of lead glass. Each micro-channel constitutes a miniature electron multiplier producing an electron cloud at the postion of the micro channel on the back side of the MCP (Slightly adapted from [25]).

In order to optimize the electron multiplication factor, the channels are inclined by 8° to the front plane of the MCP, so that secondary electrons which are accelerated vertically to the plane of the MCP by the high voltage between front and back plate, are forced to further collisions with the inner walls of the micro channels. MCPs can be used singly or in a cascade, therefore allowing to spatially resolve the hit position of weakly charged particles[7] together with ultra-high time resolution (< 100 ps). In each of our two detectors a stack of two MCPs of diameter 80 mm in *Chevron* configuration is used, i.e. the micro channels of the two plates have opposite orientation (illustrated in Fig. 12), which further enhances amplification and reduces the probability, that ions produced in the micro channel walls will leave the MCPs on the front plate. With this setup an electron multiplication factor of about 10^6 at a voltage of about 2 kV along both plates can be achieved. When an electron avalanche is triggered within a micro channel, charge is replenished to the semi-conducting walls by the external power supply. This causes a short voltage drop, which can be read out via a capacitor and serves as a stop time t_0 for determination of the flight time and as a start time for the determination of the hit position in combination with a delay line anode. The start signal t_{start} for determination of the time of flight $TOF = t_0 - t_{start}$ is provided by an external

[7] The spatial resolution of an MCP is limited only by the channel dimensions and spacings in between.

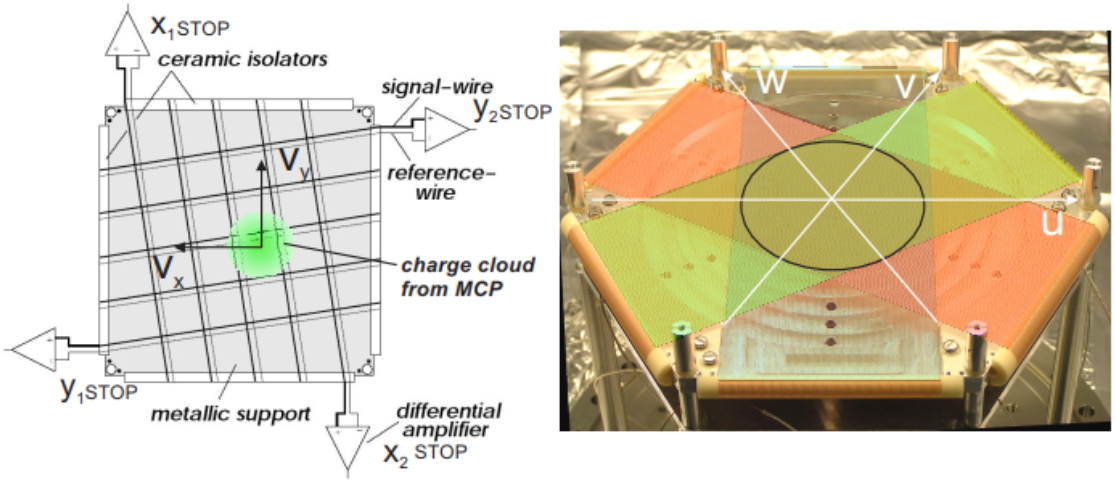

Figure 14: Left: Schematic of a simple two-layered delay-line anode. Right: Picture of a three-layered delay-line hexanode used for the electron detector in our experiment. (from [18])

trigger signal associated with the arrival of the projectile beam, e.g. coming from a PD in the case of ionization with fs laser pulses and therefore reflects the time-of-birth of an ion.

1.3.2 The delay line anode

An anode consists of different layers of parallely wound wire around a plate. Each layer consists of two parallel wires, the signal and reference wire, wound around a base plate with a spacing of $\Delta x = 1\,\mathrm{mm}$ per revolution. The base plate is insulated from the wires by ceramic rims at its edges (see Fig. 14) and there is no electrical contact between signal and reference wire in each layer or between the different layers.

When an electron cloud impinges on the delay line anode, the signal wire picks up the main fraction of the charge, because it is biased with a slightly more positive potential compared to the reference wire. At the end of both wires a signal difference between signal and reference wire is extracted via a differential amplifier. This has the advantage, that common mode noise present on both wires, is effectively substracted.

The operating principle of a delay line anode is to reduce position measurements to time measurements, as depicted in Fig. 15. When an electron cloud impinges on this delay line anode, it creates a charge distribution within neighboring windings of the anode, which travels *with equal signal speed* in both directions, thereby producing a series of voltage spikes at both ends (see Fig. 16), which are again read out capacitatively. The spatial "center of mass" coordinate of the electron cloud perpendicular to the direction of wire therefore is given by the difference of arrival times t_1 and t_2 between both *envelopes*, which belong to the series of measured voltages spikes, i.e.

$$x = v_\perp \left((t_1 - t_0) - (t_2 - t_0)\right) = v_\perp (t_1 - t_2). \tag{14}$$

In this equation $v_\perp = c\frac{\Delta x}{l}$ is the effective propagation velocity of the charge distribution perpendicular to the windings of the anode, determined by the spacing Δx between the wires and the total length l of the delay line anode wire, and it relates the measured times to the position. Because t_1 and t_2 refer to the arrival times *of the envelopes* on both ends, the

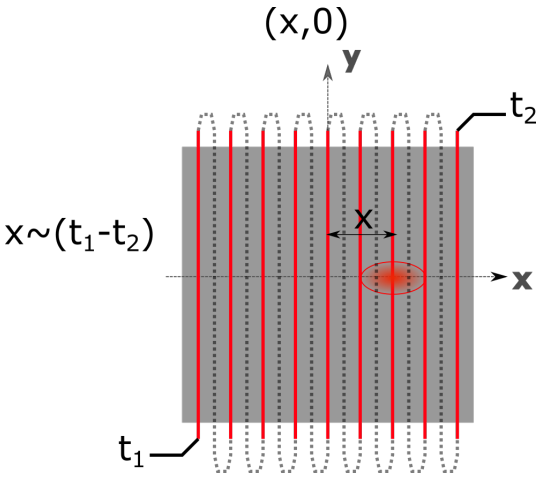

Figure 15: Simplest schematic of a delay-line anode with only one wire and one layer.

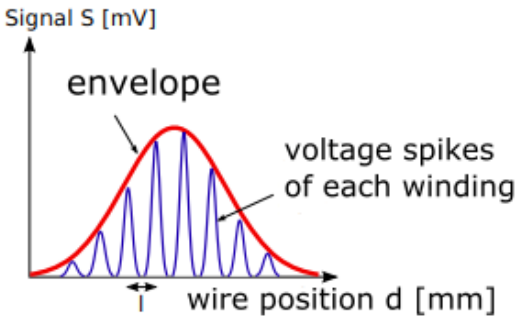

Figure 16: Typical form of a capacitively measured series of voltages spikes on one end of a layer of a delay line anode, if it was measured directly at the delay line anode. Due to dispersion in signal cables, usually only the envelope of theses spikes is visible.

position resolution of a delay line anode is not fundamentally limited by the spacing between neighboring windings. The coordinate system here is chosen such, that $x = 0$ corresponds to the middle of the delay line anode's layer. Equation 14 however is only strictly valid, when the electron cloud hits the delay line anode at $y = 0$. If the electron cloud hits the delay line anode at (x, y) the time difference $t_1 - t_2$ between both signals is increased by $2\frac{y}{c}$. In a two-layered delay line anode, this additional time delay also affects the y coordinate, so the apparent coordinates (x', y') in terms of the true coordinates (x, y) are given by

$$\begin{aligned} x' &= x + 2\frac{v_\perp}{c}y, \\ y' &= y + 2\frac{v_\perp}{c}x. \end{aligned}$$

An important consistency checks for the signals on the delay line anode is given by the time sum condition

$$t_{sum} = (t_1 - t_0) + (t_2 - t_0) = const., \tag{15}$$

for which we need the MCP hitting time t_0 as a start signal. The sum of travel times for the charge distribution to travel to the left and to the right end of the delay line anode wire is constant and independent of its position, since the signal speed is the same in both directions and the total travel time only depends on the length of the anode wire and other cables used for electronic preprocessing of the signals.

In our experiment we use a two-layered delay line anode for the ion detector and a three-layered hexanode (see Fig. 14) for the electron detector. The hexanode detector has enhanced multihit acceptance compared to the standard two-layered delay line anode and the equations for reconstruction of the hit coordinates are described in [26].

1.3.3 The signal box and data acquisition

For voltage supply of all the components within a detector, but the two grids which are supplied independently, and outcoupling of the voltage spikes which occur at high voltage on the wires of a delay line anode, we employ a signal box of which the basic outcoupling circuit is depicted in Fig. 17. The full schematic of the signal box can be found in the appendix.

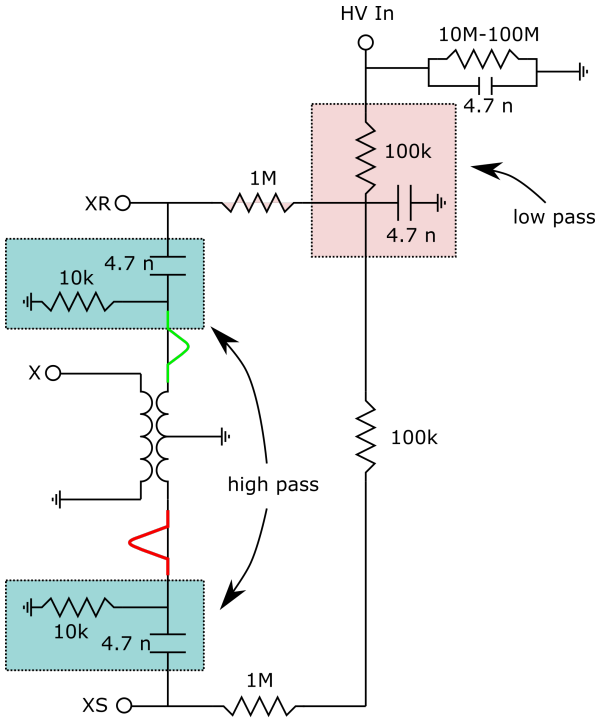

Figure 17: Basic signal box circuit for outcoupling of the voltage spikes on a delay line anode with a transformator.

The high voltage is blocked by passive high pass filters with a cut-off frequency of about $f_c \approx 3.4\,\mathrm{kHz}$ and the AC components of signal and reference wire of one layer in a delay line anode flow in opposite directions through the coil of a transformator, thereby effectively canceling out common-mode noise on both wires. The resulting voltage spike is inductively outcoupled and then post-processed by our data acquisition. Our data acquisition system is based on a Flash ADC system (Chronologic Ndigo Series) with three Ndigo5G-10 cards, each of which has four ADC channels with sample rates up to 5 Gs/s and a resolution of 10 bits, and one high resolution time-to-digital converter (TDC) channel which is compatible with NIM signals[8] and has a time resolution down to 13 ps.

The outcoupled MCP signals are analog in nature, their peak-amplitudes vary from hit to hit, while the rise-time until the peak-amplitude is reached is constant , and their form can be described to first order by a Gaussian (as illustrated in Fig. 18).

[8]The NIM standard is a logic standard in experimental particle and nuclear physics with a current-based logic and negative true (about -23 mA into $50\,\Omega \approx -1.15$ V

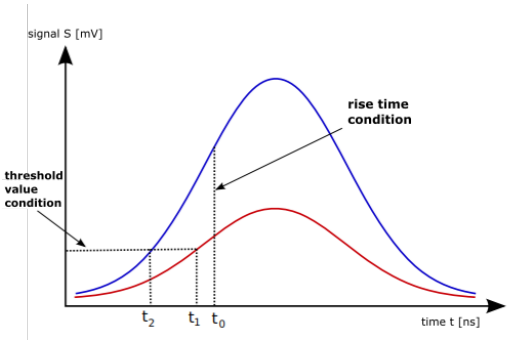

Figure 18: Illustration of difference in determination of t_0 when using threshold value condition or rise time condition.

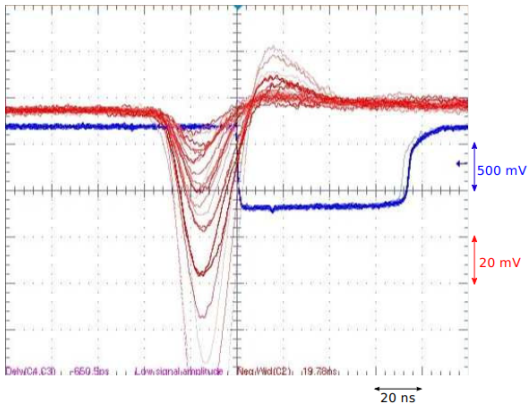

Figure 19: Illustration of NIM signal as output (blue) of our comercial CFD (Ortec-935) from an analog input signal of varying amplitude, but constant rise time.

This varying peak-amplitude would lead to a jitter in determination of t_0, which is used in the TOF determination and in the equation for the time sum Eq. 15, if the time t_0 was determined simply via a voltage threshold. Therefore a constant fraction discriminator (CFD) is used[9], which employs a so-called rise time condition, i.e. it determines the time t_0 when a certain fraction of the peak-amplitude is reached, which is independent of the total peak-amplitude.

The advantage of our Flash-ADC based data acquisition system is, that each ADC channel stores whole traces of duration of a few tens of μs, which can be post-processed via software. Therefore we can extract the time stamp t_0 of an arbitrary pulse within each traces by applying a software written CFD to it. Furthermore our data acquisition is configured to read out up to three hits, something which is not possible with just a CFD. Only the TDC channels of our cards receive NIM-signals (see Fig. 19) as an output of an electronic CFD (Ortec-935), whose input are amplified pulses from the ion MCP.

[9]Details about the working principle of a CFD can be found in the literature.

Part III
Atom-light interactions

Within the scope of this thesis, we subjected the atoms in our experiment to two types of laser fields. On one hand we applied continuous-wave (CW) lasers for laser cooling and trapping of ^{6}Li atoms and $^6Li_2$ molecules. The laser system for laser cooling had to be spectrally narrow and near-resonant with two specific cooling transitions in our ^{6}Li atoms at 670 nm. The laser system for purely optical trapping provided CW light in the near-infrared region at 1070 nm, which was far-off resonant with the laser cooling transition, but provided high powers up to 200 W. On the other hand we employed a laser system which provided spectrally broad laser pulses with a duration of about 30 fs and peak intensities of up to $\sim 10^{15}\frac{W}{cm^2}$. This laser system was used for ionization of the atoms and molecules which were trapped in our far-off resonance optical trap. The starting point for the theoretical description of the atom-light interaction with both types of laser fields is time-dependent perturbation theory, which will be shortly outlined in the following section. The main objective of 2 is however to introduce the reader to the idea, that the radiation force excerted on a two-level atom by a near-resonant CW field, comprises of a spontaneous force and a gradient force, which correspond to the phase-shifted and in-phase reponse respectively of the atom's electric dipole to the oscillating electric field. In Sec. 3, it will be explained how the spontaneous force can be used to effectively cool down an ensemble of two-level atoms and create an "optical molasse". In Sec. 3.1, the reader will be acquainted with the level structure of ^{6}Li relevant for laser cooling, which will leave clear how the approximation of a two-level system can be accomplished by just driving two cooling transition in ^{6}Li. Furthermore Zeeman shifts in the level structure of ^{6}Li will be outlined, which are necessary to understand, how a magneto-optical trap confines ^{6}Li atoms and is loaded by slowing down thermal atoms (see Sec. 4). Subsequently in Sec. 5, it will be explained how the gradient force can be used for purely optical trapping of atoms and how inelastic collisions can shorten the lifetime of the trapped atomic ensemble. Finally in Sec. 6, the most important ionization mechanism for atoms in strong fields will be outlined.

2 Radiation force on a two level atom at rest

In general, in order to calculate the time evolution of an atom in a time-dependent radiation field, the total Hamiltonian is split into a time-independent part $H_0$and the time-dependent perturbation $W(t)$

$$H(t) = H_0 + W(t).$$

H_0 describes the atom *only with static magnetic and/or electric fields* and its time-independent Schrödinger equation

$$H_0|\varphi_n\rangle = E_n|\varphi_n\rangle$$

in general can be solved by numerical diagonalization[10]. The interaction of the atom with the radiation field is described by $W(t)$ and the electromagnetic field is treated classically. The general solution of the time-dependent Schrödinger equation

$$H(t)|\Psi_n(\mathbf{r},t)\rangle = i\hbar\partial_t|\Psi_n(\mathbf{r},t)\rangle \tag{16}$$

[10]In the case of the hyperfine ground states of ^{6}Li, it has been done analytically (see [27]).

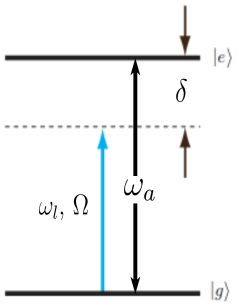

Figure 20: Two level atom. Ground and excited state are seperated by a transition with frequency ω_a.

is then expanded in the eigenfunctions of H_0, i.e. $|\Psi(\mathbf{r},t)\rangle = \sum_k c_k(t)|\Phi_k(\mathbf{r})\rangle e^{-iE_kt/\hbar}$[11], so that the time-dependent Schrödinger equation 16 becomes equivalent to [28]

$$\frac{dc_j(t)}{dt} = \frac{1}{i\hbar}\sum_k c_k(t)W_{jk}(t)e^{i\omega_{jk}t}, \tag{17}$$

where $W_{jk}(t) = \langle\phi_j|W(t)|\phi_k\rangle$ is the perturbation matrix element and $\omega_{jk} = (E_j - E_k)/\hbar$ the transition frequency. There are two important approximation, within which eqns. 17 can be solved:

1. **Perturbation approximation:**
   (a) The system is initially in state $|i\rangle$, i.e. $c_k(t=0) = \delta_{ik}$
   (b) The perturbation is very weak and/or applied for a short period of time, i.e. $|c_k(t)| \ll 1$ for all $k \neq i$.
2. **Two-level approximation:** The summation of eqns. 17 gets truncated to just two terms, describing the coupling between a single ground and excited state.

The latter approximation is the famous Rabi two-level problem [29], which is typically realized when a spectrally narrow laser (or maser) is tuned in or close to an atomic resonance frequency of a transition between a single ground $|g\rangle$ and an excited state $|e\rangle$[12].

When an atom is subjected to a monochromatic, plane travelling light wave with unit polarization vector ϵ, travelling in positive z-direction $\mathbf{E}(z,t) = \mathrm{Re}\left[E_0\epsilon e^{i(kz-\omega_l t)}\right]$, the coupling between two discrete levels *in dipole approximation* is described by the perturbation

$$W(t) = -\mathbf{d}_a \cdot \mathbf{E}(t),$$

where $\mathbf{d}_a = -e\mathbf{r}$ is the atomic dipole moment and $\mathbf{E}(t) = \mathrm{Re}\left[E_0\epsilon e^{-i\omega_l t}\right]$ evaluated at $z = 0$ because the spatial variation of the electric field over the atom's extension is considered to be neglible for optical wavelengths[13]. Since $\mathbf{r}$ has odd parity, its diagonal matrix elements vanish

[11] which is mathematically equivalent to a transformation into the rotating frame or interaction picture

[12] It was first studied by Rabi in the context of magnetic resonance, sixteen years before the first maser was produced by Townes.

[13] An atom's extension is on the order of several Bohr radii $a_B \approx 0.05$ nm, so the dipole approximation only seizes to be valid for wavelengths in the X-ray regime or shorter.

and the perturbation matrix elements $W_{ij} = \langle i|W(t)|j\rangle$can be written in the $\{\,|g\rangle, |e\rangle\}$basis as

$$W(t) = \begin{bmatrix} 0 & \Omega \\ \Omega & 0 \end{bmatrix} \cos\left[\omega_l t\right] \tag{18}$$

where the coupling strength between the two levels is given by the resonant real Rabi frequency

$$\Omega \;=\; \frac{E_0}{\hbar} \cdot \langle e|\epsilon \cdot \mathbf{d}_a|g\rangle,$$

which is an angular frequency. The transition electric dipole moment integral $\langle e|\mathbf{d}_a|g\rangle \sim \langle e|\mathbf{r}|g\rangle$ only does not vanish if the transition is a dipole-allowed transition and $\langle e|\epsilon\cdot\mathbf{d}_a|g\rangle$ only does not vanish if the transition is allowed with the polarization ϵ on angular-momentum grounds. Since the characteristic time for the change of the internal atomic state is considerably higher, than the period of oscillation of the light field, we aim not for an exact, but a time averaged evolution of Eq. 17 with the specific Hamiltonian stated in Eq. 18, by neglecting all high frequency components, i.e. all terms which rotate with ω_l or faster. This is called the Rotating-Wave-Approximation (RWA). The Rabi problem for a dipole-allowed transition after application of the RWA, then amounts to solving

$$i\frac{dc_g(t)}{dt} \;=\; c_e(t) \cdot \Omega^* \frac{e^{i\delta t}}{2} \tag{19}$$

$$i\frac{dc_e(t)}{dt} \;=\; c_g(t)\Omega \frac{e^{-i\delta t}}{2}, \tag{20}$$

where one defines the laser detuning from the atomic resonance frequency as$\delta \equiv \omega_l - \omega_a$. For initial conditions $c_g(0) = 1$ and $c_e(0) = 0$ the solution for the ground and excited state coefficient

$$\begin{aligned} c_g(t) &= \left(\cos\frac{\Omega' t}{2} - i\frac{\delta}{\Omega'}\sin\frac{\Omega' t}{2}\right) e^{i\delta t/2} \\ c_e(t) &= -i\left(\frac{\Omega}{\Omega'}\right)\sin(\frac{\Omega^{'} t}{2})e^{-i\delta t/2}, \\ \Omega^{'} &= \sqrt{\Omega^2 + \delta^2}, \end{aligned}$$

where $\Omega^{'}$ is the off-resonant Rabi frequency, shows that the populations of $|g\rangle$ and $|e\rangle$ undergo undamped (Rabi) oscillations and in the resonant case $\delta = 0$ a complete population inversion is possible after $t = \frac{\pi}{\Omega}$. Since only an electric dipole coupling between exactly two levels is considered, the solution fulfils $|c_g(t)|^2 + |c_e(t)| = 1$ at any time, i.e. total population is conserved. The solution to the Rabi problem gives answer about the effect of a spectrally narrow radiation field on the electronic state of a two-level atom.

However the radiation field also exerts a radiation force for which the expression is given by [30]

$$F(\mathbf{r}, t) = \langle \mathcal{D}_e(\mathbf{r}, t) \cdot \nabla E(\mathbf{r}, t)\rangle, \tag{21}$$

where $\mathcal{D}_e = \mathrm{Tr}\,(\rho d_{a,\epsilon})$ is the quantum mechanical expectation value of the projection of the dipole moment on the light field's polarization vector

$$d_{a,\epsilon} = \epsilon \cdot \mathbf{d}_a,$$

and$\langle \cdots \rangle$ refers again to a time-averaging equivalent to the RWA, because the radiation force is a time-averaged effect. Acknowledging that the diagonal elements of the dipole moment vanish, and using the complex Rabi frequency $\hbar\Omega(\mathbf{r},t) = \langle d_\epsilon \cdot E(\mathbf{r},t)\rangle$, Eq. 21 can be written for a general light field $E(r,z)$

$$F(\mathbf{r},t) = \hbar\left(\left(\nabla\Omega(\mathbf{r},t)\right)\rho_{eg}^{*} + \left(\nabla\Omega^{*}(\mathbf{r},t)\right)\rho_{eg}\right),$$

where the off-diagonal elements $\rho_{eg} = c_e^* c_g$ of the density matrix are the optical coherences, which must be determined from the so-called *optical Bloch equations*, see next section on molasse cooling. Let's consider the idealized case of a plane wave with only axial dependence $E(z) = \mathrm{Re}\left[E_0(z)e^{i\varphi(z)}\right]$. The gradient of the Rabi frequency can be divided into a real and an imaginary part by writing it with help of the logarithmic derivative $\frac{\partial\Omega(z)}{\partial z} = (q_r + iq_i)\Omega$:

$$F_z = \underbrace{\hbar q_r\left(\Omega\rho_{eg}^{*} + \Omega^{*}\rho_{eg}\right)}_{F_{grad}} + \underbrace{i\hbar q_i\left(\Omega\rho_{eg}^{*} - \Omega^{*}\rho_{eg}\right)}_{F_{sp}} \tag{22}$$

At this specific case, it can be seen that the force excerted on an atom by a light field can be split into two components:

- the *spontaneous* force F_{sp}, which is the imaginary part and proportional to the gradient of the phase $\varphi(z)$, and
- the *optical dipole* or *gradient* force F_{grad}, which is the real part and proportional to the gradient of the field $E_0(z)$.

The spontaneous force is also called *dissipative*, because it cannot be derived from a potential and as it name tells, it is based on subsequent deexcitation of the excited state by spontaneous emission, which has to be taken into account for determination of the optical coherences. A concrete expression for the spontaneous force in the case of a travelling plane wave will be derived in the next section 3 on molasse cooling. The gradient force on the other hand is *dispersive*, because it is conservative and therefore can be represented by a potential. It vanishes for an idealized, unphysical plane travelling wave, but a real laser beam, which is a solution of the scalar wave equation, exhibits curvatures in radial, as well as in axial direction and therefore always has a non-vanishing gradient force. The gradient force can trap an atom in the focus of a laser beam, because that's where the gradient of the field $E_0(z)$ is strongest.

In the near-resonant case, the spontaneous force is several orders of magnitude stronger than the optical dipole force and it is responsible for molasse cooling as described in the next section 3. However an important difference between the two types of forces is, that the magnitude of the spontaneous force has an upper limit, directly connected to the decay rate of the excited state, which it cannot surpass no matter how much power is put into the light field. The gradient force in contrast can in principle be made arbitrarily large by increasing the power or the gradients of the light field.

The optical dipole potential already emerges from the Rabi problem as an *AC stark shift (or light shift)* of the energy levels of the ground and excited state. By performing a change of basis $|e\rangle \rightarrow e^{i\delta t}|e'\rangle$ the time-dependence can be removed from $W(t)$ and the Hamiltonian can be written as

$$\hat{W} = \frac{\hbar}{2}\begin{bmatrix} 0 & \Omega \\ \Omega & -2\delta \end{bmatrix}.$$

The corresponding energies of this Hamiltonian are

$$E_e = \frac{\hbar}{2}\left(-\delta - \Omega'\right) \tag{23}$$

$$E_g = \frac{\hbar}{2}\left(-\delta + \Omega'\right). \tag{24}$$

A Taylor expansion of these eigen energies for large detunings $|\delta| \gg \Omega$ shows that the energy of each state is shifted by an amount

$$\Delta E = \pm\frac{\hbar\Omega^2}{4\delta} \tag{25}$$

that is proportional to the light intensity, has respectively opposite sign for ground and excited state, and its overall sign depends on the sign of the detuning δ. The optical dipole force will be explained in more detail in 5.

3 Molasse cooling

The spontaneous force on a two-level atom results from repeated spontaneous absorption of a photon and subsequent de-excitation by spontaneous emission. A net momentum transfer occurs, because spontaneous emission occurs isotropically, i.e. the averaged recoil momentum due to spontaneous photon emission is zero. However each time a ground state atom absorbs a photon by spontaneous absorption, it receives a recoil momentum $\hbar k$ in direction of propagation $\frac{\mathbf{k}}{k}$of the photon.

When dealing with a large ensemble of atoms, which cannot necessarily be described by a pure state function $|\Psi(\mathbf{r},t)\rangle$, a statistical description within the density matrix formalism becomes necessary. The time evolution of the density operator $\rho_{ij} = c_i c_j^*$ without spontaneous decay of the excited state can be derived from Eq. 19 and 20. The effect of spontaneous emission on the time evolution of the density operator can be phenomenologically described as an exponential decay of the coefficient $\rho_{eg}(t)$ with a constant rate $\gamma/2$

$$\left(\frac{d\rho_{eg}(t)}{dt}\right) = -\frac{\gamma}{2}\rho_{eg}(t),$$

where $\gamma = \frac{1}{\tau}$ is the decay rate of the excited state and the angular frequency corresponding to the natural linewidth $\Gamma = \frac{1}{2\pi\tau}$. By including this effect and taking into account that the loss of population of the excited state, leads to a gain of population in the ground state, we obtain a set of four equations for the four elements of density operator, which are called *optical Bloch equations* (OBE)*[28]*. By solving the OBE for different perturbations $W(t)$ and inserting the solution into Eq. 22, one arrives at expression for the spontaneous and optical dipole force. By solving the OBE for the steady state, i.e. when all time derivatives $\frac{d\rho_{ij}}{dt}$ are set to zero, we obtain expressions for the population difference $w = \rho_{ee} - \rho_{gg}$ and the optical coherence ρ_{eg}:

$$w = \frac{1}{1+s}$$

$$\rho_{eg} = \frac{i\Omega}{2(\gamma/2 - i\delta)(1+s)},$$

where the saturation parameter s is given by

$$s \equiv \frac{|\Omega|^2/2}{\delta^2 + \frac{\gamma^2}{4}} \equiv \frac{s_0}{1 + (2\delta/\gamma)^2},$$

and the on-resonance saturation parameter $s_0 \equiv I/I_s = \frac{2|\Omega|^2}{\Gamma^2}$ defines the saturation intensity $I_s \equiv \frac{\pi hc}{3\lambda^3\tau}$. From this we obtain the important statement, that the excited state population in steady state is given by

$$\rho_{ee} = \frac{s_0/2}{1 + s_0 + (2\delta/\gamma)^2},$$

which saturates in the limit of high intensity $s_0 \gg 1$ and approaches1/2. This saturation effect then also shows for the de-excitation rate $\gamma_p = \gamma\rho_{ee}$ which saturates accordingly at $\gamma/2$. The equation for the de-excitation rate as a function of detuning δ for $s_0 \gg 1$ can be written as

$$\gamma_p = \left(\frac{s_0}{1+s_0}\right)\left(\frac{\gamma/2}{1+(2\delta/\gamma')^2}\right) \tag{26}$$

with $\gamma' = \gamma\sqrt{1+s_0}$ and shows that the linewidth is broadened from its natural linewidth γ to a power-broadened value γ'.

If we consider again a travelling plane wave $E(z,t) = \frac{E_0}{2}\left(e^{i(kz-\omega t)} + c.c.\right)$ interacting with a two-level atom, the gradient of the complex Rabi frequency (after RWA) is proportional to the gradient of the phase because the amplitude is constant, i.e.$q_r = 0$ and $q_i = k$. If we insert the logarithmic derivative and the optical coherence for the steady state situation into Eq. 22 we obtain an expression for the spontaneous force

$$\begin{aligned} F_{sp} &= \hbar k\gamma\rho_{ee} \\ &= \frac{\hbar k s_0\gamma/2}{1 + s_0 + (2\delta/\gamma)^2}. \end{aligned} \tag{27}$$

The spontaneous force always acts in direction of the wavevector of the plane wave with which the atom is interacting. Since the spontaneous force is proportional to the excited state population in the steady state, it saturates at large intensities $s_0 \gg 1$ and its maximum value is given by $F_{sp} = \hbar k\frac{\gamma}{2}$. The spontaneous force does not grow unboundedly with increasing intensity, since that would increase the rate of stimulated emission, which gives the atom a recoil momentum opposite to the photon's direction of propagation.

The spontaneous force given in Eq. 27 does not assume anything about the velocity v of the atom with respect to the direction of propagation of the photon. If the atom with some finite velocity $v > 0$ counterpropagates the traveling wave, then in the atom's frame the light frequency is Doppler shifted to the blue by $\delta_{Doppler} = \frac{v}{\lambda} > 0$ and the detuning δ in Eq. 27 has to be replaced by an effective detuning $\delta_{eff} = \delta + \delta_{Doppler}$. If in addition an external non-zero magnetic field effectively shifts the transition energy $\hbar\omega_a$ energy levels of ground and excited state to $\hbar(\omega_a + \delta_{Zeeman})$, the effective detuning for the scattering force must be

$$\delta_{eff} = \delta + \delta_{Doppler} - \delta_{Zeeman}.$$

In addition to the velocity-independent spontaneous scattering force F_{sp} of Eq. 27 in a travelling wave, a two-level atom experiences a velocity-dependent damping β, so that the total force on the atom reads

$$F = F_{sp} - \beta \cdot v.$$

This damping coefficient can be derived from the OBE by treating the atom's velocity as a small perturbation and adding first order corrections to the steady state solutions of the OBE for an atom at rest[28] and its expression for a travelling wave is

$$\beta = -\hbar k^2 \frac{4s_0(\delta/\gamma)}{(1 + s_0 + (2\delta/\gamma)^2)^2}.$$

The expression for the damping coefficient is valid for all intensities, and just like the de-excitation rate, it saturates in the limit of high intensity $s_0 \gg 1$. Its maximum value of $\beta_{max} = \frac{\hbar k^2}{4}$ is obtained for $\delta = -\gamma/2$ and $s_0 = 2$. If a two-level atoms moves in the light field of two counter propagating travelling waves, resulting in a standing wave, the velocity-independent spontaneous force spatially averages out and the remaining force is

$$F_{OM} = -\hbar k^2 \frac{8 s_0 \frac{\delta}{\gamma}}{\left(1 + s_0 + (2\delta/\gamma)^2\right)^2} \cdot v. \tag{28}$$

This is intuitively right, because it corresponds to double the damping coefficient of one travelling wave. However Eq. 28 is only valid for low saturation $s_0 \ll 1$. The basic picture behind this damping mechanism, which is called *optical molasse,* is that with light tuned below resonance $\delta < 0$ an atom counterpropagating one travelling wave is Doppler shifted towards the resonance, and farther away from the resonance of the co-propagating travelling wave. Therefore the atom will scatter more light from the counterpropagating beam, than from the co-propagating beam and therefore its velocity is decreased.

However contrary to Eq. 28, the atoms will not be slowed down to $v = 0$, because it does not account for the discrete momentum changes in momentum $\Delta p = \hbar k$ after each cycle of directional spontaneous absorption followed by non-directional spontaneous de-excitation. This non-directionality of spontaneous emissions leads to a heating rate that competes with the cooling rate of optical molasse damping. The minimum temperature in a 1D optical molasse in a steady equilibrium between optical molasse cooling and heating by spontaneous emission is achieved at $\delta = -\gamma/2$ and given by

$$T_D = \frac{\hbar \gamma}{2 k_B}.$$

This temperature is called the Doppler limit and is a fundamental limit in laser cooling. It is directly proportional to the linewidth $\gamma = \frac{1}{\tau}$ of the excited state and therefore inversely proportional to the excited state lifetime. Atomic species which exhibit an electric-dipole transition to a long-lived excited state, therefore have particurarly low Doppler limit temperatures, which is advantageous for further loading and cooling in optical traps. ^{6}Li exhibits a dipole transition to an excited state with a lifetime of $\tau = 27.102\,\text{ns}$ [31], which results in a Doppler limit of $T_D \approx 141\,\mu\text{K}$. An even more fundamental limit on the temperature achievable in an optical molasse is given by the recoil temperature T_R, which is the temperature associated with the kinetic energy gain due to the recoil an atom at rest would experience by absorption of a photon of wavenumber k, via

$$\begin{aligned} \frac{1}{2} k_B T_R &= \frac{(\hbar k)^2}{2m} \\ \Leftrightarrow T_R &= \left(\frac{h}{\lambda}\right)^2 \frac{1}{m \cdot k_B}. \end{aligned} \tag{29}$$

Polarization-gradient or Sysiphus cooling is a laser cooling technique, that is able to achieve temperatures below the Doppler limit and its realization for ^{6}Li has been reported in [32], though it had long been thought to be inhibited due to the unresolved hyperfine structure of the excited state. Cooling techniques with which temperatures below the recoil temperature can be achieved do require dispersive interaction in an optical dipole trap, as described in Sec. 5.

	g-factor	Value
Total nuclear g-factor	g_I	-0.0004476540
Total electronic g-factor	$g_J\left(2^2S_{1/2}\right)$	2.0023010
	$g_J\left(2^2P_{1/2}\right)$	0.668
	$g_J\left(2^2P_{3/2}\right)$	1.335

Table 1: Total nuclear and electronic g-factor for ^{6}Li according to [38]

We now turn to the subject of spatial confinement of a laser cooled atomic gas. Although there have been reports on all optical traps working solely with spontaneous forces [33, 34, 35], in most cases laser cooling in an optical molasse alone does not spatially confine atoms. In order to trap atoms , the optical molasse has to be combined with a magnetic field gradient, as will be explained in section 4. But before, the next section will outline some optical properties of ^{6}Li and discuss its interaction with a static magnetic field[14].

3.1 Level structure and Zeeman shifts of ^{6}Li

All atoms are multilevel system, but a requirement of laser cooling is that the atom has a closed transition such that the atoms remain in the cooling cycle and the atom mimics the behaviour of a two-level atom. Alkali metals, like lithium, exhibit closed (or nearly closed) optical transitions which lie in a convenient optical range and therefore are often chosen for laser cooling and trapping experiments [15]. The fermionic isotope ^{6}Li has a nuclear spin $I = 1$ and its coupling to the spin-orbital angular momentum additionaly leads to a hyperfine splitting of the energy levels, which is unresolved in the $J = \frac{3}{2}$ excited state and amounts to $\frac{\Delta E_{HFS}}{h} = 228.2\,\mathrm{MHz}$ in the ground state (see Fig. 21).

The spin orbit coupling in the excited $l = 1$ state of ^{6}Li leads to an energy splitting of $\Delta_{FS} = 10.056\,\mathrm{GHz}$, which is the so-called D line double $^2S_{\frac{1}{2}} \rightarrow^2 P_{\frac{1}{2}}, {}^2P_{\frac{3}{2}}$. Precise frequency comb based measurements for absolute transition frequencies of the D line double have been reported in [37] and the centers of gravity (cog) values for the D1 and D2 line have been put into the level scheme in Fig. 21. For laser cooling, the D_2 line is used because it exhibits a stronger dipole coupling to the ground state. The cooling transition $|2^2S_{1/2}, F = 3/2\rangle \leftrightarrow |2^2P_{3/2}, F = 1/2,\, 3/2\rangle$is almost closed, because an atom an atom excited into $|2^2P_{3/2},\, F = 1/2, 3/2\rangle$ can by spontaneous emission decay back to $|2^2S_{1/2}, F = 1/2\rangle$. Therefore a second frequency resonant with $|2^2S_{1/2}, F = 1/2\rangle \leftrightarrow |2^2P_{3/2}, F = 1/2,\, 3/2\rangle$ is used to optically pump from the $|2^2S_{1/2}, F = 1/2\rangle$ level.

The interaction of the atom's hyperfine structure with an external static magnetic field $\mathbf{B}$ can be treated as a perturbation, as long as the Zeeman interaction

$$H_B = -\mu \cdot \mathbf{B} = -\mu_B \left(g_J \mathbf{J} + g_I \mathbf{I}\right) \cdot \mathbf{B},$$

is small compared to the hyperfine interaction $H_{HFS} = hA\mathbf{I} \cdot \mathbf{J}$, where g_J, g_I are the g-factor and $\mathbf{J}$, $\mathbf{I}$ the angular momentum projection operator respectively. In Table 1 are summarised all electronic and nuclear g-factors of ^{6}Li.

[14] An extensive overview of properties of ^{6}Li relevant for laser cooling and cold atom physics in general, can be found in [36].

[15] Moreover what makes lithium interesting in strong-field physics is its low first ionization potential of about 5.4 eV.

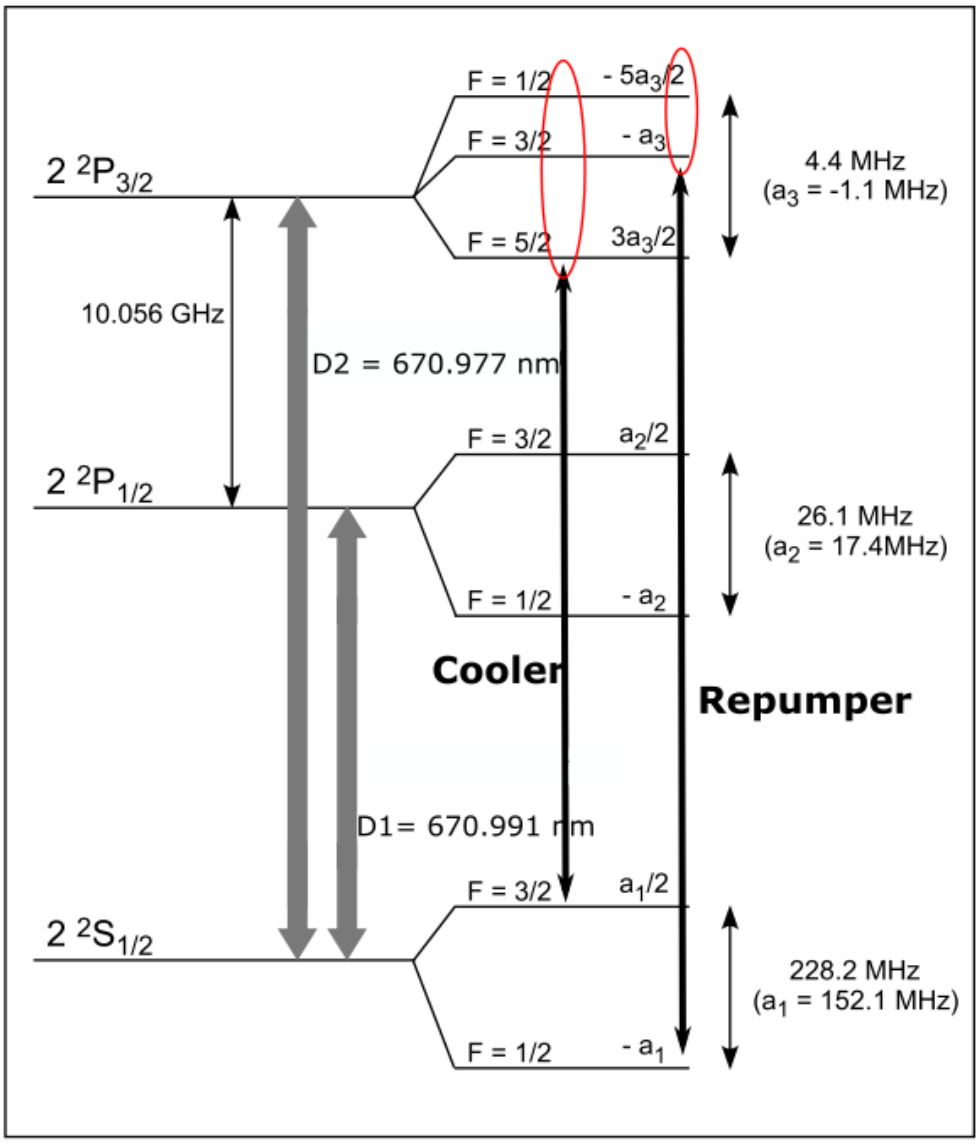

Figure 21: Scheme of relevant energy levels of neutral ^{6}Li for laser cooling.

When H_B is a perturbation to H_{HFS}, $\mathbf{J}$ and $\mathbf{I}$ are still coupled, F is a good quantum number and the Zeeman shift of the magnetic sublevels can be found via perturbation theory as

$$\Delta E_f = \mu_B g_F m_F B, \tag{30}$$

with $m_F \in \{-F, -F+1, \ldots, +F\}$ and where the g-factor g_F is given by

$$g_F = g_J \frac{F(F+1) - I(I+1) + J(J+1)}{2F(F+1)} + g_I \frac{F(F+1) + I(I+1) - J(J+1)}{2F(F+1)}.$$

For the $F = 1/2$ splitting in the low field regime of the $2S_{1/2}$ ground state of ^{6}Li ($B \leq 10\,\mathrm{G}$), we obtain $g_F = -\frac{2}{3}$, which means $m_F = \frac{1}{2}$ is the energetically lowest state. In the high field Paschen-Back regime ($B \geq 150\,\mathrm{G}$) of the ground state where the hyperfine interaction is small compared to the Zeeman interaction, $\mathbf{J}$ and $\mathbf{I}$ decouple and the eigenstates of the system are the eigenstates of H_B given by the pure product states $|Jm_J\rangle\,|Im_I\rangle$ and the eigenvalues are

$$\Delta E_z = \mu_B (g_J m_J + g_I m_I) B \tag{31}$$

are the Zeeman shifts. Since the nuclear g-factor $g_I = -0.0004476540$ is much smaller than the electronic g-factors g_J of $2S_{1/2}$, $2P_{1/2}$ and $2P_{3/2}$, the Zeeman shift for high magnetic fields can be approximated as

$$\Delta E_z \approx \mu_B g_J m_J B. \tag{32}$$

An exact solution for the eigenenergies in the intermediate regime where the total Hamiltonian is given by

$$H_{tot} = hA\mathbf{I}\cdot\mathbf{J} - \mu_B(g_J\mathbf{J} + g_I\mathbf{I})\cdot\mathbf{B},$$

and H_B cannot be treated as a perturbation anymore, can be given for the special case $J = \frac{1}{2}$ by the so-called Breit-Rabi formula

$$E(B)_{|F=I\pm1/2,\, m_F\rangle} = -\frac{\Delta E_{hfs}}{2(2I+1)} + \mu_B g_I m_F B \pm \frac{\Delta E_{hfs}}{2}\sqrt{1 + \frac{4m_F}{(2I+1)}x + x^2}, \tag{33}$$

where $x = \frac{(g_J - g_I)\mu_B B}{\Delta E_{hfs}}$ is the field strength parameter and ΔE_{hfs} the splitting between two hyperfine levels in the absence of a magnetic field B. An approximation for the Zeeman shift of the $|F = I \pm \frac{1}{2},\, m_F\rangle$ state results from Eq. 33 by neglecting all terms proportional to g_I, expanding the square root around $x = 0$ up to second order and finally substracting all magnetic field independent terms:

$$\Delta E(B) = \pm\frac{\mu_B}{(2I+1)} g_J m_F B \pm \left(1 - \left(\frac{2m_F}{(2I+1)}\right)^2\right)\frac{\Delta E_{hfs}}{4}\left(\frac{g_J\mu_B B}{\Delta E_{hfs}}\right)^2 \tag{34}$$

This formula approximates the Zeeman shift of hyperfine sublevels of the ground state $2^2S_{1/2}$ in the intermediate regime $B \leq 150\,\mathrm{G}$, where neither Eq. 30 nor Eq. 32 is valid. The Zeeman shifts of the hyperfine sublevels of the $2^2S_{1/2}$ ground state of ^{6}Li are depicted in Fig. 22.

The hyperfine splitting of the excited state $2^2P_{3/2}$ of ^{6}Li is about 50 times smaller than that of the ground state, which is why $\mathbf{J}$ and $\mathbf{I}$ already decouple for magnetic field strengths $\geq 3\,\mathrm{G}$ and Eq. 32 is valid.

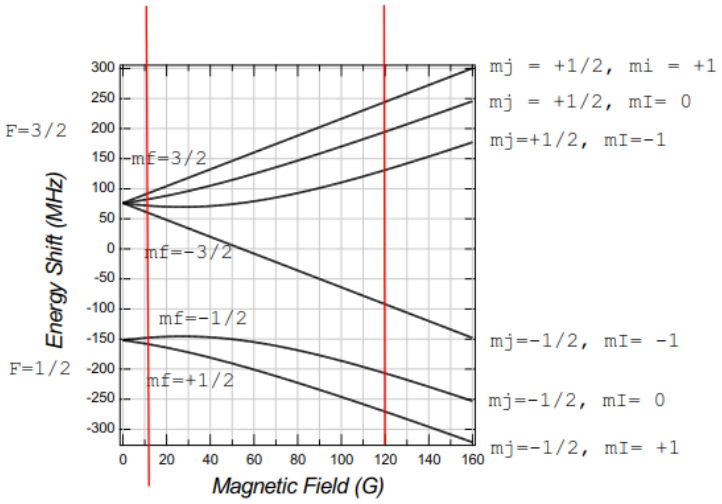

Figure 22: Magnetic-field dependence of the $2^2S_{\frac{1}{2}}$ ground state of ^{6}Li. Taken, with slight modification, from [36].

4 The magneto-optical trap

A magneto-optical trap, as schematically depicted in Fig. 23, spatially confines a cloud of atoms in three dimensions by virtue of the radiation force from three pairs of counterpropagating beams and making the radiation force position-dependent by a applying simultaneously a quadrupole magnetic field. Each beam has a specific circular polarization so that, depending on the direction of the quantization axis, it only drives either $\Delta m_F = +1$ or $\Delta m_F = -1$ transition. The latter is the definition of σ^+ or σ^- photon, which carry a spin angular momentum $+\hbar$ or $-\hbar$ respectively with respect to the quantization axis defined by the direction of the magnetic field. In other words the $+$ and $-$ of $\sigma^\pm$ refers to the sign of the photon's spin angular momentum projection on the local magnetic field. Because of conservation of angular momentum, an atom's hyperfine spin does not change unless by interaction with a photon. Since the direction of the magnetic field is different on each side of the zero crossing, the projection of an atoms hyperfine spin on the local magnetic field, quantified by the azimuthal quantum number m_F, also changes, see Fig. 24. The same applies for the sign of projection of the photon's spin angular momentum on the local magnetic field. Therefore a σ^-photon approaching from the left, becomes a σ^+ photon on the right side of the zero crossing.

For the proper understanding of the workings of pressure forces in a MOT, it is important to note, that in Fig. 24 $\sigma^\pm$ refers to the sign of the projections of a photon's spin angular momentum on the local quantization axis defined by the local magnetic field, not to the type of circular polarization of the photon. Then it becomes clear, that a σ^- polarized beam travelling from right to left with a specific detuning δ_L, because of the Zeeman shift of Eq. 30, becomes resonant at a specific position $z = R_C$ with the $\Delta m_f = -1$ transition of an atom and therefore creates a maximum spontaneous force at this position. In contrast the counterpropagating beam, which is σ^+ polarized at the same position, is far off-resonant with the $\Delta m_f = +1$ transition of the atom (see Fig. 24). Therefore an atom gets driven back by a maximum spontaneous force on the left side. The fact that the counterpropagating beam has σ^+ polarization is accomplished by letting the beam pass through a $\lambda/4$ waveplate before it is retroreflected by a mirror.

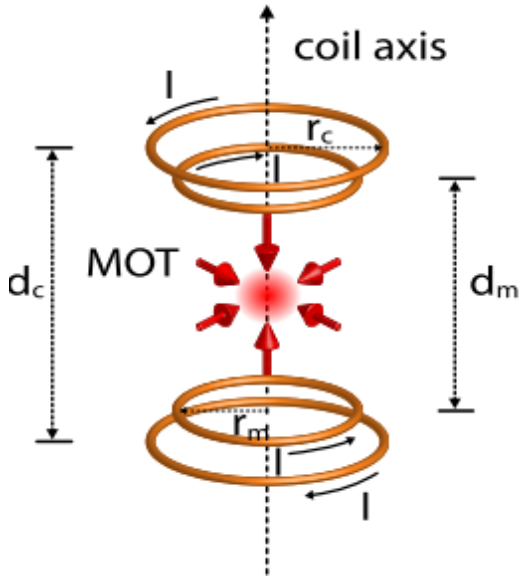

Figure 23: Schematic of a magneto optical trap: A pair of coils in Anti-Helmholtz configuration and six counterpropagating beams of circular polarisation. The second pair of coils with opposing currents as compared to the first pair, is a detail of our setup for faster magnetic field decay in the outer regions.

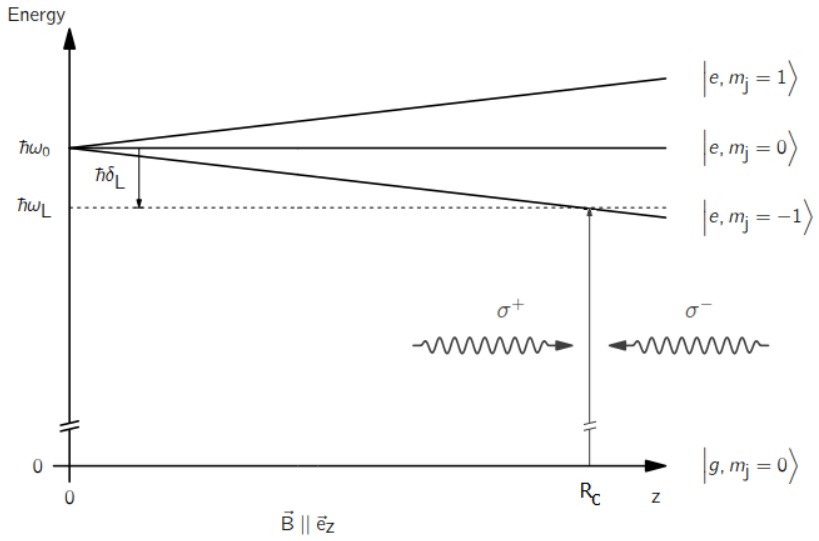

Figure 24: 1-D dimensional model of a magneto optical trap with a simple model fine structure and $g_F > 0$.

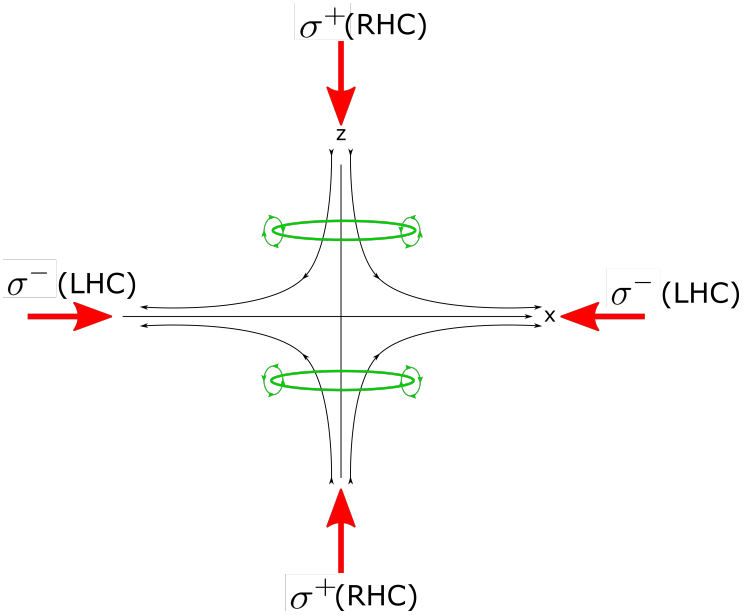

Figure 25: Schematic of a possible configuration of polarisations in x and z direction depending on the orientation of quadrupole field.

The respective positions on both sides of the zero crossing where the spontaneous force is maximum, designate the capture radius $R_c$and is given by

$$R_c = \frac{h\delta_0}{\Delta\mu\frac{\partial B}{\partial z}},$$

where $\Delta\mu = \mu_e - \mu_g$ refers to the difference of magnetic moment of the involved ground and excited state and $\frac{\partial B}{\partial z}$ is the applied magnetic field gradient. The capture velocity v_c is the maximum velocity for atoms in order to be trapped by the spontaneous force and it is related to the maximum spontaneous force $F_{max} = \frac{\hbar k\gamma}{2}$ by

$$v_c \approx \sqrt{\frac{2F_{max}R_c}{m}}.$$

In our experiment, in addition to the pair of coils for the quadrupole field in Anti-Helmholtz configuration, there exists an outer pair of compensation coils for faster decay of the magnetic field in the outer regions (compare Fig. 23), when the compensation coils are driven with opposing currents as to the direction of current in the MOT pair of coils. The magnetic field gradient along the z axis generated by the two pairs of coils in Anti Helmholtz configuration and when the two pairs of coils have opposing current, amounts to$\frac{\partial B}{\partial z} \approx 0.556\,\frac{\mathrm{G}}{cm}$ at $I = 1\,\mathrm{A}$. Because the divergence of quadrupole field vanishes and it is symmetric around the z-axis with $\frac{\partial B}{\partial z} = -2\frac{\partial B}{\partial r}$ and $\frac{\partial B}{\partial x} = \frac{\partial B}{\partial y}$, one has to choose for the radial direction a polarisation opposite to the polarisation for the z-direction (see Fig. 25).

The capture radius in x direction can be calculated by averaging over the difference of magnetic momenta $\Delta\mu_z(m_{F,e}, m_{F,g}) = \mu_B\left(g_F\left(2^2P_{3/2}\right)m_{F,e} - g_F\left(2^2S_{1/2}\right)m_{F,g}\right)$ of all possible transitions for $\sigma^\pm$ radiation by weighing them with the relative transition strengths

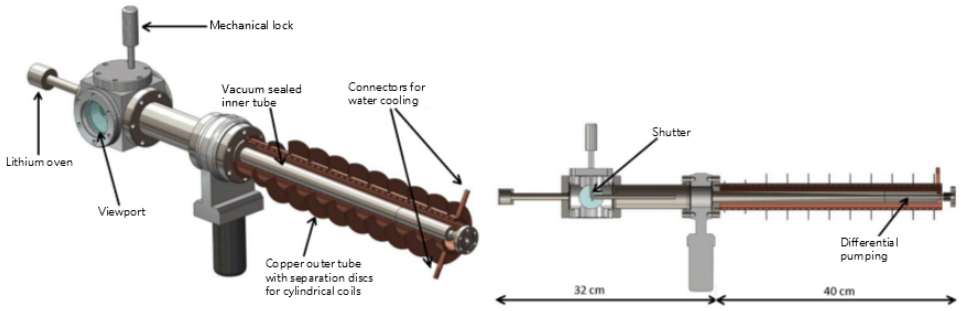

Figure 26: CAD drawing of a typical Zeeman slower very similar to the one which is used in our experiment.

$|c_{F_eF_g}|^2 = |\langle F_e m_{F,e}| \, d(1) \, |F_g m_{F,g}\rangle \, / \, \langle J_e = 3/2| \, d(1) \, |J_g = 1/2\rangle|^2$, so that

$$\begin{aligned} \Delta\mu &= \sum_{m_{F,e}, m_{F,g}} |c_{F_eF_g}|^2 \Delta\mu_z(m_{F,e}, m_{F,g}) \\ &\approx 0.5 \cdot \mu_B. \end{aligned}$$

For typical experimental parameters used in our experiment, a of $\delta = -5\gamma$, where $\gamma = \frac{1}{2\pi\tau} \approx 6\,\mathrm{MHz}$ is the natural linewidth, a radial magnetic field gradient of $\frac{\partial B}{\partial r} \approx 17\,\frac{\mathrm{G}}{\mathrm{cm}}$, we obtain a capture radius in radial direction of

$$R_c \approx 2.5\,\mathrm{cm}.$$

This in turn yields for the same parameters a capture velocity in x-direction of

$$v_x \approx 300\,\mathrm{m/s}. \tag{35}$$

4.1 The Zeeman slower and loading dynamics of a MOT

In order to trap atoms inside the magneto-optical trap, they have to be initially slowed down below the capture velocity. A common method for alkali metals is to produce a thermal atomic beam from a hot lithium vapor emerging from an effusive oven and slow it down by overlapping it with a resonant laser beam. The laser beam is kept resonant by the use of a position-dependent magnetic field, designed in such a way that atoms along a certain deaceleration distance are slowed down with the maximum spontaneous force F_{max}. This results in a continuous atomic flux of atoms of atoms arriving at a velocity below the capture velocity to the trapping region.[16] A CAD drawing of a Zeeman slower is shown in Fig. 26.

The effusive oven is seperated from the main chamber by a long thin tube for differential pumping, in order to not deteriorate substantially the ultra high vacuum in the main chamber. The atomic flux through the trapping region depends on many factors such as temperature of lithium vapor in the oven, aperture diameter of the oven opening, de-aceleration distance and distance from end of Zeeman slower to the trapping region. Ideally the end of the Zeeman slower is so close to trapping region, that the slower magnetic field could be merged with

[16] An alternative method is to sweep the frequency of the slowing beam, which would result in a bunched packages of slowed atoms arriving at the trapping region.

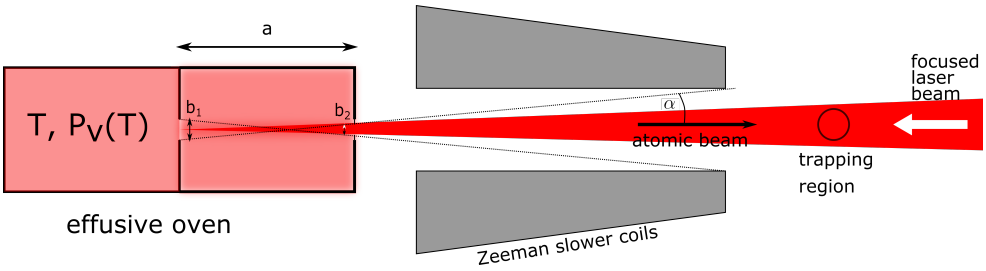

Figure 27: Schematic view of a Zeeman slower arrangement comprising an effusive oven from which a thermal gas of lithium atoms emerges, an arrangment of Zeeman slower coils and a focused laser beams travelling in opposite direction of the atomic beam.

the MOT magnetic field and the atoms can de-acelerated all the way to the trapping region. However this is not realized in our experiment and due to the large dimensions of our vacuum chamber, there is a large gap between the end of the Zeeman slower and the trapping region, where the magnetic field basically drops to zero. It is important to note that a slower beam overlapped with the atomic beam antiparallel to its direction of propagaton, will not cool in the transversal direction of the atomic beam. Therefore the end velocity v_e is chosen not lower than the capture velocity of the MOT for a particular detuning, since otherwise the transversal spread in velocity of the atomic beam would lead to an unnecessary decrease of flux of atoms with $v_e \leq v_c$. Under the ideal assumption of a maximum spontaneous force $F_{sp} = \hbar k \gamma/2$ effecting the atoms on a deceleration distance l, the atoms would get slowed down according to $a_{max} = F_{sp}/m = \dot{v}(t)$, which would result in

$$v(z) = \sqrt{v_{max}^2 - 2 \cdot a_{max} \cdot z}, \tag{36}$$

where

$$v_{max} = \sqrt{v_e^2 + 2 a_{max} l} \tag{37}$$

would be the maximum velocity in the velocity distribution of the atomic beam, that could be deacelerated by the Zeeman slower. The velocity distribution of the atoms in the oven is described by a 3D Maxwell-Boltzmann velocity distribution $P_v(T) \sim \left(\frac{m}{k_B T}\right)^{\frac{3}{2}} v^2 \exp\left(-\frac{mv^2}{2k_B T}\right)$ with a mean velocity of $\overline{v} = 2\frac{v_{mp}}{\sqrt{\pi}}$, where the most probable velocity v_{mp} is given by $v_{mp} = \sqrt{\frac{2k_B T}{m}}$. In order to better collimate the atomic beam, our oven has two apertures 1 and 2 of diameter b_1 and b_2 respectively, which are a distance a apart (see Fig. 27).

As shown in [39], the atomic flux θ through the second aperture into a solid angle $\omega = 2\pi\,(1 - \cos\alpha)$ is given by

$$\theta = \frac{1}{4} n \overline{v} \frac{f^2}{1 + f^2},$$

where n is the atomic density in the oven and $\tan\alpha = \frac{b_1/2 + b_2/2}{a}$. Since the probability to leave the oven is proportional to its velocity, [39] concludes that the velocity distribution within an atomic beam changes to

$$P_v'(T) = C' \left(\frac{m}{k_B T}\right)^2 v^3 \exp\left(-\frac{mv^2}{2k_B T}\right), \tag{38}$$

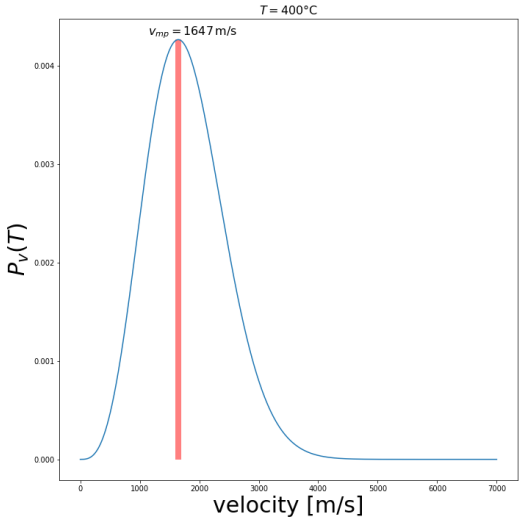

Figure 28: Velocity distribution inside a thermal atomic beam according to Eq. 38 for a typical oven temperature of $T \approx 400$ °C.

of which the most probable velocity is given by $v_{mp} = \sqrt{\frac{2k_BT}{m}}$. The oven temperature usually is in the range of $T = 400\,°\text{C}$, which yields $v_{mp} \approx 1647\,m/s$, as illustrated in Fig. 28.

By adjusting the individual current amplitude of each of the ten coils in the Zeeman slower, the magnetic field $B(z)$ can be tailored so that it compensates by virtue of a position-dependent Zeeman shift along the deceleration distance l for the position dependent Doppler shift $\delta_{Doppler}(z) = f' - f$, where f is the central frequency of the laser and f' the frequency the atom sees in its reference frame. If the atom moves with a positive velocity $v(x) > 0$ towards the slowing beam, the frequency f in the atom's reference frame is blue shifted to

$$f' \quad = \quad f\left(1 + \frac{v(z)}{c}\right).$$

and the absolute shift equivalently would be

$$\delta_{Doppler}(z) = f' - f = \frac{v(z)}{\lambda} \tag{39}$$

. In combination with the laser detuning δ from resonance, the magnetic field must be designed in such a way that the Zeeman shift compensates for Doppler shift and laser detuning, i.e.

$$\begin{aligned} \Delta E(B) + hf \quad &= \quad h\left(f\left(1 + \frac{v(z)}{c}\right) + \delta\right) \\ \Leftrightarrow \Delta E(B) \quad &= \quad \frac{h}{\lambda} \cdot v(z) + h\delta. \end{aligned} \tag{40}$$

The Zeeman shift $\Delta E(B)$ in Eq. 40 refers to the total Zeeman shift of both ground and excited state, i.e.

$$\Delta E(B) = \Delta E_e(B) - \Delta E_g(B). \tag{41}$$

In a Zeeman slower, magnetic fields from zero to hundreds of Gauss are possible and the question of how the magnetic field curve $B(x)$ exactly should look like depends on which

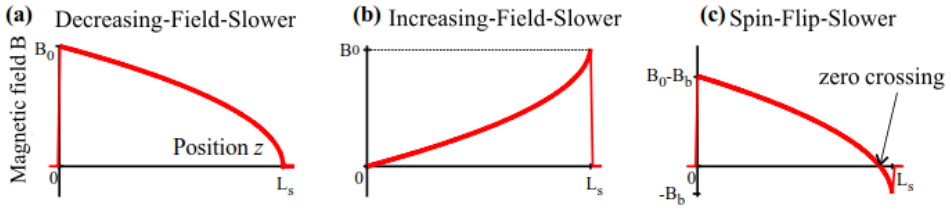

Figure 29: Possible ideal magnetic field curves for the ideal Zeeman slower.

transition one chooses for the spontaneous force and which boundary conditions $B_0 = B(z = 0)$ and $B_f = B(z = l)$ it should fulfill. However as long as we obtain a linear relation between $\Delta E(B)$ and B, from Eq. 36, it is clear that the magnetic field curve $B(z)$ matching the resonance condition in Eq. 40 has the generic form

$$B(z) = B_0\sqrt{1 - \frac{z}{l}} + B_f.$$

with two free parameters $B_0$and B_f, depending on which we distinguish three configurations of the magnetic field (see Fig. 29):

1. **Decreasing-Field-Slower ($B_f = 0$):** In this configuration the maximum slowable velocity v_{max} is determined by the initial value of the magnetic field B_0 and the detuning δ of the laser beam, while the end velocity $v(z = l) = -\delta/\lambda$ is solely determined by the detuning δ of the laser. The obvious advantage of this configuration and the main reason why it is chosen in our experimental setup is, that there are no residual magnetic fields at the end of the deceleration distance, which might disturb further experiments. Its disadvantage is that atoms leaving the Zeeman slower and entering the magnetic-field free space are still in resonance with the laser light and might eventually even be pushed back into the Zeeman slower. Furthermore the off-resonant but highly saturated Zeeman slowing beam might disturb the magneto-optically trapped atoms.

2. **Increasing-Field-Slower ($B_f = -B_0$):** In this configuration the maximum slowable velocity $v_{max} = -\delta/\lambda$ is given solely by the detuning δ and in order to be resonant the slowing beam must be detuned by several hundred Megahertz up to a few Gigahertz. For example if the maximum slowable velocity should be the most likely velocity in an atomic ^{6}Li beam of $T = 400\,°\mathrm{C}$ (see Fig. 28), the necessary detuning in order to compensate for the Doppler shift at 670 nm would amount to $\delta = -2.5\,\mathrm{GHz}$. The advantage of this configuration is, that the slowing beam is so-far off-resonant that is doesn't disturb neither the atoms leaving the Zeeman slower, nor the magneto-optically trapped atoms. On the other hand the maximum of the magnetic field is close to the experiment, which requires additional measures for a fast decay of the magnetic field behind the Zeeman slower.

3. **Spin-Flip-Slower ($-B_0 \leq B_f \leq 0$):** This configuration in a way combines the advantages of the first two configuration, since on one hand the magnetic field close to the experiment is not very large, which makes a fast decay of the magnetic field outside the Zeeman slower easily possible. On the other hand has the slowing beam a fairly large detuning of a few hundreds of Megahertz, so that it doesn't disturbe the magneto-optically trapped atoms or the atoms leaving the Zeeman slower. A disadvantage is the

zero crossing of the magnetic field curve $B(z)$ at which the spin flips and atoms might be pumped into a dark state and become unavailable for further cooling on the chosen cooling transition.

We now turn to the question for which transition the magnetic field curve $B(z)$ should be designed for. Since in a Zeeman slower, magnetic fields of at least 50 Gauss are employed, the Zeeman shift of the excited state $\Delta E_e(B)$, along the whole deceleration distance of the Zeeman slower, can in good approximation be described by Eq. 32, for which with $g_J(2^2P_{3/2}) = \frac{4}{3}$ we obtain

$$\Delta E_e(B) = \frac{4}{3}\mu_B m_J B.$$

For the ground state, we see from Eq. 34, that we only obtain a linear relation for the hyperfine state ground states with $F = \frac{3}{2}$ and $m_F = \pm\frac{3}{2}$, which the would be

$$\Delta E_g(B) = \pm\mu_B B.$$

As can be seen from Fig. 22 in Sec. 3.1, the relation for the Zeeman shift of the states $|F = \frac{3}{2}, m_F = \pm 3/2\rangle$ is linear throughout all regimes of magnetic field strength and therefore along the whole deceleration distance of the Zeeman slower. Now, depending on the polarisation of the Zeeman slower beam, at low magnetic field with $\sigma^{\pm}$ light we drive the closed transitions

$$|F = \frac{3}{2}, m_F = \pm\frac{3}{2}\rangle \overset{|g\rangle}{\leftrightarrow} |F = \frac{5}{2}, m_F = \pm\frac{5}{2}\rangle \overset{|e\rangle}{}.$$

At high magnetic field the excited states $|e\rangle = |F = \frac{5}{2}, m_F = \pm\frac{5}{2}\rangle$ transition into $|I = 1, J = \frac{3}{2}, m_I = -1, m_J = \pm\frac{3}{2}\rangle$ which both have the Zeeman shifts

$$\Delta E_e(B) = \pm 2\mu_B B.$$

Therefore the magnetic field curve $B(z)$ can be designed such that it compensates for either one of following total Zeeman shifts

$$\Delta E(B) = \pm\mu_B B.$$

Since the Doppler shift for atoms with the most likely velocity in the atom beam is initially on the order of several Gigahertz, in order to compensate for it with moderately high magnetic field and moderately high red detuning δ, it is advantageous, according to Eq. 40, choosing $\Delta E(B) = \mu_B B$, so that we obtain as expression for the ideal magnetic field curve

$$\begin{aligned} B(z) &= \frac{h}{\mu_B}\left(\frac{v(z)}{\lambda} + \delta\right) \\ &= \frac{h}{\mu_B}\left(\frac{1}{\lambda}\cdot\sqrt{v_{max}^2 - 2\cdot a_{max}\cdot z} + \delta\right), \delta < 0 \end{aligned} \tag{42}$$

The maximum spontaneous deaceleration $a_{max} = F_{sp}^{max}/m$ for a ^{6}Li atom, corresponding to the D_2 transition of ^{6}Li, is

$$a_{max} \approx 1.83 \cdot 10^6\, m/s^2.$$

The performance of the Zeeman slower is the better, the higher the fraction of the initial velocity distribution in Fig. 28 is slowed down in the slower, which in turn directly depends

on the length of the Zeeman slower. If the atoms are supposed to be slowed down to the capture velocity in x direction in Eq. 35 at $z = l$, then the maximum velocity of atoms in the atomic beam, which can be slowed down is according to Eq. 37

$$v_{max} \approx 0.76 v_{mp},$$

with $l = 40$ cm being the length of our ideal Zeeman slower and v_{mp} the most probable velocity of the atoms in our atomic beam at $T = 400°\mathrm{C}$. In order to calculate the desired currents for the Zeeman slower coils, so that the ideal magnetic field curve in Eq. 42 is reproduced, we have to numerically minimize the integral

$$\int_{x=0}^{x=l} dx \left(B(z) - \sum_{n=1}^{10} I_n B_n(z) \right)^2, \tag{43}$$

which can be performed by a non-linear least-squares algorithm. The expressions $B_n(x)$ in Eq. 43 represent the magnetic field curves per Ampere for each Zeeman slower coil, which have been determined prior to attaching the Zeeman slower to the vacuum chamber. Thereforey the magnetic field of each coil has been measured at roughly equidistant points along its symmetry axis and fitting the measured curve to the expression for the magnetic field of a solenoid along its symmetry axis

$$B_n(z) = \mu_0 \frac{N \cdot I}{l} \sum_{s=-1,+1} \frac{s \cdot z + l/2}{2\sqrt{R^2 + (sz + l/2)^2}},$$

where l is its length, N is the number of windings, R is the radius and I is the current in Ampere employed. Further details can be found in [40].

We can simulate the atoms trajectories in the atomic beam by numerically solving $\ddot{z} = F_{sp}/m$, where the spontaneous forceF_{sp} is given as in Eq. 27, but with an effective detuning in the atom's rest frame of

$$\delta_{eff} = \delta_{doppler} + \delta_{Zeeman} + \delta,$$

where $\delta_{Doppler}$ is the blue shift due to the Doppler effect as stated in Eq. 39 and $\delta_{Zeeman} = -\frac{\Delta E}{h}$ the red shift of the laser frequency in the atom's frame due to the combined Zeeman energy shift of both ground and excited state as defined in Eq. 41. The result of the simulation for a saturation parameter of $s_0 = 90$ and a laser detuning of $\delta = -242\,\mathrm{MHz} \approx 40.3\Gamma$ is shown in Fig. 30.

As one can clearly see from Fig. 30, the effect of the Zeeman slower is a compression of the velocity distribution of the atomic beam, since all atoms reach the same final velocity at the same position, regardless of their initial velocity. The Zeeman slower in Fig. 30 ends at about $z = -30\,cm$ while the cloud of ^{6}Li atoms is trapped at $z = 0\,\mathrm{cm}$. This gap between the end of the Zeeman slower and the position where the atoms are trapped is about 30 cm and unusually big for a cold atom experiment. In a conventional cold atoms experiment, the gap between the trapping region and the end of the Zeeman slower is usually so small, that the magnetic field of the Zeeman slower in a decreasing-field configuration can be directly merged with the quadrupole magnetic field of the MOT. A problem evident from the simulation in Fig. 30 is, that all atoms are deacelerated already to 0 m/s already at $z = -30\,\mathrm{cm}$ or even before and therefore won't reach the trapping region. The large gap in our experiment was inevitable because of the dimensions of the vacuum chamber and the size of the spectrometer.

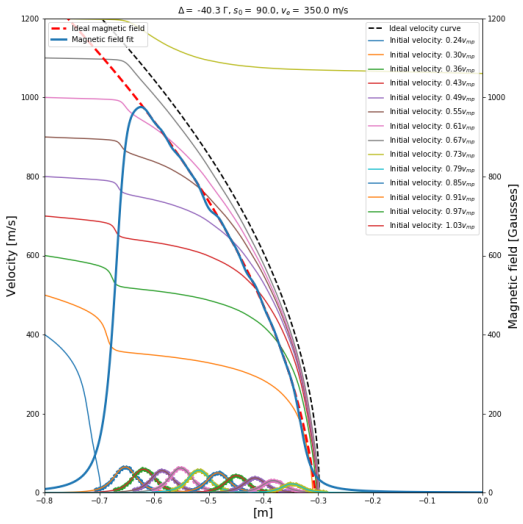

Figure 30: Blue curve represents the resulting magnetic field $\sum_{n=1}^{10} I_n B_n(z)$ with the magnetic fields B_n of each Slower coil shown on the bottom, and each I_n obtained from numerical minimization of 43. The red dashed curve represents the ideal magnetic field of Eq. 42 and the thin black dashed curve the ideal velocity curve according to Eq. 36.

However it means that the atomic flux through the trapping region of atoms with velocities below the capture velocity v_c depends on a suttle interplay of the power in the slower beam, the slower beam detuning, the end velocity after the Zeeman slower, of which the latter two in turn determine the currents for the Zeeman slower coils:

Power-broadening in the Zeeman slower beam leads to considerable off-resonant scattering after the atoms leave the Zeeman slower, which again broadens their velocity distribution and can further deacelerate and even push some of the atoms back into the Zeeman slower. If the atomic beam interacted with a collimated Zeeman slowing beam, the velocity distribution in the atomic beam transversal to the direction of propagation of the Zeeman slower beam would not get compressed, but, on the contrary, further broadened due to heating by spontaneous emission [30], leading to an increase of the root-mean-square deviations of transverse momentum projections according to

$$\Delta p_{x/y}^{rms} = \hbar k \sqrt{\alpha_{x/y} N(t)},$$

where $N(t)$ is the average number of photons scattered between $t = 0$ and t. This in turn leads to an increase in angular divergence of the atomic beam after the Zeeman slower, which drastically reduces the atomic flux through the MOT region. It is possible to mitigate this heating effect by focusing the Zeeman slower beam, as seen in Fig. 27, so that there is a small transverse component in the spontaneous scattering force acting on the transverse velocity distribution. A more direct measure is to setup transversal cooling beams before or after the Zeeman slower section. However the better option is to install the transversal cooling stage after the Zeeman slower in order to collimate the divergence of the atomic beam, which is due to the aforementioned heating by spontaneous emission, as demonstrated in [41].

The dynamics of the atom number $N(t)$ is governed by following rate equation [42]

$$\frac{dN}{dt} = L - RN - \beta \int_V n(\mathbf{r}, t)^2 d^3r - \gamma \int_V n^3(\mathbf{r}, t) d^3r. \tag{44}$$

In this equation L is the loading rate in atoms per second corresponding to the flux of atoms through a sphere of capture radius R_c, and with velocities v below the capture velocity v_c. R is the so-called single-particle loss coefficient accouting for collisions of trapped Li atoms with background gas particles. This loss rate $R = \sum_X R_X$ is composed of the loss rates R_X of different background gas species X (e.g. N_2), which in turn directly depend on the corresponding number density n_X via

$$R_X = n_X \sigma_{X-Li} v_X^{rms},$$

where σ_{X-Li} is the respective collisional cross section, and $v_X^{rms} = \sqrt{\frac{3k_B T}{m_X}}$ the root mean square speed of the background gas. From this equation it becomes clear, that the operation of a magneto-optical trap ideally takes place in an ultra-high-vacuum (UHV) with pressures in the regime of 10^{-10} mbar or lower. The third term $\beta \int dV n(\mathbf{r})^2$ accounts for two-body losses ocurring due to state changing collisions between trapped atoms in different electronic or hyperfine states, or via radiative escape (see Sec. 8). For the usual atom number densities encountered in a MOT of $10^9 - 10^{11}$ atoms/cm^3, the two-body loss rate is small compared to one-body losses. Therefore if we neglect two-body losses, the atom number loading is determined from Eq. 44 to be

$$N(t) = \underbrace{\frac{L}{R}}_{=N_{max}} \left(1 - e^{-R \cdot t}\right), \tag{45}$$

if the initial condition is $N(t = 0) = 0$. The loading rate L can be quantified by determining the slope of the loading curve for $R \cdot t \ll 1$, when the loading curve can be approximated by $N(t) \approx L \cdot t$. If the oven beam is interrupted, the atom number N_0 will decay according to

$$N(t) = N_0 e^{-Rt}.$$

5 The optical dipole trap

In experiments with cold quantum gases, the route to quantum degeneracy is usually achieved by loading pre-cooled atoms from a magneto-optical trap into a dipole trap, because the temperature of the atomic sample in the magneto-optical trap is fundamentally limited by the recoil temperature which is about $7\,\mu$K for ^{6}Li. In order to achieve lower temperatures, one has to rely on non-dissipative cooling techniques, that do not imply a lot of scattering of photons. As outlined in Sec. 2, the radiation force on a two level atom is comprised of a dissipative component, the spontaneous force, and a dispersive component, the gradient force, where the latter can be derived from a time-averaged interaction potential. This interaction potential for a two level system is an energy shift of ground and excited state with opposite sign respectively, as illustrated in Fig. 31.

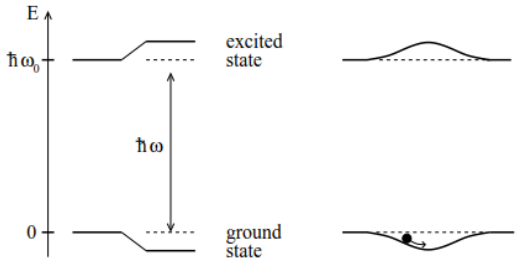

Figure 31: Energy shifts due to interaction of a far-off resonant light field $|\delta| \gg \Omega$ with a two-level system for $\delta < 0$. Figure taken from [42].

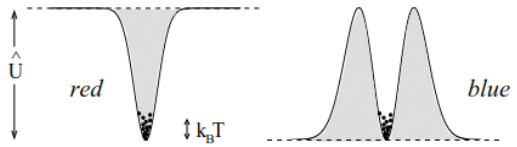

Figure 32: Needed radial intensity distributions for a red or blue detuned light field to have a trapping effect on e.g. the ground state of a two-level system. Figure taken from [42].

It is important to note, that the overall sign of the energy shifts and therefore the resulting gradient force depends on the sign of the detuning δ. Depending on the sign, different laser beam modes generate the right intensity distribution for the gradient force to have a trapping effect. If the laser field had a blue detuning $\delta > 0$, two-level atoms in the ground state would seek regions of low intensity, therefore e.g. a Laguerre-Gaussian LG_{01} mode would be needed, while in the case of red detuning a simple TEM_{00} mode would generate the needed intensity distribution, as illustrated in Fig. 32. Since the TEM_{00} mode is technically much easier to generate, than other laser modes, a red detuned TEM_{00} beam is the most common choice for a gradient force trap. In a laser field with radial field distribution corresponding to that of aTEM_{00} mode, having power P and a beam diameter $2w_0$

$$\begin{aligned} \mathbf{E}(\mathbf{r},t) &= \mathbf{e}_r E_0(r)\cos(\omega t - k\cdot z) \\ E_0(r) &= \frac{2}{w_0}\left(\frac{2P}{c}\right)^{1/2}\exp\left(-\frac{r^2}{2w_0^2}\right) \end{aligned}$$

the ratio of gradient force to spontaneous force is in on the order of magnitude [30]

$$\frac{F_{grad}}{F_{sp}} \approx \frac{\delta}{\gamma}\frac{\lambda}{2\pi w_0}.$$

In order to make the spontaneous force negligible small compared to the gradient force, it is possible to increase the detuning δ and strongly focus the beam, thereby making the beam

diameter $2w_0$ as small as possible at the focus. This idea is called a far-off resonance (focused-beam) trap (FORT) and it has been first realized in 1986 in the group of Steven Chu [43]. A considerable number of cold atoms experiments with this type of optical trap have been performed up to now and one of the main issues for long trapping times at low trap depth has been identified to be fluctuations in the laser power, as explained in Sec. 5.1.1. By implementing optical traps with ultrastable IR lasers, trap storage times on the order of tens of seconds have been reported [44, 45]. Another physical requirement to achieve long storage time is to actually trap a collisionally-stable atom sample. Both aspects will be treated in Sec. 5.1 on trap loss mechanism.

Since atoms trapped in a FORT mostly reside in their ground state, the interaction potential of the trap commonly refers to the energy shift of the ground state and is called dipole potential U_{dip}, because it refers to the fact, that a monochromatic field $\mathbf{E}(\mathbf{r},t) = \mathrm{Re}\left[\mathbf{e}_r E_0(\mathbf{r})\cdot e^{-i\omega t}\right]$ with angular frequency ω produces a harmonically oscillating atomic dipole moment

$$\begin{aligned}\mathbf{p}(\mathbf{r},t) &= \langle\Psi(t)|d_{a,\epsilon}|\Psi(t)\rangle \\ &= \mathrm{Re}\left[\alpha(\omega)\mathbf{e}_r E_0(\mathbf{r})e^{-i\omega t}\right]\end{aligned}$$

with the same frequency, where the $\alpha(\omega)$ is the scalar dynamic atomic (or molecular) dipole polarizability (DDP), which is frequency-dependent and in general of complex value. The DDP is a measure for the deformation of the charge distribution under the influence of an oscillating electric field. In analogy to the identification made at the end of Sec. 2, the dipole potential is given by[42]

$$U_{dip} = -\frac{1}{2}\langle\mathbf{p}\cdot\mathbf{E}\rangle = -\frac{1}{2\epsilon_0 c}\mathrm{Re}\left[\alpha\right] I(\mathbf{r}), \tag{46}$$

where the field intensity I is given by $I = \frac{\epsilon_0 c}{2}|E_0|^2$. In other words the dipole potential is proportional to the in-phase component of the oscillation of the induced dipole moment $\mathbf{p}(\mathbf{r},t) = \alpha\mathbf{E}(\mathbf{r},t)$,which is the dispersive part of the interaction. The dissipative part of the interaction is the power being absorbed and re-emitted as dipole radiation, given by

$$P_{abs} = \langle\dot{\mathbf{p}}\mathbf{E}\rangle = \frac{\omega}{\epsilon_0 c}\mathrm{Im}\left[\alpha\right] I.$$

This re-emitted power does not change the internal state of the atom if the electric field is far detuned, but just results from the radiation emitted by the radiating dipole, a process called Rayleigh scattering. Since the re-emitted power comes as flux of photons of energy $\hbar\omega$, the scattering rate can be identified to be

$$\Gamma_{sc}(\mathbf{r}) = \frac{P_{abs}}{\hbar\omega} = \frac{1}{\hbar\epsilon_0 c}\mathrm{Im}\left[\alpha\right] I(\mathbf{r}).$$

In a semi-classical approach the scalar dynamical polarizability of a two-level atom for a given polarization ϵ is [46]

$$\alpha(\omega) = \frac{3\pi\epsilon_0 c^3}{\omega_a^3}\Gamma_{eg}\left\{\frac{1}{\omega_a-\omega-i\Gamma_{eg}/2}+\frac{1}{\omega_a+\omega+i\Gamma_{eg}/2}\right\}, \tag{47}$$

where the damping rate

$$\Gamma_{eg} = \frac{\omega_a^3}{3\pi\epsilon_0\hbar c^3}|\langle e|d_{a,\epsilon}|g\rangle|^2$$

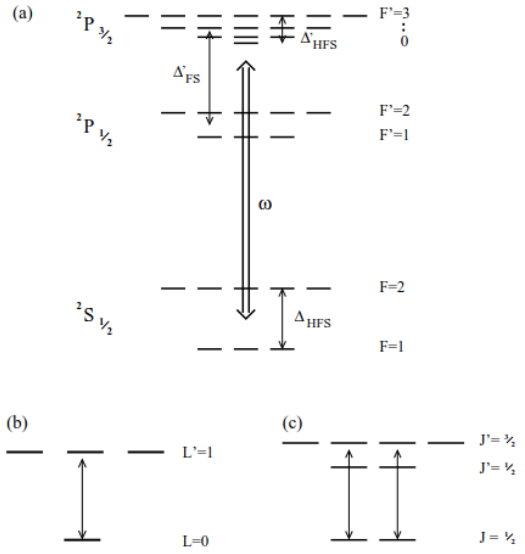

Figure 33: (a) Level scheme of an alkali atom, showing the energy splitting due to fine and hyperfine interaction, where $\Delta_{FS} \gg \Delta_{HFS}$ (b) Reduced level scheme for $\delta \gg \Delta_{FS}$ which is our relevant case. Figure from [42]

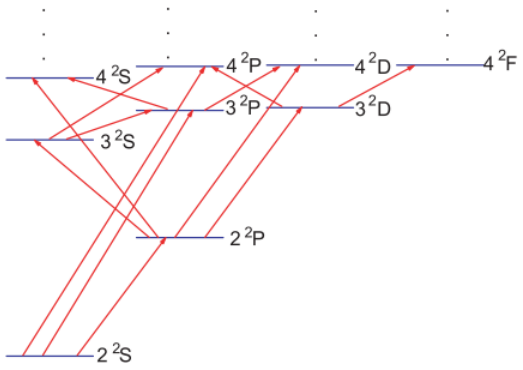

Figure 34: Low-lying energy levels of a Li atom, which have to be taken into account for calculation of polarizabilities. Red arrows designate a non-vanishing dipole transition element. Figure from [47].

corresponds to the spontaneous decay rate of the non-degenerate excited level to the non-degenerate ground level via a dipole-allowed transition [17] and $\omega_a = \omega_{eg} = \frac{E_e - E_g}{\hbar}$ is the resonance frequency of the unshifted two-level atom. Equation 47 describes the polarizability of the ground state of a two level atom, which has only a contribution from the excited state and results in the case of large detunings $\delta \gg \Gamma_{eg}$ into following quantitative equations for the dipole potential and the scattering rate

$$\begin{aligned} U_{dip}(\mathbf{r}) &= \frac{3\pi c^2}{2\omega_a^3}\frac{\Gamma_{eg}}{\delta} I(\mathbf{r}) \\ \Gamma_{sc}(\mathbf{r}) &= \frac{3\pi c^2}{2\hbar\omega_a^3}\left(\frac{\Gamma_{eg}}{\delta}\right)^2 I(\mathbf{r}). \end{aligned} \tag{48}$$

It is worth noting that the dipole potential for a two-level system in Eq. 48 is merely a re-expression of Eq. 25 in more practical lab quantities. We now adress the question in how far the approximation of a two-level system is justified for a multi-level atom like ^{6}Li. In our case of application, we have $\delta \gg \Delta_{FS}$, therefore the multilevel atomic structure of ^{6}Li can be reduced significantly by neglecting hyperfine and fine splitting (see Fig. 33) .

The polarizability of the ground state may be approximated by only taking the contribution from the 2^2P excited level, since the contribution to the 2^2S $\leftrightarrow$ 2^2P transition scales inversely with δ. However the energy shift of the 2^2P level must take into consideration the

[17] For a two level system, where the ground state has a degeneracy of g_1 and the excited state a degeneracy of g_2, the spontaneous decay rate would be connected to the transition matrix element via $\Gamma_{eg} = \frac{g_1}{g_2}\frac{\omega_a^3}{3\pi\epsilon_0\hbar c^3}|\langle e|d_{a,\epsilon}|g\rangle|^2$[46].

contributions from other low-lying energy levels as well (see Fig. 34), which have approximately the same detuning as 2^2P has from 2^2S. Therefore for an atom with more than two levels, the polarizability of a state a must be calculated from a generalization of Eq. 47 by summing over all dipole-allowed transitions to another state b

$$\alpha_a(\omega) = 3\pi\epsilon_0 c^3 \sum_{a\neq b} \frac{\Gamma_{ab}}{\omega_{ab}^3} \left\{ \frac{1}{\omega_{ab} - \omega - i\Gamma_{ab}/2} + \frac{1}{\omega_{ab} + \omega + i\Gamma_{ab}/2} \right\},$$

where $\omega_{ab} = \frac{E_a - E_b}{\hbar}$ is the unshifted transition frequency and $\Gamma_{ab} = \frac{\omega_{ab}^3}{3\pi\epsilon_0\hbar c^3}|\langle b|d_{a,\epsilon}|a\rangle|^2$ the decay rate from the higher lying to the lower lying level. By realizing that the damping term Γ_{ab} is much smaller than ω_{ab}, and writing the polarizability in terms of a single denominator, following more compact equation is obtained

$$\alpha_a(\omega) \approx \sum_{a\neq b} f_{ab} \left[\frac{\frac{e^2}{m}}{\omega_{ab}^2 - \omega^2 - i\omega\Gamma_{ab}} \right], \quad f_{ab} = \frac{2m\omega_{ab}}{e^2\hbar}|\langle b|d_{a,\epsilon}|a\rangle|^2,$$

where f_{ab} is the so-called oscillator strength. Averaging over all polarizations ϵ leads to an extra factor of $\frac{1}{3}$ for the oscillator strength. The polarizability of the 2^2S ground and 2^2P excited state of Li has been calculated in [47] and at roughly the detuning of our FORT ($\lambda = 1070\,\mathrm{nm}$) the polarizabilities are

$$\alpha_{2^2\mathrm{S}} = 250.265(1)\,\mathrm{a.u.} = 4.126 \cdot 10^{-39} \frac{\mathrm{Cm}^2}{\mathrm{V}} \tag{49}$$

$$\alpha_{2^2P} = 185.542(1)\,\mathrm{a.u.} = 3.059 \cdot 10^{-39} \frac{\mathrm{Cm}^2}{\mathrm{V}}. \tag{50}$$

Unlike in the two-level atom picture, the 2^2P excited state also experiences an energy shift to lower energies and, if one ignores the collisional aspect, could be trapped in a FORT. In order to give estimates on trap depth $\hat{U}$ (see Fig. 32) and the differential AC Stark shift between 2^2S and 2^2P, we need to evaluate the intensity distribution for a focused Gaussian beam for which the intensity distribution is given by

$$I_{FB}(r,z) = \frac{2P}{\pi w^2(z)} \exp\left(-2\frac{r^2}{w^2(z)}\right),$$

where P is the power in the beam and $w(z)$ the $1/e^2$ radius given by

$$w(z) = w_0\sqrt{1 + \left(\frac{z}{z_R}\right)^2} \quad z_R = \frac{\pi w_0^2}{\lambda}$$

and $2w_0$ is the $1/e^2$ beam diameter at the focus position. The trap depth U_0 then is given by

$$U_0 \equiv U_{dip}(r=0, z=0) = \frac{3c^2}{\omega_a^3}\frac{\Gamma}{\delta}\frac{P}{w_0^2}. \tag{51}$$

By expansion of the dipole potential of the focused beam to quadratic order around $r = 0$ and $z = 0$

$$U_{FB} \approx -U\left[1 - 2\left(\frac{r}{w_0}\right)^2 - \left(\frac{z}{z_R}\right)^2\right],$$

one obtains the oscillation frequencies in radial and axial direction for atoms well-localized with the optical trap:

$$\omega_r = \left(\frac{4U_0}{mw_0^2}\right)^{1/2} \quad \omega_z = \left(\frac{2U_0}{mz_R^2}\right)^{1/2}. \tag{52}$$

In comparison to ^{87}Rb, another popular element in cold atom experiments, which has a dynamic polarizability at the frequency of the Nd:YAG laser at 1064 nm of 769 ± 61 a.u.[48], the polarizability of ^{6}Li at this frequency is roughly only 1/3 and therefore rather weak. In order to achieve a similar trap depth for the same trap geometry, one therefore has to triple the power in the beam. which on the other side again might lead to a technical difficulty, called thermal lensing. Thermal lenses can occur in pass-through elements like AOM crystals and lenses and lead to a shift in focus size and focus position.

In contrast to the magneto-optical trap, the optical dipole trap also allows for trapping of molecules, and the trap depth for these molecules depends on the magnitude of their static or dynamic electric polarizability, or even their permanent electric dipole moment (e.g. polar molecules like CO, NO, NH, NH_3, ... or Rydberg molecules). In order to account for anisotropies in the molecular polarizability, the molecular polarizability tensor $\alpha = \begin{bmatrix} \alpha_{xx} & \alpha_{xy} & \alpha_{xz} \\ \alpha_{yx} & \alpha_{yy} & \alpha_{yz} \\ \alpha_{zx} & \alpha_{zy} & \alpha_{zz} \end{bmatrix}$ is defined. If the internuclear axis of the molecule coincides with the z axis of a molecule fixed-reference frame, then α has the independent components $\alpha_{\|} = \alpha_{zz}$ and $\alpha_{\perp} = \alpha_{xx} = \alpha_{yy}$ and the average polarizability usually is defined as $\overline{\alpha} = (\alpha_{zz} + 2\alpha_{\perp})/3$. The static electric polarizability of several alkali dimers have been calculated in [49] and for the lowest singlet and triplet state of Li_2 and the vibrational ground state $\nu = 0$ following average polarizabilities in atomic units haven been reported:

$$\begin{aligned} \overline{\alpha}_{\nu=0}(a^3\Sigma_u) &= 399.4, \\ \overline{\alpha}_{\nu=0}(X^1\Sigma_g) &= 226.8. \end{aligned}$$

However for vibrationally highly excited molecules, the polarizability in good approximation is given by twice the atomic polarizability, since the atoms on average are far apart.

5.1 Trap loss mechanisms

In order to optimize the storage time of atoms trapped in an optical-dipole potential, it is important to be aware of trap loss mechanism. Trap loss mechanisms can roughly be divided into categories,

1. Heating rates, and
2. State-changing collisions.

The following two sections give an outline on both types of trap loss mechanism, and how their effects can be avoided or at least mitigated.

5.1.1 Heating in an optical trap

The sources of heating in an optical dipole trap are of fundamental and technical noise related nature. The fundamental heating rate is due to far-detuned elastic scattering, which leads to

an increase of thermal energy by $2E_{rec} = k_B T_{rec}$ in a time Γ_{sc}^{-1}, which effectively leads to a heating rate of

$$\dot{Q}_{rec} = 2E_{rec}\Gamma_{sc},$$

where Γ_{sc} is the total scattering rate. This heating rate gives rise to an estimate of the maximum storage time of $U_0/\dot{Q}_{rec}$ [50]. It can be shown that rate of temperature increase due to spontaneous heating in a red detuned dipole trap in thermal equilibrium with a separable potential is proportional to the trap depth U_0 [42]

$$\dot{T} = \frac{2/3}{1+\kappa} T_{rec} \frac{\Gamma}{\hbar|\Delta|} U_0, \tag{53}$$

for $U_0 \gg k_B T$. In this equation, $\kappa = \frac{\overline{E}_{pot}}{\overline{E}_{kin}}$ is the ratio of mean potential and mean kinetic energy and Γ is the decay rate of the excited state. The order of magnitude storage time $U_0/(k_B \dot{T})$ however should be independent of the trap depth. However there were reports, that far red detuned traps suffer from heating rates, which might not entirely be accounted for by spontaneous heating. In [51] storage times of a few seconds have been reported and they found that the storage time was longer, the lesser the total trapping power and that for powers less than 1 W, trap loss was dominated by background gas collisions. It has been pointed out in [52, 53] that the rate of heating and therefore trap storage times might sensitively depend on the technical noise spectrum of the laser in use. Within a 1D fluctuating harmonic oscillator model, they modelled intensity fluctuations as variations in the spring constant and beam pointing fluctuations as fluctuations of the minimum of the harmonic oscillator. Within this model, apart from a *constant* heating rate due to a beam pointing instability, they find that intensity fluctuations of the laser, incoorperated in their model by fractional fluctuations $\epsilon(t) = \frac{I(t) - \langle I(t) \rangle}{\langle I(t) \rangle}$, lead to an *exponential* heating rate according to

$$\langle \dot{E} \rangle = \frac{\langle E \rangle}{T_I},$$

where the $T_I = T_I(\mathrm{sec})$ is the energy e-folding time in seconds, given by

$$T_I = \frac{1}{\pi^2 \nu_{tr}^2 S_\epsilon(2\nu_{tr})}, \tag{54}$$

and the frequency spectrum of the laser intensity noise $S_\epsilon(\nu) = \frac{2}{\pi} \int_0^\infty d\tau \cos(\omega\tau) \langle \epsilon(t)\epsilon(t+\tau) \rangle$ is normalized so that

$$\int_0^\infty d\nu S_\epsilon(\nu) = \langle \epsilon^2(t) \rangle \equiv \epsilon_0^2, \tag{55}$$

where ϵ_0^2 is the mean square variation in fractional fluctuations of the laser intensity. The noise spectrum being evaluated at twice the trap frequency, shows that fluctuations at twice the trap frequency can parametrically drive the oscillatory motion of the atoms.

By making the simple assumption on the noise spectrum of being evenly distributed over a certain bandwidth, one can give estimates for the upper bounds on the fractional intensity noise depending on the energy e-folding time and the trap frequency. From Eq. 54, it follows that the requirement on the fractional intensity noise is the more stringent, the higher the trap frequency is. In order to achieve an energy e-folding time $T_I \geq 100\,\mathrm{sec}$ at trap frequency

of 74 kHz a value of $S_\epsilon(2\nu_{tr}) \approx 1.85 \cdot 10^{-11}$ Hz is necessary. If we assume, that the power spectrum is constant over a 40 kHz bandwidth, i.e. from Eq. 55 follows

$$40\,\text{kHz} \cdot S_\epsilon = \epsilon_0^2,$$

so that from Eq. 54 we find that

$$\epsilon_0 \leq 8.6 \cdot 10^{-5}.$$

This emphasizes, that low intensity fluctuations are required at high trap frequencies. By inserting the trap frequencies of a focused Gaussian beam trap of Eq. 52 into Eq. 54, we see that the energy e-folding time is inversely proportional to the trap depth. In [44] it is stated, that by use of a laser which has a relative intensity noise of $S_\epsilon(2\nu_{tr}) \leq 10^{-14}\text{Hz}^{-1}$, they were able to achieve storage times of several tens of seconds and they found agreement for their measured storage times with Eq. 54 up to a factor of 2. But the noise spectrum of a laser also can be actively counteracted with an AOM via a feedback loop which use one or two photodetectors. Improvement of lifetimes by one order of magnitude has been demonstrated in [45] with a dual photodetector scheme. To the knowledge of the author, the current record in trap storage time of ≈ 300 s is reported in [54], where they employed an ultra-stable CO_2 laser at 10.6 μm with a fractional intensity noise of $S_\epsilon(9.4\,\text{kHz}) \leq 1.0 \times 10^{-13}\text{Hz}^{-1}$ and $S_\epsilon(440\,\text{Hz}) \approx 1.1 \cdot 10^{-11}$ Hz at twice of the radial and axial trap frequency respectively.

5.1.2 Collisional stability

State-changing, or *inelastic*, collisions pose one of the biggest challenge in achieving high density atomic samples in optical traps. Only collisionally stable electronic and spin mixtures can efficiently be trapped within a shallow dipole force trap. Especially in cold collisions, when the deBroglie wavelength λ_{dB} is becoming comparable to the interparticle distance, the wavefunctions of the colliding atoms mostly probe the long range part of their interaction potential, which for two identical atoms has the general form [28]

$$U(R) = -\frac{C_n}{R^n} + \frac{\hbar^2 l(l+1)}{2\mu R}.$$

The n in the leading term depends on the electronic state of the colliding atoms. In case of two ground state atoms $S + S$, the interaction potential is given by the Van-der-Waals potential with $n = 6$. If both atoms are in the excited state $P + P$, the leading term is $n = 5$, corresponding to a quadrupole-quadrupole interaction. Interestingly, the interaction potential has the longest range with $n = 3$ for collision of one ground state and one excited state atom $S + P$. In this case the two atoms share the excitation forth and back, which is why it is described a resonant dipole-dipole interaction [55]. The cross-section for these inleastic excited state collisions can be of several orders of magnitude higher than that of pure ground state collisions, which is why they represent the dominant trap loss mechanism in spontaneous-force optical traps [56] and are addressed first.

Inleastic excited state collisions Excited state collisions play an important role in optical traps, since laser cooling uses near-resonant light leading to a large fraction of atoms in the excited state. The dominant loss mechanism in this context is radiative or light-assisted escape. In a collision between two ground state atoms, one of the two atoms can get excited by absorption of a photon at the condon point R_C, where $\hbar\delta = -\frac{C_3}{R_C^3}$, so that the two atoms

start interacting on the attractive S-P potential energy curve (PEC). They thereby form a transient molecule which has a lifetime related to the lifetime of the atomic excited state. This is the principle of photo-associative spectroscopy (PAS), which will be explained in more detail in Sec. 8 as a method to produce cold homonuclear dimers in our experiment. Since the PEC of the resonant dipole-dipole interaction is $\sim \frac{1}{R^3}$, and therefore much steeper than the $S+S$ PEC which is $\sim \frac{1}{R^6}$, the atoms get accelerated towards each other and eventually the excited state atom emits a photon at much smaller internuclear seperation with less energy than the absorbed photon, resulting again in a free pair of atoms but with much higher kinetic energy. The gain in kinetic energy can be larger than the trap depth of the optical trap. Another possibility would be a fine-structure changing collision, where the transient molecule emits a photon making the excited atom transition to a different state in the fine structure of the atom. The difference in potential energy between these two states is converted into kinetic energy and the gain in kinetic energy again can be larger than the trap depth.

Inelastic ground state collisions Elastic collisions are need for long trap lifetime and moreover play an important role in rapid thermalization in forced evaporative cooling. The dominant loss mechanism in ground state collisions $S+S$ are spin-exchange collision. These result from exchange potential, which is the difference potential between singlet and triplet spin configuration of the two colliding atoms. The triplet potential ${}^3\Sigma_u^+$ is much shallower than the singlet potential ${}^1\Sigma_g^+$. The total spin quantum number m_T is conserved in a spin-exchange collision. For example in a spin mixture^{6}Li, the antisymmetric two particle spin state which have $m_T=-1$ are $|\{3,1\}\rangle$, $|\{4,2\}\rangle$ and $|\{5,3\}\rangle$, given in the order of energy from lowest to highest. Therefore exothermic spin exchange collisions from e.g. $|\{5,3\}\rangle$ to $|\{3,1\}\rangle$, $|\{4,2\}\rangle$ could happen, but also non-exothermic spin-exchange transition from $|\{3,1\}\rangle$ to the other $M_T=-1$ states can take place by borrowing from the atoms' trap potential energy. This can be effectively suppressed in an optical dipole force trap by applying a small offset magnetic field so that the energy difference between the states $|\{4,2\}\rangle$ and $|\{5,3\}\rangle$ and that of $|\{3,1\}\rangle$ is more than the maximum relative kinetic energy, i.e. twice the well depth [57]. Apart from spin-exchange collisions which conserve the total magnetic quantum number, magnetic dipole-dipole transitions of the electrons where the total magnetic quantum number is not conserved may contribute to trap loss. The loss rates for due to such processes however are usually several order of magnitudes lower than of spin-exchange collisions.

Because of the aforementioned loss mechanisms, atomic samples of ^{6}Li in optical dipole traps are usually in their ground state and prepared in the energetically lowest $m_T=0$ state $|\{1,2\}\rangle$, which is collisionally stable against spin-exchange transitions like$|1\rangle \rightarrow |5\rangle$, $|2\rangle \rightarrow |4\rangle$ that are energetically suppressed even at zero magnetic field. Furthermore this spin mixture is most easily created by optical pumping from the $F=3/2$ manifold to the $F=1/2$.

5.2 Loading procedure

The trapping depth of an optical trap, as outlined in 5, depends on the polarizability of the atom's electronic state. In order to avoid density reducing inleastic collisions, atoms are loaded into their dipole trap while they are in their stable electronic ground state. However the trap depth, for alkali atoms like ^{6}Li in their electronic ground state is usually, for moderate dipole trap parameters, on the order of a few milikelvins. Therefore it is difficult to efficiently load a dipole trap directly from a atomic beam of thermal atoms. The conventional approach instead is to first trap and laser cool the atoms down to a few milikelvins and then turn on the trapping potential of the dipole trap. During this procedure usually up to a few percents

of the magneto-optically trapped atoms are transferred into the optical dipole trap. In [58] it has been reported that about 2% of the atoms trapped in their MOT, remain in the optical dipole trap. [44] reports only about 0.5%, while the remainder is lost in the first 60 ms.[45] reports that after 1 s of plain evaporative cooling about 0.4 % of the magneto-optically trapped atoms remain their crossed dipole trap. The transfer efficiency is measured by recapturing the optically trapped atoms into the MOT. Since the MOT has a trap depth and also a trapping volume much larger, than that of the dipole trap, the recapturing efficiency is close to 100%. In order to achieve a high transfer efficiency, the phase-space density of the atomic sample should be maximized, i.e. making the atoms as cold and as dense as possible, prior to switching off the MOT. As can be seen from the expression for the velocity-dependent force on a two-level atom in a standing wave Eq. 28, this can be achieved by lowering the beam intensities and reducing the detuning from the resonance. A typical sequence of analog voltages which control detuning (Beat VCO), MOT beam intensities (Cooler and Repump VCA), dipole trap depth (Dipole and RF driver power) and MOT magnetic field (MOT current) can be seen in Fig. 75 in chapter 11.2. The temperature of the dipole trapped atoms after 200 ms of initial evaporative cooling was measured and is plotted in Fig. 80.

6 Photoionization of atoms

Photoionization denotes the process of removing an electron from an atom or a molecule by the presence of a light field. The dynamic of how and the probability that the electron is removed, depends on the ionization potential of the atom, the photon energy and the intensity of the light field. If the photon energy $\hbar\omega$ is larger than the ionization potential E_{IP}, absorption of one photon is enough to lift an electron from the ground state into the continuum with an excess energy given by (see Fig. 35)

$$E_{excs} = E_{IP} - \hbar\omega, \quad \hbar\omega > \mathrm{E_{IP}}.$$

This process is called *single-photon ionization*. If the photon energy is much lower than the ionization potential, $\hbar\omega \ll E_{IP}$, single photon ionization is impossible. Nowadays, ultrashort and intense pulses can be created with field intensities on the order or above the atomic unit of intensity

$$I_a = \frac{1}{2}\epsilon_0 c \epsilon_a^2 \approx 3.5 \cdot 10^{16} \frac{\mathrm{W}}{\mathrm{cm}^2}, \tag{56}$$

where $\epsilon_a = \frac{e}{(4\pi\epsilon_0)a_0^2} \backsimeq 5.1 \cdot 10^9 \frac{\mathrm{V}}{\mathrm{cm}}$ is the electric field exerted on an electron on the first Bohr radius of atomic hydrogen. An important quantity in photoionization experiments with ultrashort pulses is the peak intensity I_0 in the focus

$$I_0 = \frac{2\frac{\overline{P}}{\nu_{rep}}}{\pi\tau w_0^2},$$

where $\overline{P}$ is the average power being focused, ν_{rep} the repetition frequency of the available laser system, τ the pulse duration of the employed pulses and $2w_0$ the diameter of the fs laser beam at its focus. The electric field strength itself is related to peak intensity I_0 by $I_0 = \frac{cn\epsilon_0}{2}|E_0|^2$.

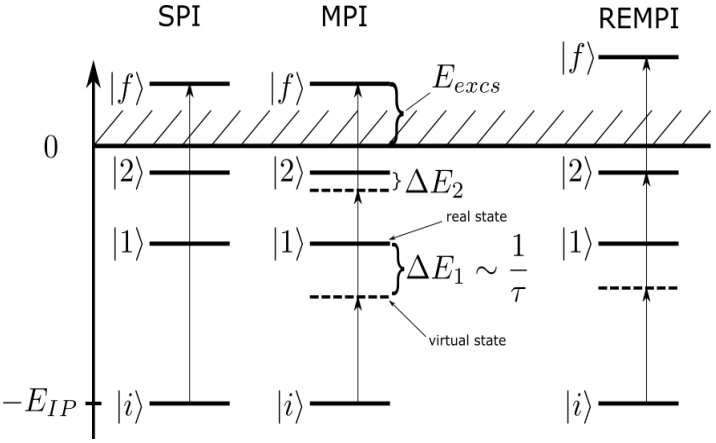

Figure 35: Illustration of single-photon, multi-photon and resonance-enhanced multi-photon ionization via real and virtual intermediate states.

Using such intense laser fields, ionization is possible even in the non-resonant case by a process called multi-photon ionization (MPI). If the uncertainty principle of quantum mechanics $\Delta E \cdot \Delta t \geq 1$ is taken into account, an electron can be found in a virtual state, whose lifetime τ is associated with the energy difference to a nearby real state, i.e. $\tau \sim \frac{1}{\Delta E_1}$ (see Fig. 35).

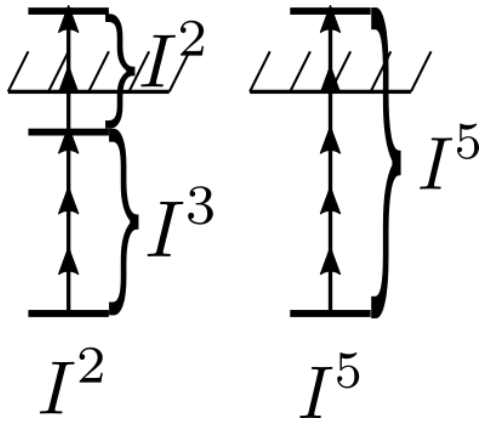

Figure 36: The order of non-linearity of a multi-photon process illustrated in two schemes with and without a real intermediate level.

The lifetime of these virtual states are orders of magnitude smaller, than the lifetimes of real states. If the photon flux is high enough, the electron can be excited within the lifetime of the virtual level to another real or virtual level. Therefore, even when $\hbar\omega < E_{IP}$ holds, for high enough photon fluxes an electron can be lifted into a continuum state above the ionization potential by "simultaneous" absorption of n photons. If the electron is excited into a continuum state and all intermediate states are virtual levels, then this process is called *(non-resonant) multi-photon ionization* (MPI). The excess energy of the electron in the case of MPI is be given by

$$E_{excs} = n\hbar\omega - IP.$$

MPI is a non-linear process, because from lowest order-perturbation theory (LOPT) follows that the ionization rate W is characterized by a power law dependence

$$W \sim I^{n_0},$$

where n_0 is the minimum integer number of photons, so that $n_0\hbar\omega >$ IP, and n_0 is referred to as the order of non-linearity.

It also exists the possibility, that a multiple m of the photon energy matches the energy difference between the initial state and one of the real intermediate states (see Fig. 35). If at least one of the intermediate states is real, the process is called *resonance-enhanced multi-photon ionization* (REMPI). In this case the order of non-linearity is strongly reduced and the excess energy of the electron is given by

$$E_e = (n - m) \cdot \hbar\omega - E_{IP}.$$

The order of non-linearity of the process therefore is determined by the number of photons needed to ionize from the last real intermediate state (see Fig. 36).

The question, which intermediate states, whether real or virtual, contribute significantly to the transition matrix element, also depends on selection rules in electric dipole approximation. In multi-photon ionization with linear polarized light only transitions between states of oppositve parity are allowed ($\Delta l = \pm 1$, $\Delta m = 0$).

The cross section of non-resonant multi-photon ionization is much smaller than that of single-photon or resonance enhanced multi-photon ionization and it requires a high photon

flux. Multi-photon ionization of atoms and molecules therefore is a high intensity effect which typically requires minimum intensities on the order of $I > 10^{10} \frac{\mathrm{W}}{\mathrm{cm}^2}$. For intensities $I > 10^{11} \frac{\mathrm{W}}{\mathrm{cm}^2}$, the already free electron might even absorb another photon in excess of the number of photons n_0, which are required for multi-photon ionization. The excess energy of the electron is then given by

$$E_{excs} = (n_0 + s)\hbar\omega - E_{IP},$$

where s is the number of excess photons absorbed. This is a phenomenon called above-threshold ionization (ATI) and in the electron energy spectrum, the intensity dependence of these features, still follows the LOPT prediction, i.e. $\sim I^{n_0+s}$. From intensities of $10^{12} \frac{\mathrm{W}}{\mathrm{cm}^2}$ and above, the field cannot be considered a small perturbation anymore, because ponderomotive effects have to be taken into account. The electron is oscillating fast in the external laser field and its cycle-averaged kinetic energy U_p, also called the *electron ponderomotive energy*, is given in a monochromatic field by

$$U_p = \frac{e^2|E_0|^2}{4m\omega^2},$$

where E_0 is the electric field strength and m is the mass of the electron, and ω is the frequency of the monochromatic field. The energies of Rydberg and continuum states are shifted upward by this amount. At low intensities, this ponderomotive shift is small compared to the excess energy of the photoelectrons, but as the intensity is increased, the ATI peaks in the energy spectrum of the electrons are reduced in magnitude, because the ionization potential is AC Stark shifted by the ponderomotive energy, leading to an effective ionization potential

$$E_{IP^*} = E_{IP} + U_p.$$

In strong fields with intensities beyond $10^{14} \frac{\mathrm{W}}{\mathrm{cm}^2}$, the ponderomotive shift U_p can reach values of several 10 eV and the energy of the detected electron will depend on the phase and the intensity of the laser field at the time it was liberated. For light field intensities of these intensities, the atomic potential is distorted by the strong field, leading to different ionization dynamics like tunnel ionization or over-the-barrier ionization (see Fig. 37). In tunneling ionization, the light field bends the atomic potential at a certain phase to such an extent, that a potential barrier forms, through which the electron can tunnel out. If the initial energy level of the electron is high enough, this could mean that the electron can escape the atomic potential without absorption of a photon. Eventually, when the intensity exceeds a critical intensity I_C, the barrier is lowered so much, that the outermost electron is not bound anymore and classically escapes "over the top" of the barrier. This process is also called "over-the-barrier" ionization (OBI). For atomic hydrogen, the value of the critical intensity I_C, where the effective potential is lowered to a value equal to the ionization potential of the bound electron is $1.4 \cdot 10^{14}\, W\, cm^{-2}$.

An important quantity, that includes the different dependencies of the ionization dynamic, ionization potential IP, frequency ω, and intensity I_0 into one single dimensionless parameter is the Keldysh parameter

$$\gamma_K = \left(\frac{E_{IP}}{2U_P}\right)^{\frac{1}{2}},$$

where U_p is the ponderomotive shift of the electron, which itself depends on frequency ω and field intensity I_0. The value of the Keldysh parameter decides, which ionization mechanism

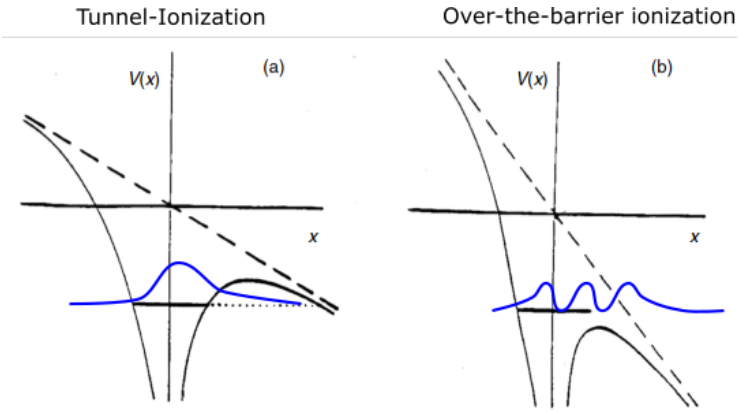

Figure 37: Ionization dynamics for $\gamma_K \lesssim 1$: (a) The electron might tunnel from the ionic potential or (b) it might escape over the barrier without tunneling. (Fig. from [59])

regime	necessary intensity $\frac{\mathrm{W}}{\mathrm{cm}^2}$	Keldysh parameter γ_K
MPI	$\geq 10^{10}$	≥ 1
ATI	$\geq 10^{11}$	
Ponderomotive Shifts	$\geq 10^{13}$	≤ 1
Tunnel and OBI	$\geq 10^{14}$	

Table 2: Ionization regimes and typical orders of magnitude of minimum intensities.

is dominant. In Tab. 2 are summarized the different ionization mechanism, sorted by their respective required minimum intensities and their respective Keldish parameter γ_K . In this table, Ponderomotive shifts are meant to become non-negligible compared to the electron excess energies for peak intensities on the order of 10^{13} and higher.

Part IV
Production of homonuclear ^{6}Li dimers as a target in a ReMi

The theme of this thesis is to extend a reaction microscope with a MOT by a far-off resonance trap in which association techniques can be applied to form translationally cold molecules from translationally cold atoms. These cold molecules then can be investigated e.g. by ionizing them with fs pulses. Fundamentally, when talking about association techniques, molecule formation from an ultracold gas of atoms most likely happens through either of following two processes:

- Photoassociation, i.e. if during the collision of two atoms in their electronic ground state, one of the atoms absorbs a photon of the right frequency, both atoms are excited into a short-lived electronically excited molecular dimer.

- Three body recombination, i.e. in the collision of three atoms in their electronic ground-state, two atoms bind together into a ground-state dimer, while the excess energy is carried away by the third atom.

Since photoassociation only requires two collision partners, while three-body recombination requires three, their dimer formation rates scale proportional to n^2 and n^3 respectively, where n denotes the density of the atomic sample. Photoassociation (PA) can happen by trapping light or an additional photoassociation beam and will be explained in more detail in 8. Usually cold molecule production by spontaneous decay of a short-lived electronically excited molecules tends to populate only higher-lying vibrational levels of the electronic ground state molecules according to the Franck-Condon principle. However when the short-lived excited molecule is deexcited by a second photon with the right energy, even deeply-bound ground state dimers can be created in any vibrational state with high efficiency. Therefore photoassociation of molecules from atoms is a very flexible technique, that in principle allows creation of ground state molecules in any vibrational state.

On the other hand the use of the photo-association technqiue limits the accessible phase-space, since it relies on scattering. In contrast, efficient dimer formation by three-body recombination enables to reach regimes of high phase space density. This technique is suited for production of weakly-bound dimers, i.e. groundstate molecules which are occupying the highest vibrational level just below dissociation threshold. When such a weakly bound molecule is created, the excess energy carried away by the third atom is on the order of the temperature of the gas, and the atomic sample does not excessively heat up. Three-body recombination can be enforced by increasing the phase-space density of the atomic sample, which is commonly done by a non-dissipative technique like forced evaporative cooling. For an atomic species like ^{6}Li, efficient forced evaporative cooling requires tuning the effective long-range interaction between the atoms by applying an external magnetic field to a value close to a Feshbach resonance. This technique is therefore coined "magneto-association" and will be explained in more detail in Sec. 9. Before theses association techniques are explained, the reader will be acquainted in Sec. 7 with the basic notation for molecular potential energy curves in Hund's case (a) and (b), which explain how the different angular momenta in the molecules of our interest will couple.

7 Born-Oppenheimer potentials, molecular orbitals and selection rules of homonuclear dimers

In a non-relativistic, rotation-free approximation of the dimer, only the largest energy scale given by the electrostatic interaction between electrons and nuclei in a particular molecular orbital is taken into account, but no spin-orbit or hyperfine interactions. These molecular orbitals must fulfill certain symmetries in order to satisfy (anti-)symmetrization constraints of the total molecular wavefunction. In this initial treatment, the bond axis of the dimer is fixed in space, and one can compute the potential energy $E_{el}(R)$ of the pair of electrons at each atomic separation R (see e.g. [60]). The resulting potential curves $E_{el}(R)$ are referred to as "adiabatic Born Oppenheimer potentials". If, besides the electrostatic energy E_{el}, also kinetic energy from its motional degrees of freedom is taken into account, then the total energy E_{tot} of a diatomic molecule also has contributions from vibrational E_{vib}, and rotational energy E_{rot}:

$$E_{tot} = E_{el} + E_{vib} + E_{rot},$$

where E_{vib} is the vibrational energy corresponding to one normal mode of vibration, and E_{rot} is the rotational energy associated to the rotational angular momentum $\mathbf{N} = N \cdot \mathbf{e}_B$ of the relative motion of the nuclei, which is always perpendicular to the bond axis (see Fig. 38).

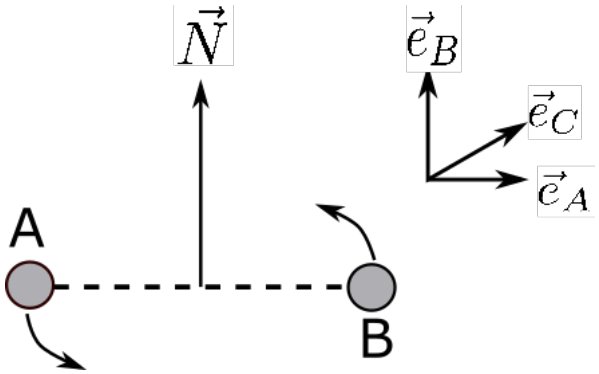

Figure 38: Rotational angular momentum associated with the relative motion of the nuclei in a diatomic molecule.

The total angular momentum operator $\mathbf{J}$, ignoring nuclear spin for the moment, of a diatomic molecule would further take into account orbital and spin angular momentum of electrons,

$$\mathbf{J} = \mathbf{L} + \mathbf{N} + \mathbf{S},$$

where $\mathbf{L} = \mathbf{l}_1 + \mathbf{l}_2$ is the total electronic orbital angular momentum, and $\mathbf{S} = \mathbf{s}_1 + \mathbf{s}_2$ the total molecular electron spin angular momentum. If we also take into account the nuclear spin, $\mathbf{S}$ had to be replaced by the total molecular spin $\mathbf{G} = \mathbf{S} + \mathbf{I}$. There are many ways the molecular angular momenta can couple between each other, like $L-S$, $J-S$, $J-L$, $N-S$, ... coupling etc. Depending on which coupling defines the dominant energy scale, we can determine which quantities are conserved and therefore provide good quantum numbers. The five Hund's cases (a)-(e) describe some idealized cases of how the angular momenta might couple together in a di-atomic molecule, depending on the relative strength of the different couplings. The two most important Hund's cases are (a) and (b), in which due to the electrostatic field along the

bonding axis, the total electron orbital angular momentum $\mathbf{L}$ is strongly coupled to the bond axis, therefore L is not a good quantum number, but the projection of the electronic orbital angular momentum

$$\Lambda = |\mathbf{L} \cdot \mathbf{e}_A| = |m_L|, \quad \Lambda = 0, 1, 2, \ldots, L$$

on the bond axis is. The value of the projection Λ of the total electronic orbital angular momentum is replaced in the spectroscopy notation by Greek letters:

$$0 \equiv \Sigma,\ 1 \equiv \Pi,\ 2 \equiv \Delta,\ 3 \equiv \Phi.$$

In Hund's case (b), the most important relativistic interaction, the molecular spin orbit coupling $\sim \mathbf{L} \cdot \mathbf{S}$ is weak, therefore $\mathbf{S}$ is only weakly coupled to the bond axis and S is a good quantum number. In this case the total molecular orbital angular momentum$\mathbf{K} = \mathbf{L} + \mathbf{N}$ is given by

$$\mathbf{K} = \Lambda \cdot \mathbf{e}_A + N \cdot \mathbf{e}_B,$$

and

$$\mathbf{J} = \mathbf{K} + \mathbf{S}.$$

Therefore in Hund's case (b), a molecular state can be described by following relevant quantum numbers: (Λ, K, S, J). The spectroscopic notation for molecular orbitals in Hund's non-relativistic case (b) is

$$^{2S+1}\Lambda^{+/-}_{g/u}, \tag{57}$$

where the subscript g/u refers to an inversion symmetry due to the antisymmetry of the total molecular wavefunction in case of fermions, and the superscript $+/-$ refers to a reflection symmetry along an arbitrary plane containing the internuclear axis, which only Σ states exhibit. In a homonuclear dimer in which both atoms are in the same electronic state, the quantum numbers S, Λ, and $\pm$ uniquely determine the quantum number g/u. The molecular term symbol of Σ states, is preceded by a letter (not shown in Eq. 57), depending on if the electron spins combine to a singlet state ($S = 0$) or to a triplet state ($S = 1$):

1. Singlet state: The electronic ground state is preceded by X, while the next state is preceded by an A (or 1), followed by a B (or 2) and so on.

2. Triplet state: The ground state is preceded by lower-case a or 1, the next optically accessible state is b (or 2), then c (or 3) and so on.

These spectroscopic term symbols serve as labels for the different Born-Oppenheimer potentials in a non-relativistic approximation. In Fig. 39, several potential energy curves of the Li_2 molecule are shown of low lying states labeled with their corresponding spectroscopic notation for the molecular orbital. As can be seen, both potentials dissociating to the $2S - 2S$ limit have Van-der-Waals character with an effective potential range of $R_0 \approx 10a_0$. Hund's case (b) is e.g. realized for a Σ state, in which the spin-orbit coupling vanishes.

The description of the molecular spin-orbit interaction depends on the range of R, in which it is considered. For large $R \gg R_0$, when the molecular wavefunction can be accurately described by the product of two atomic wavefunctions, the molecular spin-orbit interaction

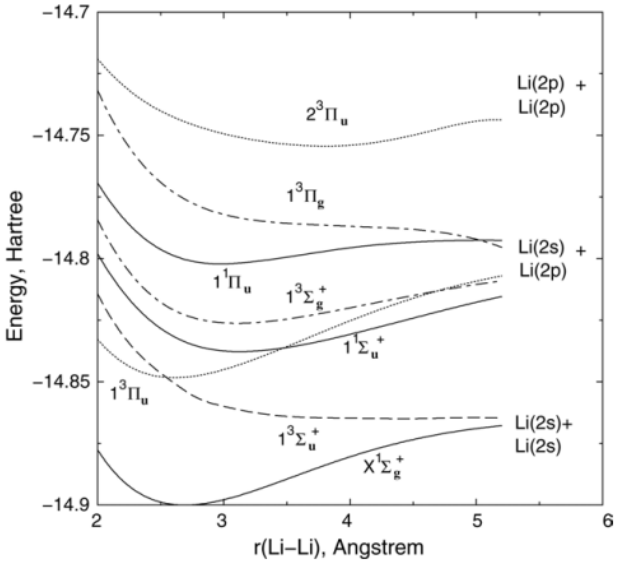

Figure 39: Calculated Born Oppenheimer potential energy curves for Li_2 molecules (from [61])

is the sum of the atomic spin-orbit interaction. At short range $R \leq R_0$ the electron clouds distort and a more complex effective Hamiltonian might be required, that also describes the R dependence of the spin-orbit interaction.

Hund's case (a) considers the situation in which the electrostatic coupling of $\mathbf{L}$ to the bond axis is strong and the molecular spin orbit coupling $\sim \mathbf{L}\cdot\mathbf{S}$ is relatively strong, so that the total spin $\mathbf{S}$ interacts as well strongly with the axial field of the molecule. Therefore the projection of the molecular spin

$$\Sigma = \mathbf{S}\cdot\mathbf{e}_A = m_S, \quad \Sigma = -S, -S+1, ..., S$$

on the bond axis is a conserved quantity. The quantum number Σ is not to be confused with the value 0 for the quantum number Λ in spectroscopic notation. Furthermore also the projection of the total angular momentum

$$\Omega := |\Lambda + \Sigma| \tag{58}$$

is a good quantum number, which takes values in $\{\max(|\Lambda - S|, 0), \max(|\Lambda - S|, 0) + 1, \ldots, \Lambda + S\}$. The vector $\mathbf{\Omega} = (\Lambda + \Sigma)\cdot\mathbf{e}_A$ represents the total electronic angular momentum pointing along the bond axis. The total angular momentum of the molecule then is given by

$$\mathbf{J} = \mathbf{\Omega} + \mathbf{N},$$

with $\mathbf{N} = N\cdot\mathbf{e}_B$ being perpendicular to the bond axis. Therefore each electronic energy level with $\Lambda \geq S$ corresponds to a series of $2S+1$ rotational levels with different values of J, where $J \geq \Omega$. In Hund's case (a) the set of relevant quantum numbers for a molecular state is $(\Lambda, S, \Sigma, \Omega, J)$. Hund's case (a) does not apply to Σ states or singlet states, since if either $\Lambda = 0$ or $S = 0$ the spin-orbit coupling vanishes. The spectroscopic notation for molecular states with intermediate spin-orbit interaction is given by

$$\Omega_{g/u}^{+/-}.$$

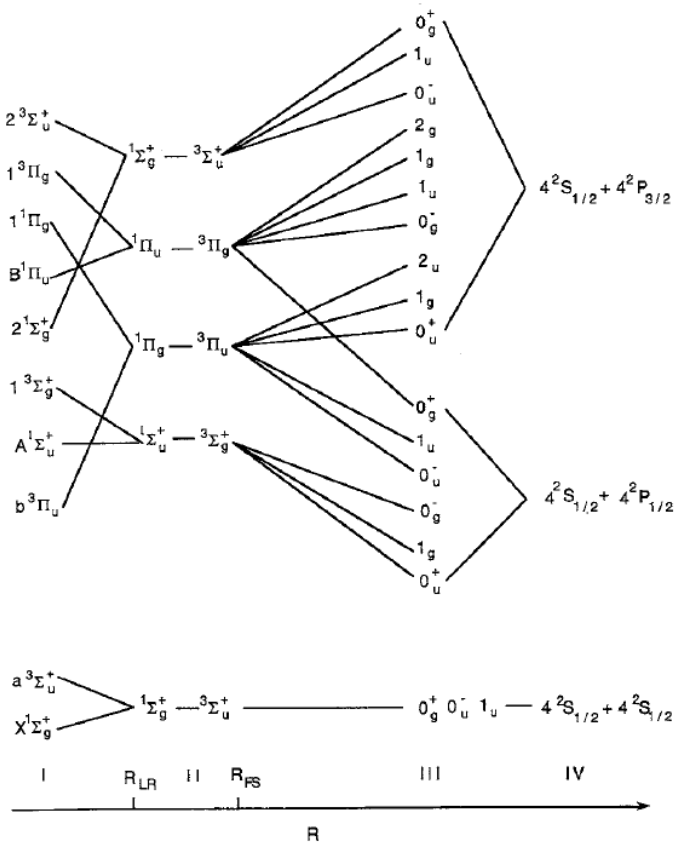

Figure 40: Relativistic adiabatic potentials for homonuclear alkali-metal dimers and their connection to adibatic Born-Oppenheimer potentials.

This labeling is not unique since the same values occur multiple times for different dissociation limits (see Fig. 40). In order to distinguish better the different attractive potentials, it is useful to additionally specify the dissociation limit, e.g. $0_g^+(4^2S_{1/2} + 4^2S_{1/2})$. The energy splitting caused by spin-orbit coupling is about 100 times smaller, than the energy scale defined by the electrostatic interaction at small range. Therefore this energy splitting only becomes important at large internuclear distances, as is illustrated in Fig. 40. An interesting point is that in alkali metals the relativistic potentials $0_g^-(^2S+^2P_{3/2})$ and $1_u(^2S+^2P_{3/2})$ have a potential well with a minimum at long range around $70a_0$, which is deep enough to support several bound states. These long-range potentials might play a role in photo-association via trapping light in a magneto-optical trap (see Subsec. 12.2). The Born-Oppenheimer potentials $1^3\Sigma_g^+$ and $A^1\Sigma_u^+$ whose vibrational levels can be adressed via a 1-photon dipole transition in PA spectroscopy, correlate at long range to the relativistic adiabatic potential $1_g(^2S+^2P_{1/2})$, $0_g^-(^2S+^2P_{1/2})$ and $0_u^+(^2S+^2P_{1/2})$ respectively. The latter potentials belong to Hund's case (c), where the internuclear distance is sufficiently large, so that the spin-orbit coupling becomes stronger, than the electrostatic coupling of $\mathbf{L}$ to the bond axis.

The selection rules between molecular states depend on which quantum numbers are good in the initial state and final state. In Hund's case (a) with relevant quantum numbers

$(\Lambda, S, \Sigma, \Omega, J)$ the selection rules between ro-vibrational levels can be summarized as follows:

$$\begin{aligned}
\Delta\Lambda &= 0, \pm 1, \\
\Delta S &= 0, \\
\Delta\Sigma &= 0, \\
\Delta\Omega &= 0, \pm 1 \\
\Delta J &= 0, \pm 1.
\end{aligned}$$

However $\Delta J = 0$ is forbidden, when $\Omega = 0$ both in initial and final state. Furthermore for symmetrical diatomic molecules, only transitions between states with opposite parity are allowed, i.e. $g/u \leftrightarrow u/g$. In Hund's case (b) with relevant quantum numbers (Λ, K, S, J) the selection rule for J is replaced by a selection rule for K:

$$\Delta K = 0, \pm 1.$$

However for $\Sigma \leftrightarrow \Sigma$ transitions, $\Delta K = 0$ transitions are electric-dipole forbidden. Allowed $\Sigma \leftrightarrow \Sigma$ transitions with $K = -1$ are called the P branch, while $\Sigma \leftrightarrow \Sigma$ transitions with $K = +1$ are called R branch. Also for Σ states, reflection symmetry is not changed, i.e. $\pm \leftrightarrow \pm$. Transitions between ro-vibrational levels are subject to

$$\Delta\nu = \pm 1\,(\pm 2, \pm 3, \text{etc.})$$

8 Cold ground state molecules via cw photoassociation

In general, when two atoms approach each other along the molecular potential of their entrance channel in the presence of an optical field of moderate intensity (i.e. less than $1\,\mathrm{kW\,cm^{-2}}$), this pair of free atoms can be excited into a bound molecular level of a different molecular potential [62], which can be accessed via a dipole-transition according to selection rules. If the photon energy $E_\gamma = E_{at} - E_b - E_{th}$ matches at a particular distance $R_{\nu+}$, so that the photon is in resonance with a free-bound transition, the pair of free atoms end up in a bound level of the electronically excited state, i.e. a bound state of the $S-P$ molecular potential energy curve.

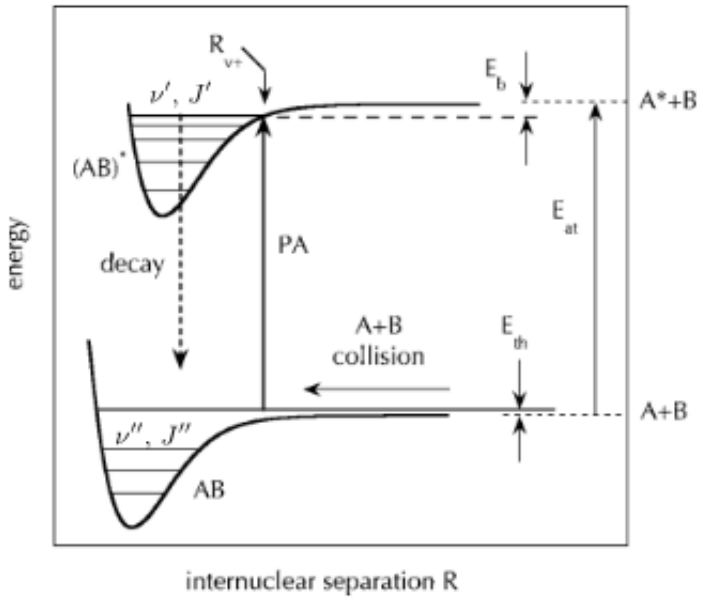

Figure 41: PA scheme of process $A + B + \gamma \rightarrow (AB)^*$(from [55]) in which a continuum-bound process is driven. The decay process is either $(AB)^* \rightarrow A + B + \gamma_d$ or $(AB)^* \rightarrow AB + \gamma_d$.

This association process is illustrated in Fig. 41, in which a free pair of atoms $A + B$ with collision energy E_{th}, given by the temperature of the atomic gas, collide on the (AB) potential energy curve in the entrance channel, from where, by absorption of a photon with the right detuning δ at the condon point $R_{\nu+}$, they are excited into a short-lived molecular state ν', J' with binding energy E_b[18] of the $(AB)^*$ potential energy curve:

$$A + B + h\nu_{PA} \rightarrow (AB)^*$$

[18] defined as the energy difference between the dissociation threshold of the $(AB)^*$ potential energy curve and the respective vibrational level ν

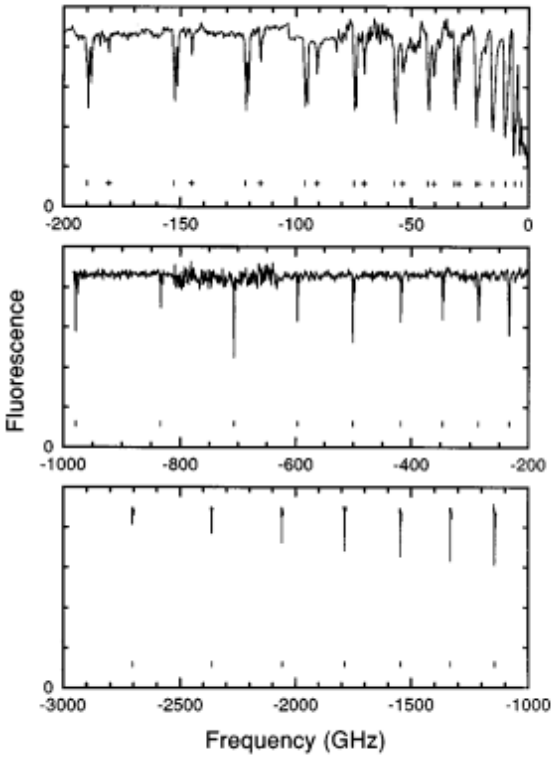

Figure 42: Photoassociative spectrum of $^6Li_2$ identifying vibrational levels from $v' = 84$ to $v' = 56$. High lying vibrational resonances exhibit a well-resolved substructure due to rotational energy, where the $J = 1$ final state is dominant due to predominant s-wave scattering. From [63].

Most commonly the two atoms are in their electronic ground state, so the entrance channel molecular potential would be given by the $S - S$ potential energy curve. From there a photon can excite one of the two atoms via a dipole-allowed transition into the first electronically excited state P, so the $(AB)*$ potential would correspond to the $S + P$ potential energy curve. As mentioned in Sec. 5.1 on trap loss mechanisms, the long-range behaviour of the $S - P$ PEC is in its leading term $\sim -\frac{1}{R^3}$, therefore the condition for the condon point can be stated as

$$\hbar\delta = -\frac{C_3}{R_{\nu+}^3}.$$

In the low energy limit $k_B T \to 0$, the condon point $R_{\nu+}$ can be identified with the outer classical turning point of vibrational level ν'. The electronically excited molecule has a relatively long radiative time, which allows it to vibrate many times before it spontaneously decays by re-emitting a photon of energy $h(\nu_{PA} + \delta_{SP})$:

$$(AB)^* \begin{array}{ll} \nearrow & (AB) + h(\nu_{PA} + \delta_{SP}) \quad \delta_{SP} > 0 \\ \searrow & A + B + h(\nu_{PA} + \delta_{SP}) \quad \delta_{SP} < 0 \end{array}.$$

Depending on the sign of the detuning δ_{SP} two reaction channels are possible, either decay into a bound state $(AB)(v'')$ of the electronic ground state potential, or decay into a pair of free

atoms $A+B$ with kinetic energy E. For this reverse process of dissociation the spontaneous-emission probability for the decay from a resonance v' comes from two contributions, either a bound-bound or a bound-free transition[64]:

$$A_f(\nu') \;=\; \sum_{\nu''} A_{\nu''J''\leftarrow\nu'J'} + \int dE \frac{dA_{El\leftarrow\nu'J'}}{dE},$$

where the probability for spontaneous emission from an initial state (ν', J') into a lower bound state (ν'', J'') is given by

$$A_{\nu''J''\leftarrow\nu'J'} = \frac{4}{3}\frac{e^2}{\hbar c^3}\omega^3_{v'v''}|\langle v'|\mu(R)|v''\rangle|^2, \tag{59}$$

where $\omega_{\nu'\nu''} = (E_{\nu'',J''} - E_{\nu'J'})/\hbar$ is the frequency of the bound-bound transition, and the probability for dissociation into a continuum state with energy between E and $E+dE$ is given by

$$dE\frac{dA_{El\leftarrow\nu'J'}}{dE} = dE\frac{4}{3}\frac{e^2}{\hbar c^3}\omega^3_{v'E}|\langle v'|\mu(R)|E\rangle|^2,$$

where $\omega_{\nu'E} = (E_{\nu'',J''} - E)/\hbar$ is the frequency for the bound-free transition. If $\delta_{SP} < 0$, since the $S-P$ potential is much steeper than the $S-S$ potential, the atoms have been accelerated, so that their relative kinetic energy ϵ'' is usually much larger than the trap depth. If $\delta_{SP} > 0$ the re-emitted photon has a frequency ω_B, so that the excited molecule decays back according to selection rule into a vibrational state of the $S-S$ PEC. The ground-state molecule does not participate in a cooling cycle, therefore it cannot be trapped by scattering forces and its fluorescence cannot be detected. In either case, the result is trap loss which is reflected in a decrease of the fluorescence signal coming from the atoms in the MOT. This method of detecting vibrational levels of the $S-P$ PEC is termed 1-photon spectroscopy and it has been applied in [63] to $^7Li_2$ and $^6Li_2$. In these single-color PA experiments, the energies of high lying vibrational levels $\nu' = 56-84$ of $1^3\Sigma_g^+$ and $A^1\Sigma_u^+$ have been determined. This is possible because at zero external magnetic field, the two-atom scattering state is a superposition of singlet and triplet state, where the triplet state has more statistical weight than the singlet state. Since according to selection rules, the total spin S is not changed, the two possible type of transitions are

$$X^1\Sigma_g^+ \rightarrow A^1\Sigma_u^+$$
$$a^3\Sigma_u^+ \rightarrow 1^3\Sigma_g^+$$

and are called weak and strong series respectively. Compared to single color PA in a dipole trap, performing single color PA in a MOT offers the advantage of a continuous signal, while the frequency of the PA laser is slowly swept over the resonance. By careful calibration of the PA laser's frequency, this then results in trap loss spectra, like in Fig. 42. However in a MOT the atom loss induced by the PA competes with the loading rate of the MOT, therefore only transitions which are strong enough can be observed in a MOT. Furthermore ground-state molecules created by spontaneous decay are not trapped in the MOT, but fall out of the trapping region due to gravity. In contrast, single-color PA can be performed also in a dipole trap, which due long trapping times of many seconds, also offers long irradiation times and usually higher atomic densities in the range of $10^{11} - 10^{12}/\mathrm{cm}^3$, compared to densities of $10^9/\mathrm{cm}^3$in a MOT. Although taking a PA spectrum like that in Fig. 42 takes longer with

a dipole trap, since the loading cycle takes several seconds, the decisive advantage is, that homonuclear dimers like $^6Li_2$ due to their polarizability comparable to that of atoms, should see the same (or even higher) trap depth like the atoms and therefore stay trapped. Furthermore atoms in a dipole trap are usually prepared in a well-defined hyperfine state, which reduces the number of possible transitions. PA on an optically trapped quantum degenerate gas of ^{6}Li atoms has been demonstrated in [65, 66] in order to determine the energies of deeper lying levels of $A^1\Sigma_u^+$ and $1^3\Sigma_g^+$. An overview of the current knowledge of the vibrational levels in the triplet system of ^{6}Li is shown in Fig. 43.

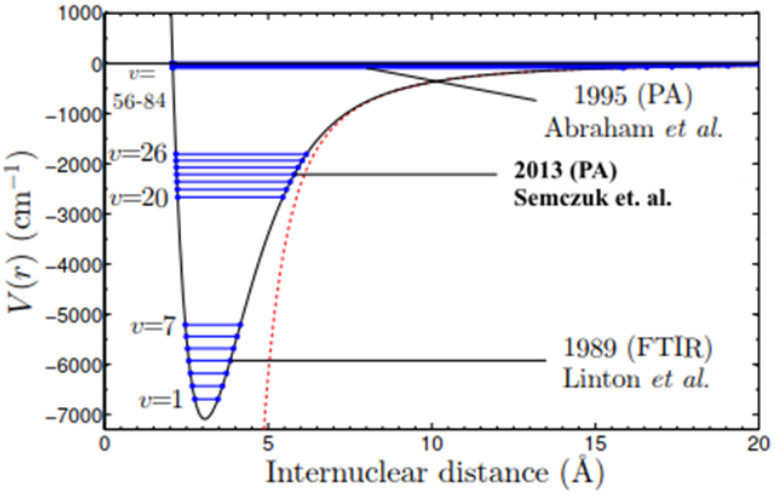

Figure 43: The experimental knowledge of vibrational level of the $1^3\Sigma_g^+$ PEC of $^6Li_2$. From [65].

In oder to properly interpret PA spectra, one needs to know the possible transitions free-bound transitions for both weak and strong series. In PA spectroscopy between Σ states, where the coupling is described by Hund's case (b) and two unbound $2S_{1/2}$ atoms colliding,$\mathbf{K} = \mathbf{N}$and $\mathbf{J} = \mathbf{N} + \mathbf{G}$. Therefore the set of good quantum numbers Λ, K, G, J reduces to N, G and the initial (antisymmetric) two-body eigenstate, consisting of two composite fermions, can be written as

$$|N, G, f_1, f_2\rangle,$$

where N is the rotational quantum number, G the total molecular spin angular momentum

$$\mathbf{G} = \mathbf{f}_1 + \mathbf{f}_2 \ ,$$

and f_i the hyperfine level belonging to

$$\mathbf{f}_i = \mathbf{i}_i + \mathbf{s}_i,$$

where $\mathbf{i}_i$ is the nuclear spin and $\mathbf{s}_i$ the electron spin of atom i. The energy of the unbound colliding pair of atoms is measured with respect to the energy the complex would have without hyperfine coupling (i.e. with respect to the hyperfine center of gravity) and given by

$$E_{N f_1 f_2 G} = \frac{a_{2S}}{2}\left[f_1(f_1+1) + f_2(f_2+1) - \frac{11}{2}\right],$$

where $a_{2S} = 152.137\,\mathrm{MHz}$ is the atomic hyperfine constant of the $2S_{1/2}$ ground state. The two-body eigenstates are composed of a spin and an orbital part. The ^{6}Li atoms (consisting of 3 protons, 3 neutrons, and 3 electrons) are composite fermions, therefore exchange symmetry requires the two-body wavefunction to be antisymmetric upon exchange of the nuclei. Since (odd) even N levels are (anti-)symmetric upon exchange of nuclei, proper symmetrization of the total wavefunction requires odds N levels to be associated with symmetric spin states, which they are for $G = f_1 + f_2, f_1 + f_2 - 2, \ldots$. For ^{6}Li with its nuclear spin of $i = 1$, possible hyperfine levels are $f = 1/2$ or $3/2$. In a cold quantum gas p-wave collisions are usually strongly suppressed, therefore the initial state most likely has rotational quantum number $N = 0$. In accordance with the outlined symmetry properties of the rotational and spin levels, the allowed combinations of quantum numbers for two colliding ground state atoms, are shown at the bottom of Fig. 44. Moreover in a dipole trap, all atoms are pumped into the $f = 1/2$ manifold, therefore $G = 0, 1$, but only antisymmetric $G = 0$ state is possible. The final states of $1^3\Sigma_g^+$ and $A^1\Sigma_u^+$ are described by Hund's case (b), where the total electronic (nuclear) spin orbit couplings $\sim \mathbf{L}\cdot\mathbf{S}$, $\sim \mathbf{L}\cdot\mathbf{I}$ are small. Also, the spin rotation couplings $\sim \mathbf{S}\cdot\mathbf{N}$ and $\sim \mathbf{I}\cdot\mathbf{N}$ are considered small, since the nuclear rotation is relatively small. Therefore S and I are good quantum numbers, making the total molecular spin

$$\mathbf{G} = \mathbf{S} + \mathbf{I}$$

a good quantum number. In a magnetic field the rotational and spin levels could split up with projection numbers M_N and M_G, however we will assume zero magnetic field, making them degenerate. Given that $\Lambda = 0$, the set of good quantum number for the final states therefore reduces to

$$|N, S, I, G\rangle.$$

Each rotational level $|N\rangle$ is therefore split into hyperfine sublevels with energies

$$E_{NSIG} = \frac{b}{2}\left[G(G+1) - S(S+1) - I(I+1)\right],$$

where b is a coupling constant. For the final states in $1^3\Sigma_g^+$ and $A^1\Sigma_u^+$, the total electronic spin S and therefore the symmetry of the spin wave function is well defined and following symmetry properties upon exchange of the nuclei are valid:

- $1^3\Sigma_g^+$: (odd) even N levels are (anti) symmetric.
- $A^1\Sigma_u^+$: (even) odd N level are (anti) symmetric.
- Similarly for the total electronic spin of the unbound atoms in the initial state, in the final state the nuclear spin state I is symmetric for $I = i_1 + i_2, i_1 + i_2 - 2, \ldots$, while the rest of the states i antisymmetric. Since $i_1 = i_2$ this means even I states are symmetric, while odd I states are not.

The nuclei are bosons, therefore the total nuclear wavefunction must be symmetric. Therefore in the triplet system, even N levels pair with even I levels, while in the singlet system even N levels pair with odd I levels. For given values I and S, the total spin G of the excited state may assume values between $|I - S|$ and $|I + S|$ (see Fig. 44). Selection rules for electric dipole-allowed transition between initial and final states can from the general selection rules of Hund's case (b) be derived as:

$$\begin{aligned} \Delta G &= 0, \\ \Delta N &= \pm 1. \end{aligned}$$

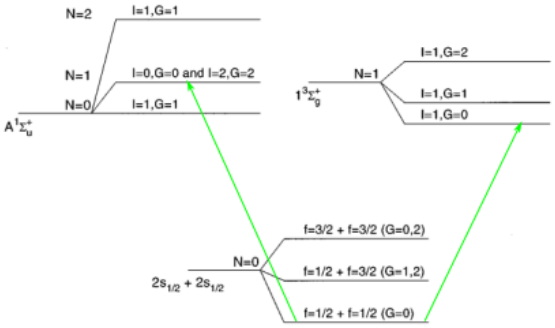

Figure 44: Possible $\Sigma - \Sigma$ transitions in a dipole trap (green arrows) for an ensemble of ^{6}Li atoms, where all atoms are pumped into the $f = 1/2$ manifold and s-wave collisions dominate.

If the temperature of the atomic gas is so low, that s-wave collisions dominate (i.e. starting from $N = 0$), there is exactly one possible transition each in the singlet and triplet system. However, as reported in [65], a weak spin rotation coupling might lead to a splitting of all levels with $N \geq S$ into $2S + 1$ sublevels. In that case, G is not a good quantum number anymore and the total angular momentum is defined without the nuclear spin as

$$\mathbf{J} = \mathbf{N} + \mathbf{S},$$

and PA resonances which were previously labeled with N are labeled according to $J = N + S, \ldots, |N - S|$. For $N < S$, each N level splits into $2N + 1$ sublevels, therefore there is no splitting for the $N = 0$ level.

8.1 Ground state molecule production by spontaneous decay

The dynamics of the ground state molecule number in an optical dipole trap during photoassociation can in good approximation be expressed in a rate equation, similar to that of the dynamics of atom number in a MOT in Eq. 44

$$\dot{N}_{mol} = L(t) - R \cdot N_{mol} - \beta' \int_V n_{mol}(\mathbf{r}, t) n_{atom}(\mathbf{r}, t) d^3r,$$

where $L(t)$ is the production rate of ground state molecules by spontaneous decay, the second term represents loss of molecules due to collisions with background gas, and the third term represents loss of molecules due to collisions between atoms and ground state molecules with β' being the two-body loss constant for inelastic atom-molecule collisions. Losses due to molecule-molecule collisions should play a minor role, due to the low molecular densities involved, and are therefore ignored in the following. In general, the time-dependent ground-state molecule production rate can be written as

$$L(t) = \beta N_{at}(t) n_{at}(t),$$

where $N_{at}(t)$ is the time-dependent atom number and $n_{at}(t)$ the time-dependent atom density, and β is the two-body loss constant for atom-atom collisions. The ground-state molecule production rate into a specific vibrational level ν'' is given by

$$\dot{N}_{mol}(\nu'') = A_{\nu''\nu'} N^*_{mol}(\nu'),$$

where $A_{\nu''\nu'}$ is the bound-bound spontaneous emission probability in s^{-1} and $N^*(\nu')$ is the number of excited molecules in vibrational level ν'. The total ground state molecule production rate $\dot{N}_{mol}$ we then obtain by summing over all vibrational levels ν'', i.e.

$$\dot{N}_{mol} = \left(\sum_{\nu''} A_{\nu''\nu'} \right) N^*_{mol}(\nu')$$

The number of excited molecules in turn obeys following rate equation

$$\dot{N}^*(\nu') = \underbrace{n_{at} \Phi \kappa_{f\to b}(\nu') \cdot \frac{N_{at}}{2}}_{L} - \underbrace{A_f(\nu')}_{R} N^*(\nu'), \tag{60}$$

where $\kappa_{f\to b}(\nu')$ is the free-bound absorption rate coefficient for a specific vibrational level v' and a specific temperature (around 1 mK) in cm^5, $\Phi = \frac{I}{h\nu}$ is the photon flux (in $\mathrm{cm}^{-2}\mathrm{s}^{-1}$), n_{at} is the atomic density in cm^{-3}, N_{at} the atom number, and $A_f(\nu')$ is the total spontaneous emission coefficient from vibrational level ν'into either the continuum or a ground-state molecule. The free-bound absorption coefficients $\kappa_{f\to b}(\nu')$ describe the absorption rate of a single pair of atoms normalized to the photon flux and the atomic density and have been calculated in [67]. If the exposure to the photoassociation light t is short enough, so that the atomic density n_{at} and the atom number N_{at} doesn't change considerably, Eq. 60 can be solved analogously to Eq. 44 to yield

$$N^*(\nu')(t) = \frac{\Phi \kappa_{f\to b}(\nu')}{A_f(\nu')} n_{at} \frac{N_{at}}{2} \left[1 - e^{-A_f(\nu')\cdot t} \right] \approx \frac{\Phi \kappa_{f\to b}(\nu')}{A_f(\nu')} n_{at} \frac{N_{at}}{2}.$$

The last approximation was done, because although t might be short enough to not considerably change the atom number, it is still much higher than the lifetime of the excited states. The initial total production rate of ground state molecules via de-excitation of excited molecules in vibrational level ν' under this circumstance is given by

$$\begin{aligned} L &= \frac{(\sum_{\nu''} A_{\nu''\nu'})}{A_f(\nu')} \Phi \kappa_{f\to b}(\nu') n_{at} \frac{N_{at}}{2} \\ &\approx \left(\sum_{\nu''} q_{\nu''\nu'} \right) \frac{\Phi \kappa_{f\to b}(\nu')}{2} n_{at} \frac{N_{at}}{2}, \end{aligned} \tag{61}$$

where in the last line the branching ratio of transitions between vibrational states of different electronic levels $\frac{A_{v'v''}}{A_f(\nu')}$ was approximated by the Franck-Condon factor, i.e.

$$\frac{A_{v'v''}}{A_f(\nu')} \approx q_{\nu''\nu'} = |\int \Psi_{\nu''}(R) \Psi_{\nu'}(R) dR|^2,$$

This is the Franck-Condon approximation, which assumes that the molecular transition moment in Eq. 59 does not strongly depend on the internuclear separation, because the electronic transition happens on a much faster time scale than the nuclear motion. Thus, this dependency can be factored out as an overlap integral $\int \Psi_{\nu''}(R) \Psi_{\nu'}(R) dR$, the square of which is the so-called Franck-Condon factor $q_{\nu''\nu'}$. Therefore, in the Franck-Condon approximation, the position of the nuclei can be considered fixed during an electronic transition and it can be drawn as a vertical line on the potential energy curve diagram (see Fig. 45). The total

probability of a bound-bound transition from an excited state vibrational level v' can then be approximated as

$$p_{\nu'} = \sum_{\nu''} q_{\nu'\nu''}.$$

In contrast the probability of a bound-free transition is then given by $1 - p_{v'}$. Since the $S - S$ PEC is short-ranged, while the $S - P$ is long-ranged, the wavefunctions of the respective vibrational levels usually occupy different regions of space, which is why the overlap in general can be quite poor.

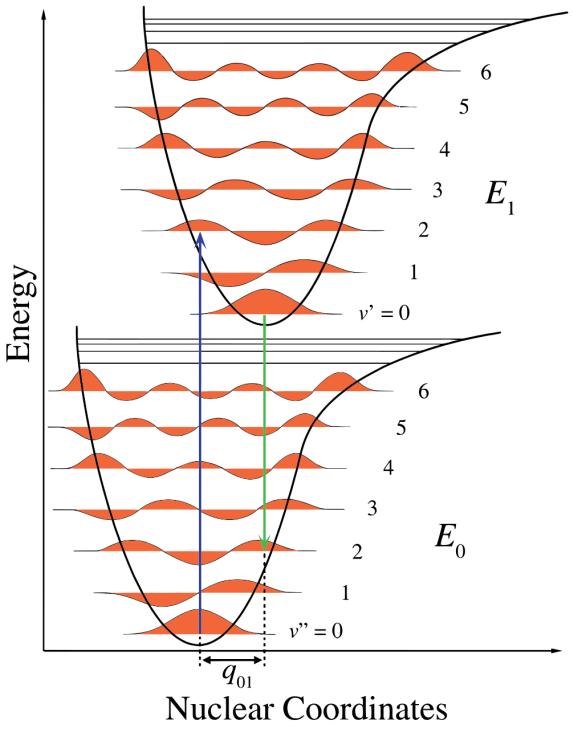

Figure 45: Illustration of Franck-Condon approximation: Electronic transitions happen on a much smaller time scale than nuclear vibration, therefore the distance between nuclei can be considered fixed, and transition between vibrational levels are vertical. [68, 69]

Therefore the ratio between bound-bound and bound-free spontaneous emission is usually very small. Especially higher-lying vibrational levels v' predominantly decay back into the continuum and only a small percentage decays back into high lying vibrational levels of the ground state potential. The Einstein A coefficients $A_{v'v''}$ and the branching ratios $q_{v'v''}$ for transitions between bound states of the $2s + 2p$ and the $2s + 2s$ potential energy curve for ^{6}Li and ^{7}Li have been calculated in [70], where the authors also suggest which levels should be excited in order to obtain as many molecules as possible by spontaneous decay in only the highest lying vibrational states of their respective molecular groundstate potentials.

The challenge to cold-molecule production in a specific rovibrational level v'' by spontaneous decay, is to populate an excited state vibrational level v' which has a relatively high branching ratio to decay back into a particular vibrational level v'' of the ground state. Although the total decay ratio between decay into ground-state molecules and decay into continuum is less favorable for higher lying levels in $1^3\Sigma_g^+$ or $A^1\Sigma_u^+$, when an excited molecule

decays from there, it decays predominantly into the least-bound, vibrationally highly excited state of the respective ground state potential. With this higher final state selectivity, it was found in [70] that e.g. for triplet transitions of $^6Li_2$ the bound-bound spontaneous emission probability $A_{v'v''}$ is highest for transitions from $1^3\Sigma_g^+(\nu' = 51)$ to $a^3\Sigma_u^+(\nu'' = 9)$ where $v'' = 9$ is the least-bound vibrational level of the ground state triplet potential $a^3\Sigma_u^+$. From $\nu' = 51$ about

$$\sum_{v''} q_{51v''} \approx 11\%$$

decay back into a vibrational level of the ground state with a high branching ratio of about 96.2% of them decaying back into the highest lying level $v'' = 9$ of the ground state triplet potential $1^3\Sigma_u^+$. However to the knowledge of the author, the low-lying levels between $\nu' = 55$ and $\nu' = 51$ have not yet been determined experimentally. In the singlet system of ^{6}Li, the excited level $A^1\Sigma_u^+(\nu' = 70)$ has the highest branching ratio: About 93.2% of the excited molecules decay into the least-bound vibrational level $X^1\Sigma_g^+(\nu'' = 38)$ and the decay fraction into discrete levels is given by

$$\sum_{\nu''} q_{70\nu''} \approx 7.4\,\%.$$

9 Quantum degenerate matter: Cold molecules in a BEC via magneto association

Magneto-association is a technique for association of molecules from cold atoms, which employs Feshbach resonances in different atomic species. Feshbach resonances make it possible to magnetically tune the effective long-range interaction between atoms and therefore play a fundamental role in cold atom physics. The effective long-range interaction between atoms is characterized by the so-called *scattering length*, which can be tuned from extremly large and negative (strongly attractive) to extremly large and positive (strongly repulsive). Depending on the sign of the scattering length the ground state of an ensemble of atoms is either a molecular BEC or a BCS superfluid. The transition between these two ground states is called the "BEC-BCS crossover". In order to understand what a Feshbach resonance and a scattering length is, it is instructive to first look at the special case of a zero-energy resonance, which is connected to a rapid change in scattering phase of the outgoing wavefunction of two colliding atoms in the low energy limit $k \to 0$, depending on the well depth, if the depth of the interaction potential could be artificially tuned. In the following, unless otherwise stated, we always refer to a binary collision, i.e. the type of collisions which dominates in a dilute quantum gas, unless we enter the regime of quantum degeneracy.

9.1 Zero-energy resonances, halo states and universality

In binary scattering theory, the scattering between two atoms is treated as an *isotropic* interaction of a particle of reduced mass m_r with a centro-symmetric scattering potential $V(r)$, where r is the relative distance of the atoms. For simplicity, the atoms are first considered to be structureless. Independent of the detailed form of $V(r)$, each interaction potential can be assigned a characteristic range r_0, beyond which the interaction energy maybe neglected, even for extremly low collision energies.

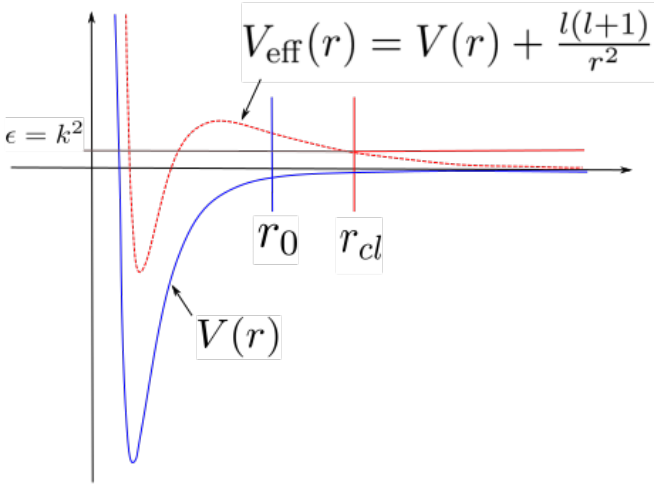

Figure 46: Example of a Van-der-Waals interaction with rotational barrier as centro-symmetric scattering potential.

When treating the quantum motion of two structureless atoms, the term *asymptotic* always refers to a distance $r \gg r_0$ between the two particles. The relative kinetic energy in such a

collision is given by $E = \frac{(\hbar k)^2}{2m_r}$, where the relative wavenumber $k = \frac{\Delta p}{\hbar}$ is related to the asymptotic momentum difference of the two atoms and will later parametrize the energy dependence of the collisional cross section. Furthermore the deBroglie wavelength $\lambda_{dB} = \frac{h}{\sqrt{2mk_BT}}$ of an atomic gas at temperature T can be associated to the relative wavenumber by

$$k \sim \frac{1}{\lambda_{dB}}.$$

Since we aim to describe a dilute cold atomic gas with slow moving atoms, which can be characterized by $\lambda_{db} \gg r_0$, this condition can equivalently be expressed by the dimensionless parameter kr_0 as

$$kr_0 \ll 1. \tag{62}$$

The initial wavefunction is assumed to belong to a quantum state with sharp momentum, i.e. a plane wave $\sim e^{ikz}$. However, because of the spherical symmetry of the interaction potential, the plane wave is decomposed into spherical waves corresponding to sharp angular momentum states with $l = 0, 1, 2, \ldots$. This is also called the spherical wave decomposition, where a s,p,d,... -wave belongs respectively to $l = 0, 1, 2, \ldots$ and it leads to a set of decoupled radial wavefunctions for each quantum number l

$$\chi_l'' + \left[\epsilon - U(r) - \frac{l(l+1)}{r^2}\right]\chi_l = 0, \tag{63}$$

where $\epsilon = \frac{2m_rE}{\hbar^2} = \pm k^2$ and $U(r) = \frac{2m_rV(r)}{\hbar^2}$ are the reduced energies, and $\chi_l = rR_l(r)$ the reduced wavefunction. Continuum state solution are retrieved from this equation for positive energies $\epsilon > 0$ and bound state solutions for $\epsilon < 0$. The effect of the interaction potential is, as will be explained in the following in more detail, that it imprints a scattering shift δ_l on the outgoing asymptotic spherical wave. The total elastic cross section of the collision is given by

$$\sigma = \sum_l \sigma_l,$$

where each spherical wave contributes the partial cross section

$$\sigma_l = \frac{4\pi}{k}(2l+1)\sin^2\delta_l.$$

The classical turning point $r_{cl} = \frac{\sqrt{l(l+1)}}{k}$ is the point, where the rotational energy of the two atoms exceeds the total energy ϵ (see Fig. 46) and from a classical perspective the wavefunction is exponentially suppressed for all $r < r_{cl}$ and therefore is not affected by this part of the potential. With the condition for a cold quantum gas Eq. 62, we obtain the statement

$$kr_0 = \sqrt{l(l+1)}\frac{r_0}{r_{cl}} \ll 1,$$

meaning that for all spherical waves with $l > 0$ the classical turning point lies much farther out, than the effective range of the potential. These spherical waves are therefore not influenced by $V(r)$ and don't experience a phase shift. If only s-waves, i.e. spherical waves with $l = 0$, contribute to elastic scattering in a cold atomic gas, the total elastic cross section is given by the s-wave partial cross section

$$\sigma \approx \sigma_0 = \frac{4\pi}{k^2}\sin^2\delta_0.$$

The asymptotic s-wave radial wavefunction is the general solution of the radial wave equation for a free particle ($l = 0$ and $U(r) = 0$ in Eq. 63) and given by

$$R_0(k, r) = \frac{c_0}{kr} \sin(kr + \delta_0) \,. \tag{64}$$

The asymptotic scattering shift $\delta_0 = \delta_0(k)$ must be zero for a free particle, in order for $R_0(k, r)$ to not be singular in the origin. For a model potential like the spherical square well potential (see Fig. 47), the phase shift of an s-wave scattering state with energy $\epsilon = +k$ can from the boundary condition at $r = r_0$ be calculated to be

$$\begin{aligned} \delta_0(k) &= -k \cdot a(k), \\ a(k) &= r_0 + \frac{1}{k} \arctan\left(\frac{k}{K_+ \cot(K_+ r_0)}\right). \end{aligned} \tag{65}$$

In this context one defines the s-wave scattering length via the s-wave phase shift in the zero energy limit, i.e.

$$\begin{aligned} a &\equiv -\lim_{k\to 0} \frac{\sin \delta_0(k)}{k}, \\ &\cong -\lim_{k\to 0} a(k), \end{aligned}$$

where the second equation only is valid as long as $k \cdot a(k) \ll 1$. Therefore the total elastic cross section in the zero energy limit reduces to

$$\sigma = 4\pi a^2,$$

which could be interpreted as the collision cross section of hard spheres of radius a. From this equation it becomes obvious, that the magnitude of the scattering length characterizes the effective range of interaction between the atoms. The character of the effective interaction depends on the sign of the scattering length. By definition of the well parameter $\gamma \equiv \kappa_0 r_0$, which characterizes the well depth and range of the spherical square well, one arrives at following expression for the scattering length

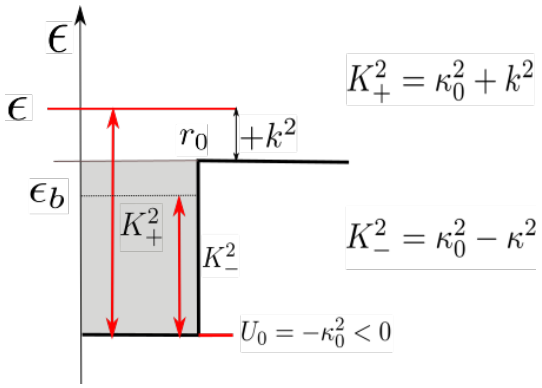

Figure 47: Spherical square well potential with an effective range r_0 given by the well radius with notations used in the text.

$$a = r_0 \left(1 - \frac{\tan \gamma}{\gamma}\right).$$

From this equation it becomes evident, that the s-wave scattering length, becomes singular at $\gamma = \frac{\pi}{2} + n\pi$. An introspection of the s-wave bound states shows that

1. a minimum well parameter of $\gamma = \frac{\pi}{2}$ is required to support the first bound state and that

2. next vibrational levels appear for $\gamma = (\nu + \frac{1}{2})\pi$, where $\nu = 0, 1, \ldots \nu_{max}$ is the vibrational quantum number.

Therefore, in the limit of very low collision energy, as the well parameter γ of our model parameter is increased from zero, the scattering length decreases and eventually diverges to $-\infty$ at $\gamma = \frac{\pi}{2}$ when the first bound state appears (compare Fig. 48). As the well parameter is further increased the scattering length decreases from $+\infty$ and eventually diverges again to $-\infty$ when the potential well is deep enough to support the next bound state. This behaviour keeps repeating as the well parameter is increased and the singularities of the s wave scattering length are so-called zero energy resonances.

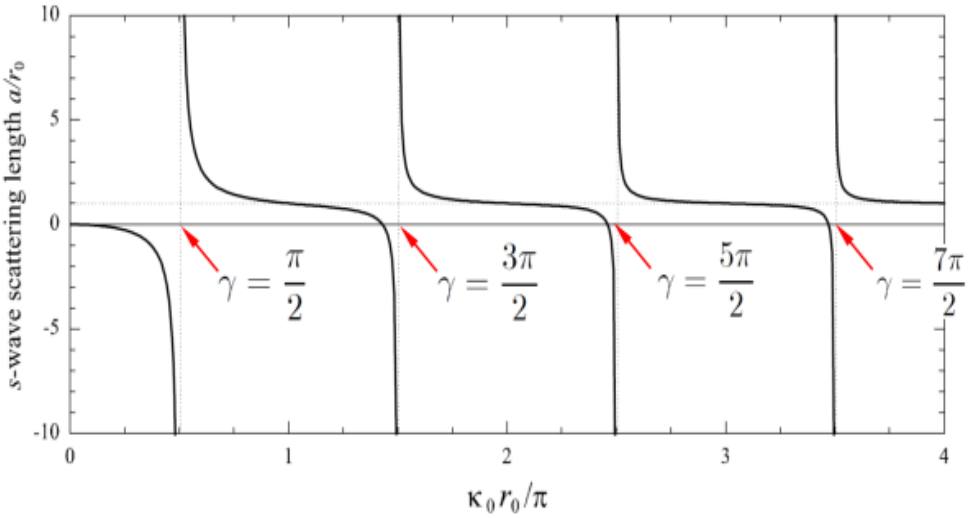

Figure 48: Resonance behaviour of s wave scattering length in the zero energy limit.

The s-wave bound states oscillate inside the well and decay exponentially outside the well (see Fig. 49). In the vincinity of a zero energy resonance, where $a \gg r_0$, it can be shown that

1. the limiting shape of the scattering state becomes independent of r_0 and κ_0, and

2. the binding energy $-\kappa^2$ of a weakly bound s level for $\kappa \to 0$ is related to the scattering length by $\kappa \approx 1/a$.

The range of $\kappa_0 r_0$, where the limiting shape of the scattering state and the binding energy of a weakly bound s level, do not depend anymore on the detailed form of the model potential, is called *universal range*. The least-bound state, for $\kappa r_0 \ll 1$, turns into a *halo state*, of which its probability density is mostly found outside the potential well. The spatial extension of a halo dimer, which could be defined as the radius R, where $\frac{|\chi_0(R)|^2}{|\chi_0(0)|^2} = \frac{1}{e^2}$ is then given by the scattering length a. Therefore a direct mapping of a molecular halo state via Coulomb explosion, ${}^6\mathrm{Li}_2 + \mathrm{n}\gamma_{\mathrm{fs}} \to {}^6\mathrm{Li}^+ + {}^6\mathrm{Li}^+$, could be seen as an alternative method to measure the scattering length of strongly interacting fermions. Halo dimers are "long-range molecules", since their spatial extension can be orders of magnitude larger than that of deeper bound molecules.

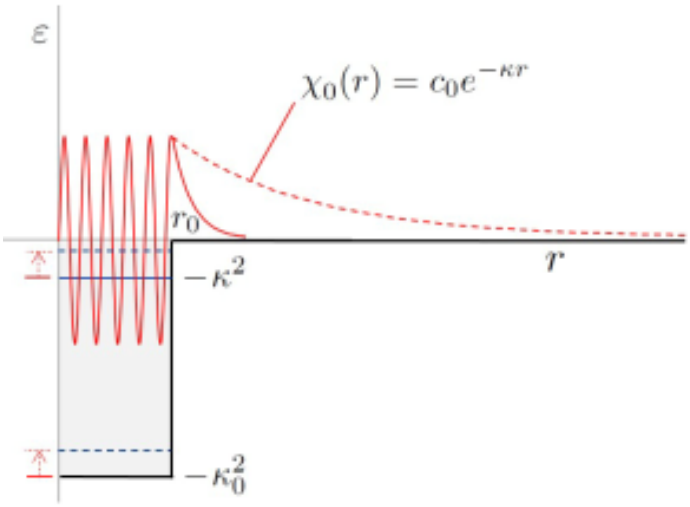

Figure 49: S-wave bound state of flat spherical well: For $r < r_0$ the solution oscillates, while for $r \geq r_0$ is decays exponentially. Taken from [71].

The relation between the binding energy of the least-bound state and the scattering length in the universal range

$$E_b = -\frac{\hbar^2}{2m_r a^2}, \tag{66}$$

has been deduced in the specific context of the flat spherical well, but it can be shown to hold for an arbitrary short-range potential, in particular for van der Waals potentials.

As seen from the discussion about Fig. 48, in the vincinity of a zero energy resonance, when the scattering length is large and has negative sign, there exists an almost-bound state, which turns into a weakly bound state when the well depth is increased above a threshold depth and the scattering length becomes large and positive. Together with the fact, that the asymptotic wavefunction becomes independent on details of the interaction potential in the universal range, Fig. 50 sums up the geometrical interpretation of the scattering length's sign in the universal range: In the low energy limit, i.e. $\delta_0 \approx -k \cdot a \ll 1$, the shape of the asymptotic wavefunction in Eq. 64 is

$$\begin{aligned} \frac{\sin(kr + \delta_0)}{k} &\approx \frac{\sin(kr) + \delta_0 \cos(kr)}{k} \\ &\approx r - a. \end{aligned}$$

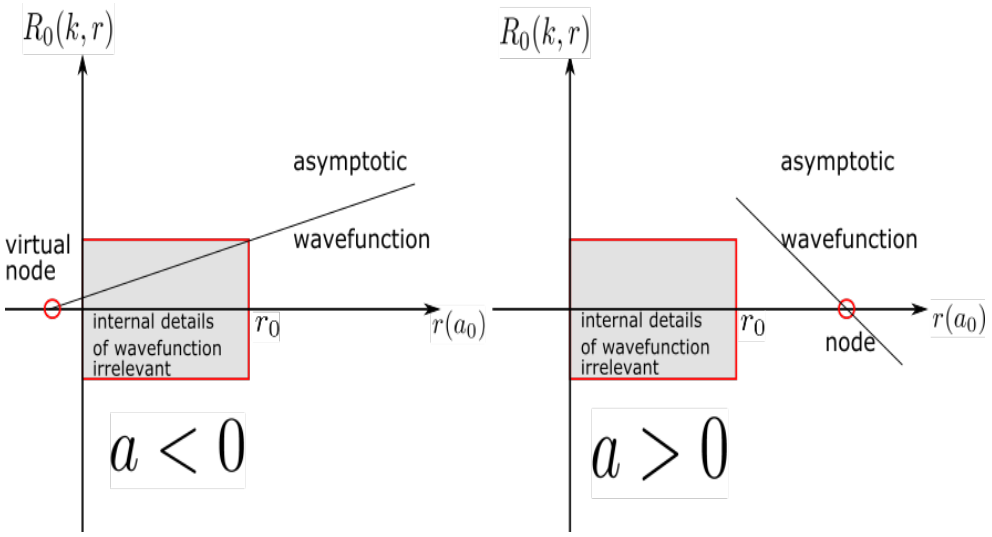

Figure 50: Geometrical interpretation of the sign of the s wave scattering length depending on the asymptotic wavefunction.

By extrapolation of the linear asymptotic wavefunction, it will intersect with the r axis, and the position of the node on the r axis is given by the scattering length. In the universal range, the position of the node evidently does only depend on the scattering length, not on details of the wavefunction within the potential range for $r < r_0$.

Finally, a zero-energy resonance is accidentally realized in the $a^3\Sigma_u^+$ potential energy curve of $^6Li_2$, in which an almost-bound state exists, which would turn into a bound state, if the triplet potential was only 0.03% deeper [36].

9.2 Feshbach resonances in ^{6}Li

Although molecular potential depths evidently cannot be modified and are fixed by nature, it is possible to find similar resonances in the collision of two real atoms $i = 1, 2$, which have internal structure like electronic and nuclear spin. The hyperfine states q_i, in which the atoms are prepared at large distances $R \gg r_0$, define a scattering channel. The channel of the intial asymptotic scattering state, is called *entrance channel*, while the channel of the final asymptotic state is termed *closed channel* (see Fig. 51).

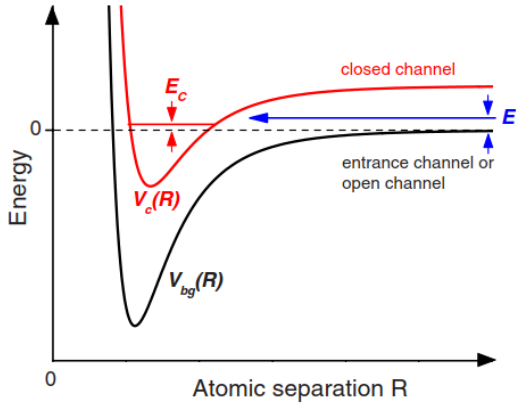

Figure 51: Two channel model of a Feshbach resonance

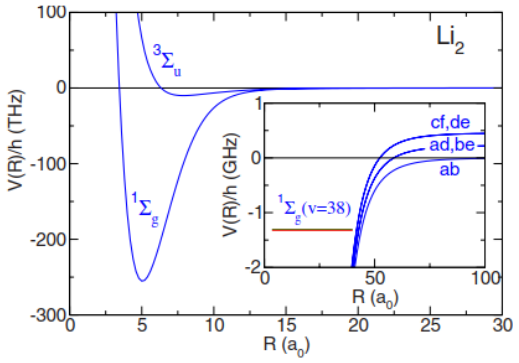

Figure 52: Scattering channels involved in the Feshbach resonance of a_{12} in ^{6}Li

Depending on how the two atomic orbitals combine, the molecular potential energy curves differ and their bound states exhibit different symmetries, as is outlined in Sec. 7. A Feshbach resonance is the phenomenon, that an approximate bound state exists in the closed channel potential with a different symmetry in a different potential than that of the entrance channel. This abstract language can readily be illustrated by the Feshbach resonance in ^{6}Li, where the scattering length a_{12} of two electronic ground state atoms, initially in the singlet state of the hyperfine Zeeman sublevels $|1\rangle$ and $|2\rangle$, diverges at $B_0 = 834\,\mathrm{G}$. For this resonance the entrance channel is given by the singlet potential $^1\Sigma_g$ and the closed channel by the triplet potential (see Fig. 52). The triplet molecular potential energy curve is much shallower, because its spatial bound state wavefunctions have a zero crossing at the inversion center. The decreased probability of finding the valence electron pair at the inversion center between the nuclei increases their Coulomb repulsion, therefore decreases the binding energy of the molecule. The difference in magnetic moment $\Delta\mu$ between the singlet and triplet state marks the asymptotic energy $\Delta\mu \cdot B$ difference for $R \gg r_0$ at a given externally applied magnetic field B. A Feshbach resonance occurs, when a closed channel bound state of binding energy $E_c$becomes degenerate with the energy E of the incoming asymptotic scattering state (see Fig. 51) by adjusting $\Delta\mu \cdot B$ via an external magnetic field B.

Therefore a Feshbach resonance is a magnetically tunable resonance of the (s,p,d,...)-scattering length and the variation of the s-wave scattering length in the vincinity of a Feshbach resonance can be described by a simple formula (introduced by [72]) expressing it as as a function of the magnetic field

$$a(B) = a_{bg}\left(1 - \frac{\Delta}{B - B_0}\right). \tag{67}$$

Here B_0 denotes the resonance position, Δ the resonance width and a_{bg} the background scattering length. In this thesis we rely on other research groups' detailed prior investigations of the s-wave Feshbach resonances of fermionic Lithium (see [72, 27, 73]) and their use for magneto-association of weakly bound dimers (see [74, 75]).

In the case of the $|1\rangle - |2\rangle$ s-wave scattering length a_{12} of ^{6}Li at $B_0 = 834\,\mathrm{G}$ is given by $\Delta \backsimeq 100\,\mathrm{G}$. The background scattering length a_{bg} is directly related to the last vibrational level of the entrance channel with molecular potential $V_{bg}(r)$. As mentioned in Sec. 9.1, the

triplet potential $a^3\Sigma_u^+$ has a quasi-bound state close to the dissociation threshold, therefore it is related to a rather large and negative background scattering length. Triplet and singlet background scattering lengths of ^{6}Li have been measured in [76] to be

$$\begin{aligned} a_{\mathrm{T}} &= (-2160 \pm 250) a_0 \\ a_S &= (45.5 \pm 2.5) a_0, \end{aligned}$$

with a_0 being the Bohr radius. In general there exist three experimental schemes involving magneto-association for creating ultracold molecules:

1. **Adiabatic magnetic field ramp:** The magnetic field is adiabatically ramped across the resonance, so that two interacting atoms are adiabatically converted into one molecule.

2. **Oscillating magnetic field:** An oscillatory magnetic field drives the transition from the scattering state to the molecular state.

3. **Three-body recombination:** At large scattering length, the outcome of a three-atom collision results in a molecular di-atomic state and a free atom carrying away excess kinetic energy, a process coined as three-body recombination

Though ramping an external field across a Feshbach resonance is the most commonly adopted scheme for creating ultracold molecules with conversion efficiencies up to 85% (see [77]), for a ^{6}Li $|1\rangle - |2\rangle$ spin mixture, due to the extraordinary stability against inelastic decay of the molecular state through atom-molecule collisions [58] , the simplest method to obtain molecules is three-body recombination during forced evaporative cooling at constant magnetic field of about 764 G, at the low-field side of a broad Feshbach resonance, in the range where the s-wave scattering length is large and positive. The excess energy carried away by the third atom is on the order of the temperature of the atomic sample and therefore does not lead to excessive heating of the atomic sample. Forced evaporative cooling in the vincinity of a Feshbach resonance therefore yields vibrationally, highly excited molecules, which inherit their temperature from the atomic gas. This kind of molecules have been coined as Feshbach molecules. Since almost no heating is involved, it is possible that Feshbach molecules, which are composite bosons, can condense into a BEC below a critical temperature. Therefore forced evaporative cooling of an atomic sample in the vinicinity of a Feshbach resonance of ^{6}Li is a way to obtain quantum degeneracy in a sample of ultracold $^6Li_2$ Feshbach molecules.

Part V

Experimental setup and measurements

In this part of the thesis, the reader will first be introduced in Sec. 10 to the optical setups established during the course of this thesis, which are necessary for operation of a magneto-optical trap and an optical dipole trap. The optical setup for single-color PA spectroscopy will be separately described in 12.3. Furthermore in 10.4 the architecture and working principle of our femto laser system will be explained to the reader. Following that in Sec. 11 a series of characterization measurements concerning loading, temperature, and density of atoms in the magneto-optical trap and the optical dipole trap will be presented. In Sec. 12 results from atomic and molecular ionisation pathways in a magneto-optically trapped target and a purely optically trapped target, are presented. Finally in Sec. 13, the design of the Feshbach coils for future experiments, that employ the magneto-association technique, will be outlined. Furthermore some ideas will be outlined, how momenta of charged particles can be reconstructed in such a setup, where a pair of coils produces an axially inhomogeneous magnetic field.

10 Optical setup

10.1 The magneto-optical trap

The laser setup for the operation of the magneto-optical trap is comprised of two frequency stabilized lasers (see Fig. 53 for a scheme of our laser setup). The first laser, in the following referred to as frequency laser, served as a frequency reference and it was locked via modulation transfer spectroscopy to the atomic $D2 : 2^2S_{1/2} \leftrightarrow 2^2P_{3/2}$ transition in a lithium vapor cell. The second laser, which delivered the power for our MOT beams and in the following is referred to as MOT laser, was locked relatively to the frequency laser via a locking technique called beat-offset lock [78]. This locking scheme was chosen, because it provides a wide tunability range for the MOT laser, necessary for absorption imaging at high magnetic field in a later stage of the experiment.

Each laser lock has two PID channels at its disposal, one which regulates the laser current constituting a fast channel and one which regulates the piezo voltage as a slow channel. The frequency laser (Toptica DL100) is locked at the D2 line via both channels. The MOT laser already passively has an excellent bandwidth of about 20 kHZ, which is why a high bandwidth feedback lock would rather transfer the frequency noise of the DL100 onto the MOT laser and therefore increase the actively-regulated bandwidth of the MOT laser. A requirement for exactly imaging the atom number in the MOT, is that the laser's bandwidth is significantly smaller than the linewidth of the excited state. Therefore the best option for the laser lock of the MOT laser was to stabilize it by employing only the slow piezo feedback loop which has a limited -3dB-bandwidth of 18 kHz [79].

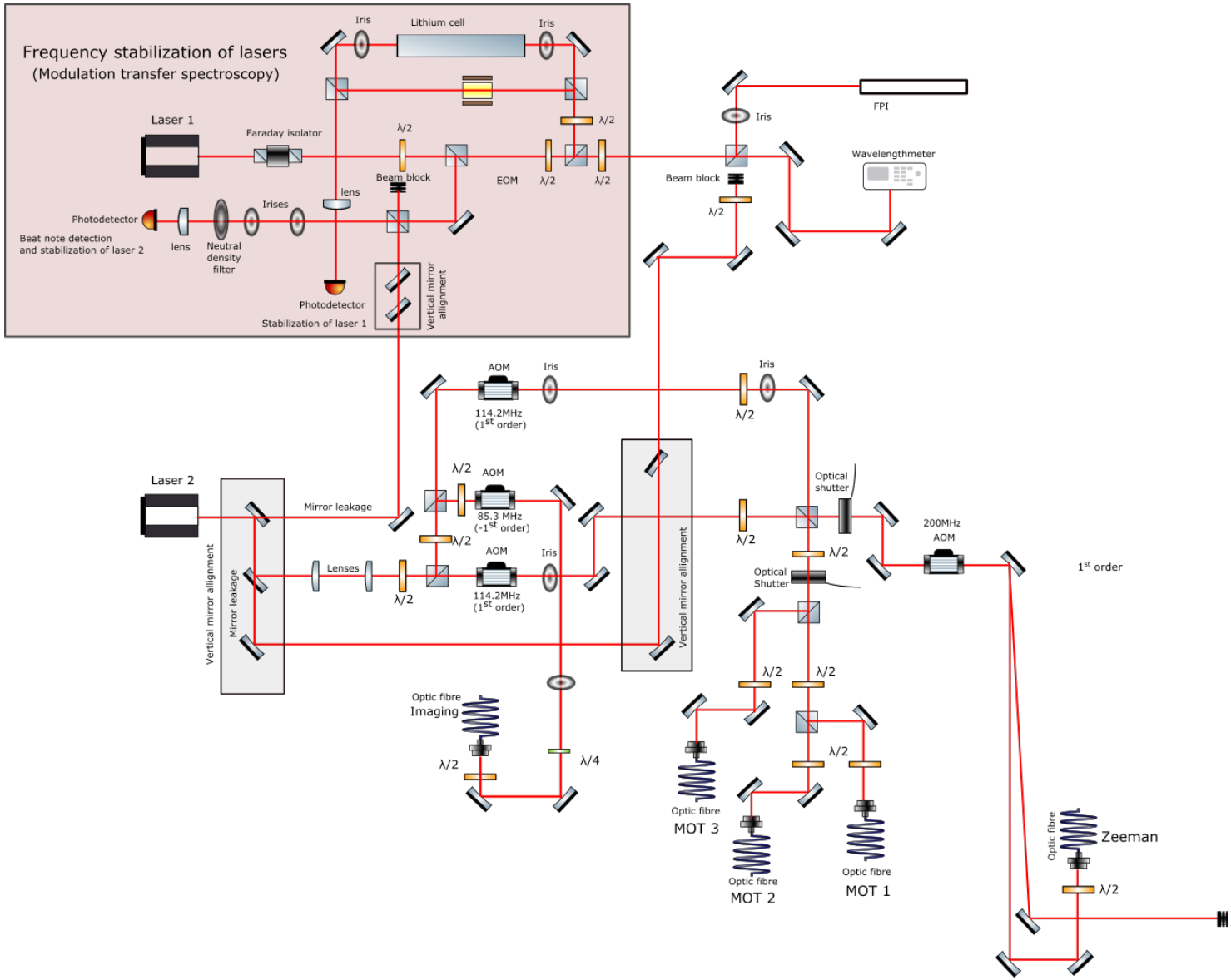

Figure 53: Sketch of the optical setup necessary for operation of the magneto-optical trap, Zeeman slower and resonant absorption imaging.

10.1.1 Frequency-stabilization of lasers

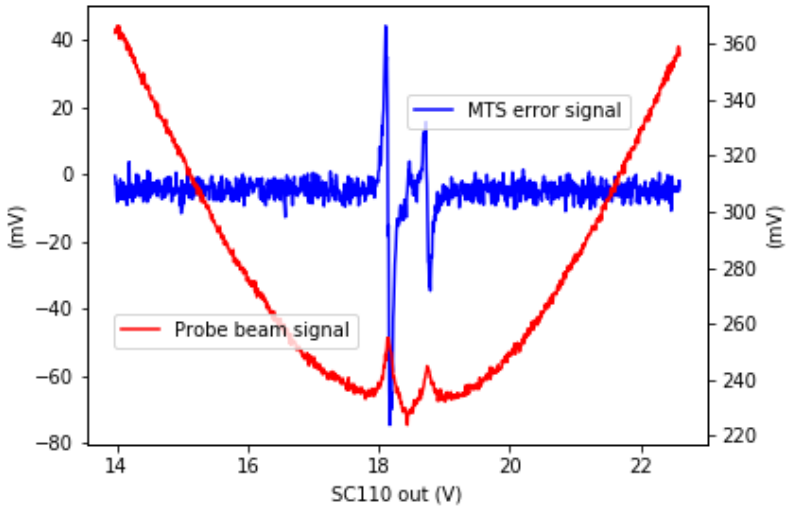

Figure 54: Oscilloscope trace during scanning of frequency laser via varying the grating angle. Red trace is signal of probe beam measured at PD. Blue trace is error signal is the resulting error signal.

The frequency laser is locked to the cooling transition $2^2S_{1/2}\,(F = 3/2) \rightarrow 2^2P_{3/2}\,(F = 5/2, 3/2, 1/2)$. The error signal for the frequency laser, shown in Fig. 54, is produced by modulation transfer spectroscopy, which requires phase-modulating a pump beam which goes through a ^{6}Li gas cell. Although the required phase modulation of the pump beam could be done internally via the laser current, we noticed it had a detrimental effect on the quality of the MOT laser lock. Therefore the pump beam was modulated externally via an EOM (Qubig GmbH). The frequency stability of the locked laser was estimated by the RMS error of the error signal in locked state to be about 0.4 MHz.

Since, as outlined above, the actively-regulated bandwidth of the MOT laser is in the range of a few tens of kHz and therefore much better than the linewidth of the DL100, another method to estimate its linewidth is to look at the beat signal of both lasers, while they are being locked (see Fig. 55). The FWHM of the averaged beat signal between both lasers is about 1.078 MHz, which is on the same order.

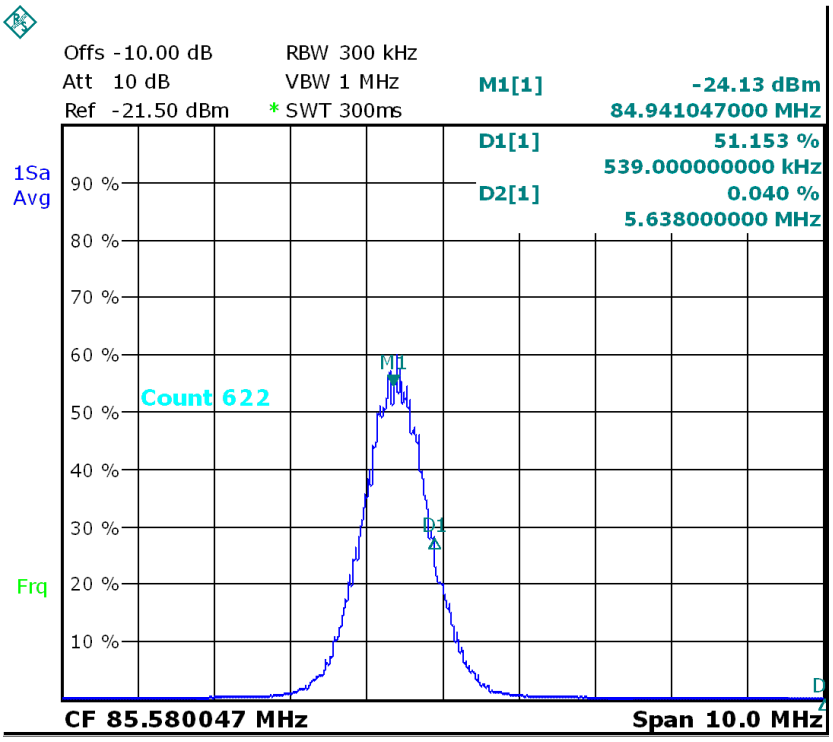

Figure 55: Averaged beat-signal between locked frequency and MOT laser.

Beat-Offset Lock test An example of an error signal with several zero crossings is shown in Fig. 56. While being locked to any zero crossing of this error signal, the shown RMS error of the error signal was about 10.9 mV. The frequency difference between two zero crossings amounts to about 22.96 MHz and the slope at each zero crossing therefore is roughly given by 15.83 mV/MHz, so the RMS error of the laser lock is about 0.688 MHz.

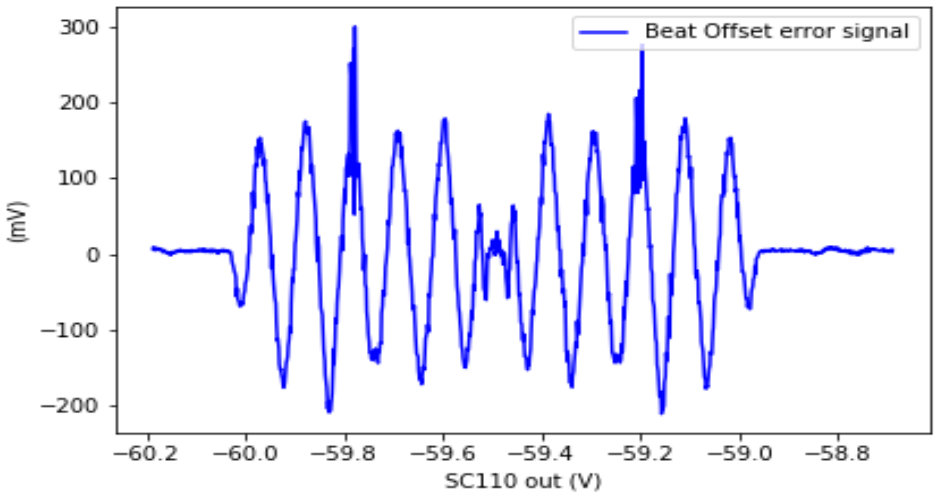

Figure 56: Error signal for the MOT laser, while scanning over the piezo voltage.

During experimental sequences, the laser frequency of the MOT laser is being changed e.g. for the transfer of the atoms in the dipole trap or for resonant absorption imaging. The upper limit in changing the frequency is given by the slow cavity lock following any change of frequency of the master laser diode. From Fig.57 it can be seen, that the fastest allowed ramp rate for the frequency of the master diode laser, before the MOT laser lock jumps to a different lock point, is given by approximately 2.04 MHz / μs. From Fig. 58 it can be seen, that there is no delay between change of VCO control voltage and change of frequency, if the ramp rate is below approximately 51 kHz / μs.

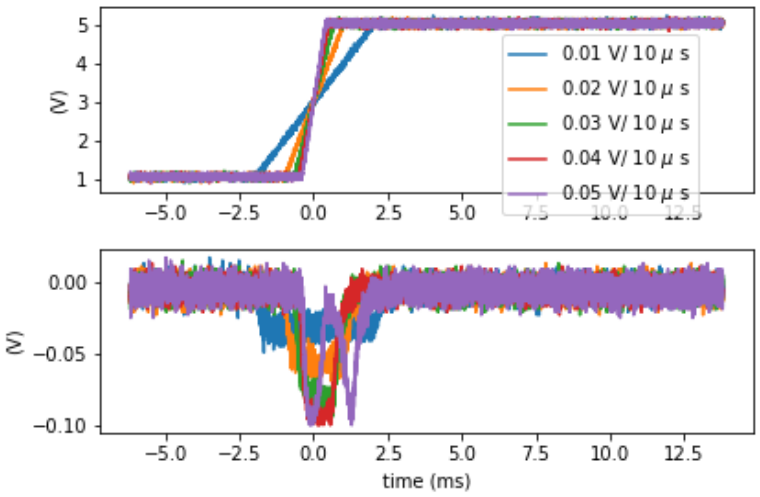

Figure 57: Upper plot shows ramps of VCO control voltages and the lower plot shows the output voltage of the SC 110 Toptica module in response to a change of the frequency offset with respest to the frequency of the MTS-locked master laser.

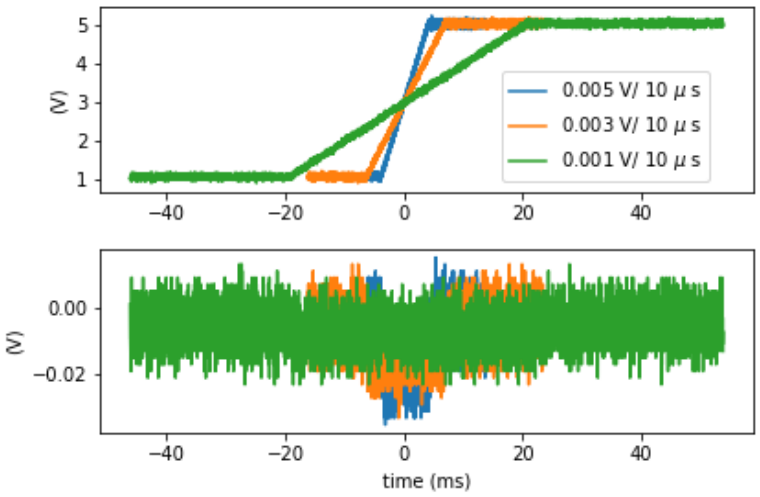

Figure 58: In the lower plot, it can be seen that for a ramp rate of 0.001 V/ 10 μs, the MOT laser follows without delay any frequency change.

10.2 Optical diagnostics

The interaction of atoms with a light field comprises three fundamental processes: Stimulated absorption and emission and spontaneous emission. Spontaneous emission is the fundamental process underlying fluorescence imaging, which is described in the next section. If light passes through an atomic sample stimulated absorption and spontaneous emission lead to (a) to an attenuation and (b) to a phase-shift of the transmitted light. The first property can be used for an absorptive imaging method described in section 10.2.2, in which a laser beam in resonance with an atomic transition is absorbed by an atomic sample and its shadow recorded on a CCD camera.

10.2.1 Measuring atom number and peak density via fluorescence

As outlined in Section 3, the cooling force on a two-level atom relies on a cycle of stimulated absorption and spontaneous emission. During MOT operation the fluorescence of the atomic cloud is recorded by a CCD camera (pixelfly qe), which is positioned roughly in a distance L mm from the atomic cloud (see Fig. 59).

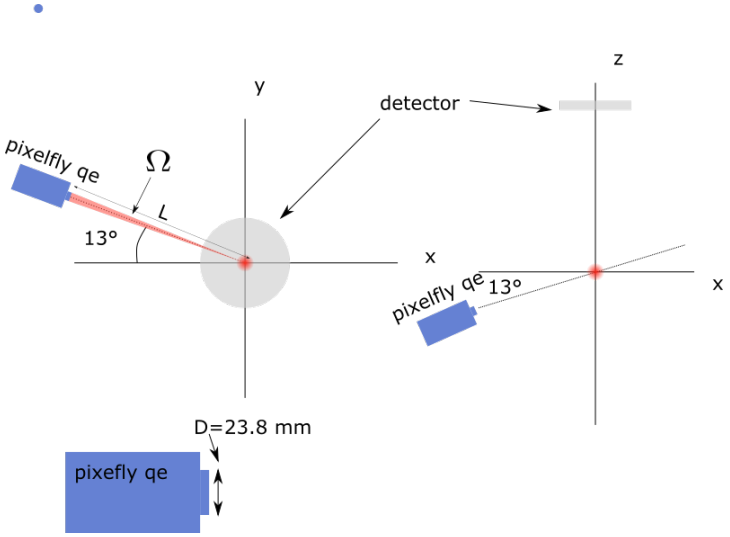

Figure 59: Schematic of fluorescence imaging setup. The CCD camera is positioned in a distance $L \approx 319$ mm from the atomic cloud and pointing under an angle of 13° both with respect to the xz- and xz-plane towards the center of the chamber. The CCD camera has an objective lens diameter of $D = 23.8$ mm.

The CCD camera's objective has a lens diameter D mm, so the solid angle Ω in which photons are scattered and detected by the CCD camera can be approximated by $\Omega = \frac{\pi}{4}\left(\frac{D}{L}\right)^2 \approx 0.00437$ sr in our setup. During an exposure time t_{exp} the total energy $E = N_\Omega E_\gamma$ by the total number N_Ω of into the solid angle Ω scattered photons has been deposited on the CCD chip, where E_γ is the energy of one photon of wavelength 671 nm. The total number of scattered photons N_{phot} then simply is given by

$$N_{phot} = \frac{4\pi}{\Omega} N_\Omega$$

and this number can be related to the number of atoms by the approximation, that each atom scattered $t_{exp} \cdot \gamma_p$ photons during the time of exposure t_{exp}, where γ_p is the scattering rate of

the photons. Then the number of atoms N_{atoms}, which scattered N_{phot} photons is given by

$$N_{atoms} = \frac{N_{phot}}{t_{exp} \cdot \gamma_p} = \frac{4\pi}{\Omega} \frac{E}{E_\gamma} \frac{1}{\gamma_p t_{exp}}$$

In order to convert number of signal counts C_s due to spontaneously scattered photons from the atomic cloud into the deposited energy E, we have to previously find the calibration η for the CCD camera, which relates those two quantities by

$$E = \frac{C_s}{\eta}.$$

Our CCD camera for fluorescence imaging (pixelfly qe) has two different gain modes (low and high) for which respectivly we measured $\eta_{low} = 3.25 \cdot 10^8 \frac{\text{counts}}{\text{nJ}}$ and $\eta_{high} = 7.62 \cdot 10^8 \frac{\text{counts}}{nJ}$. The signal counts C_s, originating from spontaneously emitted photons in the atomic cloud, are usually obtained by substracting from the total counts C_{tot} the counts C_{stray} which (mostly) originate from stray light, i.e. $C_s = C_{tot} - C_{stray}$. Therefore the atom number relates to the total counts and stray light counts by

$$N_{atoms} = \frac{4\pi}{\Omega} \frac{C_{tot} - C_{stray}}{\eta E_\gamma} \frac{1}{\gamma_p t_{exp}}.$$

Assuming a resonant scattering rate $\gamma_p \approx \Gamma/2$ where $\Gamma = 36.90$ MHz[19] is the decay rate of the $2P_{3/2}$ excited state of ^{6}Li, in dependence of the exposure time in ms and the pixel counts, the atom number for low and high gain respectively is given by

$$\begin{aligned} N_{atom,high} &= 0.691 \cdot \frac{C_{tot} - C_{stray}}{t_{exp}}, \\ N_{atom,low} &= 1.62 \cdot \frac{C_{tot} - C_{stray}}{t_{exp}}. \end{aligned}$$

The known pixel area of $A = 6.45 \times 6.45\,\mu m^2$ of the pixelfly qe CCD chip and the number of counts $C(i,j)$ in a pixel (i,j) allow the measurement of a "column density" $\frac{N_{atoms}(i,j)}{A}$ from which an estimate for the volume density in that column can be made, by estimating the "length of the column" l. Looking at pixels with the highest counts, it is therefore possible to extract values for the peak density in the atomic cloud.

10.2.2 Implementation of Resonant Absorption Imaging

If a weak probe laser beam ($s/s_0 \ll 1$) passes through an atomic sample, the interaction can be described by the complex index of refraction of the atoms $n_{ref} = \sqrt{1 + 4\pi n\alpha}$ and the resulting complex electric field behind the atomic sample is

$$\begin{aligned} \mathbf{E}(x,y) &= \mathbf{E}_0 \exp\left(-\frac{2\pi i}{\lambda} \int [n_{ref} - 1]\, dz\right) \\ &= t\mathbf{E}_0 e^{i\Phi} \end{aligned}$$

where t is the transmission and $\Phi$the phase shift of the electric field.

[19] justified in case of strong saturation $s_0 \gg 1$ and resonant interaction $\delta = 0$

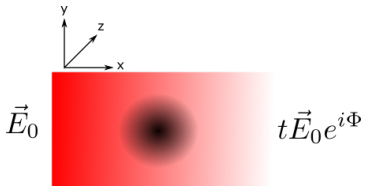

Figure 60: Weak probe beam passing through an atomic sample.

The index of refraction for a two-level system, assuming $n_{ref} - 1 \ll 1$, in the rotating-wave approximation can be written as [80]

$$n_{ref} = 1 + \frac{\sigma_0 n \lambda}{4\pi}\left[\frac{i}{1+\delta^2} - \frac{\delta}{1+\delta^2}\right],$$

where $\sigma_0 = \frac{3\lambda^2}{2\pi}$ is the resonant cross-section for a closed transition driven with with σ-polarized light along the quantization axis (defined by the magnetic field), $\delta \equiv \frac{\omega-\omega_0}{\Gamma/2}$ is the detuning in units of half linewidths, and $n = n(x,y,z)$ is the density of the atomic sample. The transmission then can be written as

$$t = \exp\left(-\frac{\widetilde{n}\sigma_0}{2}\frac{1}{1+\delta^2}\right) \equiv e^{-OD/2},$$

where $\widetilde{n} = \widetilde{n}(x,y) = \int n dz$ is the column-density of the atomic sample and we can define the off-resonant optical density OD as

$$OD = OD(x,y) = \frac{\widetilde{n}\sigma_0}{1+\delta^2},$$

a quantity which takes values between 0 (no absorption) and ∞. Resonant absorption imaging retrieves the resonant optical density by acquiring one picture of the intensity distribution with atomic sample $I(x,y) = |\mathbf{E}(x,y)|^2 = t^2 I_0(x,y)$ on the chip of a CCD-camera and one picture of the intensity distribution of the weak probe beam $I_0(x,y)$, i.e. without atomic sample. Then the resonant optical density can be calculated from

$$OD(x,y) = \widetilde{n}\sigma_0 = -\ln\frac{I(x,y)}{I_0(x,y)}.$$

The last equation is solution of the known Lambert-Beer law $\frac{dI}{dz} = I_0 e^{-\widetilde{n}\sigma_0 z}$. In practice, each CCD chip exhibits dark counts, even if not illuminated, which is why a third image $I_{drk}(x,y)$ is taken when the imaging beam is switched off and only the dark counts of the CCD chip are registered. This reference picture has to be substracted, so the optical density gets calculated from

$$OD(x,y) = -\ln\frac{I(x,y) - I_{drk}(x,y)}{I_0(x,y) - I_{drk}(x,y)}$$

Furthermore the images $I(x,y)$ and $I_0(x,y)$ are usually taken in quick succession in order to minimize the influence of intensity fluctuations in the weak probe beam. In order to calculate the number of atoms per pixel $N(i,j)$, one has to take into account the magnification M of the telescope behind the atomic sample, which reduces the column density $\widetilde{n}(i,j)$ by a factor of M^2:

$$\begin{aligned} N(i,j) &= \frac{1}{M^2} A\widetilde{n}(i,j) \\ &= \frac{A}{M^2}\frac{OD(i,j)}{\sigma_0}, \end{aligned} \qquad (68)$$

where A is the area of one pixel. In our setup we used a telescope with magnification $M = 1$ and a camera (pixelfly usb) with a pixel size of $6.45\,\mu\text{m} \times 6.45\,\mu m$.

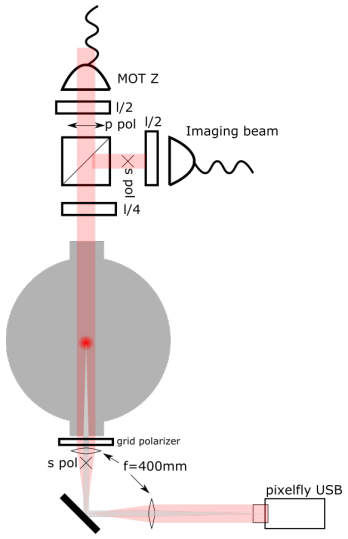

Figure 61: Absorption Imaging setup in the pre-BEC setup. The viewport used for the z-direction of the MOT, is reused for the imaging beam.

The main difficulty of resonant absorption imaging is that it requires a careful optics setup, so that the CCD camera is placed in the focal plane of the shadow, while the imaging beam hits the CCD chip collimated. In Fig. 61 one can see the 4f-setup of absorption imaging in our pre-BEC setup, using a 1:1 telescope for focusing the shadow on a CCD chip. The difficulty in our setup is, that we had to use the pair of viewports, which was already used for the z beam of the MOT. A grid polarizer is used at the bottom window, instead of a mirror, so that it reflects the linear polarization of the MOT z beam, but transmits the linear polarisation of the imaging beam. However the fluorescence of the atomic cloud in the MOT cannot be seen directly on the CCD chip of the pixelfly USB, since it is overshone by a few μW of leakage from the MOT Z cooling beam, while the power shone from an fluorescencing atom cloud of $2 \cdot 10^6$ atoms (at maximum scattering rate of $\approx$37 MHz) into a solid angle of 0.00437 sr (the same as for the pixelfly qe) is only about 100 nW. Therefore the optimum position of the pixelfly USB where the shadow of the atom cloud is going to be focused on the CCD chip could not be determined with absolute certainty. The main advantage of resonant absorption imaging is, that the evaluation of the atom number does not rely on any calibration of the CCD camera or estimation of solid angles, as it is the case for the method of fluorescence imaging. It could also be seen as an advantage, that the method requires to shine in only a small amount of optical power, so that the condition $\frac{s}{s_0} \ll 1$ is fulfilled and the atoms virtually only decay back by spontaneous emission.

Resonant absorption imaging is often called a destructive imaging method due to the fact, that the atomic sample is accelerated by the recoil of the photons in the direction of the imaging beam, which may cause a significant blurring during long exposures, especially for light atoms like ^{6}Li. Therefore the exposure time for resonant absorption imaging typically is held short and in the range of a few tens of μs. Anyway the imaging beam in our setup only contains one frequency, so atoms are pumped quickly into the other hyperfine state. This makes it necessary to precisely time the exposure of the CCD chip and the switching on of the imaging beam and to not choose too large exposures in order to optimize the signal-to-noise ratio.

10.3 A Singly-focussed Gaussian beam optical trap

We implemented a far off-resonant optical trap (FORT) by strongly focusing an infrared beam into our vacuum chamber with a lens of focal length 350 mm. The source of the IR beam was an active-fiber laser at 1070 nm with a maximum output power of about 200 W. A schematic of the small optical setup for the FORT in conjunction with other elements of our REMI is seen in Fig. 62. From the fiber head of our laser emerges a collimated IR beam, which then passes through an AOM. After the AOM, the 0th order is sent into a cooled beam dump, while the first order is used for the dipole trap. Lithium has a comparable weak induced electric dipole moment, which is why high powers to achieve trap depth, which are about ten times higher than the final temperature of the atoms in the MOT at the time of transfer. A complication arising from using such high powers is the possible heating therefore the occurence of thermal lenses within optical elements. This in turn can lead shift of focus position of up to a few mm [58], which is problematic for proper alignment of the IR beam focus with trapping volume of the MOT at the time of transfer, especially with a short Rayleigh length. Therefore special care has been taken in the selection substrate material for lenses, which exhibit the lowest absorption at 1070 nm. Our choice was a high purity fused silica (Corning 7979 IR Grade) with low OH content. This fused silica, according to its data sheet, exhibits an absorption of $\leq 10\,\mathrm{ppm/cm}$ and has a thermal coefficient of $0.58\,10^{-6}/\mathrm{K}$ compared to $\sim 1000\,\mathrm{ppm/cm}$ and a thermal coefficient of $8.3 \cdot 10^{-6}/\mathrm{K}$ of the standard substrate BK7 used for Thorlab lenses.

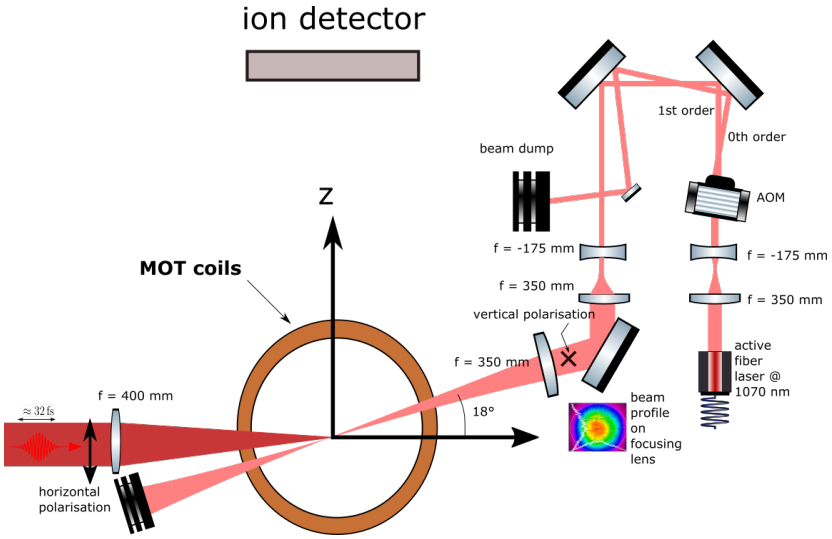

Figure 62: Schematic of FORT optical setup used for ionization experiments.

The AOM is actively water cooled and after optimization of its alignment a maximum power of $P_{-1st} \approx 148\,\mathrm{W}$ could be achieved in the first diffracted order which corresponded to about 80 % diffraction efficiency. The IR beam was collimated as well as possible (with a divergence of $\theta \approx 0.34\,\mathrm{mrad}$) and hit the focusing lens with a diameter of $\approx 5.17\,\mathrm{mm}$. From this properties a beam diameter at the focus of the Gaussian beam of $2w_0 \approx 96\,\mu$mis calculated by Gaussian beam optics equations. From Eq. 46 and the polarizability given in Eq. 50, a full trap depth of

$$\frac{U}{k_B} \approx 2.3\,\mathrm{mK}$$

should be achieved for ^{6}Li atoms in the $2S$ groundstate. For $^6Li_2$ molecules trap depths of up to 4.6 mK can be expected. This full trap depth corresponds to an AC Stark shift of the ground state by about $\frac{U}{h} \approx 48$ MHz to lower energies. The excited state $2^2P_{3/2}$ at full trap depth is shifted by about 36 MHz to lower energies. From this results a differential AC stark shift of the D line dublett at full trap depth of about 12 MHz to the blue. The corresponding trap frequencies in axial and radial direction at full trap depth according to Eq. 52 are given by

$$\begin{aligned} \omega_r &\approx 74\,\text{kHz}, \\ \omega_z &\approx 373\,\text{Hz}. \end{aligned}$$

10.4 Femto-laser system

The production of ultra-short and ultra-intense pulses of duration of a few tens of femtoseconds relies on spatial mode-coupling by a non-linear effect in a crystal, the so-called Kerr effect. In order to generate the short pulses of high peak intensity, the different longitudinal modes of a cw laser have to be superposed spatially, so that at least at one point in space, all the different modes are in phase and interfere constructively. This procedure is called mode-locking and a passive variant of it can be achieved by placing a saturable absorber inside a cavity. The idea behind a saturable absorber is, that an absorbing medium, like a sponge, can only absorb to a certain degree, so that high-intensity peaks see less loss and hence can lase while low-intensity background is prevented to lase.

One possible realization of a saturable absorber is a $Ti : Al_2O_3$ crystal with an aperture (see Fig. 63). The Kerr effect is a nonlinear optical effect, that leads to a local change in refractive index $n(I)$ depending on the intensity distribution $I(\mathbf{r})$ within the optical medium:

$$n(I) = n_0 + n_2 I.$$

The change in index of refraction due to the Kerr effect only becomes significant for intensities of $\geq 10^9 \frac{\mathrm{W}}{\mathrm{cm}^2}$. If a pulse is more intense in its center due to a Gaussian radial intensity distribution $I(\mathbf{r})$, the local increase of refractive index has the equivalent effect of a lens, i.e. high-intensity pulses are focused. If one places an aperture at the focus, short pulses will be favored, while the losses for low-intensity cw modes are too high in order to lase. This so-called Kerr lens mode-locking leads to an amplification and shortening of the high-intensity pulses after many round-trips, while low-intensity pulses are increasingly weakened.

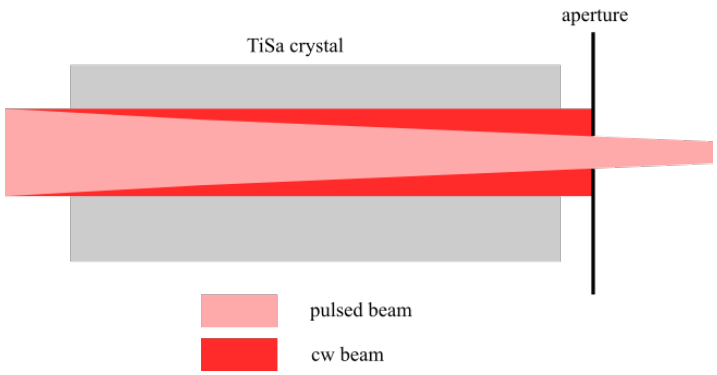

Figure 63: Principle of a passive mode locking with a Kerr lens.

In order for the crystal to not take damage due to the high peak intensites, the pulses are stretched in time by a grating pair, prior to entering the amplifier. After leaving the amplifier, the amplified pulses are temporally compressed again, by letting them travel through glass wedges, where the different frequencies within the pulse are spatially separated, so that the optical path length for frequencies that are "ahead" is longer. After travelling through this wedges, the different frequencies are recombined again into a short pulse. This concept has been coined "Chirped Pulse Amplification" (CPA) and is schematically depicted in Fig. 64.

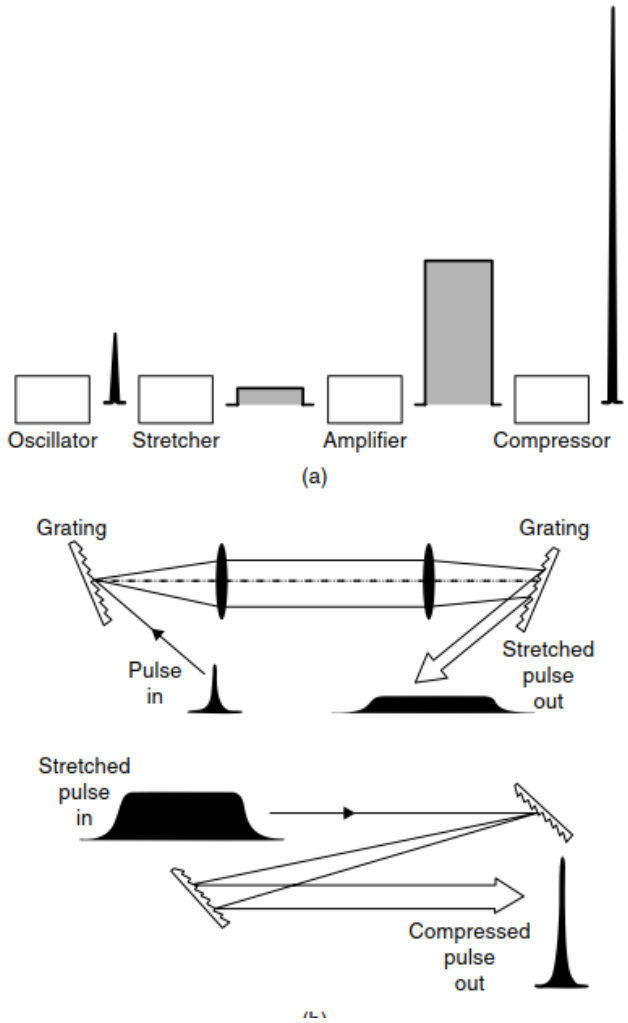

Figure 64: Chirped pulse amplification (CPA) method. From [81]

The pulses entering the amplifier are provided by an oscillator, which provides pulses of duration of several hundred femtoseconds, which are then subsequently stretched by about a factor of 10^4 up to a duration of a nanosecond. In the amplifier the pulse energy is increased by a factor of about $10^{11}$and then finally the compressor compresses the pulses again by a factor of about 10^4.

Femtolaser pulses are mainly characterized by their pulse spectrum, pulse duration and pulse energy. The femto laser system used in our experiment is capable of producing pulses of duration of $\approx 32\,\mathrm{fs}$ for optimized compressor settings, at a repetition rate of $4\,\mathrm{kHz}$, a pulse energy of up to $750\,\mu\mathrm{J}$ at a central wavelength $810\,\mathrm{nm}$. The pulse spectrum is characterized by the spectral intensity $I(\lambda)$ or $I(\omega)$ which in turn is connected to the complex electric field amplitude $E(\omega)$ by

$$I(\omega) = E(\omega) \cdot \overline{E}(\omega),$$

where

$$E(\omega) = \frac{1}{\sqrt{2\pi}} \int_{-\infty}^{+\infty} E(t) \exp(i\omega t) dt$$

is the Fourier transform of the temporal shape of the electric field amplitude $E(t)$ and vice versa. Because of this Fourier relation, it is clear that short pulses exhibit a tremendeously broad spectral intensity. The variance bandwidth $\Delta\omega$ of the spectral intensity $I(\omega)$ is connected to the pulse duration Δt by the uncertainty relation [82]

$$\Delta\omega \cdot \Delta t \geq K \cdot 2\pi,$$

where K is a constant on the order of unity, that depends on the temporal pulse envelope shape. For a given bandwidth $\Delta\omega$, the shortest possible pulse duration is given by

$$\Delta t = 2\pi K (\Delta\omega)^{-1}$$

and pulses with this shortest duration are called "Fourier limited". The spectral intensity of our fs laser system at the output of the compressor was measured with a spectrometer (Ocean Optics USB4000) and is shown in Fig. 65. The spectral intensity has a 2σ bandwidth of $2\sigma_\nu \approx 15.3\,\mathrm{THz}$ for which, with an envelope $\sim e^{-(4\ln 2)\frac{t^2}{\Delta t^2}}$ and $K = 0.441$, we obtain a Fourier limited pulse duration of $\Delta t \approx 28.8\,\mathrm{fs}$.

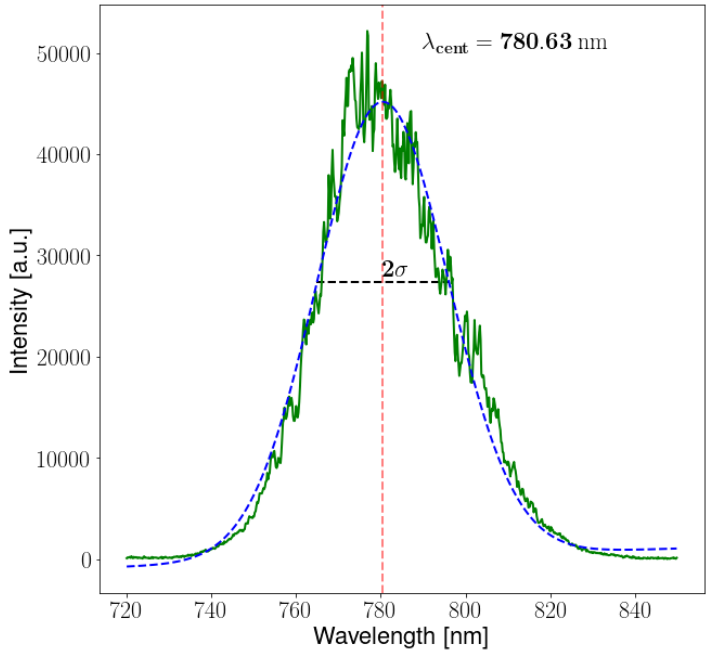

Figure 65: Spectral intensity $S(\lambda)$ of our fs laser system, showing a central wavelength of $\lambda_{cent} = 780.63\,\mathrm{nm}$ and a standard deviation of $\sigma \approx 15.5\,\mathrm{nm}$. This corresponds to a central photon energy of $1.59 \pm 0.03\,\mathrm{eV}$.

11 Pre-BEC setup

In this thesis, what is referred to as "Pre-BEC setup" is our MOTRemi extended by a focused beam trap. While the current setup does not enable the creation of a BEC, since our MOT coils are not designed to carry high currents, it allows us to ionize optically trapped atoms or cold molecules. Before results of these measurements are presented in Sec. 12, a few characterization measurements are presented, which concern the atom number and density in the MOT, the temperature of ^{6}Li atoms in the MOT at loading and transfer parameters, the initial atom number and density in the dipole trap under various conditions, and the lifetime of the atoms in the dipole trap under various conditions.

11.1 Characterization of magneto-optical trap

11.1.1 Optimization of loading rate and measurement of atom number

In Sec. 4.1 it has been pointed out, that in our setup, due to the dimensions of our vacuum chamber, there is a gap between the end of the Zeeman slower and the trapping region of the atoms. Depending on the magnitude of the employed currents, only atoms up to a certain velocity class v_{max} can be decelerated, which in turn results, under the assumption of an ideal Zeeman slower, in a specific end velocity after the atoms leave the Zeeman slower. The idea of an ideal Zeeman slower is, that according to Eq. 36, the deceleration zone strictly starts and ends at specific points. In reality, because of power broadening and decay of the magnetic field, slowing starts already before the Zeeman slower begins, and long after the Zeeman slower ends. In any case we can tune the atomic flux by adjusting the different currents in the Zeeman slower, which assume different end velocities v_{end} for the ideal Zeeman slower. The idea is, that the loading rate is optimum for a certain end velocity, because if v_{end} is too slow, the atomic beam's divergence decreases the atomic flux, yet on the other hand if v_{end} is too high, many atoms might not be captured by the MOT.

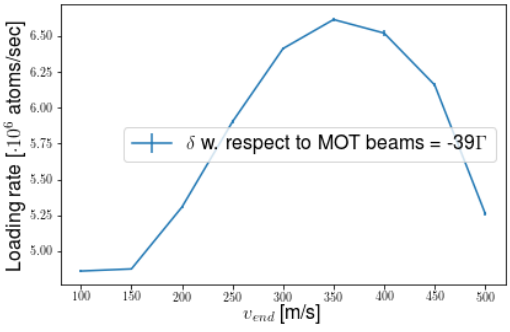

Figure 66: Loading rate for different current configurations of the Zeeman slower (at Zeeman slower beam detuning of $\approx -39\Gamma$) corresponding to different achieved end velocity.

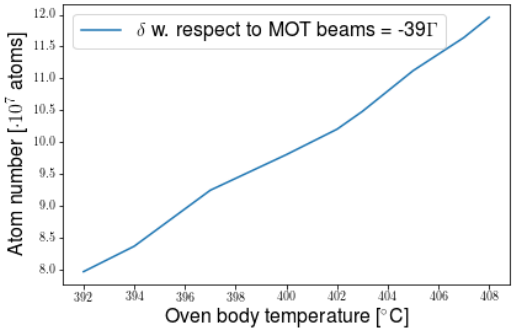

Figure 67: Equilibrium atom number in dependence of the oven body temperature.

This optimum value for v_{end} has been determined experimentally by adjusting different Zeeman slower currents and from Fig. 66, it can be seen that the optimum value is located

around $v_{end} = 350\,\mathrm{m/s}$. Finally for this optimum current configuration of the Zeeman slower, the dependence of the equilibrium number of atoms on the oven body temperature has been measured. As can be seen from Fig. 67 the equilibrium atom number rises linearly with oven temperature and increase by $\approx 6.3 \cdot 10^5 \mathrm{atoms/°C}$. For both measurements the fluorescence of the cloud has been captured at a detuning of $\delta \approx -5\Gamma$ with a CCD camera and the scattering rate was calculated using Eq. 26 and the assumption of a high saturation of $s_0 \approx 30$. The loading rate has been determined from the slope of the linear part of the loading curve. A typical loading curve given by Eq. 45 is shown in Fig. 68.

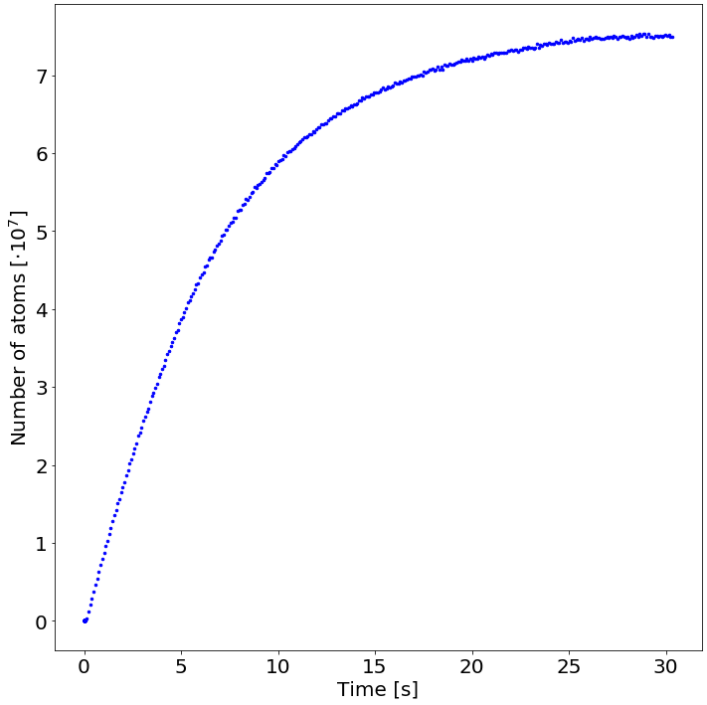

Figure 68: Atom number during loading with Zeeman slower beam and magnetic field.

11.1.2 Temperature of atom cloud

The time-of-flight (TOF) technique is standard method for determining the temperature of an atom cloud along a specific axis. In its standard implementation it requires a spatially calibrated CCD camera. When the trapping beams of the MOT are switched off, the atoms freely[20] expand isotropically. The integrated cloud profile along a specific direction can be fitted to a Gaussian $\sim e^{-\frac{(x-\mu)^2}{2\sigma(t)^2}}$, in which the time-dependent variance is given by a quadratic function

$$\sigma(t)^2 = \sigma_0^2 + \bar{v}^2 t^2,$$

[20] with exception of a small Zeeman shift when the magnetic gradient is not switched off too. However this Zeeman shift can be considered negligible if the cloud temperature is on the order of several hundred Microkelvins.

where $\sigma_0 = \sigma(t = 0)$ and the mean velocity $\bar{v}$ along the axis is related to the temperature by

$$\begin{aligned} \frac{k_B T}{2} &= \frac{m\bar{v}^2}{2}, \\ \Leftrightarrow \bar{v} &= \sqrt{\frac{k_B T}{m}}. \end{aligned}$$

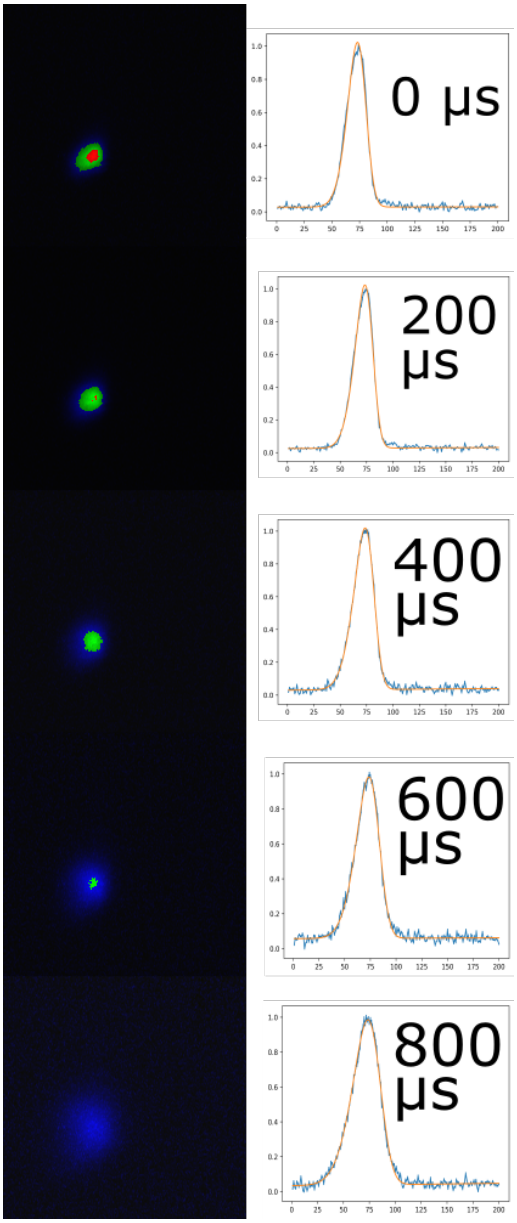

Figure 69: Example of a ballistic expansion of an atom cloud by switching off the trapping beams for a determined time. The CCD pictures of the expanding cloud have been false-coloured in order to highlight the changes in density.

An example for a ballistic expansion of an atom cloud, when it is not confined by the trapping forces of the MOT beams is shown in Fig. 69. Cloud temperatures have been

determined at loading parameters ($\delta \approx -5\Gamma$, $s_0 \gg 1$) and after compression ($\delta \approx -\Gamma/2$, $s_0 \approx 2$), where compression refers to the process of decreasing the red detuning and lowering the intensity of the trapping beams. The aim of latter measurements was to determine the parameters (δ, s_0) for which the atomic cloud was as cold and dense as possible. Ideally, the temperature of the atom cloud after compression should be $\approx 1/10$ of the estimated trap depth of the optical trap. Theoretically the minimum temperature follows from Eq. 28 to be $(\delta, s_0) = (-\Gamma/2, 2)$, but since it follows from a 1D model, these optimum parameters can be different in experiment, as also has been noted in [83].

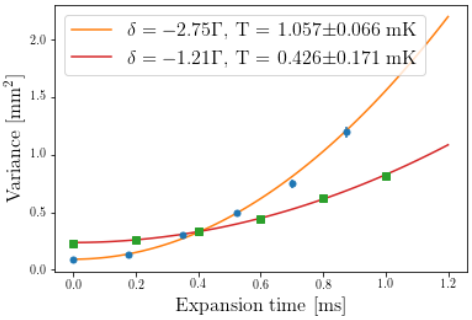

Figure 70: Quadratic fit to the variances of the cloud Gaussian profiles during a ballistic cloud expansion. The orange curve for $\delta = -2.75\Gamma$ correspond to the MOT cloud temperature at a (δ, s_0) which is used for optimum loading rate. The red curve corresponds to the temperature of the MOT immediately after compression, i.e. simultaneously changing the detuning and beam intensities to a final value $(\delta_{cool}, s_{0,cool})$ at which the atom cloud is cool and dense.

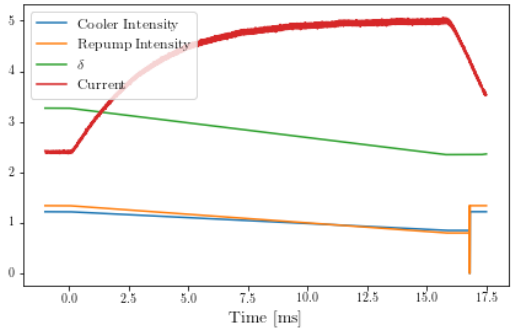

Figure 71: Timing of analog signals like beam intensities,detuning and current during compression of the MOT cloud.

As can be seen from Fig. 70, the temperature of the atoms at loading detuning of the MOT beams is about 1 mK, while after compression a temperature of down to 426 μK can be achieved. A typical example of the timing of analog signals in an experimental sequence used to compress the MOT cloud, is shown in Fig. 71. As can be seen, in order to to achieve the highest phase-space density, the detuning, beam intensities and the magnetic gradient are changed gradually at the same time. For other objectives like photoassociation, where the PA rate is $\sim n^2$ and long illumination times up to 1500 msmight be needed, it is imperative to find conditions how to achieve a high peak density for a relatively long time. In the atom cloud at loading detuning $\delta \approx -7\Gamma$ the peak density is $\approx 2 \cdot 10^9$atoms/cm^3. It was determined as the column volume density $N_{atom}(i,j)/(A \cdot l)$ of a column of area A and length l by looking at the pixel with the highest counts in the region of interest. The length of the column l was assume to be 2σ,where σ of was the atom cloud's Gaussian profile along a particular direction. In Fig. 72 the peak intensities in the MOT cloud with different methods of compression for variable "molasse cooling time"[21] are compared. The blue curve refers to the above mentioned

[21] actually in none of the sequences the magnetic field of the MOT was switched off during the cooling

compression for loading the optical dipole trap, which yields the highest phase-space density, but not the highest density. If only the MOT beam detuning is changed and the magnetic gradient increased, the resulting green curve shows, that one initially obtains almost ten times higher density, however the peak density decays very fast and after 600 ms is estimated to be already below $2.5 \cdot 10^{10}$ atoms/cm^3. Since the measurement only shows peak densities for molasse cooling times > 10 ms, it is not seen, that the green curve actually starts out with the highest peak density. A comparable peak density in the range from $0.5 - 2 \cdot 10^{11}$ atoms/cm^3 for molasse cooling times up to 1500 ms is achieved by just changing the detuning of the MOT beams

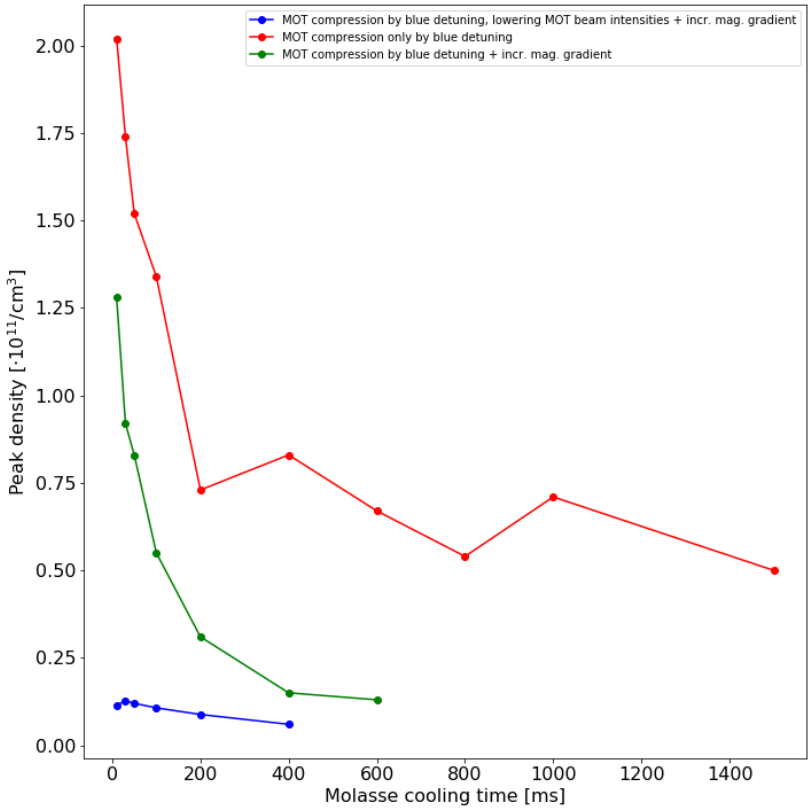

Figure 72: Peak density of an atom cloud after different methods of atom cloud compression.

11.1.3 Measurement of atom number via Resonant Absorption Imaging

The implementation of resonant absorption imaging did turn out to be quite delicate in our current setup because of the reasons mentioned in Sec.10.2.2. The lack of free viewports and the dimension of our vacuum chamber and the available space around it, made it only possible to use the pair of viewports, which is used for the z direction of the MOT. This on the other hand made it impossible to directly see the fluorescence on the CCD camera, since the extinction ratio of the employed polarizing beam splitter cubes is typically 1000:1, which at a moderate beam power of 15 mW, still leads to a leakage of about $\approx 15\,\mu W$ through the grid polarizer. On the other hand, an upper estimate for the optical power of an atom cloud of $2 \cdot 10^6$ atoms, scattering at maximum scattering rate into the small solid angle of the CCD camera, can be given as 100 nW. With our resonant absorption imaging setup, we were able to see the shadow of magneto-optically trapped atoms (see Fig. 73).

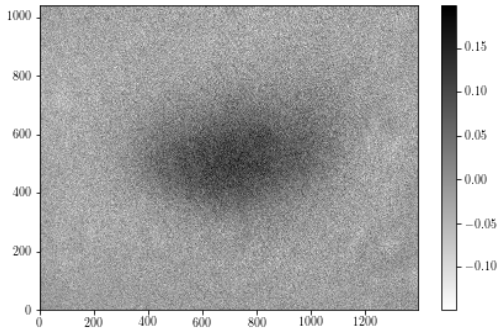

Figure 73: Optical density of MOT cloud calculated from two pictures taken in quick succession (about 150 ms).

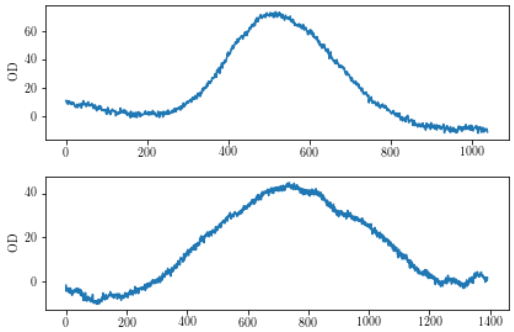

Figure 74: Profiles of OD resulting resulting from column (top) - and rowwise (bottom) summation. The sum profiles have been shifted, so that the summed background optical density roughly adds up to zero.

From Eq. 68, we obtain the total atom number by summing over all pixels. Ideally the optical density in the regions of no shadow, would average to zero. However intensity fluctuations in the imaging beam can lead to different light levels between the two exposures and beam pointing instabilities due to vibrations in the setup can lead to fringes in the resulting optical density. For the optical density plotted in Fig. 73, we obtain as average from the summed profiles in horizontal and vertical direction an atom number of

$$N = \sum_{i,j} N(i,j) \approx 4.1 \cdot 10^6,$$

which is consistent with the result we obtained from fluorescence imaging at that time.

11.2 Characterization of optical trap

For some of the properties of our dipole trap, like trap depth and trap frequencies at full trap depth we only gave estimates in Sec.10.3. In principle, trap frequencies can also be determined experimentally by parametrically exciting resonances of trapped atoms [84, 85], however for our experiment we focused on the transfer efficiency, density and temperature of the optically trapped atoms.

11.2.1 Measurement of transfer efficiency and atom number density

A standard method to determine the transfer efficiency into the dipole trap, is to load the dipole trap by overlapping it with the compressed MOT, and only wait the minimum time after the MOT magnetic field and the MOT beams have been switched off, in order for all non-trapped atoms to leave the trapping region. Immediately, after that, the MOT beams can be switched on again in order to collect fluorescence from the optically trapped atoms. An example of such an experimental sequence is shown in Fig. 75. In our experiment, the waiting time until all non-trapped atoms have left the trapping region is not more than 10 ms. In order to accurately estimate the number of trapped atoms, one should image the optically trapped atoms resonantly. Therefore at full trap depth, a small differential Stark shift of the

cooling transition has to be taken into account. The optimum detuning at full trap depth with respect to the cooling transition in ^{6}Li has been determined to be $\delta \approx -0.32\Gamma \approx -1.06\,\mathrm{MHz}$ (see Fig. 76).

Imaging the dipole trapped atoms at the resonant frequency after 200 ms of optical trap time with full trap depth, resulted in the picture in Fig. 77.

The total counts $C_s = 184392$ in the ROI on top of the dipole trapped atoms of Fig. 77 collected during an exposure time of $t_{exp} = 0.1$ ms, amounts to an atom number of

$$N_{atoms}^{dip} \approx 6.24 \cdot 10^5 \,\text{atoms}.$$

With a MOT equilibrium atom number of $\approx 7 \cdot 10^7$ atoms, this corresponds to a transfer efficiency of $\approx 0.9\,\%$. Furthermore from the spatial profile the radial extension of the trapping volume can be approximated with the σ of the Gaussian distribution, which was determined by the fit in Fig. 78 to be

$$\sigma \approx 90\,\mu\text{m}.$$

Let the trapping volume be approximated by $V = \frac{4}{3}\pi\sigma^3$, then the average atomic density in the dipole trap is estimated to be

$$n \approx \frac{N_{atoms}^{dip}}{V} \approx 0.59 \cdot 10^{10}\,\frac{\text{atoms}}{\text{cm}^3}.$$

The resulting spherical volume of $V \approx 1.23 \cdot 10^{-4}\,\text{cm}^3$also agrees pretty well with the theoretical assumption of an ellipsoid volume $V = \frac{4}{3}\pi w_0^2 z_R \approx 1.226 \cdot 10^{-4}\,\text{cm}^3$, where the length of two half axes correspond to the waist $w_0 \approx 50\,\mu m$ at the focus, and the length of the half-axis along axial direction is assumed to be the Rayleigh length z_R.

Since the density in the dipole trap is also position-dependent and should be highest in the center of the trapping volume, at the very focus of the IR beam, and lowest in the wings of the focused IR beam, the peak density in the dipole trap at the IR beam focus is actually higher. The peak density in our optical dipole trap has been determined by extracting the counts *in one pixel* of the trapping volume with maximum counts. For each duration of optical trapping, the MOT beams have been switched to full power at the detuning determined above, to resonantly scatter the remaining atoms. By determining the pixel with the maximum counts and assuming as column length double the standard deviation of the Gaussian profile of the cloud in transversal direction, we obtained estimes for the peak volume densities which have been plotted in Fig. 79. The peak densities in the dipole trap have been determined for three different settings regarding optical pumping. In the first setting, shown by the blue curve, the atoms in the dipole trap have been pumped into the $F = 1/2$ hyperfine state by switching off the repumper frequency about $100\,\mu$searlier, than the cooler frequency. It clearly can be appreciated that the dipole trap has high peak densites of $> 1.25 \cdot 10^{11}$atoms/cm^3 even for optical trapping times up to 1.5 s. To illustrate the detrimental effect of spin changing collisions on the lifetime of the atoms in the dipole trap, in another measurements the atoms have been pumped once into $F = 3/2$ for $100\,\mu$s. As can be seen in red curve in Fig. 79, the peak density decreases exponentially fast, since the hyperfine groundstate splitting is much larger than the trap depth of the atoms. The green curve shows the time development of the peak density, if no optical pumping is applied.

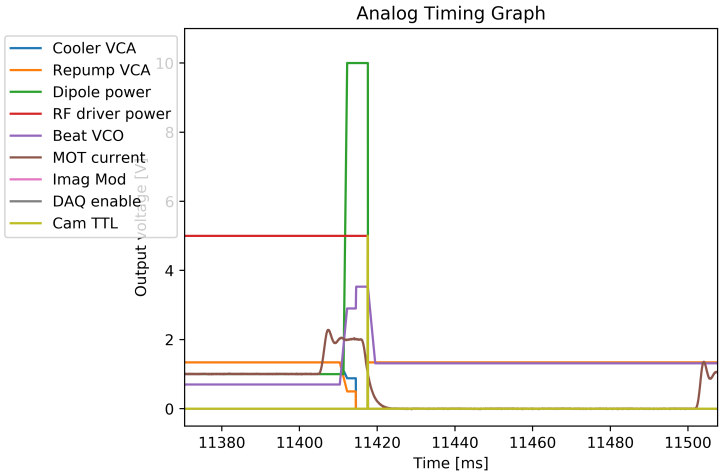

Figure 75: Analog and digital control voltages and measured MOT coil current during experimental sequence for determination of the resonant frequency of dipole trapped atoms at full trap depth. The atoms are dipole trapped for about 8 ms, enough time for non-trapped atoms to escape from the trapping region and the MOT magnetic field to switch off.

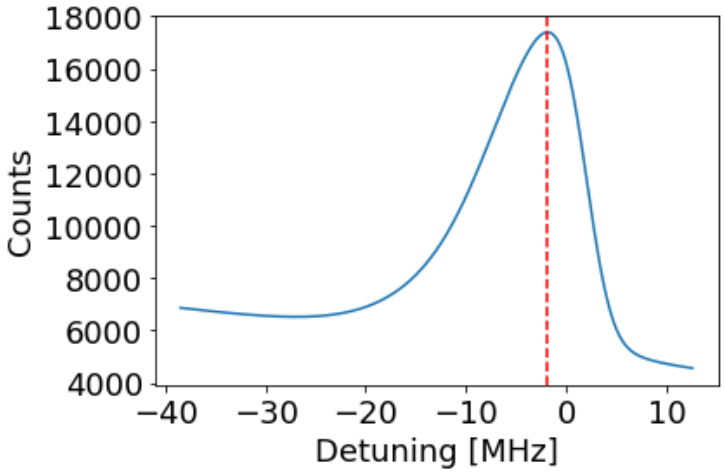

Figure 76: Gaussian fit to the collected fluorescence of optically trapped atoms versus detuning of MOT beams. From the fit the resonant detuning for imaging the dipole trapped atoms at full trap depth is determined to be at $\delta = -0.32\Gamma \approx -1.87\,\mathrm{MHz}$.

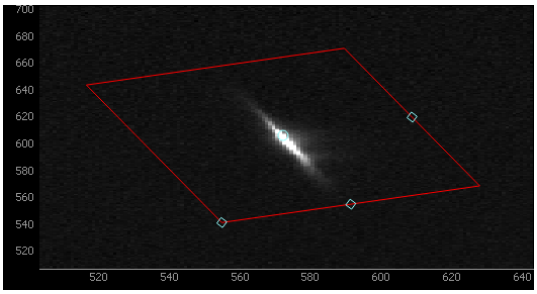

Figure 77: Fluorescence of dipole trapped atom captured on CCD chip of pixelfly qe after 200 ms of optical trap time at full trap depth and driving resonantly the cooling transition in the last 100 μs of trapping time. The contribution of scattered IR light already has been substracted.

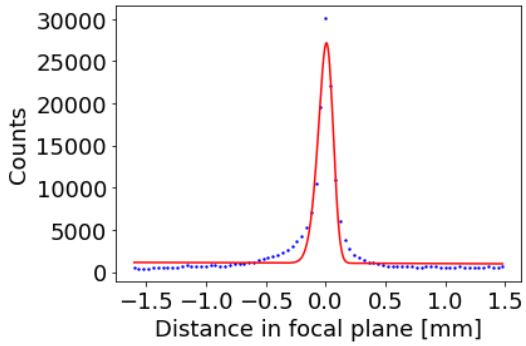

Figure 78: Fluorescence profile (blue curve) of imaged dipole trapped atomic cloud, by summing ROI columns perpendicular to beam direction.

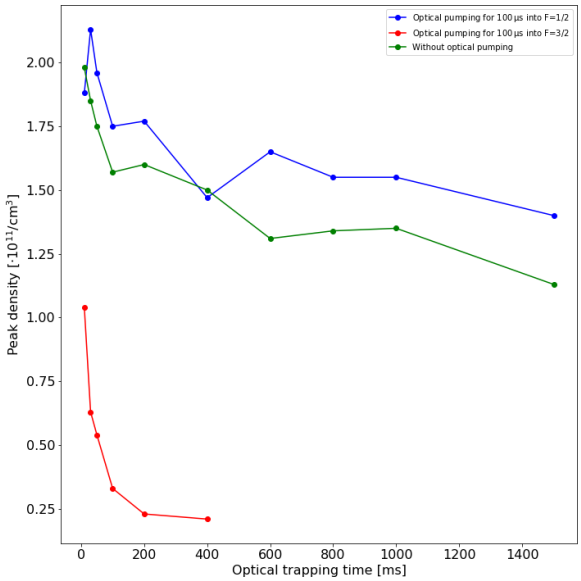

Figure 79: Peak density in dipole trap as measured with timing sequence in Fig. 75 for different optical trapping durations.

11.2.2 Temperature of atom cloud after initial stagnation of evaporative cooling

An analogous measurement, to that of Subsec. 11.1.2, has been performed for the optically trapped atoms after about 200 ms of optical trapping time, after which natural evaporative cooling should have stagnated and the hottest atoms should have left the optical trap (see Fig. 80). The temperature of the atoms in the optical trap is consistent with the temperature of the MOT cloud after compression.

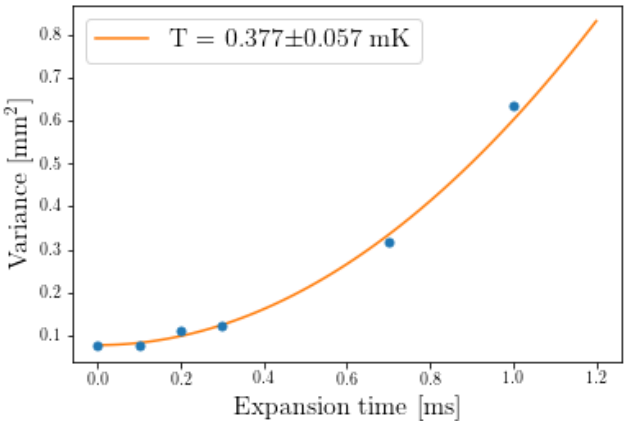

Figure 80: Measurement of temperature of optically trapped atoms, after 200 ms optical trapping when initial natural evaporative cooling has stagnated

12 Experimental results

12.1 Resonance-enhanced multi-photon ionization (REMPI) of an optically trapped target

In the following section I report on coincident detection of electrons and $^6Li^+$ ions after resonance-enhanced strong-field multi-photon ionization (REMPI) of optically trapped atomic ^{6}Li with fs laser pulses ($\tau \approx 32\,\text{fs}$, $\hbar\omega = 1.59\,\text{eV}$), i.e.

$$4\gamma_{fs} + {}^6\text{Li} \rightarrow {}^6\text{Li}^+ + e^-.$$

As outlined in Sec. 1, the momentum of the photon can be neglected in this reaction and momentum conservation then dictates the three dimensional momentum vectors of $^6Li^+$ and e^- to be of opposite direction. Since the ^{6}Li atoms are trapped in a far-off resonance trap, they reside most of the time in their electronic ground state $2S$, and ionization occurs essentially from the electronic ground state. The relevant energy levels of ^{6}Li and the possible transition pathways for multi-photon ionization from the electronic groundstate $2S$ are shown in Fig. 81. Our femtolaser system has a Gaussian distributed spectral intensity with 1σ-width of 0.03 eV (see Fig. 65). We take the 3σ interval to be the energy uncertainty of each photon, i.e. $\Delta E = 0.09\,\text{eV}$. After absorption of n photons, the final virtual state has an energy uncertainty of $\pm n \cdot \Delta E$.

For non-resonant ionization from the ground state, a minimum number of $n_0 = 4$ photons would be required, producing a kinetic excess energy of $0.97 \pm 0.36\,\text{eV}$ or an atomic momentum of 0.27 ± 0.05 a.u. for the photo-electron. For higher intensities the AC Stark or Ponderomotive shift of high lying levels and of the ionization potential has to be taken into account. All measurements in this section were performed in the multi-photon regime with peak densities well below $10^{13}\,\frac{\text{W}}{\text{cm}^2}$, for which with the central wavelength of our fs laser a maximum AC stark shift of the ionization potential and the high lying states $(4p, 5p, 4f, 5f)$ of 0.57 eV is expected. At low peak intensity $< 10^{10}\,\frac{\text{W}}{\text{cm}^2}$, the states $5p$ and $5f$ lie within the bandwidth of the final virtual state after absorption of three photons. Therefore, these real intermediate states then get populated and since single-photon ionization from a real state has a much larger cross section, it leads to an enhancement in ion yield. Therefore, this process is called resonance-enhanced multi-photon ionization (REMPI). Also, at peak intensities of $4 \cdot 10^{12}\,\frac{\text{W}}{\text{cm}^2}$, REMPI is again realized because the AC stark shift is sufficient to shift the highly excited states $4f$ and $4p$ into resonance, while the ionization potential shifted by the amount. In summary, at different peak intensities, apart from MPI, also REMPI is realized in atomic ionization of $^6Li^+$ and for each possible ionization pathway, we expect different excess energies momenta for the photo electron and accordingly $^6Li^+$ recoil ion, which are tabulated in Tab. 3.

Property	MPI	4p-resonance	4f-resonance	5p-resonance	5f-resonance
E_{el} [eV]	0.97	0.72	0.74	1.04	1.05
E_{ion} [μeV]	88.7	65.8	67.7	95	96.0
p [a.u.]	0.267	0.230	0.233	0.276	0.278

Table 3: Excess energies for $^6Li^+$ ions and photo electrons for different ionization pathways, where the excess energy for MPI is given for low intensities when the Ponderomotive shift is negligible.

Upon absorption of a fs photon the angular momentum of the electron changes by $\Delta l = \pm 1$. The final momentum distribution and the electron's partial wave for the different ionization

paths has s-, d- or g-wave character (see Fig. 81). Since usually several ionization paths are involved in the atomic ionization, the electron's wavefunction is a superposition of these different partial waves and the contribution of different partial waves will be visible in the angular distribution of electron momenta.

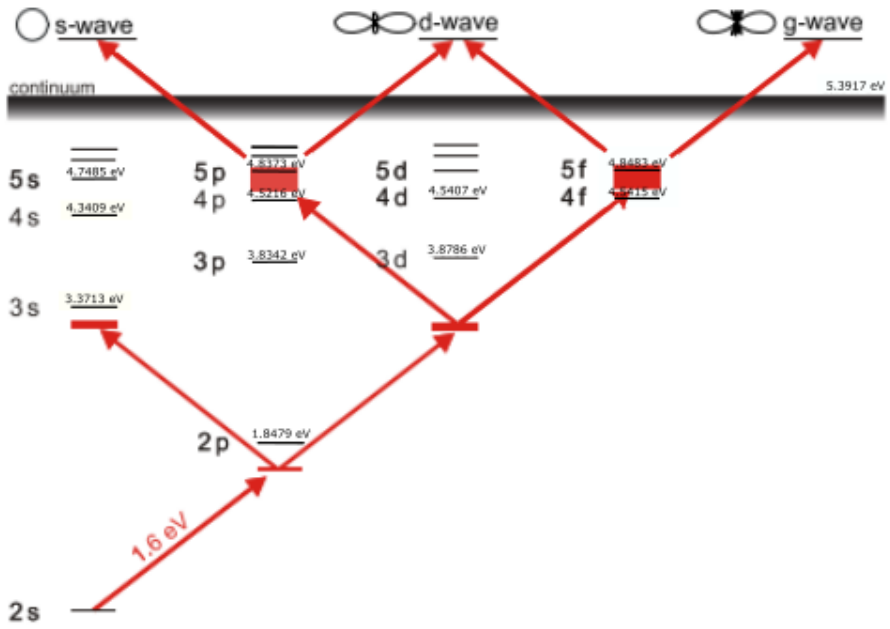

Figure 81: Relevant energy levels for multi-photon ionization of optically trapped ^{6}Li [86]. Fig. from [87]

Additionally, if the atom after the fs pulses is left in one of the states $4p, 5p, 4f, 5f$, it can be directly ionized by absorption of an IR photon of energy 1.16 eV from the trap laser, resulting in electron excess energies of 0.29 ± 0.01 eV or 0.61 ± 0.01 eV respectively. However this excess energy cannot be measured sharply, since ionization of an highly excited atom by absorption of an IR photon can take place at any time within the lifetime of the highly excited state, which is on the order of a few hundreds of nanoseconds [88] . This process will therefore be called "delayed IR ionization" in this thesis.

Because of the dipole trap's long storage times of tens of seconds [44, 45], femto laser induced ionization of optically trapped atoms does not demand a fast decay of the magnetic field on the order of hundreds of microseconds, which requires fast-switching of MOT coil currents. As shown in Fig. 82, the MOT magnetic field switching takes about $7 - 8$ ms, after which the femto shutter is opened and our data acquisition is enabled. Ionization, therefore, basically occurs "field-free", in the sense that only the spectrometer electric extraction, the magnetic guiding field, and the IR electromagnetic trapping field, are present. The IR electric field has a maximum power density at full trap depth of a few MW/cm^2 in its focus. Therefore the ponderomotive shift caused by the IR field can be considered negligible.

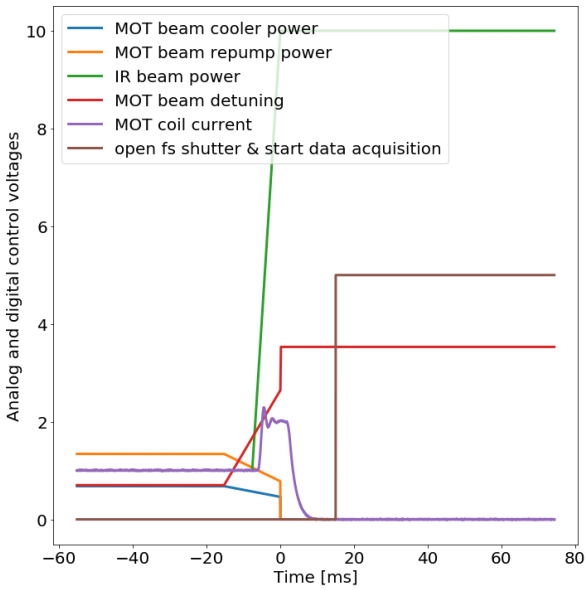

Figure 82: Analog and digital control voltages of ADWin sequence for ionization out of optically trapped ^{6}Li.

These field-free conditions make it possible to coincidentally detect photo electrons and recoil ions after multi-photon ionization of optically trapped ^{6}Li. The delayed IR ionization of excited states is observed as tail at longer flight times in the time-of-flight distribution of the recoil ions (see Fig. 83). Delayed IR ionization also led to a considerable increase in ionization rate, which was used in the experiment for optimization of the overlap between fs focus and IR focus.

A raw position spectrum for recoil ions, in which the IR polarization was aligned perpendicular to the spectrometer axis, while the fs laser polarization was parallel to the spectrometer axis, is shown in Fig. 84. The events due to delayed IR ionization can be readily noted, since the position spectrum is not rotationally symmetric, but exhibits two lobes in direction of the vertical IR polarisation. We recorded the ionization rate from the dipole trap as a function of time, and used it as an alternative method to estimate the number of initially trapped atoms. Therefore the fs power $\overline{P}$ was adjusted high enough to measure an exponential decay of the ionization rate (see Fig. 85) after opening the fs laser shutter. The initial atom number in the optical dipole trap can be obtained from the area under the curve of ionization rate versus ionization time . The measurement in Fig. 85 has been averaged over many loading cycles and shows that dipole trap has not yet been depleted by ionization events after 7 s.

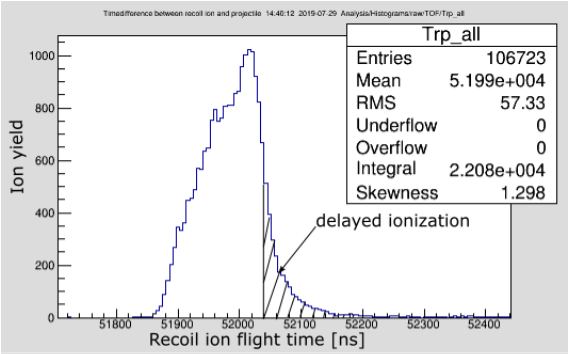

Figure 83: Raw recoil ion TOF spectrum after multi-photon ionization of optical trapped ^{6}Li atoms.

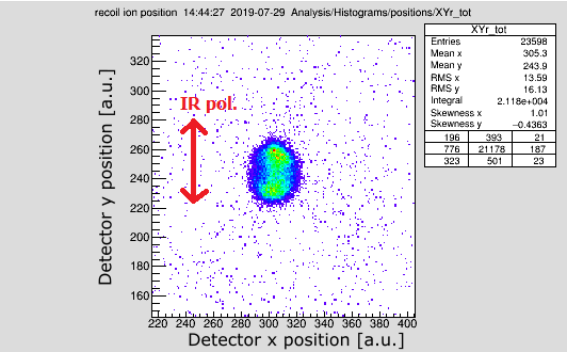

Figure 84: Raw recoil ion position spectrum after multi-photon ionization of optically trapped ^{6}Li atoms. The polarisation of the fs- laser pulses was along the spectrometer axis, i.e. perpendicular to the plane. The polarisation of the focused IR beam was as indicated.

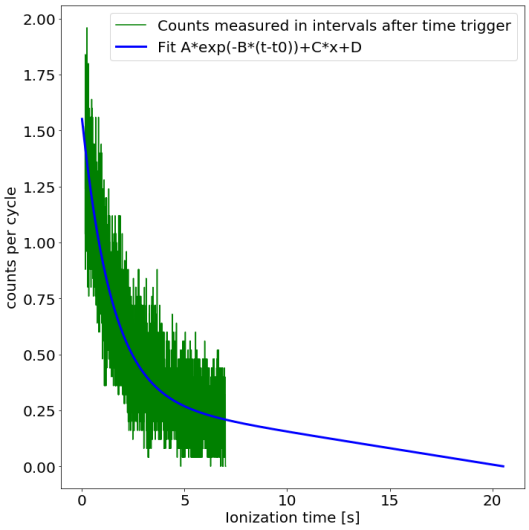

Figure 85: Measured counts from ionization events in dipole trap a certain time after optical trap time has begun. The ionization curve has been taken for a femto laser power of $P_{femto} \approx 305\,\mathrm{mW}$.

By fitting an exponential curve $f(t) = A \cdot e^{-B(t-t_0)} + C \cdot x + D$, the point of time at which the count rate is zero and the dipole trap finally depleted, is extrapolated to be at $t \approx 20.5\,\mathrm{s}$. By making an assumption about the detection efficiency of recoil ions on the detector (see Sect. 1.3), the area under the curve until t reflects a lower estimate on the atom number in the dipole trap. With this fit we obtain an area an estimate of $1.37 \cdot 10^4$ atoms, which is on the same order of magnitude as the number which we obtained via collection of the fluorescence signal of optically trapped atoms at that time.

12.1.1 Momentum resolution of recoil ions and photo-electrons

A challenge for ionization of dipole trapped atoms with high momentum resolution is the high initial target density, which results in a high initial ionization rate with several charged fragments being detected from a single laser shot, even for low peak intensities on the order of $10^9\,\mathrm{W/cm^2}$. More than three ions per shot in turn can lead to space-charge effects which blur the momentum resolution. Another issue is the delayed IR ionization, which blurs out the TOF distributions of ions and electrons. In order to obtain an estimate on the momentum resolution of our spectrometer, TOF spectra of recoil ions and photo electrons at low count rate and without delayed IR ionization were taken. In order to suppress the delayed IR ionization, there are two methods. One method is switch off the IR laser, and therefore the dipole trap, in a small time window of about 1 μs of width, so that (see oscilloscope traces in Fig. 86) the trap field is absent for several hundred nanoseconds before and after arrival of the fs laser pulse. This fast switching was achieved by cutting the RF power of the AOM providing the first order beam for the optical trap.

Figure 86: Oscilloscope trace showing trap modulation relative to arrival of fs laser pulse. Green trace corresponds to femto laser trigger and blue trace corresponds to trap depth of optical trap.

With this fast modulation, the raw recoil ion TOF and position spectrum were resolved and had no overlap with ionization from the highly excited states (see Fig. 87 and 88). The side effect of this approach is, that it drastically reduces the lifetime of the atoms in the dipole trap, which can be attributed to atom loss and ensemble heating, caused by the rapid trap modulation. However this method guarantees, that IR photons will not participate in excitation or ionisation of atoms or molecules, which is why it will be used in later measurements.

The other method to supress the delayed IR ion yield, is to limit the spectrum of our femtolaser to a small band around 793 nm, so that after absorption of the three photons, the virtual state is exactly between $4p$ and $5p$ or $4f$ and $5f$ and real levels are avoided as intermediate levels. Momentum spectra, in which the magnitude of the transversal momentum is plotted versus the longitudinal momentum, are shown in Fig. 89 and 90 for recoil ions and photo-electrons respectively. The main intensity of the recoil ion momentum spectrum lies on a circle with excess momentum 0.266 a.u., which would be expected for MPI. Furthermore a structure is visible with three distinct lobes, which means, that the electron dominantly emerges as d- or g-wave after ionization. In the momentum electron spectrum shown in Fig. 90 shows, the main intensity of electron momenta is again on a circle with excess momentum

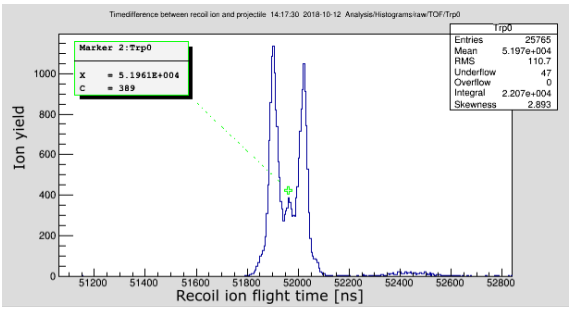

Figure 87: Raw recoil ion TOF spectrum after multi-photon ionization of optically trapped ^{6}Li atoms with fast modulation of trap depth at $I_{fs} = 1.14 \cdot 10^{13} \frac{\mathrm{W}}{\mathrm{cm}^2}$.

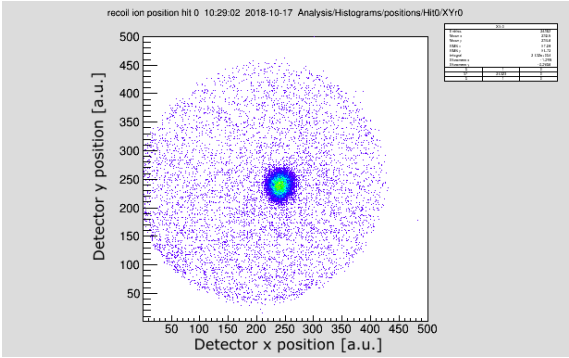

Figure 88: Raw recoil ion position spectrum after multi-photon ionization of optically trapped ^{6}Li atoms with 50 length units corresponding to 1 cm. The polarisation of the fs - laser pulses was along the spectrometer axis, i.e. perpendicular to the plane.

≈ 0.266 a.u.. Furthermore, some of the electrons are ejected with an excess momentum of ≈ 0.4 a.u., which corresponds to above-threshold ionization (ATI), i.e. the already free electron absorbing another photon from the fs field.

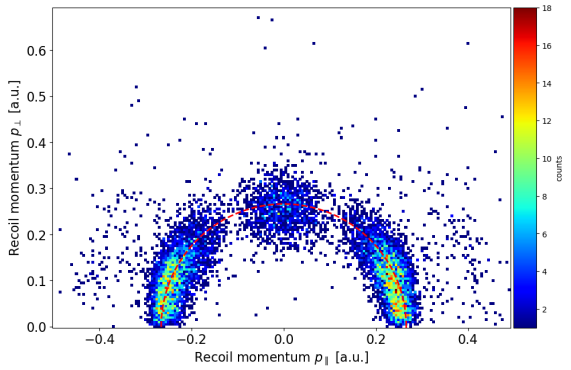

Figure 89: Example $p_\perp$ vs $p_\parallel$ spectrum for recoil ions measured.

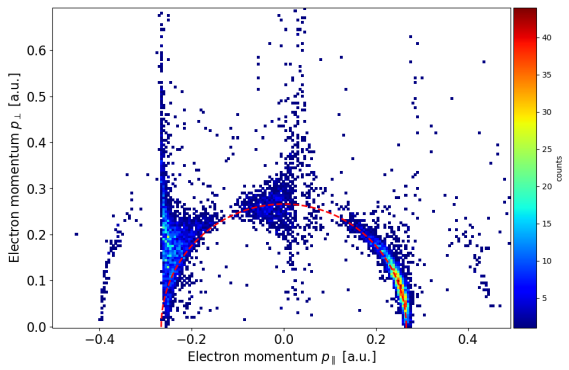

Figure 90: Example $p_\perp$vs p_z spectrum for electrons measured at one value for electric extraction and magnetic guiding field.

The correlation between longitudinal momenta for ions and coincident electrons is shown in Fig. 91, which is basically an illustration of conservation of momentum. In this basic reaction, the momentum of recoil ion and photo-electron is of same magnitude, but opposite direction, since the momentum of the photon can be neglected. The longitudinal momentum resolution of the recoil ions can be estimated as the FWHM of the gaussian distribution obtained by plotting the recoil momentum distribution at a specific electron momentum, e.g. $p_{\parallel,e} = 0$. This yielded an estimate on the longitudinal momentum resolution of 0.107 ± 0.002 a.u. for recoil ions and 0.087 ± 0.002 a.u. for photo electrons. The total momentum resolutions can be extracted by the FWHM width of the circles from Fig. 89 and 90. A total momentum

resolution of 0.055 a.u. and 0.03 a.u. for recoil ions and photo electrons is obtained respectively.

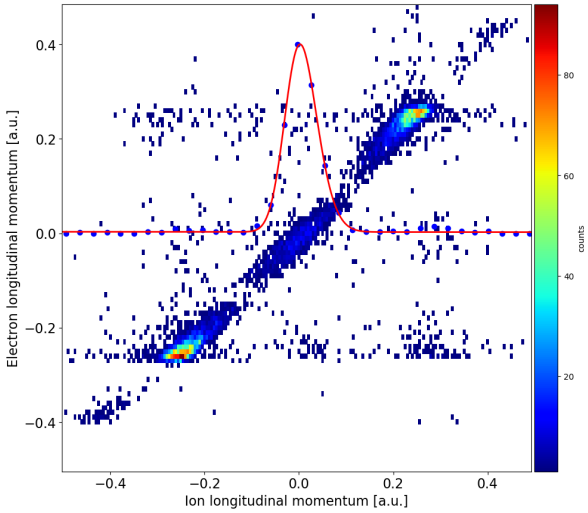

Figure 91: Correlation diagram for the measured longitudinal recoil ion and photo electron momenta for multi-photon ionization of optically trapped ^{6}Li atoms. The white curve corresponds to a cut at $p_{ez} = 0$

12.2 Photoassociative ionization via ladder excitation of magneto-optically trapped ^{6}Li

In a MOT a significant fraction of 20-40% of the atoms is in the excited state, therefore (multi-photon) ionization of magneto-optically trapped ^{6}Li, yields atomic ions with momenta corresponding to ionization from the ground and the excited state. In the experiments, described in this section, we studied the interaction of the fs pulses with colliding atom pairs, where at least one atom is in the first excited state $2P$. As shown in Fig. 92, the fs-pulse induces a $2p \rightarrow 3s$ transition, eventually leading to excitation into the $2p + 3p$ PEC. At small interatomic distance the pair autoionizes into a bound level of the lowest lying $^6Li_2^+$ cation molecular state. The autoionizing state is reached by resonant ladder excitation via atomic states, in which altogether two photons of the MOT beams and one fs photon of the low-energy tail of our fs laser spectrum ($\lambda_0 = 815\,\mathrm{nm}$) are involved.

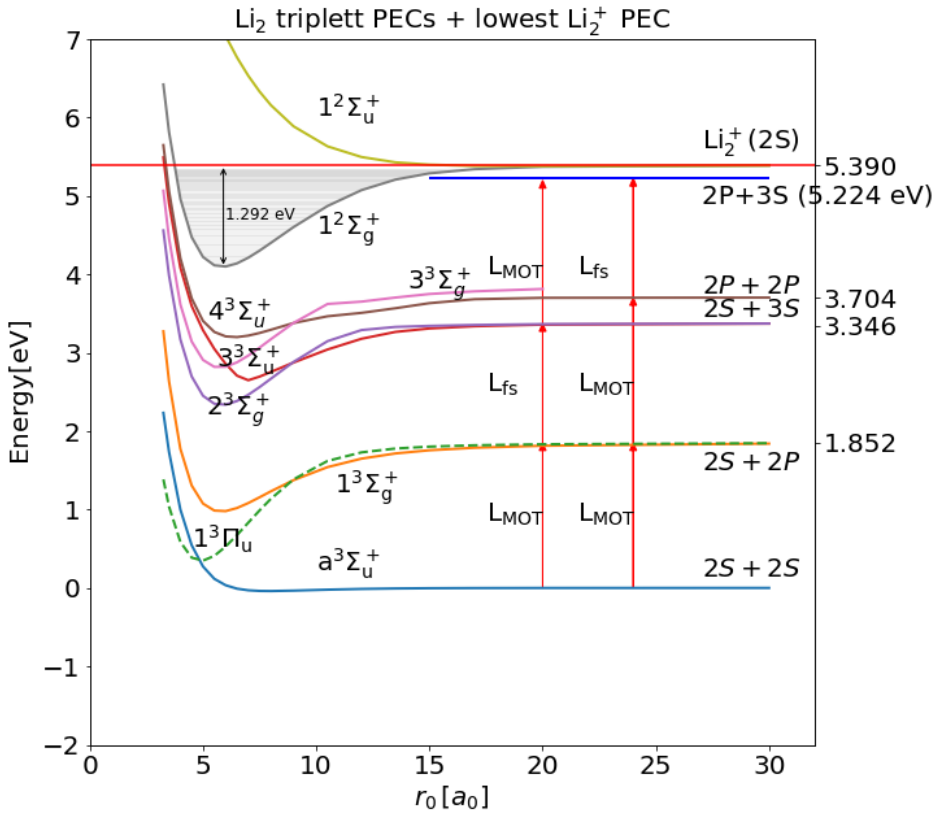

Figure 92: Ladder excitations that lead to formation of molecular ions by curve crossing of the $1^2\Sigma_g^+$ PEC with the $2P + 3S$ PEC.

As result, although the MOT in principle is a purely atomic target, we observe a $^6Li_2^+$ molecular signal (see Fig. 93) by ionization of our magneto-optically trapped target at sufficiently low fs power in order to avoid multi-hit effects and given that the density of the ^{6}Li cloud is sufficiently high. We performed ionization of the magneto-optically trapped target under various condition, in order to corrobate that the molecular signal is due to ladder excitation into an autoionizing state. In the outlined ionization experiments, the magnetic quadrupole field of the MOT was left on, which leads to a distortion of the momentum spectrum, as

outlined in Sec. 1. This distortion is also present in longitudinal direction, therefore the recoil ion momentum distribution in Fig. 93 with longitudinal recoil momenta of up to 0.688 a.u. (kinetic excess energies of 6.44 eV) does not represent the true momentum distribution, but is "stretched" due to the effect of the magnetic quadrupole field.

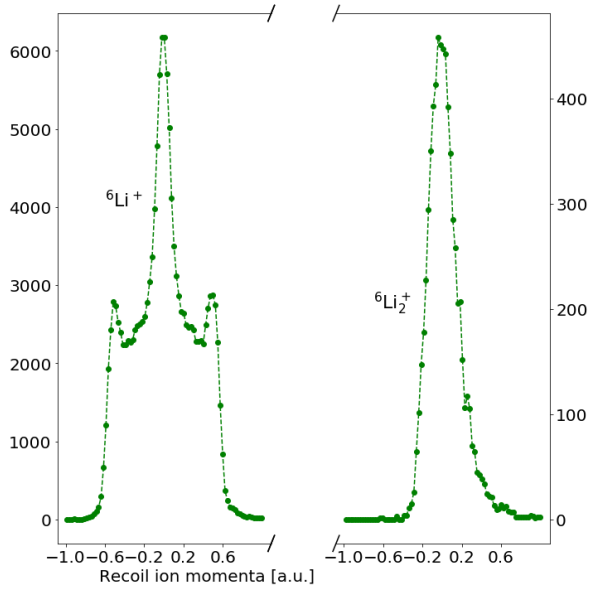

Figure 93: Atomic and molecular ion yield from ionization of magneto-optically trapped target.

Molecular signals from MOTs have also been reported by other groups in ionization experiments with ^{133}Cs and ^{85}Rb MOTs [89, 90, 91, 92]. The dimer formation mechanism in those experiments has been stated to not be completely understood, however the dependence of the dimer formation rate on density and MOT trapping light intensity, as reported in [89, 91, 92] for the ^{133}Cs and ^{85}Rb MOTs respectively, shows that three-body recombination is unlikely to be the dominant dimer formation mechanism. Instead it is suggested that trapping light plays a role in the photoassociation into bound molecular states closely below the $S + P_{3/2}$ asymptote, from where they spontaneously decay to loosely bound vibrational states in the molecular electronic ground state. Thus, in [89, 93, 91, 90] the observed molecular signal was predominantly due to ground-state molecules either in their $X^1\Sigma_g^+$ or $a^3\Sigma_u^+$ potential, from where they are detected by direct photo-ionization. In contrast, the molecular signal observed in our measurements is present only if the fs laser interacts with laser-excited $\mathrm{Li}^*(2p)$ atoms. This was verified by switching off the MOT beams in a small time window several hundreds of nanoseconds before arrival of the fs laser pulse until several hundred nanoseconds after, so that ^{6}Li atoms have sufficient time to relax back into their ground state and the fs laser pulse only finds atoms in their electronic groundstate. As can be seen from Fig. 94, the molecular signal vanishes when the MOT beams are switched off synchronized to the arrival of the fs laser pulse.

Moreover, the asymmetric shape of the $^6Li_2^+$ molecular ion TOF distribution in Fig. 93, is not characteristic for direct photo-ionization, but rather indicates an ionization mechanism, which still can occur a few 10 ns after excitation by the fs-laser corresponding to the lifetime of the $3s$ excited state. Our findings are similar to the molecular signal observed from a ^{85}Rb MOT reported in [92], in which it has been suggested that pairs of atoms are excited via a ladder of a molecular states into a neutral molecular state which autoionizes due to curve

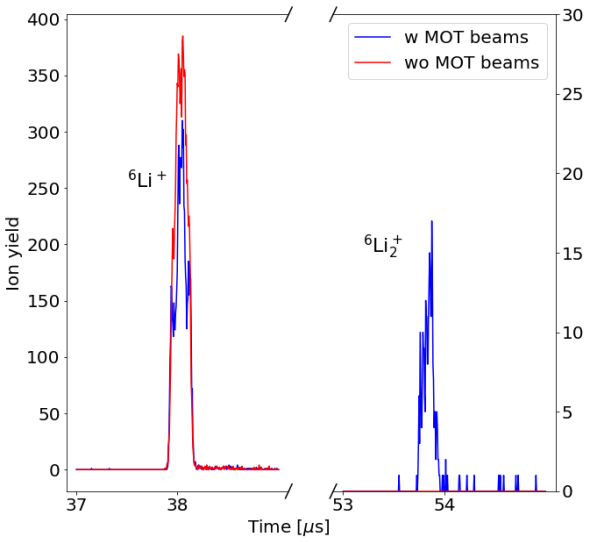

Figure 94: Atomic ion and molecular ion yield with and without MOT beams on during ionization.

crossing with the dissociative curve of a molecular ion, given that the radiative decay time is long enough for the nuclei to approach this curve crossing. In our experiments the following signatures confirm this ionization mechanism. We observed that the molecular ion yield

1. showed a resonance in the photon energy of the fs pulse, for the $2p \rightarrow 3s$ transition
2. as well as a linear dependence on the femtolaser peak intensity, since this is a one photon transition
3. and could be suppressed by the presence of the focused IR beam, when the IR focus was overlapped with the fs focus. This is since Li_2^+ is dissociated.

In order to test the dependence on the photon energy, the spectrum of the fs laser was tuned with a movable slit in the compressor section, effectively realizing a band-pass filter for the spectrum of the femtosecond pulse. For each filtered spectrum, roughly the same fs power was adjusted in order to exclude an effect due to the peak intensity dependence of the ion yield. The result in Fig. 95 shows, that the molecular ion yield exhibits a maximum in the low energy tail of the femto laser spectrum at an energy of roughly 1.52 eV ($\lambda_0 = 815$ nm) at the applied peak intensity, which is within the 2σ interval from the central photon energy.

This corresponds well to the transition energy between $2p$ and $3s$ (compare Fig. 81). Therefore two ^{6}Li$^*(2p)$ atoms end up, by absorption of one fs photon at long range, on the $2p - 3s$ PEC, which exhibits a curve crossing with the lowest $^6Li_2^+$ PEC $1^2\Sigma_g^+$ (see Fig. 92). The first step in this ladder excitation is the absorption of a trapping light photon, so that in the collision of two ground state atoms, one of the atoms is excited into the first excited state $2p$. However a molecular state which is accessed by the trapping light, does not seem to be involved. The molecular ion yield steadily decreases for increasing detunings of the MOT lasers (see Fig. 96), which indicates that at least up to the detuning of about -0.8Γ, no molecular state is accessed. Instead only the density of atoms in the first excited $2p$ state seems to play a role. The maximum of the atomic ion yield at 1.58 eV shown in Fig. 95, on the other hand is due to the fact that from the first excited $2p$ state two photons are enough to excite into the highly excited $6p$ level, therefore realizing REMPI.

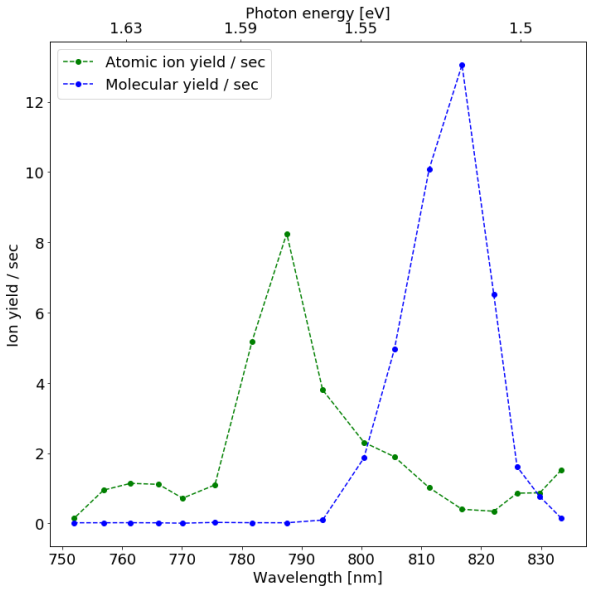

Figure 95: With bandpass filtered spectra of femtolaser pulses compared to the full spectrum.

For the narrowed spectrum with a central photon energy of 1.52 eV, the molecular ion yield has been measured for different femto laser powers (see Fig. 97). The linear dependence shows, that the femto-laser field is involved in the ionization only as an one-photon process.

Another observation is, that the presence of a the focused IR beam, whose focus is overlapped with the fs focus, does suppress the molecular ion yield signal (see Fig. 98), though it enhances the atomic ion yield. The increase in atomic yield is due to delayed ionization of excited states $^6\mathrm{Li}^*(nl)$ via absorption of IR photons. The decrease of the molecular ion yield can be due to absorption of an IR photon which dissociates the molecular cation $^6\mathrm{Li}_2^+$ $1^2\Sigma_g^+$ before it is extracted from the reaction volume and therefore suppresses the cation detection. Energetically all vibrational levels from $\nu' = 28$ to the last vibrational level $\nu' = 57$ [94] can be excited into the dissociative potential energy curve $1^2\Sigma_u^+$ via a dipole-transition by absorption of a 1.16 eV IR photon (see Fig. 92). On the other hand at long range, neither of the atoms on the $2p - 3s$ manifold can directly be ionized by a single IR photon.

In conclusion, the molecular signal measured after ionization of our magneto-optically trapped target, stems from following reaction mechanism, which is illustrated in Fig. 92: In collisions of two excited $\mathrm{Li}^*(2P)$ atoms, one of the atoms is further excited by one 815 nm photon from the fs laser to $\mathrm{Li}^*(3S)$. The summed excitation energy is 5.224 eV and, therefore, above the minimum of the $1^2\Sigma_g^+$ PEC of Li_2^+. The $2p - 3s$ PEC, although its course is not precisely known, must exhibit a curve crossing with the $1^2\Sigma_g^+$ PEC and the state autoionizes into a molecular cation state. As a consequence the right wing of the molecular ion TOF distribution (Fig. 93) exhibits an exponential decay with a time constant of about 21.6 ns, which would correspond to the $3s$ radiative lifetime. The photoelectrons could not be measured directly due to the MOT magnetic field gradient, but the recoil ion momenta in Fig. 93 allow to conclude on the electron energies. If we take into account, that the momentum distribution has to be scaled down, from Fig. 93 the highest longitudinal momenta for the emitted electrons is obtained to be 0.26 a.u.corresponding to an energy of 920 meV. In future experiments, where

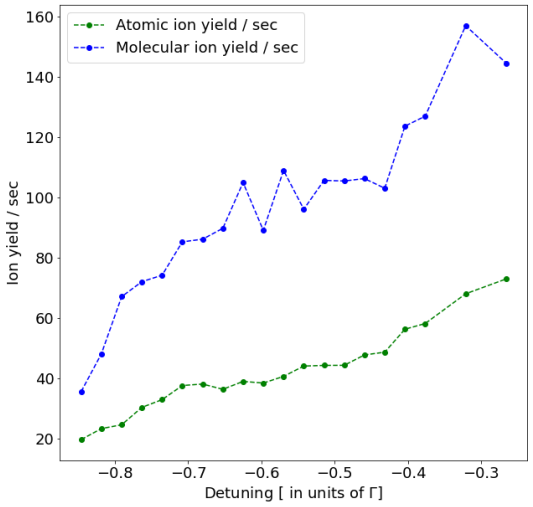

Figure 96: Dependence of atomic and molecular ion yield out of MOT from trapping light detuning.

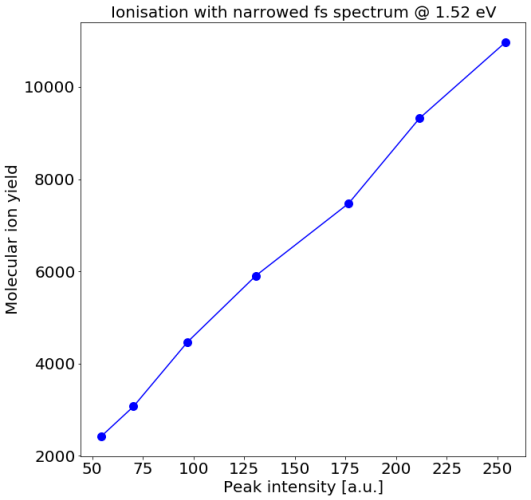

Figure 97: Dependence of molecular ion yield on femto laser intensity.

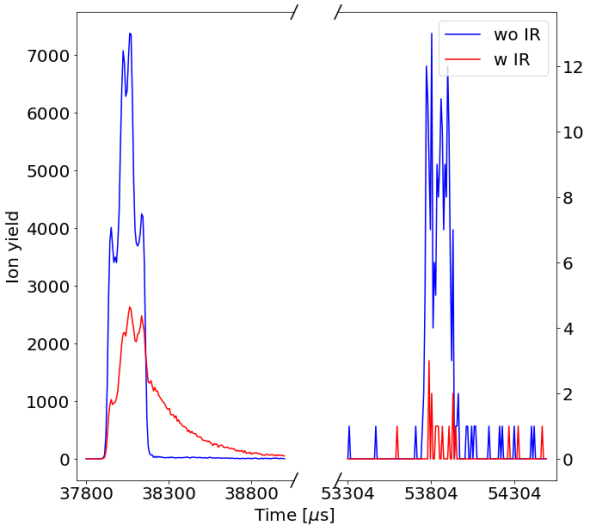

Figure 98: TOF spectrum from ionization of magneto-optically trapped atom (first three hits). The two measurements were taken for the same low fs laser peak intensity, but the second measurement (red) was performed while the IR beam of the dipole trap was switched on and superposed with the focus of the fs beam.

with short pump pulses this process will be induced in the dipole trap, photo electron energies can be measured directly.

12.3 Single-color photoassociation in the MOT

As outlined in Sec. 8, by use of a carefully tuned cw PA laser, we can excite several high lying vibrational states in the $A^1\Sigma_u^+$ or $1^3\Sigma_g^+$ potential energy curves, a part of which will subsequently decay into $^6Li_2$ ground state dimers in the highest lying vibrational state $\nu'' = 9$ of the $a^3\Sigma_u^+$ potential or $\nu'' = 38$ of the $1^1\Sigma_g^+$. In our setup we used a diode laser in Littrow configuration, whose output power was amplified by a tapered amplifier (Toptica TA 100). As shown in Fig. 99, the PA laser was stabilized by locking it with a fast feedback loop on a transmission of a 300 MHz Fabry-Perot cavity. For stabilizing this cavity, the piezo voltage of one of the end mirrors of the cavity in turn was controlled with a slow feedback loop using a scanning cavity lock for which another cavity with 2.4 GHz was continually scanned with a frequency of 30 Hz [95]. The frequency stability of the locked laser was estimated via the slope of the error signal to be around 4 MHz.

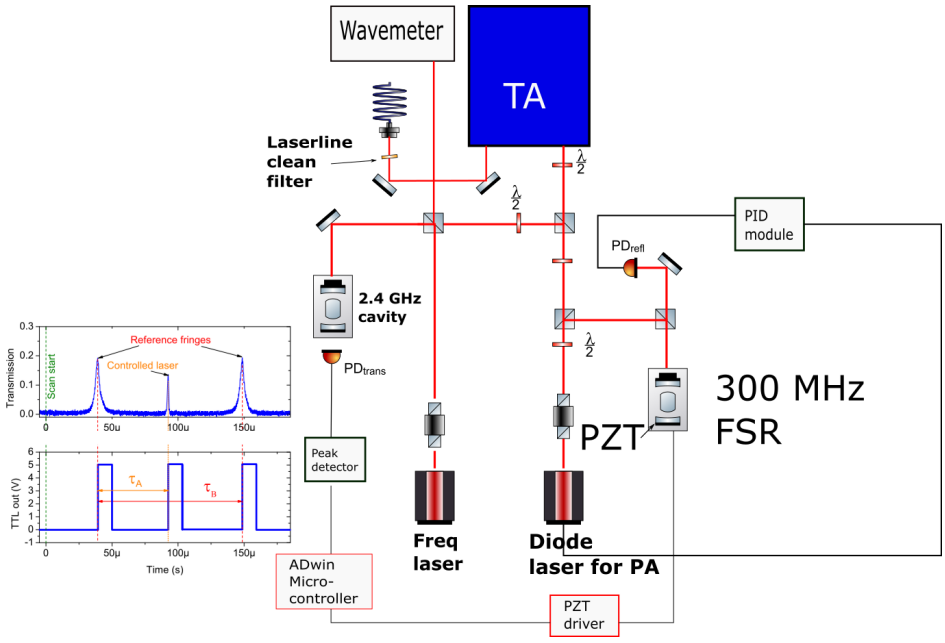

Figure 99: Sketch of setup for PA spectroscopy on the optical table. The diode laser for PA was locked using a slow and a fast feedback loop. With the fast feedback loop, the PA laser was locked onto the transmission of a 300 MHz cavity, which was freely drifting. For long term stability, in a slow feedback loop, the PA laser was locked with respect to a frequency locked laser, using a scanning-cavity lock.

In a first experiment, we aimed to reproduce excitation of highly excited vibrational states in a MOT. Therefore, a collimated PA beam was aligned on the MOT and retroreflected for maximum power density (see Fig. 100). In [63] power densities of $\approx 76\,\frac{\mathrm{W}}{\mathrm{cm}^2}$ were used, while we achieved power densities of up to $258\,\frac{\mathrm{W}}{\mathrm{cm}^2}$.With the available laser power and bandwidth of our PA laser it was possible to excite vibrational levels of the strong $^3\Sigma$ series, but it was not possible to excite those vibrational levels of the weak $^1\Sigma$ series. The tuning range of our diode laser ($\lambda = 670 - 675\,\mathrm{nm}$) only allowed us to excite vibrational levels in the $1^3\Sigma_g^+$ PEC down to $\nu'' = 57$ and $J = 1$. An example loading curve of the atom number in a MOT, where free atoms colliding on $a^3\Sigma_u^+$ were excited into $1^3\Sigma_g^+(\nu'' = 57, J = 1)$ by switching on the PA beam at $t \approx 30\,\mathrm{s}$ is shown in Fig. 101.

In the following we briefly derive the molecular production rate due to PA. The presence of the PA beam causes a reduction in the equilibrium number N_{eq} of the atoms, because the atom number N is now governed by following equation

$$\dot{N} = L - R \cdot N - \beta \cdot N^2,$$

where L is the loading rate of the MOT, R is the one-body loss constant due to collisions with background gas, and β is the effective two-body loss constant for the collisions between ^{6}Li atoms. An analytical solution to this differential equation exists and it yields an equilibrium atom number in the presence of the PA beam of

$$N_{eq,PA} = \frac{-L + L\sqrt{1 + \frac{4\beta N_{eq}}{R}}}{2\beta N_{eq}},$$

which in the case of vanishing two-body loss constant again transitions into N_{eq}. From this equation, we can determine the two-body loss constant as

$$\beta = \frac{L\left(1 - \frac{N_{eq,PA}}{N_{eq}}\right)}{N_{eq,PA}^2}.$$

From the linear rising slope at the beginning of the loading curve (see Fig. 101), we obtain a loading rate of

$$L \approx 2.68 \cdot 10^6/\mathrm{s},$$

while the equilibrium numbers of atoms with and without PA beam are

$$\begin{aligned} N_{eq} &= 6 \cdot 10^7 \\ N_{eq,PA} &= 3.5 \cdot 10^6. \end{aligned}$$

From this we obtain a two-body loss constant of

$$\beta = 9.12 \cdot 10^{-8} \frac{1}{s}.$$

If we multiply the two-body loss constant with the equilibrium number of atom pairs $\frac{N_{eq,PA}(N_{eq,PA}-1)}{2} \approx \frac{N_{eq,PA}^2}{2}$ we obtain the production rate of excited molecules per second as

$$\beta \cdot \frac{N_{eq,PA}^2}{2} \approx 5.6 \cdot 10^5 \,\mathrm{molecules/sec}.$$

Note, that this is an estimate for the equilibrium photoassociation rate, which might be lower, than the initial photoassociation rate, because it depends on the square of the atomic density. In order to obtain the ground state molecules production rate, we have to multiply the photoassociation rate with the branching ratio for the particular excited vibrational level. From $\nu' = 57$ about $\sum_{v''} q_{v'v''} \approx 2.3\,\%$ of the excited molecules decay back into bound ground state [70]. This would result in an equilibrium ground state molecule production rate of

$$\approx 1.28 \,\frac{\mathrm{molecules}}{\mathrm{ms}}.$$

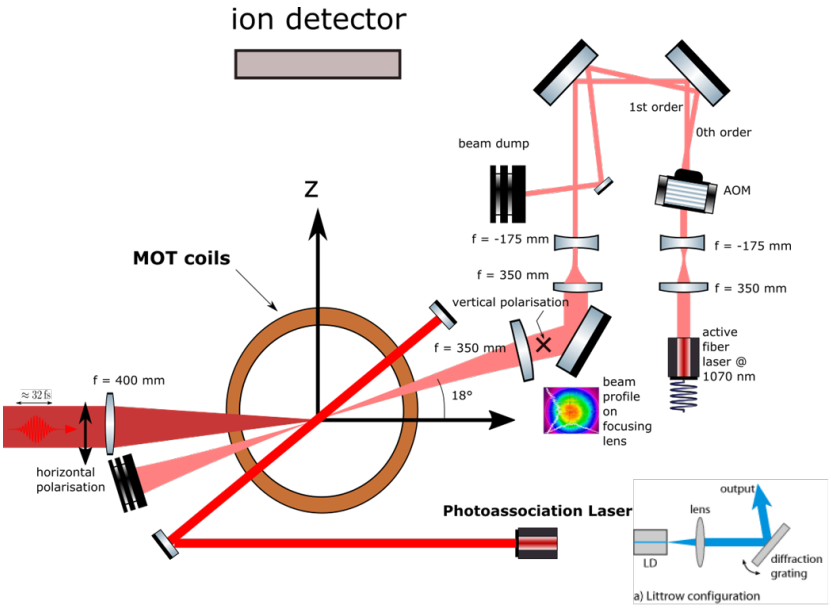

Figure 100: Photoassociation setup used for PA on magneto-optically trapped atoms.

By using Eq. 61, for an assumed initial atomic density of $n \approx 3.8 \cdot 10^{10}/\mathrm{cm}^3$ and a power density of 258 $\frac{\mathrm{W}}{\mathrm{cm}^2}$, we obtain as an estimate for the initial ground state molecule production rate

$$\approx 2.403 \, \frac{\text{molecules}}{\text{ms}}.$$

.

In order to assess, if in presence of the PA beam, a molecular signal becomes visible, that does not stem from autoionizing states, ionization of the magneto-optically trapped target was performed while switching off the MOT beams in a small time window of several hundred nanoseconds width around the arrival of the fs laser pulse. The ionization yields of atomic $^6\mathrm{Li}^+$ ions and molecular $^6\mathrm{Li}_2^+$ ions in such a synchronised MOT were measured with and without presence of the PA beam for different femto laser intensities, as shown in Fig. 102 and 103.

As can be seen from Fig. 102 the atomic yield stays the same with or without presence of a PA beam, however the atomic ion yield is several times larger in the presence of the IR laser responsible for the dipole trap due to delayed ionization of excited $5p/5f$ levels. As can be seen from Fig. 103, the molecular yield of ground state molecules is increased by a factor of roughly 1.5 when the PA beam is switched on as compared to ionization without PA beam. Although, the increase in ground state molecule ionization is modest, it is distinct and this measurement at loading parameters of the MOT is meant to demonstrate, that the presence of a resonant PA beam indeed has an influence on the ground state molecule density. By increasing the density of the atomic sample, it should be able to further enhance the molecular ion signal due to PA. Interestingly in the presence of the IR field, also the molecular ion yield further increases (blue curve in Fig. 103). This is an indication, that the IR laser also interacts with the ground state molecule, yielding molecular ions by delayed ionization from a intermediate excited molecular states.

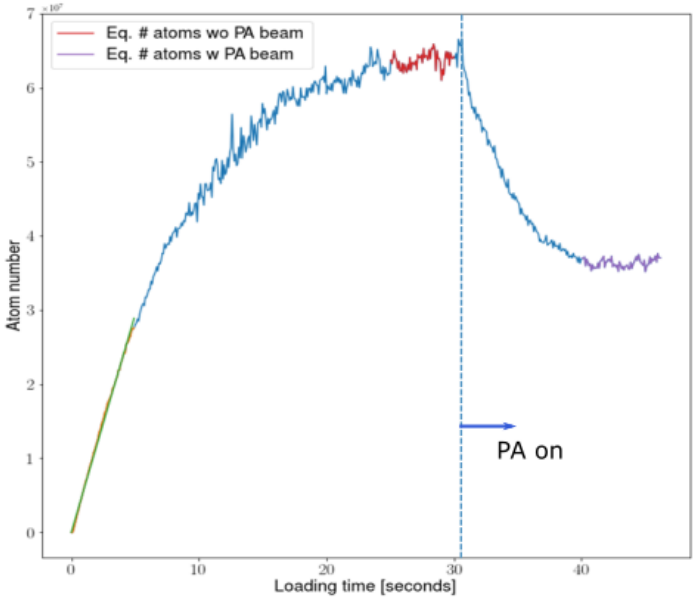

Figure 101: Atom number during MOT loading. At $t > 30\,\mathrm{s}$ the PA beam was switched on, tuned on the $a^3\Sigma_u^+(\nu'' = 57, L = 1)$ resonance at 674.560 nm.

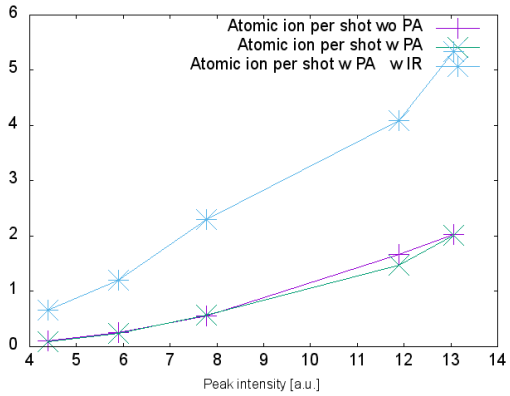

Figure 102: Atomic $^6Li^+$ yield per shot for ionization out of the synchronised MOT with varying peak intensity of the fs-laser.

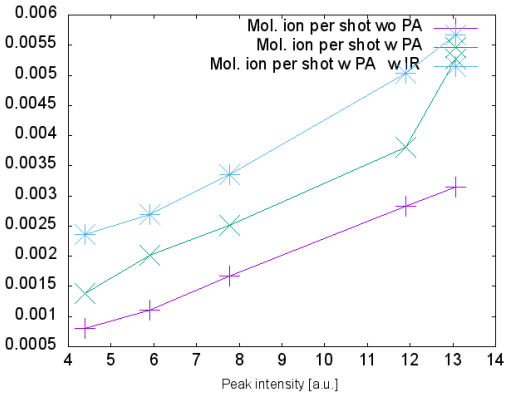

Figure 103: Molecular $^6Li_2^+$ yield per shot for ionization out of a synchronised MOT with varying peak intensity of the fs laser.

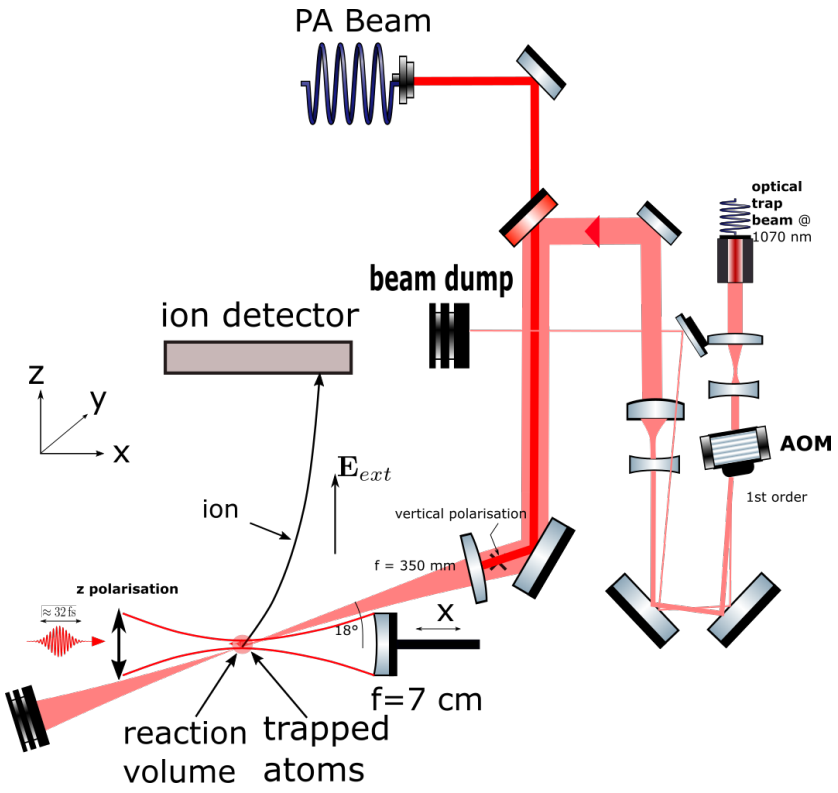

Figure 104: Experimental configuration 1 for PA spectroscopy on an optically trapped thermal gas of ^{6}Li atoms.

12.4 Single-color photoassociation in the optical dipole trap

PA spectroscopy was performed on optically-trapped, thermal gas of ^{6}Li atoms at a temperature of $\approx 370\,\mu$K with the aim of producing ground state molecules that remain trapped in the dipole trap in order to be detected by multi-photon ionization (see Sec. 8.1). The experimental configuration used for PA spectroscopy in our dipole trap is sketched in Fig. 104, in which the PA beam was sent colinearly with the IR beam, so that it was focused by the same lens which focuses the IR trapping beam. The PA beam was transported by an optical fiber and superposed with the help of a dichroic mirror with the beam path of the optical trap beam. The optimum overlap was determined by coupling simultaneously a resonant pushing beam into the fiber and finding the alignment for which atoms are pushed out of the dipole trap most efficiently. The available PA power out of the optical fiber amounted to up to 150 mW. With an assumed beam waist at the focus of $w_0 \approx 40\,\mu$m, we can achieve peak power densities of up to $3\,\frac{\mathrm{kW}}{\mathrm{cm}^2}$ in the dipole trap.

Once the PA resonances were found, by scanning the frequency of the PA laser in the vincinity of the transition energies of high lying vibrational states $\nu' = 56 - 85$ listed in [63], we mainly focused in the triplet system on the vibrational level $1^3\Sigma_u^+(\nu' = 57)$ at ≈ 674.560 nm and in the singlet system on the vibrational level $A^1\Sigma_u^+(\nu' = 65)$ at 674.482 nm. Examples for loss spectra of a dipole trapped gas of ^{6}Li are shown in Fig. 106 and Fig. 105. In these spectra, the atom number in arbitrary units after exposure to a PA beam for up to 2 s is plotted against the binding energy of the excited molecule. There are gaps in the spectra, because the scanning offset lock of the PA laser, does not allow to scan over the full free spectral range of the short

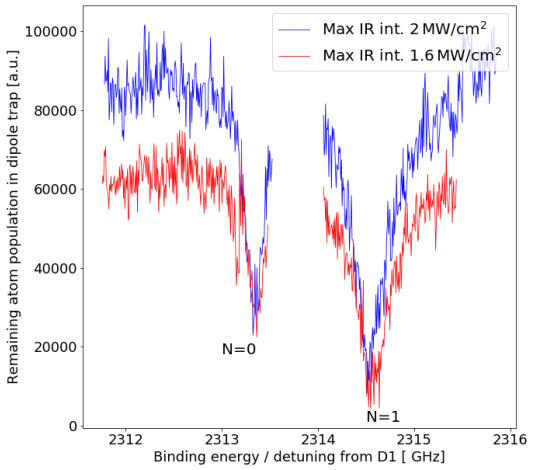

Figure 105: Example trap loss spectra as function of PA laser frequency in the optical trap at the $A^1\Sigma_u^+(\nu = 65)$ resonance. The two different feature about 1.2 GHz apart can be attributed to different rotational levels of the final state. The red trace exhibits an artefact on the left side of the left dip.

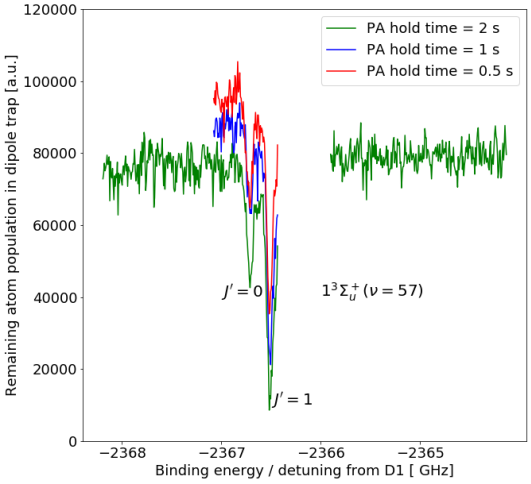

Figure 106: Example trap loss spectra as a function of PA laser frequency in an optical dipole trap while scanning over the $1^3\Sigma_g^+(\nu = 57)$ resonance. The different features about 0.25 GHz apart is attributed to a splitting of the energy due to spin-rotation coupling.

2.4 GHz cavity. Note, that the binding energies of $1^3\Sigma_u^+(\nu' = 57)$ and $A^1\Sigma_u^+(\nu' = 65)$ are given in [63] as 2363.63 GHz and 2312.43 GHz respectively. The precision for the determination of the location of PA resonances of our experiment is limited due to our wavemeter to roughly ± 1 GHz, however determination of binding energies is also not our focus and the precison of the wavemeter is sufficient to determine the right FSR of the respective PA transition.

During the experiments, roughly $4 \cdot 10^5$ atoms were loaded into our dipole trap at an initial peak density of up to $5 \cdot 10^{11}/\text{cm}^3$. In Tab. 4 are listed again the branching ratios and the total number of groundstates molecule, which will form in the dipole trap at each resonance respectively.

	Excited state	
	$a^3\Sigma_u^+(\nu' = 57, J' = 1)$	$1^1\Sigma_u^+(\nu' = 65, N = 1)$
Fraction of decays from excited state into ground-state molecules	2.29 %	7.38%
Total number of ground state molecules	9160	28520

Table 4: Branching ratios and expected number of ground state molecules for PA resonances adressed in experiment.

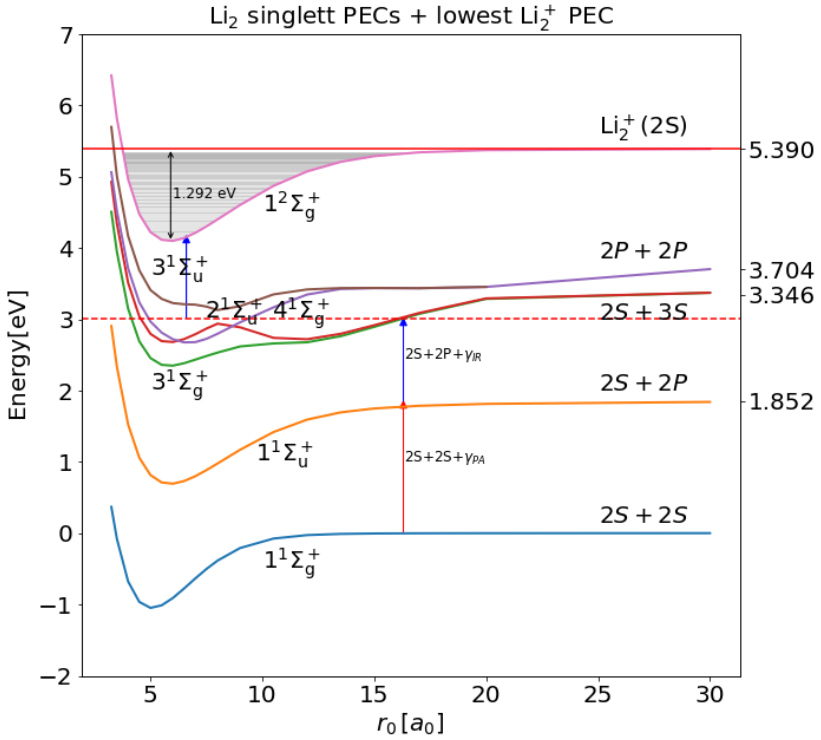

Figure 107: Stepwise ionization in singlet system of ^{6}Li, where a real intermediate level is available in the $3^1\Sigma_g^+(2S+3S)$ PEC widthin the bandwidth of the IR laser.

12.5 Photoassociation and subsequent stepwise excitation and ionization

In the singlet system of ^{6}Li, an ionization process was discovered, that produces molecular ions only by presence of the resonant PA laser and the IR trapping laser. Excited state molecules $1^1\Sigma_u^+(\nu'=65)$, which are produced in the dipole trap, absorb an IR photon at long range, so that they get excited into a molecular state of the $3^1\Sigma_g^+(2S+3S)$ PEC. The atoms then have time to approach each other to the Condon point at $R_C = 9.876\,a_0$, until a second IR photon can ionize the $3^1\Sigma_g^+(2S+3S)$ molecular state. The energy of the second IR photon is barely sufficient to populate $\nu=1$ and $\nu=0$ of the cation groundstate $1^2\Sigma_g^+$.

Since this ionization process is continuous and does not require any fs pulse, we don't have a time stamp available for the time of birth of the ions. However, since the flight time of recoil ions in our spectrometer is much larger (a few tens of microsecons) compared to the flight time of the electrons (a few hundred nanoseconds), we can obtain an approximate flight time of the ions by taking the arrival time of the coincident electrons as a time stamp. With this time stamp, we could approximately determine the transversal ion momenta of this ionization process and as can be seen from Fig. 109, they are extremly small with a maximum energy for the photo-electrons of about 80 meV. This is about consistent with the fact that the three-step excitation only reaches the lowest two vibrational levels of $Li_2^+ 1^1\Sigma_g^+$ and at most about 50 meVexcess energy is available for the photoelectron. The vibrational energies are $E_\nu(Li_2^+) = 4.11\,\text{eV} + \nu \cdot 0.032\,\text{eV}$ compared to the sum of the photon energies $E(\gamma_{PA})+2E(\gamma_{IR}) = 4.16\,\text{eV}$. The arrival times of coincident electrons also allowed to measure the continuous molecular ion yield as a function of the detuning of the PA laser from the $1^1\Sigma_u^+(\nu'=65)$ resonance (see Fig. 108). The resonant behaviour and the observation that

this ionization mechanism also occurs from neighboring vibrational levels of $1^1\Sigma_u^+$ confirms that a stepwise process via the intermediate PA excited state is responsible for the Li_2^+ yield.

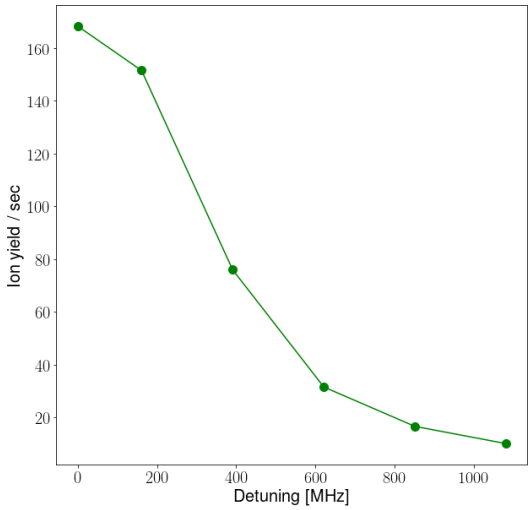

Figure 108: Dependence of continuous ionization rate of molecular ions from PA laser detuning from $A^1\Sigma_u(\nu = 65)$ resonance.

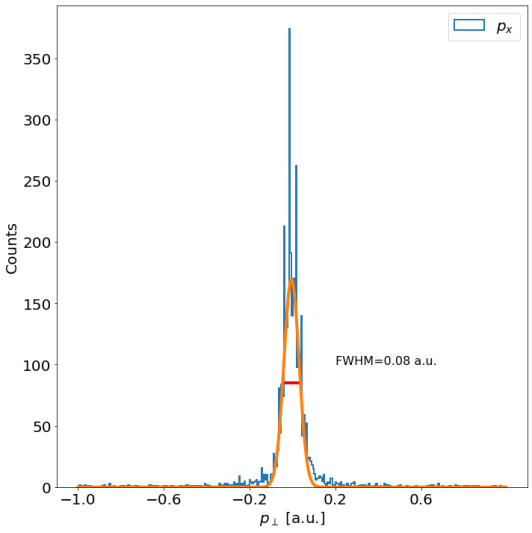

Figure 109: $p_{x,\perp}$ distribution from recoil ions for continuous ionization with PA on resonance with $1^1\Sigma_u^+(\nu' = 65)$

This process of stepwise excitation and ionization takes place resonantly in the singlet system, but not in the triplet system. In the triplet system, starting from close to the $2S+2P$ asymptote, the next possible $\Sigma - \Sigma$ transition with an IR photon would be to $3^3\Sigma_u^+(2S+3S)$ (see Fig. 110) at a Condon point of about $10.5\,a_0$. At this distance the excited state wave function is already oscillating quite fast, which might lead to an unfavorable Franck-Condon factor.

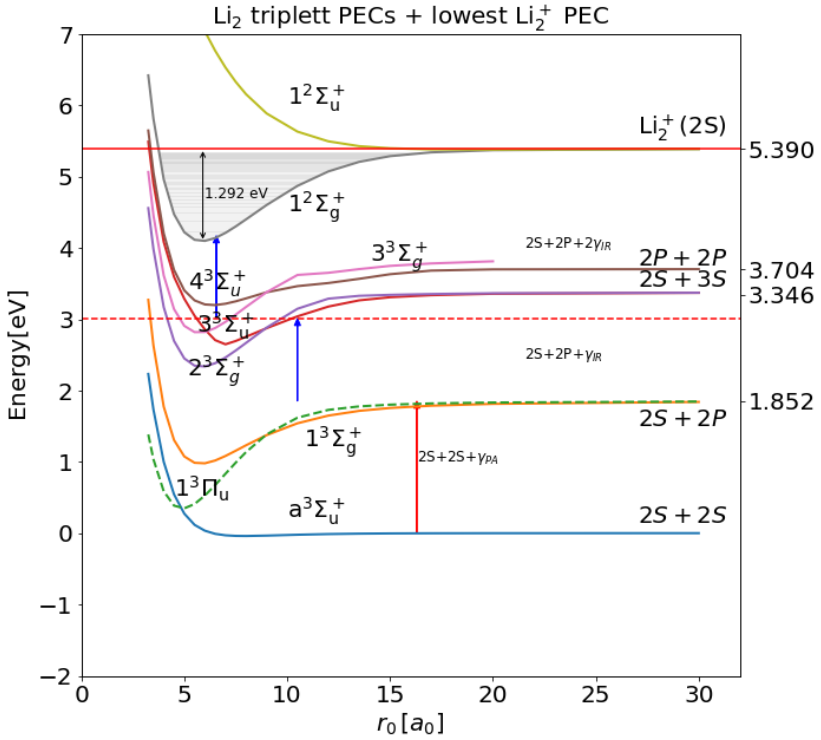

Figure 110: Alternative path for step wise ionization in triplet system, where the only possible transition is at close range via an intermediate state of $3^3\Sigma_u^+(\mathrm{Li}_2^*)$.

12.6 Photoionization of photoassociated Li_2 ground state molecules

After succesfully implementing single-color PA spectroscopy in the dipole trap, we performed ionization of the optically trapped ground state molecules by MPI with fs photons as shown in Fig. 111 for the singlet system. In a first simple type of experiment, the exposure of the optically trapped atoms to the PA light started at the same time, as the exposure to the fs laser pulses. In order to not influence the PA process, the fs power was adjusted low enough, so that the ionization rate does not essentially reduce the atom number during the PA irradiation time. Therefore, the femtolaser pulses were "probing" the ^{6}Li gas composition, while the PA beam was producing ground-state molecules.

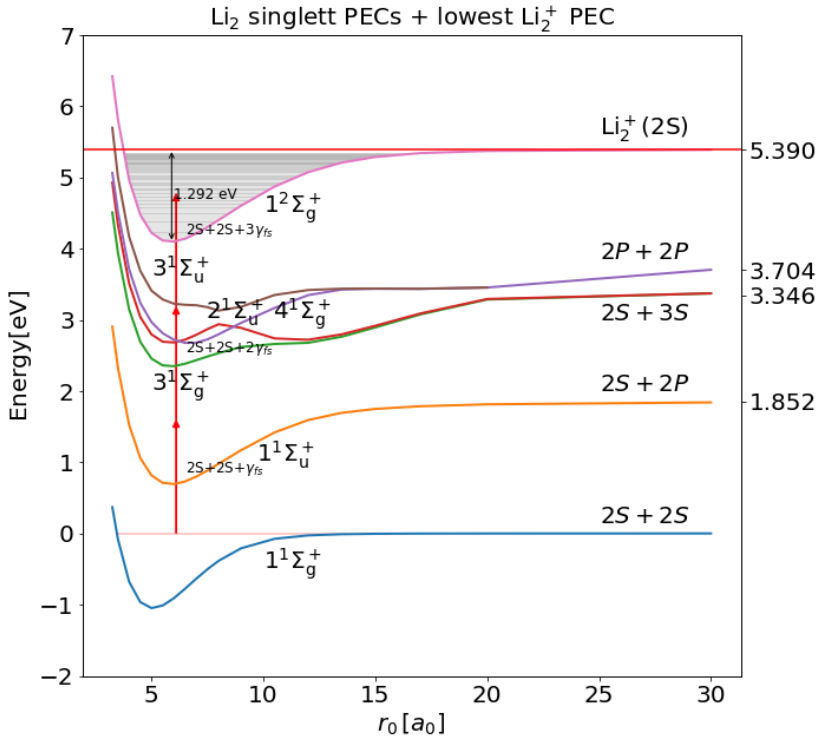

Figure 111: Direct multi-photon ionization of ground state molecules produced by photo-association.

This type of ionization experiment was performed in two different setups for the PA beam. The first setup is the same as that used for the PA spectroscopy, shown in Fig. 104, where the PA beam is superimposed and sent colinearly with the optical trap beam. In the second setup, shown in Fig. 120, the PA beam was sent colinearly with the fs beam and therefore both were focused by the same spherical mirror. As a consequence, we could overlap both foci, the PA focus and the fs focus, perfectly. The strong focus of the PA beam at 675 nm should constitute a micro-dipole trap for the molecules with a similar trap depth as the macro-dipole trap and the molecules, which are associated in the focus, might stay trapped there and therefore lead to a local increase in molecule density in the fs focus. In both setups we performed ionization while the PA laser was resonant with the singlet and the triplet resonance. However, we were only able to see a molecular signal and coincidentally detect molecular ions and photo-electrons for the singlet resonance. An example of such recoil-ion photoelectron flight-time coincidence diagram is shown in Fig. 112. Li^+ and Li_2^+ ions are found at 37 μs and 52 μs respectively. The

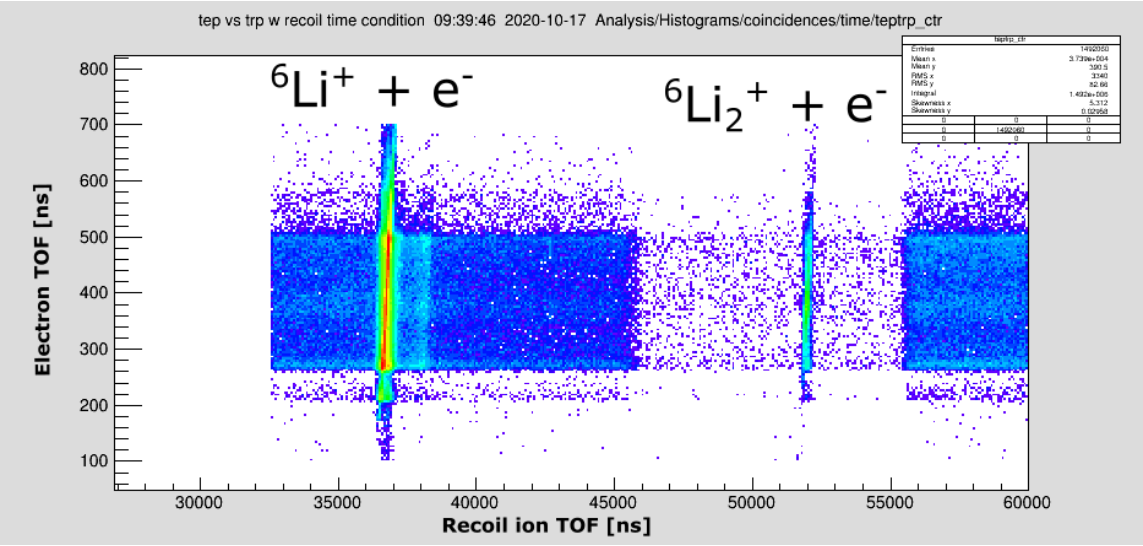

Figure 112: Recoil ion - photo electron coincidences measured in setup 1, when the PA laser was resonant with $A^1\Sigma_u^+(\nu = 65)$.

background counts all stem from the continuous stepwise ionization mechanism discussed in Sec. 12.5. In order to eliminate this background signal and to exclude the possibility, that the fs laser ionizes excited state molecules, the PA laser was switched off in a time window of 10 μs width around arrival of the fs pulse. $A^1\Sigma_u^+(\nu = 65)$ molecules have a radiative lifetime of $\approx$ 13.5 ns [67], so after this switch off delay, all excited molecules have decayed. In Fig. 112 the time window without PA laser shows up as a background free region from 45.5 μs to 55.5 μs which contains the Li_2^+ ions produced by the fs-laser pulses.

Momentum spectra of molecules after ionization in setup 1 are shown in Fig. 113 and 114. In the ionization experiment of Fig. 113, the IR field is present all the time. This leads to false coincidences of electrons coming from delayed IR ionization of ^{6}Li atoms and femtolaser ionized $^6Li_2$ molecules. Therefore, in the ionization experiment in Fig. 114, the IR beam was switched off in a small time window of about 500 ns around the arrival of the fs pulse and there are much less fake coincidences. In Fig. 115 the distribution of total photoelectron momenta from atoms and molecules from the experiment, in which the IR laser was switched, are compared.

From the groundstate PEC $1^1\Sigma_g^+$ the energy of three fs laser photons is sufficient to ionize the molecule in a vibrational state of $1^2\Sigma_g^+(\nu' = 23)$. Since the electron can take away a variable amount of excess energy, in principle also lower vibrational states could be populated with the excess energy carried away by the photo electron as high as 0.67 eV. The energy spectrum of the photo electron of the measurement in Fig. 116 however shows, that the electron excess energy stays well below 100 meV with an exponential decay towards this value.

In order to see the influence of the IR field on the molecules without the effect of delayed IR ionization of atoms producing fake coincidences, in one mesurement a different approach was chosen. The spectrum of the femto laser was filtered to a small region around 793 nm, so that, given the ponderomotive level shift is negligible, no excited states are populated. This means the summed energy of three photons is 4.71 $\pm$ 0.02 eV and therefore centered between $4f$ and $5f$, as well as between $4p$ and $5p$. The corresponding momentum spectrum of the electrons is shown in Fig. 117 and it is clearly seen that the main intensity lies at a

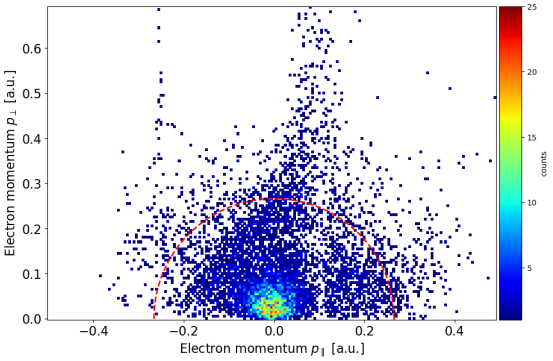

Figure 113: $p_\perp$ vs $p_\parallel$ momentum spectrum of photoelectrons from fs laser ionized $^6Li_2$ molecules in presence of IR field.

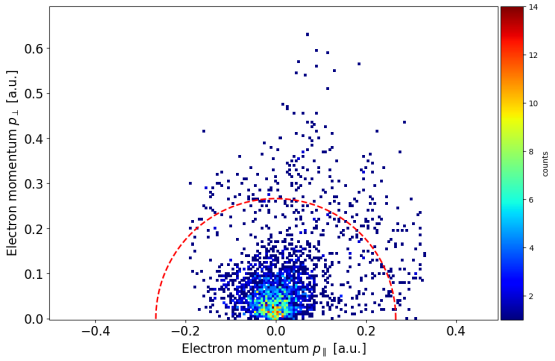

Figure 114: $p_\perp$ vs $p_\parallel$ momentum spectrum of photo electrons from fs laser ionized $^6Li_2$ molecules with IR field switched off.

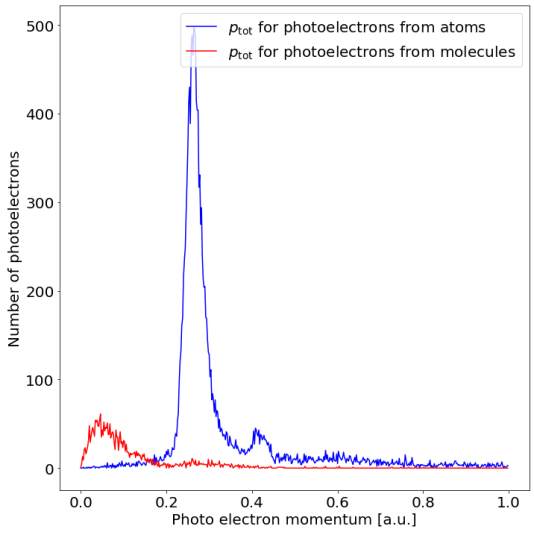

Figure 115: Comparison of distribution of total photoelectron momenta of atoms and molecules for ionisation experiment in Fig. 114, in which IR laser was switched off.

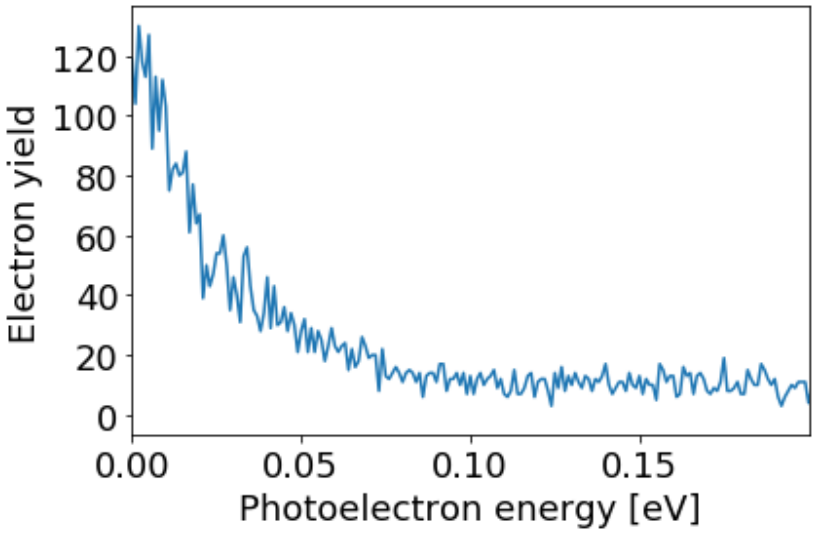

Figure 116: Energy distribution of photoelectrons coming from ionized $1^1\Sigma_g^+$ molecules.

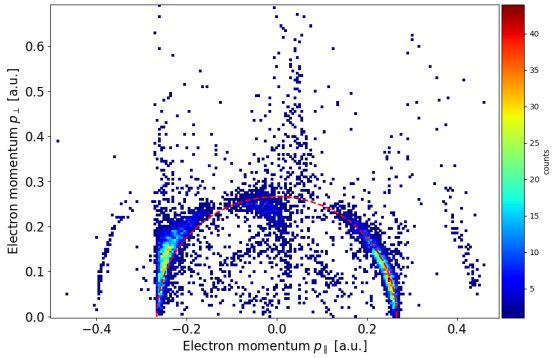

Figure 117: Photoelectron momentum spectrum for electrons coming from atoms after ionization with four fs photons of energy $1.57 \pm 0.007\,\mathrm{eV}$.

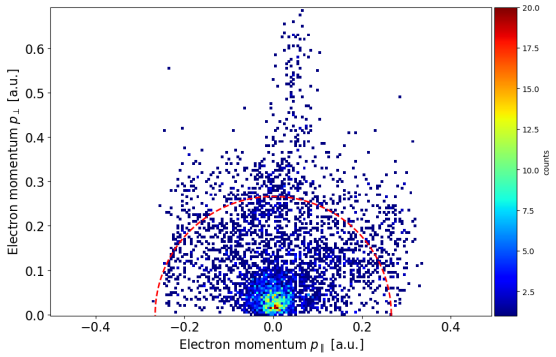

Figure 118: Photoelectron momentum spectrum for electrons coming from molecules after ionization with three fs photons of energy $1.57 \pm 0.007\,\mathrm{eV}$.

momentum of 0.26 a.u.. The excess energy is closest to the excess energy, we would expect at low intensity for MPI. Also, there are no signs of delayed IR ionization, which means no false coincidences due to delayed IR ionization should show up in the photoelectron momentum spectrum for electrons coming from molecules. As seen from Fig. 118, in this experiment the momentum range between 0.1 a.u and 0.2 a.u. is still filled with events, that stem from delayed IR ionization of excited molecules. A ground state molecule $1^1\Sigma_g^+(\nu'' = 38)$ can, by absorption of two femtolaser photons, be excited into an intermediate molecular level of $3^1\Sigma_g^+$, from where it can be ionized again by absorption of one IR photon.

Due to the fact that the continuous ionization rate due to the PA and IR lasers is the dominant contribution to molecular ion production, it reflects the photoassociation rate in our dipole trap. The ionization rate due to fs ionization of ground state molecules on the other side reflects the density of ground state molecules. By plotting molecular ionization events due to continuous and fs ionization as a function of time, we obtain interesting insights into the

photoassociation dynamics. In Fig. 119 the molecular ionization events due to these two events are plotted for the first 500 ms of ionization time. It can be seen that the photoassociation rate is immediately high after start of exposure and thereafter steadily decreases, while the fs ionization rate of ground state molecules slowly builds up until it reaches a maximum at about 28 ms, after which it also decreases steadily. If the molecules weren't trapped in the dipole trap, they would leave the dipole trap on a time scale of 3 ms due to gravity. The slow build-up of the ionization rate due to fs laser ionized molecules, however shows that the molecule density increases because they remain trapped.

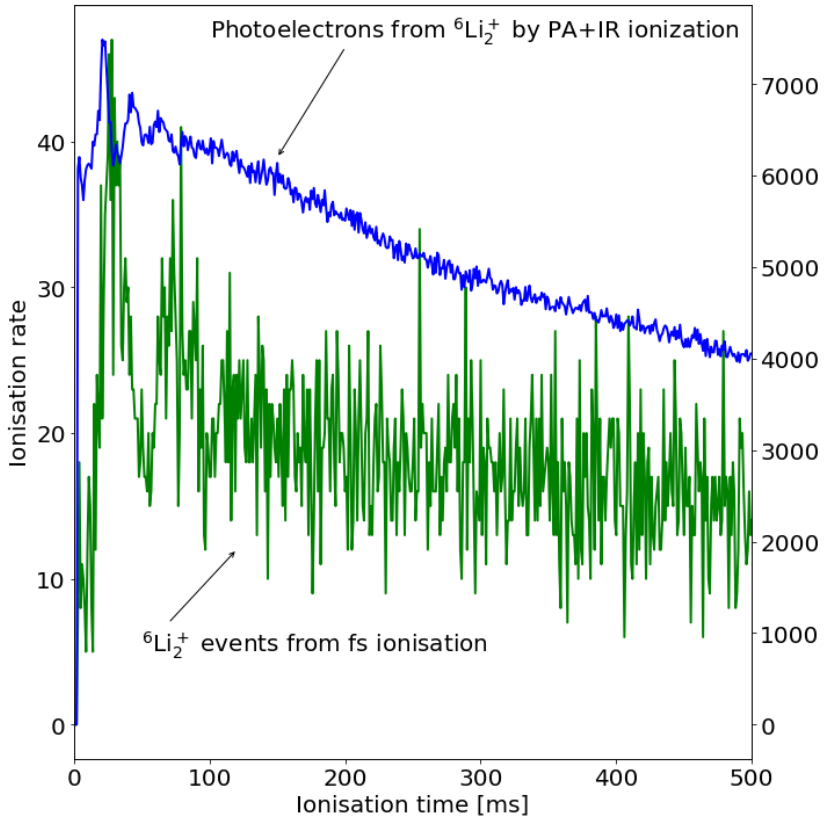

Figure 119: ionization events due to continuous ionization PA+IR and fs ionization of molecules as a function of ionization time.

Ionization of singlet ground state molecules was also performed in setup 2 (see Fig. 120), where it was also chosen to not switch off the IR laser beam, since the PA/fs focus was moved out of the IR focus. Yet again, the PA laser was switched off synchronized to the arrival of the fs pulses with the only difference being, that the time window was chosen much narrower in order to maintain a trapping effect due to the micro dipole trap. Still the PA beam was switched off roughly > 500 ns before arrival of the fs pulse, therefore leaving sufficient time for all excited molecules to decay.

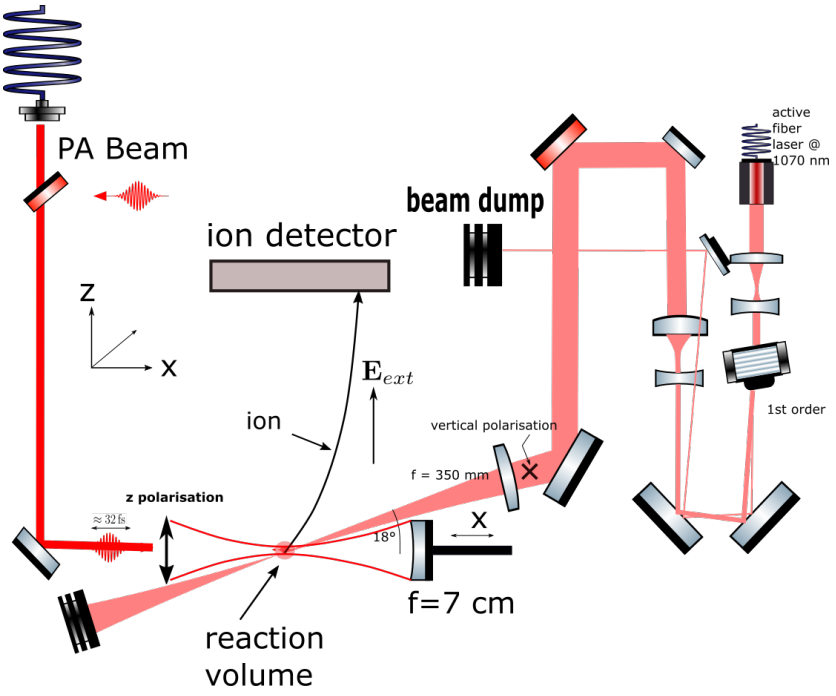

Figure 120: Sketch of experimental configuration 2, where the PA focus and fs focus were overlapped.

Atomic ion and molecular photoelectron momentum spectra measured in this setup are shown in Fig. 121 and 122. Again false coincidences are visible as an outer ring at 0.2 a.u. in the momentum spectrum of photoelectrons from molecules. These spectra confirm the picture of the measurements in setup 2, that the photo electron excess energy is small, because mostly vibrational levels around $\nu' = 23$ in of $1^2\Sigma_g^+$ are populated.

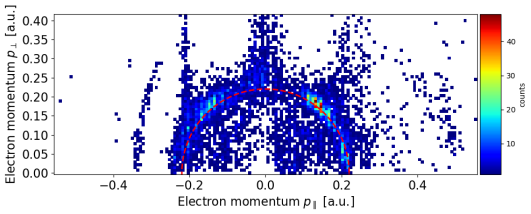

Figure 121: Electron momentum spectrum $p_\perp$ vs $p_\parallel$ for femtolaser ionized ^{6}Li atoms at a peak intensity of $\approx 9 \cdot 10^{11} \frac{\mathrm{W}}{\mathrm{cm}^2}$.

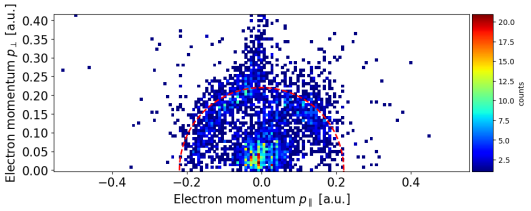

Figure 122: Electron momentum spectrum for femto-laser ionized $^6Li_2$ singlet molecules. The outer ring is due to fake coincidences with atomic ionisation.

The ionization rate of molecules by the fs laser was relatively slow, on average only 2.02 molecules/s are ionized by the fs pulse, and it depends on a proper positioning of the PA/fs focus with the IR focus. The distance between the two foci can be varied by moving the spherical focusing mirror inside the chamber, which is mounted on a manipulator. In Fig. 123, it is shown that the ionization rate of fs laser ionized molecules and the continuous PA+IR ionized molecules is lowest when the PA focus is directly overlapped with the atom cloud, while the atomic ion yield by fs ionization is of course highest. As the PA focus is

farer displaced from the IR focus, a greater fraction of ^{6}Li atoms is illuminated, which is why the PA+IR ionization rate increases. The fs laser ionised molecules rate first increases too, but reaches a maximum when both PA and IR foci are roughly 300 μm apart, after which it slowly decreases again. This supports the interpretation, that the PA focus constitutes a micro-dipole trap for the molecules, since it was outlined by Krüger et.al. [96], that in order to have the highest loading efficiency from (in our case) the macro-dipole-trap into the micro dipole trap, their trap centers have to be displaced by an optimum amount, given by

$$\mathrm{z}{=}\pm z_R\sqrt{\frac{1}{e}\frac{U_0}{2.5k_BT_{macrotrap}}-1},$$

where $z_R = \pi\frac{w_0^2}{\lambda}$ is the Rayleigh length of our PA focus, $T_{macrotrap}$ is the temperature of the atoms in the macro dipole trap and U_0 the trap depth of the micro-dipole trap.

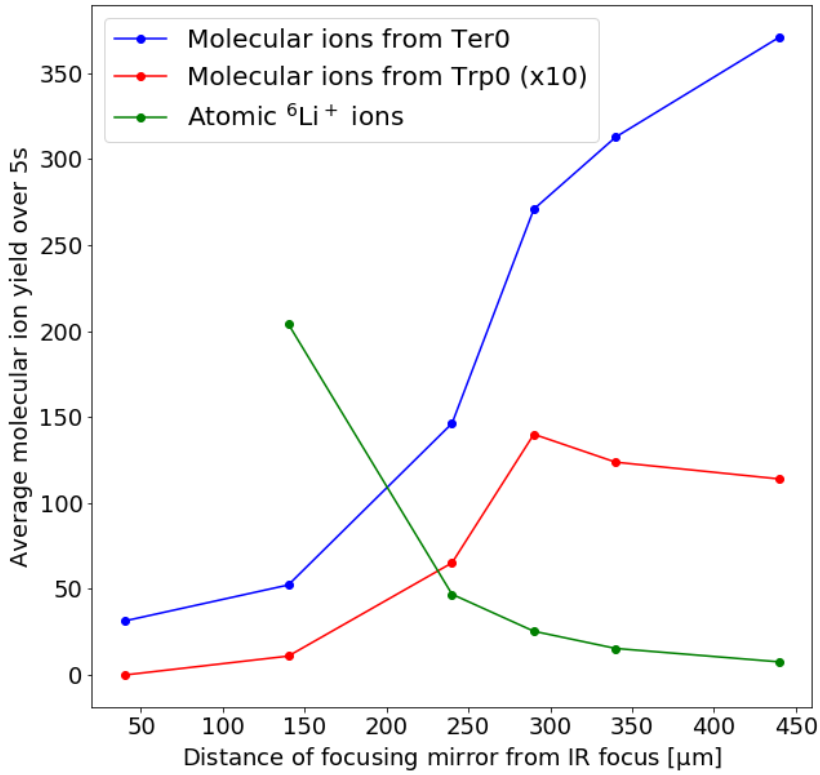

Figure 123: Comparison of three different ionization rates, atomic (green) ions and molecular (red) ions from fs ionization, and molecular ions from PA+IR ionization (blue), as a function of displacement of PA focus with respect to IR focus.

In both experimental setups we could observe a molecular signal in the singlet system, but not in the triplet system. The probability of detecting a ground state molecule by absorption of three fs laser photons depends on one hand on the density of ground state molecules, and on the other hand on the ionization probability. As outlined in Sec. 12.4, in the singlet system, we should obtain a molecule density, which is one order of magnitude higher than in the triplet system. Furthermore the ionization probability depends on the the overlap between the wavefunction of the highest vibrational state $a^3\Sigma_u^+(\nu''=9)$ and $1^1\Sigma_g^+(\nu''=38)$ respectively with the wavefunctions of the vibrational states in the cation PEC $1^2\Sigma_g^+$. The

singlet ground state molecule PEC has a trap depth comparable to the cation $^6Li_2^+$ PEC $1^1\Sigma_g^+(\nu'' = 38)$, while the triplet potential is very shallow. Therefore intuitively, the Franck Condon factors between the molecular wavefunctions of the singlet PEC and the cation PEC should be higher than those between the wavefunctions of the triplet PEC and the cation PEC, which is also confirmed by a qualitative calculation of the Franck-Condon factors in Fig. 124. The result of this calculation is, those vibrational levels in the energy range of the final state after absorption of three fs photons around $\nu' = 23$ have a much higher Franck-Condon factor in the singlet system, that in the triplet system. For $\nu' = 23$ e.g. in this calculation it is obtained $\frac{q_{singlett}}{q_{triplett}} \approx 63$. With the result from Fig. 122, that electrons do not have high excess energies and therefore mostly vibrational levels around $\nu' = 23$ are getting populated, this is an indication that the poorer Franck-Condon overlap is a factor in the question, why we don't detect a molecular signal in the triplet system.

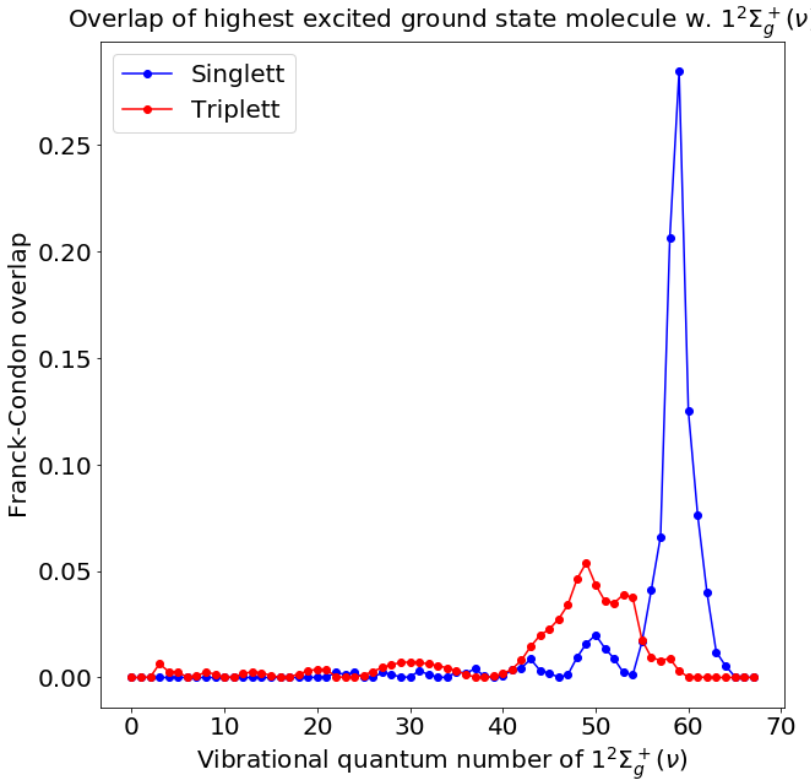

Figure 124: Calculated Franck-Condon overlap using the Numerov method with interpolated potentials for $a^3\Sigma_u^+$, $X^1\Sigma_g^+$, and $1^2\Sigma_g^+$ from values given in [94]. Note this is only a qualitative calculation, since according to [94], $1^2\Sigma_g^+$ only has 58 vibrational levels, not 69 level as was the outcome with the interpolated potentials.

12.7 Coherent two-color photoassociation in a dipole trap

A step into the direction of coherent two-color photoassociation was made, by employing a second, independent dye laser as a Raman laser. The motivation for these experiments was an expected enhancement in the molecule formation rate in the triplet system by two orders of magnitude [97]. The idea behind this is, that while the PA laser excites from the initial state $|i\rangle$ of two freely colliding atoms into an excited molecule state $|e\rangle$, the Raman laser drives Rabi oscillations between the ground state molecule $|g\rangle$ and the excited state molecule $|e\rangle$ (see Fig. 125). The concrete realization of the three level Raman scheme in the triplet system of ^{6}Li is shown in Fig. 126. In this case, the eigenstates of the system are dressed states, which have equal contributions from the molecular ground state and from the excited state. Therefore the groundstate molecule formation rate is obtained, not by multiplying the photoassociation rate with the branching ratio, but simply as half of the photoassociation rate.

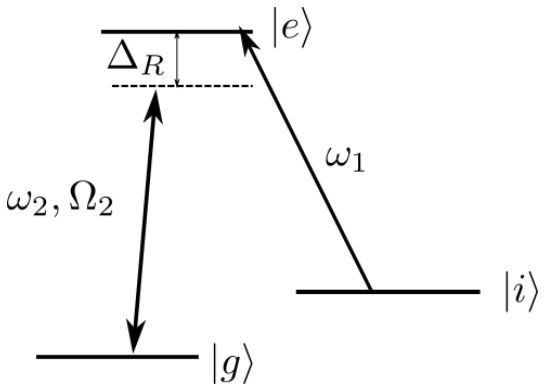

Figure 125: Scheme of a Raman transition, where in our case $|i\rangle$ is the initial state of two freely colliding ^{6}Li atoms, $|e\rangle$ is an excited-state molecule and $|g\rangle$ is a ground-state molecule, which is connected to the excited-state molecule by a dipole-allowed transition.

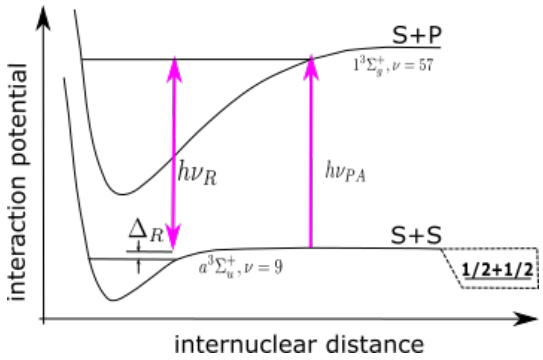

Figure 126: Realization of three level Raman scheme in triplet system of ^{6}Li, where the initial state $|i\rangle$ is a pair of free atoms.

The detection of the right transition frequency for the Raman laser is facilitated by the fact, that it can be determined experimentally via observation of the so-called Autler-Townes splitting, which in the experiment simply is detected via a change in the atom loss caused by the resonant PA light. When the Raman laser is resonantly driving Rabi oscillations with Rabi frequency Ω_2 between $|g\rangle$ and $|e\rangle$, this leads to a splitting of the energy of the excited state by

$$E_\pm = \pm\frac{\Omega_2}{2},$$

therefore shifting the PA laser out of resonance. This "revival" of the atom population was observed in our experiment by scanning the frequency of the Raman laser, while the PA laser was fixed on the resonance $1^3\Sigma_g^+(\nu' = 57, J' = 1)$ (see Fig. 127). For this measurement, we used setup 1, since with a PA beam colinear with the IR trap beam it was easier to observe PA loss features. Additionaly, we observed the doublet resulting from the Autler-Townes splitting. Therefore the Raman laser was kept at a fixed frequency for three different detunings (like in

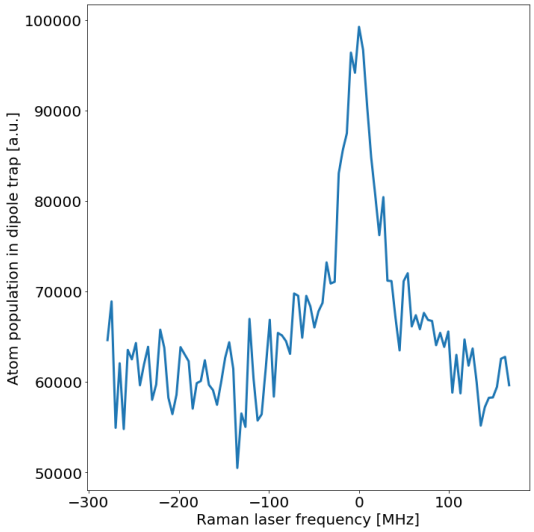

Figure 127: Atom loss spectrum while frequency of PA laser fixed and Raman laser frequency was scanned.

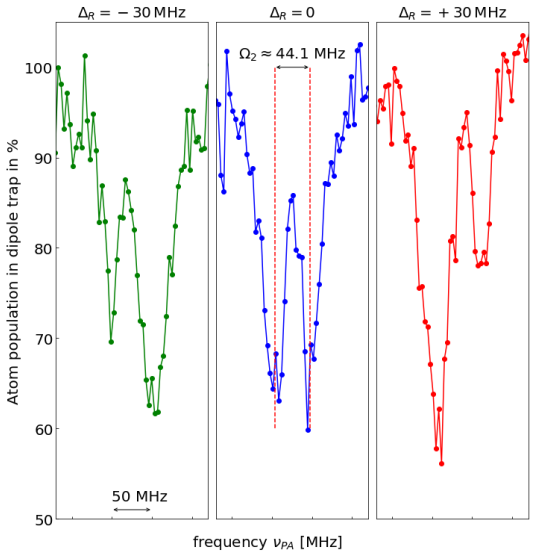

Figure 128: Atom loss spectrum when frequency of the Raman laser is kept constant (for three different detuning), while the frequency of the PA laser is swept over the $a^3\Sigma_u^+(\nu'' = 9) \leftrightarrow 1^3\Sigma_g^+(\nu' = 57, J' = 1)$ resonance.

[97]), and the PA laser frequency was swept over the resonance (see Fig. 128). In the triplet system, the binding energy of the vibrationally least bound state $a^3\Sigma_u^+(\nu = 9, N = 0)$ was exactly determined by the frequency difference of the two lasers and is known to be about $-24\,\mathrm{GHz}$.

We could observe a doublet with a frequency splitting of $\approx 44.1\,\mathrm{MHz}$, which corresponds to our Rabi frequency. The same Autler-Townes splitting could also be observed in the singlet system of ^{6}Li. In order to produce ground state molecules with half of the photoassociation rate, the PA laser has to be detuned on one of the doublets, i.e. the PA laser has to be detuned by $\pm\frac{\Omega_2}{2}$. After that, we ionised optically trapped atoms, where again the atomic sample was exposed to the PA laser resonant with the triplet resonance, Raman light and femtolaser pulses simultaneously. However, in the attempts made with setup 1, no molecular signal discernible from the background could be detected in the recoil ion time-of-flight spectrum. Although these experiments did not indicate an enhancement of molecule production, they can serve as an important starting point for other types of experiments. The problem in this Raman transitions scheme is, that the Raman laser also stimulates back into the excited state and therefore by spontaneous or induced decay back into the continuum. For a three bound levels system, the direction of transfer can be fixed by employing a STIRAP scheme [98], in which an appropriate timing sequence of PA (or pump) and Raman (or Stokes) laser is employed. However spontaneous decay of the excited state can also not be avoided if the starting level is a continuum level, i.e. a pair of freely colliding atoms, which would normally be the case in a thermal atomic sample [99]. The timed sequence STIRAP scheme however can be applied when the ensemble is quantum degenerate to transfer population between molecular states and create deeply bound dimers.

13 The BEC setup

As outlined in the introduction, the mid-term goal in this project is the creation of a BEC of $^6Li_2$ dimers inside a reaction microscope. The BEC will be achieved by use of a Feshbach resonance between the two lowest hyperfine states of ^{6}Li, which allows us to tune the effective interactions between the atoms. For the Feshbach resonance a high magnetic field of several hundred Gauss has to be applied, which is why this technique of associating cold molecules is also generally called "magneto-association". In order to implement this magneto-association technique in a reaction microscope, many things had to be taken into account, from conceptual questions regarding momentum measurement, over instrumentation like coils and current polarity switching devices to experimental modes of operation for a MOT.

In the following sections, the necessary modifications to the vacuum chamber and the design choice for the Feshbach coils and its implications for momentum measurement will be explained in detail. A rendered partial CAD model of the modifications to the vacuum chamber for the BEC setup is seen in Fig. 129 and will be discussed in the following. As outlined in Sec. 13.1, due to the large magnitude of the magnetic field, which will be employed for forced evaporative cooling in the vincinity of a Feshbach resonance of ^{6}Li, there will be no switching off of the magnetic field required to from the weakly bound halo dimers. Therefore the only logical choice is to align the axis of the pair of Feshbach coils along the spectrometer axis (see Fig. 130) such that ions move parallel to the field lines towards the detector. However in a conventional MOT beam geometry, the confinement in z direction is created by a pair of counterpropagating beams along the coil pair symmetry axis. However this laser beam direction is difficult to realize in our setup, since neither do our detectors exhibit a hole in the middle, nor is it possible due to space constraints to introduce a laser beam under a slight angle along the spectrometer axis. Therefore, as shown in Fig. 130, an unconventional MOT laser beam geometry was chosen, where the confinement in spectrometer direction is given by the combined action of four beams incident under 45° degree with respect to the spectrometer axis. The interior part of the coil rims were modified to have a step-like shape, so that the four MOT laser beams can just pass without being cut off. This pair of coils will be operated first in Antihelmholtz configuration in order to operate the MOT. After transfer of a fraction of the atoms into the optical dipole trap, the current in both coils will be turned off, the polarity of one of the coils will be switched, and the current will be ramped up again in Helmholtz configuration in order to perform forced evaporative cooling. Since the atoms in the dipole trap in principle have storage times of several seconds, the time constraint for these two current ramps before and after polarity switching is not that strict and the current ramps can take place on the order of a few ms, which is however still a demanding task. A major development by the electronic department of the MPI-K was a polarity switching device based on an H-bridge, which fulfills this task to switch from Antihelmholtz operation with relatively low current (max. 120 A) to Helmholtz operation at relatively high currents (up to 400 A) in a matter of a few ms (see Sec. 13.1.2). In order to prevent eddy currents in the rims during this switching procedure, which could lead to slowly decaying magnetic fields, the rims have been cut. Furthermore one of the two coils is attached to a two-axis manipulator in order to 1) compensate for any asymmetries and 2) to fine-adjust the Helmholtz configuration or slightly break it to create additional magnetic confinement along the axial direction of the optical dipole trap. The red colored flanges in Fig. 129 and their opposing pairs are the viewports used for the operation of the MOT in the modified vacuum chamber. The top and bottom flanges are modified to hold the coils and have connectors for water cooling of the Feshbach coils. A central viewport on top and bottom will be exclusively used for resonant absorption

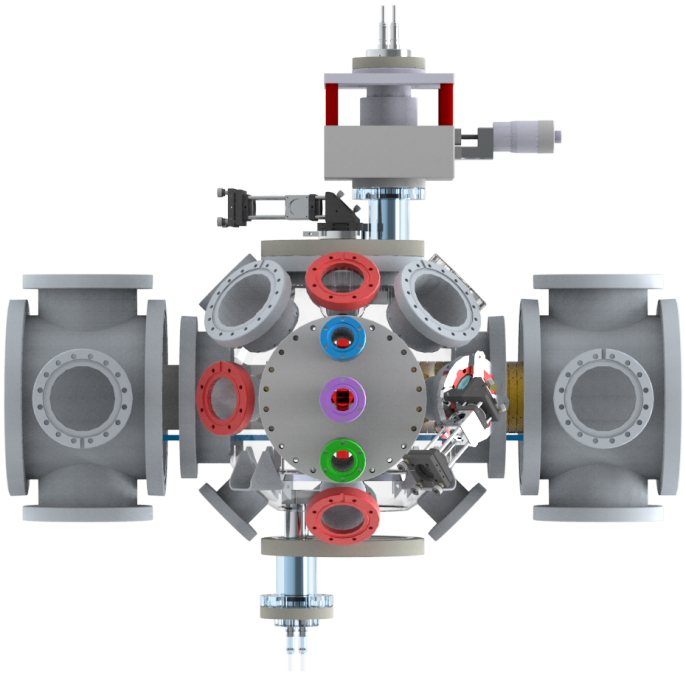

Figure 129: MOTRemi chamber changes for BEC setup

imaging (see Subsec. 10.2.2). The large flange with three CF40 flanges, which are for Zeeman slower (green), focusing mirror manipulator (purple) and focused IR beam entrance viewport (blue), has to be rotated by 90°, since beams under 18° are otherwise blocked by the coils.

13.1 Design of Feshbach coils and momentum reconstruction in an inhomogeneous magnetic guiding field

13.1.1 Feshbach coils design goals and constraints

In order to access the BEC-BCS crossover region of a ^{6}Li $|1\rangle - |2\rangle$ spin mixture, magnetic fields two orders of magnitude higher than usually applied in a ReMi are necessary. Two important trademarks of a conventional reaction microscope are that

(a) the external magnetic field is statically applied along the spectrometer axis, being homogeneous down to a deviation of less than 0.5% of the maximum value in the volume enclosed by ion and electron detector and

(b) it is usually so small (< 10 G) that it hardly influences the trajectory of the ions (even that of light ions like ^{6}Li$^+$).

The first trademark amounts to *including the detectors in the volume of homogeneous magnetic field*, a requirement which is technically very challenging to maintain for B-fields of several 100 Gauss, but also not ideal from a standpoint of momentum resolution. While the external pair of Helmholtz coils, whose dimensions are dictated by the physical dimension of our vacuum chamber, can create an extraction field for the electrons between $8 - 10$ Gausses in the center with roughly 0.23 $\frac{\text{Gausses}}{\text{Ampere}}$, the required 834 Gausses would amount to a technical highly challenging current of about 3.5 kiloAmpere and therefore probably would have required

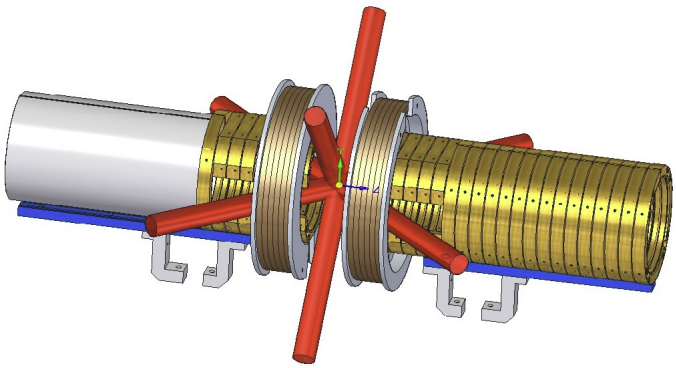

Figure 130: CAD model of the Feshbach coils together with a split spectrometer and a new beam geometry of the MOT.

the replacement of the existing coil pair by superconducting coils. Adding to the technical challenge of creating currents of that magnitude and maintaining them for several seconds, the magnetic field also would have to be applied in a pulsed manner, because it renders the operation of a MOT impossible (see Sec. 1). Moreover, apart from the technical aspect, such a tremendeous large scale and pulsed magnetic field most likely would have had a detrimental effect on other magnetic field sensitive experiments in the vicinity of our experiment. Also, from a physical standpoint, such a high magnetic field in the volume enclosed by the detectors, worsens the transversal momentum resolution: The atoms in the dimer can be as far seperated as roughly $11,000$ a.u. for a magnetic field close to 834 Gausses. The KER after Coulomb explosion due to Coulomb repulsion would amount to 2.5 meV, which would only correspond to a maximum Larmor radius of about 6.7 mm for ^{6}Li ions and therefore only cover about 10% of the total detector diameter of 80 mm. For electrons the maximum transversal momentum would amount to a spot of diameter 0.6 mm, therefore already being comparable to the spatial resolution of the detector.

The second trademark is also not given anymore in magneto-association experiments, since such a strong magnetic field of $800-1500$ Gausses will also definitely influence ion trajectories, since the gyro period of the light lithium ions will be $\approx 5\,\mu s$ at 834 Gausses, which means that many gyro periods take place before the ions hit the detector. Because of the afore-mentioned reasons, the design choice was made to use a pair of intra-vacuum, water-cooled coils, in order to place them as close to the atomic sample as possible (see Fig. 130).

The only sensible choice, in order for the charged fragments to arrive at the detectors, is to align the Feshbach coils along the spectrometer axis. At last, in order to conserve the first trademark of a ReMi, one could have placed the detectors as close as possible to the reaction volume. However this option would have implied a considerable obstruction of optical access, which is necessary to operate a MOT and a singly-focussed Gaussian beam optical dipole trap.

However, if the detectors are not included in the homogenous magnetic field volume, this has important implications on momentum reconstruction, since now the charged fragments on their way to the detector have to traverse a region of inhomogeneity. Therefore the equations of motion for longitudinal and transversal motion are no longer decoupled and significant energy transfer between longitudinal and transversal momentum components can take place. The problem of proper reconstruction of momenta in such an inhomogenous magnetic field will be addressed in Sec. 13.1.3.

The requirements we had on our coils can be listed as follows:

1. Low power consumption and good cooling in order to not heat up significantly during pulsed operation and deteriorate vacuum conditions.
2. Low inductance for fast switching times.
3. Good optical access to MOT region.

In order to guarantee a low power consumption and a good cooling, it was crucial to minimize the necessary current density in the coils, while having a good volumetric flow rate through the wires which is $\sim R^4$ for a wire with circular radius R according to the Hagen-Poiseuille equation. Roughly for electromagnets with current densities of $J \sim 10 - 20\,\frac{\mathrm{A}}{\mathrm{mm}^2}$, active water cooling with $2 - 10\,\mathrm{l/min}$ is required, while current densities of $100 - 300\,\frac{\mathrm{A}}{\mathrm{mm}^2}$ require a high water flow rate of $20 - 100\,\frac{\mathrm{l}}{\mathrm{min}}$. In a first design stage, the magnetic field of one coil with N windings can be approximated by the magnetic field of N circular current loop placed at the same position. According to the magnetic field expression for such a current loop, in order to produce a magnetic field B_z at the center between a pair of coils with radius r and N windings placed in Helmholtz condition, a current of

$$I_0 = \frac{B_z}{\mu_0}\frac{\sqrt{125}}{8}\frac{r}{N} \tag{69}$$

is needed. The minimum radius of the coils is constrained by the dimensions of our spectrometer, which dictated a minimum inner coil diameter greater than 56 mm, which is the maximum outer diameter of our spectrometer. The coil windings are hold by an aluminium rim, which has an inner radius of 59 mm, so at each position there is a distance of 3 mm between the rim and the spectrometer, leaving enough space for resistors and screw hats. A pair of Helmholtz coils with N windings and radius of $r = 6$ cm which should create a magnetic field up to $B_z = 1500$ G, requires a current per winding of ≈ 10000 A$/N$. The filling factor of the coils was maximised by choosing wires with quadratic (5x5 mm^2) cross section. This corresponds to a filling factor of 64 %, compared to about 50 % when using wires with circular diameter. Additionally, the wire has a quadratic hollow channel (3x3mm^2), which is used for active water cooling and has been coated by the company (Luvata) with a thin Kapton layer for electric insulation. The effective cross section for one winding A of this wire is therefore $A = (5^2 - 3^2)\,\mathrm{mm}^2 = 16\,\mathrm{mm}^2$ and for the chosen coil dimension with $N = 29$ windings, we estimated a maximum current density of $J \approx 22\,\frac{\mathrm{A}}{\mathrm{mm}^2}$. The Ohmic resistance of the coils can be estimated as

$$R = \frac{\rho l}{A} = \rho\frac{(N 2\pi r)}{A} \tag{70}$$

and the power $P = R \cdot I_0^2$ which is dissipated in the coils for a given magnetic field B_z is then given

$$P = \frac{\rho}{A}\left(\frac{B_z}{\mu_0}\frac{\sqrt{125}}{8}r\right)^2\frac{(2\pi r)}{N}.$$

For optimal cooling it would be advantageous to make the number of windings as high as possible, but as will be discussed in the following Subsec. 13.1.2, the magnetic field switching time is $\sim N$ and fast switching times are needed in the experiment.

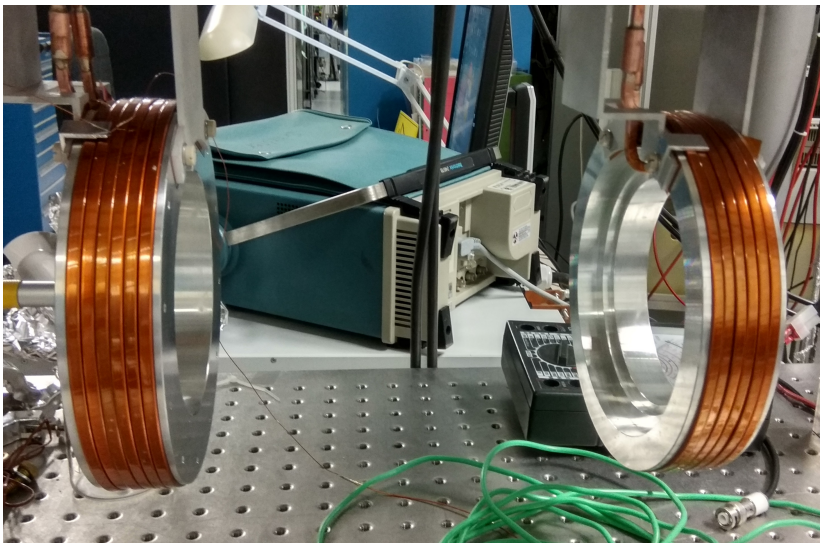

Figure 131: Photograph of the produced coils.

A more accurate design of the coils takes into accout the spatial extension of the coil, and with the Bio-Savart expression for the magnetic field of a current loop from [100], the magnetic field has been calculating by summing over the contributions from each winding, approximated as a current loop. According to this Bio-Savart calculation, the coils in Fig. 130 would generate a maximum magnetic field of 1500 Gauss at a maximum current of about 450 A. Each coil would have an estimated Ohmic resistance of 13.64 $m\Omega$ with a maximum power consumption of 2.77 kW at 450 A. The inter coil distance for the Helmholtz condition was numerically determined to be 5.3 cm, which denotes the distance between the edge of the rims. Therefore, the optical access is mainly possible in the xy-plane orthogonal to the coil axis. However the third requirement was improved by trimming steps into the aluminium rim, which holds the coil windings together. This way laser beams can pass in the horizontal plane through the 3.5 cm wide slit in the spectrometer, for which it was originally designed for (see Fig. 130). The second requirement of fast switching will be discussed in Subsec. 13.1.2. After the coils had been manufactured by the mechanical workshop (see Fig. 131), the axial magnetic field on its symmetry axis was measured with a cylindrical Hall probe (see Fig. 132 and Fig. 133).

The green curve in Fig. 132 was fitted to the measured magnetic field (red dots) with the fit function being the expression for the on-axis magnetic field of a current loop of radius r

$$B_z(z) = \frac{\mu_0 I N r^2}{2(r^2 + z^2)^{\frac{3}{2}}}.$$

The fit only shows marginal deviation from the measured axial magnetic field, which would arise from the Bio-Savart expression for the magnetic field of the coil with the depicted cross section. In Fig. 133 the fit expression (yellow curve) was used to obtain the magnetic field for a pair of coils with the previously calculated distance, which would match the Helmholtz condition, and is compared to the magnetic field of the Bio-Savart expression (blue curve). As can be seen, the fit expression does not quite reproduce a homogeneous magnetic field for this distance, but instead has an axial maximum. However this does not pose a problem, since one of the coils is attached to an an XY manipulator with a maximum travel range of

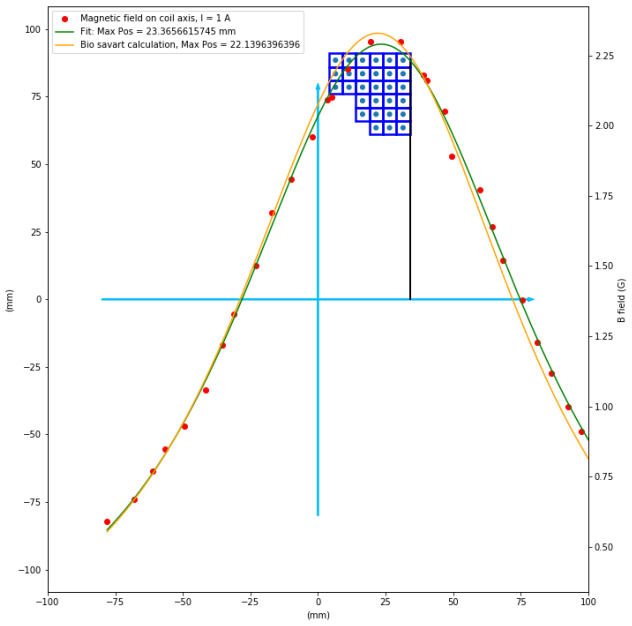

Figure 132: Comparison between measurement of Feshbach coil pair magnetic field on symmetry axis with Bio-savart calculation. The green dots indicate the position of the position of the current loops for the Bio-Savart calculation.

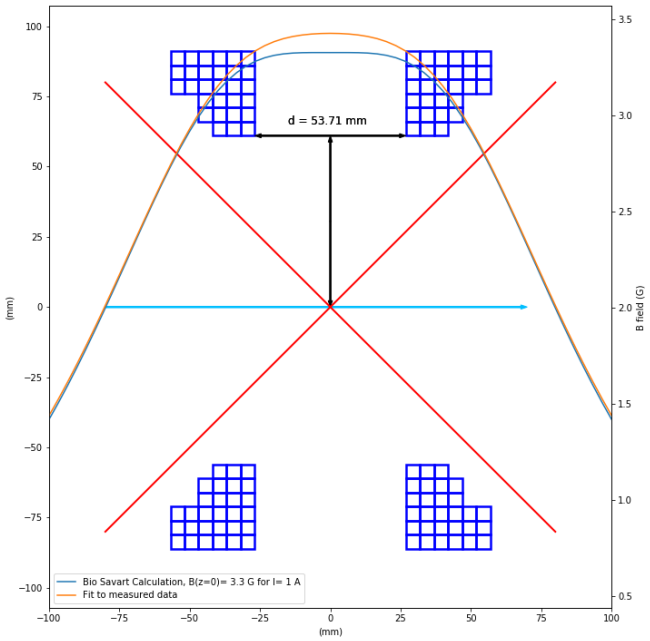

Figure 133: Magnetic field of Helmholtz coil pair on symmetry axis with distance based on Bio savart calculation for $I = 1$ A. Blue line is magnetic field based on Bio-Savart calculation. Orange line results from fit to measured data of Fig. 132.

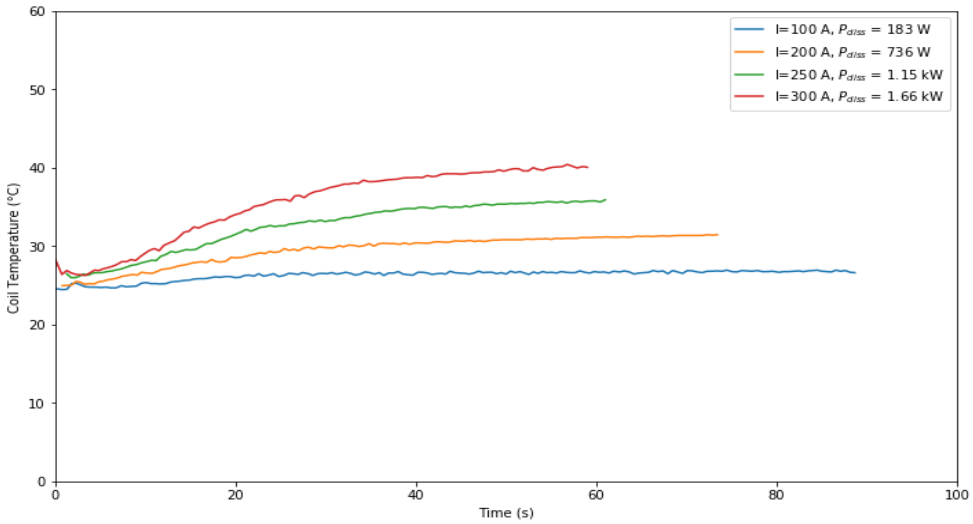

Figure 134: Temperature measurement of coil via Pt100 resistance for different dissipated powers.

±25 mm, so that the inter coil distance can be varied within the vacuum chamber. This is of particular importance since the atoms in the optical trap are trapped in magnetic high field seeking states and in the center of the Helmholtz coils two types of saddle points with different residual magnetic field curvatures can exist, when the Helmholtz condition is broken. The type of saddle point given in Fig. 133 with an axial maximum, and consequently a radial minimum, however is detrimental for the trapping performance at low trap depth (i.e. after forced evaporation), if the weak axis of the focused-beam trap is aligned along the radial direction, as it will be the case in our setup, because the radial minimum creates a weak magnetic anticonfinement in radial direction. However the type and the exact position of the saddle point in the center of the Helmholtz pair, is very sensitive to imperfections of the rotational symmetry of the coils, as has been reported in [58]. The XY manipulator not only allows for changing the type of saddle point by changing the intracoil distance, but also allows for partial compensation of any disruptions from rotational symmetry.

The cooling performance of the water cooling was tested for different current amplitudes by monitoring the temperature of the coils via a voltage drop across a Pt100 resistance which was clamped onto the outside windings in the middle of one coil (see Fig. 134). The temperature of the coil has been monitored for up to 90 s, while the current was continuously sent through one of the water-cooled coils. As one can see, even for $I = 300\,\mathrm{A}$ and a dissipated power of $P = 1.66\,\mathrm{kW}$, there is only a moderate temperature increase of roughly 15 °C from a baseline of $\approx$ 25°C. Although the baseline is probably too high due to a systematic error in the measurement of the voltage drop, it should not have an effect on the measured temperature increase. This moderate temperature increase after continuously dissipating 1.66 kW for about a minute, is promising and shows that such currents will pose even less of a problem with respect to heating in a pulsed operation. In Tab. 5 the most important properties of the constructed individual coil or a Feshbach pair are listed.

One coil		Helmholtz pair	
Ohmic resistance [mΩ]	18	Mag. field per Amp. [Gausses/A]	3.3
Inductance [μH]	135	Max B Field [Gausses]	1500
Max. heat per area [W/cm^2]	805	Max. current [Amperes]	450

Table 5: Electrical and physical characteristics of Feshbach coil or pair of coils in Helmholtz configuration.

13.1.2 Switching of the coil current

Albeit the aim is to perform "in-situ Coulomb imaging", still we require to switch the polarity of one coil in order to change from Antihelmholtz to Helmholtz configuration in an experimental sequence. Before the polarity switching in one of the coils takes place, the current in both coils has to be ramped down to zero and afterwards will be ramped up again to a comparitively high value compared to MOT operation. The times for switching on and off the coil currents should ideally not exceed a couple of miliseconds. The function of the electrical circuit breaker is typically realized by a Power MOSFET or an IGBT, in either case a Zener (or breakdown) diode is present which would limit the coil induced reverse voltage (see Fig. 135).

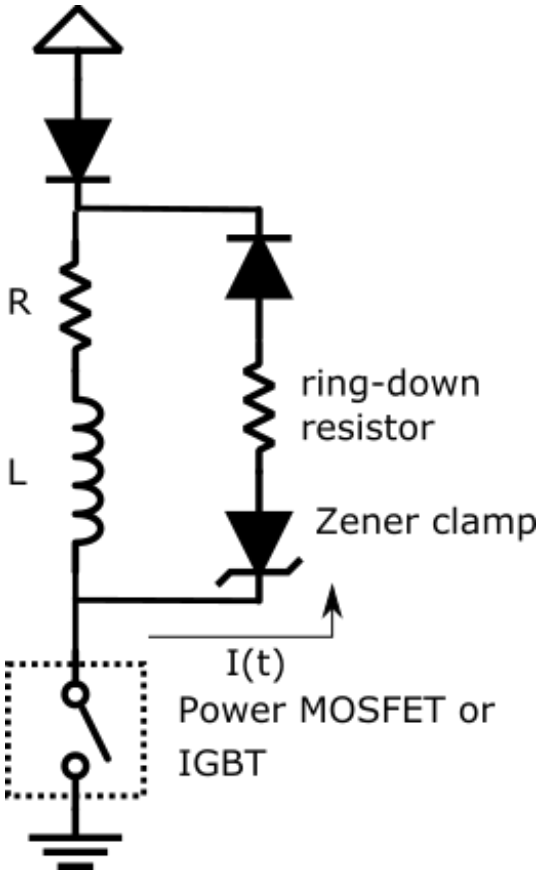

Figure 135: Switching concept circuit.

During breakdown of the diode the current would decrease according to

$$V_{so} = -L\frac{dI(t)}{dt},$$

where V_{so} is the breakdown (or clamping) voltage. Therefore during switch-off the current decreases linearly according to

$$I(t) = I_0\left[1 - \frac{t}{\tau_{\text{off}}}\right], \tag{71}$$

where

$$\tau_{\text{off}} = L\frac{I_0}{V_{so}}$$

is the switching off time constant. Equivalently the switching on time constant can be given as $\tau_{\text{on}} = \frac{L}{R}$, where R is the Ohmic resistance of the coil. For good switching times, the inductance of the coils should be as low as possible. The inductance of a coil with N windings scales as $L \sim N^2$, but fortunately $I_0 \sim \frac{1}{N}$ (see Eq. 69) and $R \sim N$ (see Eq. 70), so the on and off switching time constants scale only $\sim N$. On the other hand the dissipated power P scales $\sim \frac{1}{N}$, which should be minimized as well for best cooling performance. Therefore, in the design process of the coil pair, a trade-off had to be made in order to fulfill both conditions sufficiently well. The value $2L$ of the total inductance of two identical coils with inductance L in series,

placed a certain distance apart, however can change due to inductive coupling. For strongest inductive coupling the inductivity can go up to $4L$. The switching off time can be further reduced by using a high Ohmic "ring-down" resistance in parallel with the coil. However the true magnetic field decay is not necessarily reflected by Eq. 71 because eddy currents in the rims of the coils and the windings themselves can prevent a fast magnetic field decay. In order to suppress this effect in the rims, an angular fraction of the rims has been removed, so that no current loop is possible. The controller which switches on and off the magnetic field in both coils and changes the polarity of one of the coils is based on an H-bridge and has been developed by the electronics department of the MPI-K. A circuit diagram is shown in the the Appendix.

13.1.3 KER and momentum reconstruction in a Feshbach ReMi

For reasons outlined in the previous section, instead of maintaining the condition of a homogeneous magnetic field along the whole spectrometer, we opted for a pair of intra-vacuum coils which would locally create a strong magnetic field in the vicinity of the Feshbach resonance at 834 G of ^{6}Li and smoothly transition on the outer edges into a smaller magnetic field created by the existing pair of Helmholtz coils (see Fig. 133) .

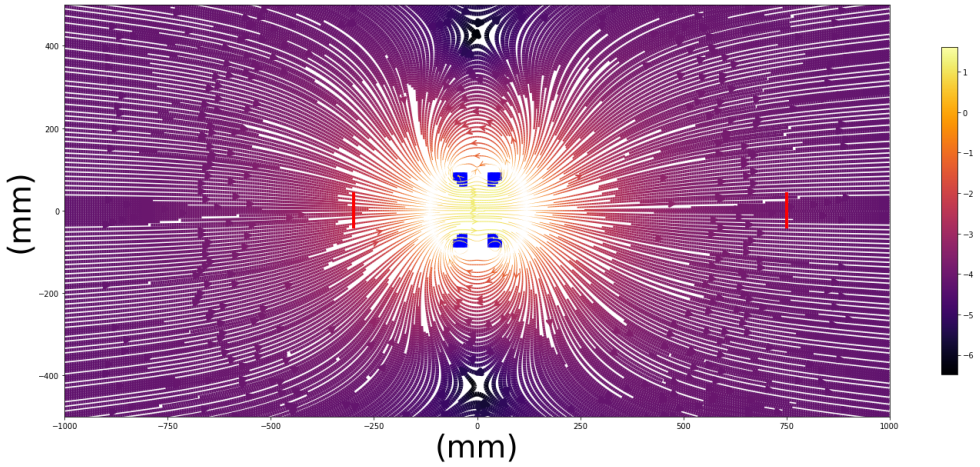

Figure 136: Magnetic field lines of Helmholtz coil pair with $I = 250$ A, superposed with magnetic field lines of external pair of Helmholtz coils with $I = 30$ A. If color code value is c, then the magnetic field is given by $\approx 1320 \cdot \frac{e^c}{5}$. The two thick vertical bars on both side represent the position of the electron (left) and ion (right) detector.

In the section about the design of the Feshbach coils, it was pointed out, that due to the strong inhomogeneous, but axially symmetric magnetic field needed for magneto-association, ions "have to be treated like electrons" in terms of transversal momentum reconstruction. Moreover another apparent consequence is that a considerable energy transfer from transversal kinetic energy to longitudinal kinetic energy will take place, while ions and electrons traverse the inhomogeneous magnetic field created by the pair of Feshbach coils and the pair of external Helmholtz coils (see Fig. 136). The energy transfer takes place because of a radial component $B_r(r,z) \cdot \mathbf{e}_r$ in the region of inhomogenuity, which together with the tangential component $v_\varphi \cdot e_\varphi$ produces a Lorentz force $q\mathbf{v} \times \mathbf{B}$ in z-direction. In other words, while transitioning from the high magnetic field region into the weak magnetic field region, ions and electrons are

accelerated by the magnetic field gradient in longitudinal (z-) direction, but decelerated in tangential direction. The inverse principle is used in magnetic mirrors, in which the longitudinal motion of ions is stopped by transitioning from a low into a high magnetic field region.

The ideal magnetic field generated by our Feshbach coils is inhomogeneous in z and r direction, but also rotationally symmetric with respect to the center axis of the Feshbach coil pair. Therefore it is of the more general form

$$\mathbf{B} = B_z(r,z)\mathbf{e}_z + B_r(r,z)\mathbf{e}_r. \tag{72}$$

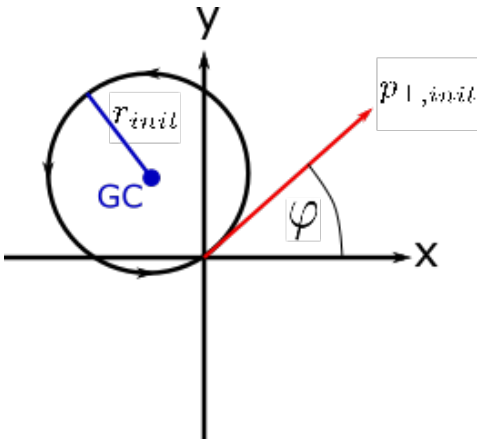

Figure 137: View of momentary cyclotron radius at time of birth of a charged fragment with initial transversal momentum $p_{\perp,init}$ emerging from point-like reaction volume on symmetry axis of Feshbach coil pair. The guiding center (GC) is the center of the cycloton motion.

Therefore this section addresses in a conceptual way the important question, of how the technique of magnetoassociation of molecules modifies the equations on momentum reconstruction in a reaction microscope, and if it is possible to reconstruct KER or even longitudinal and transversal momentum from the hit positions of the ions on the detector. All considerations in this section have been made under the (ideal) premise of the axisymmetric inhomogeneous magnetic field of Eq. 72 and a point-like reaction volume.

If a charged fragments emerges from the reaction volume in the center of the Feshbach coil pair with an initial transversal momentum $p_{\perp,init}$, its cycloton radius r_{init} will initially be given by

$$r_{init} = \frac{p_{\perp,init}}{qB_{center}},$$

where $B_{center} \approx B_z(r=0,z=0)$ is the axial magnetic field component in the center of the Feshbach coil pair. It will, on a helical trajectory, gyrate towards the detector while its cycloton radius grows $\sim \frac{1}{B(r,z)}$ since the axial magnetic field component decreases on the way to the detector. The center of this gyromotion is called guiding center (GC) and it moves along the field lines with a speed $v_{\parallel}$. The gyromotion takes place in the plane perpendicular to the field line. This division of motion into the motion of the guiding center and gyromotion is called *guiding-center approximation*.

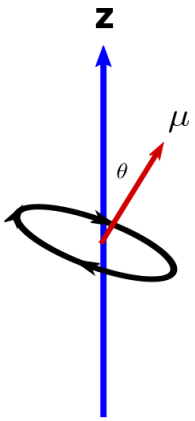

Figure 138: Magnetic dipole moment associated to a current loop of area A and current I is $\mu = I \cdot A$.

Accordingly, a moving coordinate system can be defined, the guiding center system (GCS), in which the velocity component parallel to the magnetic field $v_{\parallel}$ is zero. In the GCS the circular motion of ion or electron can be thought of as a current loop (see Fig. 138) which has an associated magnetic dipole moment of

$$\mu = \frac{1}{2} q\mathbf{r}_L \times \mathbf{v}_{\perp},$$

where $\mathbf{v}_{\perp}$ is the velocity component of the gyromotion and

$$\mathbf{r}_L = -\frac{m}{qB}\frac{\mathbf{v}_{\perp} \times \mathbf{B}}{B}$$

the position of the ion or electron in the GCS with B being evaluated at r_L, i.e. in the following always $B \equiv B(r_L, z = 0)$ in the GCS. The vector magnetic dipole moment can, in a more intuitive fashion, be written as

$$\mu = IA\mathbf{e}_z,$$

where A is the area enclosed by a loop, I the current loop, and $\mathbf{e}_z$ is the normal vector of the plane in which the gyromotion takes place (x-y plane of GCS) and its direction is that of the magnetic field, i.e. $\mathbf{n} = \frac{\mathbf{B}}{B}$. In the GCS the current of the loop can be expressed as

$$I = q \cdot \frac{\omega_g}{2\pi},$$

where ω_g is the local gyro frequency

$$\omega_g = \frac{qB}{m}. \tag{73}$$

The area A is given by πr_L^2, where r_L is the cycloton radius

$$r_L = \frac{p_\perp}{qB}, \tag{74}$$

where B is the actual magnetic field along the trajectory of the charged fragment. Therefore in the GCS the scalar magnetic dipole moment can be expressed as

$$\mu = \frac{q^2}{2m} B \cdot r_L^2, \tag{75}$$

$$= \frac{\frac{p_\perp^2}{2m}}{B} \equiv \frac{W_\perp^{GC}}{B}. \tag{76}$$

where $W_\perp^{GC}$ is the transversal kinetic energy with respect to the direction of magnetic field, which does not everywhere coincide with the direction of the spectrometer axis.

In the lab coordinate system the equations of motion $m\ddot{\mathbf{r}} = q \cdot \tilde{\mathbf{E}} + q \cdot (\mathbf{v} \times \mathbf{B})$ for a charged fragment moving in an axisymmetric, and in general inhomogeneous magnetic field given in Eq. 72 can be written in cylindrical coordinates as follows

$$\dot{p}_z = q\left[\tilde{E}_{ext} - \frac{p_\varphi}{m} B_r(r,z)\right] \tag{77}$$

$$\dot{p}_r = \left[\frac{p_\varphi}{r} + qB_z(r,z)\right] \frac{p_\varphi}{m} \tag{78}$$

$$\dot{p}_\varphi = \frac{q}{m}\left[p_z B_r(r,z) - p_r B_z(r,z)\right] - \frac{p_r p_\varphi}{mr}, \tag{79}$$

where the transversal momentum has been decomposed into a radial and a tangential component

$$\mathbf{p}_\perp = p_r \mathbf{e}_r + p_\varphi \mathbf{e}_\varphi,$$

and its magnitude is given by Eq. 74. These equations can be combined to give

$$\frac{dE_{kin}}{dt} = \dot{W}_\parallel + \dot{W}_\perp = q\tilde{E}_{ext} v_z, \tag{80}$$

where $W_\parallel, W_\perp$ is the kinetic energy parallel and perpendicular to the spectrometer axis respectively. This equation emphasizes, that of course the total kinetic energy is only changed by the static electric extraction field, and not by the magnetic field gradient. As can be seen from Eq. 76, the transversal kinetic energy can be expressed via the magnetic moment. In the special case of adiabatic invariance, i.e. $\mu = const.$, we can therefore write

$$\dot{W}_\perp = \mu \left[v_z \partial_z B(r,z) + v_r \partial_r B(r,z) \right].$$

By making the approximation $B(r,z) \approx B_z(0,z)$, which could be justified for the case of small transversal momenta, we arrive at following time evolution for the longitudinal momentum:

$$\dot{p}_\parallel = \left[q\tilde{E}_{ext} - \mu \frac{\partial B_z(0,z)}{\partial z} \right]. \tag{81}$$

If the magnetic moment μ is constant, this equation can be spatially integrated to yield the longitudinal kinetic energy $E_{\parallel,det}$ at the detector as

$$E_{\parallel,det} = E_{\parallel,center} + qU + \mu \Delta B_z,$$

where $E_{\parallel,center}$ is the initial, longitudinal kinetic energy, U is acceleration potential, and ΔB_z is the difference in axial magnetic field amplitude between the center of the Helmholtz pair of coils and at the detector

$$\Delta B_z = B_{z,cent} - B_{z,det}. \tag{82}$$

From this equation it becomes evident, that the amount of transferred kinetic energy $\mu \Delta B_z = W_\perp \left(1 - \frac{B_{det,z}}{B_{center,z}}\right)$ depends on the initial transversal kinetic energy and the magnetic field gradient between the center of the high field region and the magnetic field at the detector. For a setting close to the Feshbach resonance, with $B_{center,z} = 835.76\,\text{Gauss}$ and $B_{det,z} = 2.4\,\text{Gauss}$, about 97% of the initial transversal kinetic energy will be transferred to longitudinal kinetic energy if the trajectory to the detector is adiabatic.

Eq. 81 can be solved numerically for a particular initial condition, but it does not have an analytical solution that relates the TOF to the initial, longitudinal kinetic energy $E_{\parallel,center}$ and the used extraction voltage like Eq. 3. Only in the special case of $\mu = 0$, a charged fragment emerging with zero initial transversal momentum $p_\perp = 0$, Eq. 81 reduces to the conventional equation and we can extract directly the KER from the TOF of the charged particle. Fragmental alignment of polarizable molecules that interact with strong pulsed laser fields has been shown to be a feature in multielectron dissociative ionization [101, 102]. Therefore it might be possible in a double-pulse experiment with pulses of pulse duration $1 - 30\,\text{ps}$, peak intensities of $I \sim 10^{14}\,\text{W/cm}^2$ and a polarization aligned along the spectrometer axis to align the molecules created by magneto-association prior to Coulomb explosion imaging. This would guarantee, that a major fraction of the hit events could just be treated as in a conventional reaction microscope and the KER is mainly extracted from the TOF.

In order to assess the possibility of momentum reconstruction for $\mu > 0$, simple numerical checks haven been performed by solving the equation of motion $m_{^6Li}\ddot{\mathbf{r}} = q \cdot \tilde{\mathbf{E}} + q \cdot (\mathbf{v} \times \mathbf{B})$ of the lithium ion in the combination of electric and magnetic fields present during extraction. According to Eq. 81 the TOF of a charged fragments with $\mu > 0$ is modified to shorter times, since the longitudinal kinetic energy of the charged fragment is increased by the magnetic field gradient. On the other hand, it can be expected, that the TOF to the detector does not

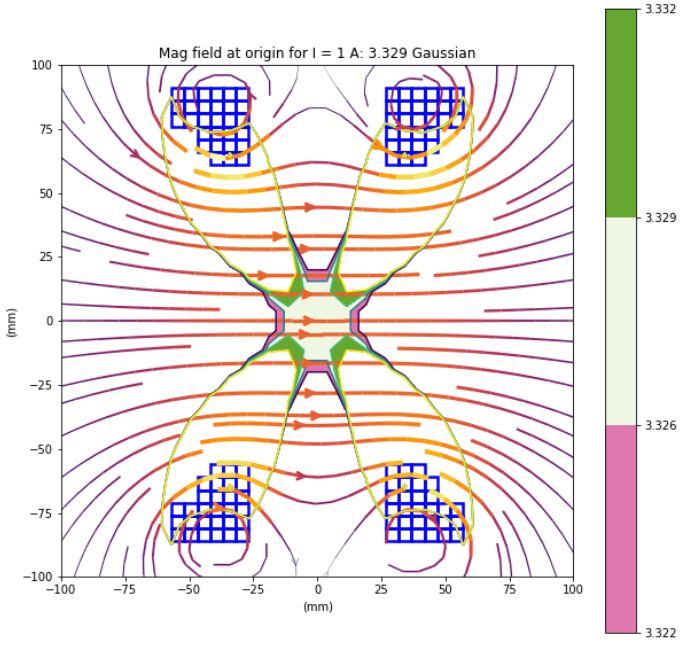

Figure 139: Vector field and contour plot of magnetic field generated by pair of Helmholtz coils for $I = 1\,\mathrm{A}$, illustrating the homogeneity of the magnetic field. The innermost greenish shaded area shows the space where the magnetic does not deviate by more than one promille of the magnetic field in the center between the two coils.

critically depend on the transverse momentum of the ion, if the ion's momentum is low enough, so that the Larmor radius is always smaller than the radius, which designates the volume of the magnetic field, which is homogeneous down to a relative change of e.g. 0.1%. This is of course the same assumption implicitely done for electron trajectories in a conventional reaction microscope. In order to estimate the magnitude of the effect on the ion TOF, it is helpful to look at the expected range of KER when performing Coulomb imaging on weakly-bound dimers. We are interested in magneto-association of halo dimers in the universal range, where the scattering lengths varies between $-4000a_0$ and $-11.000a_0$. The lower limit of the magnetic field range of interest derives from the fact, that only when the scattering length a_{12} is much higher than the characteristic radius of the Van-der-Waals-interaction potential $r_0 \approx 60a_0$, the binding energy E_{12} of the $|12\rangle$ dimers is described by the universal relation $E_{12} = \frac{\hbar}{m a_{12}^2}$ (see Subsec. 9.1). The upper limit derives from the assumed momentum resolution of the reaction microscope of $\Delta p \approx 0.05\,\mathrm{a.u.}$. Molecules of extension greater than $11000a_0$ might not be well resolved, if we want the momentum resolution to be 5% of the maximum momentum of the ions in the resulting Coulomb explosion. This would result in a range of KERs between $\approx 2.7\,\mathrm{meV}$ and $\approx 6.9\,\mathrm{meV}$ and correspondingly in a range of maximum transversal ion momenta between 1 a.u. and 1.6 a.u. At a center magnetic field of $B_0 = 834\,\mathrm{Gauss}$, the maximum transversal ion momentum of 1.6 a.u. corresponds to a local cycloton radius of 0.24mm.

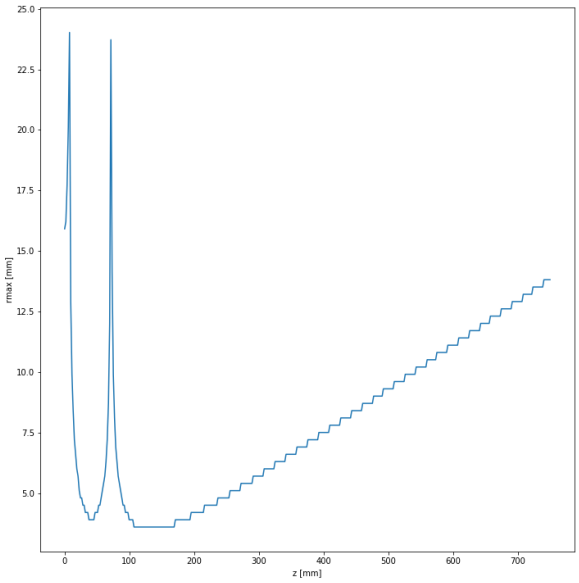

Figure 140: Above plot shows the maximum radius along the spectrometer axis, where $|\frac{B_{\parallel}(r=0)-B_{\parallel}(r)}{B_{\parallel}(r=0)}| < 0.1\%$.

If the coils are placed exactly in the Helmholtz distance, the magnetic field deviates by less than 0.1% from the value in the center in an interval of $\pm 13.8\,\mathrm{mm}$ along the spectrometer axis, while in orthogonal direction the magnetic field is homogeneous down to 0.1% in an interval of $\pm 14.7\,\mathrm{mm}$ around the center. An ion with an initial kinetic energy of $\approx 2.39\,\mathrm{eV}$, emerging from the Coulomb explosion of a dimer with mutual atomic distance of $\approx 11.4\,a_0$, gets decelerated by an extraction field of $2\,\frac{\mathrm{V}}{\mathrm{cm}}$ within $\approx 11.9\,\mathrm{mm}$, so well within the homogeneous field region.

From numerical investigation of the radial homogeneity of our pair of Helmholtz coils, in Fig. 140 it can be seen that the homogeneity in radial direction varies depending on the coordinate on the spectrometer axis and it has a minimum radius of 3.6 mm at $z = 113.6\,\mathrm{mm}$.

The z component of the magnetic field at $(r, z) = (3.6, 113.6)\,\mathrm{mm}$ is $B_z \approx 277\,\mathrm{G}$ and the resulting Larmor radius would only be smaller than 3.6 mm, if the maximum transverse momentum was smaller than $\approx 8\,\mathrm{a.u.}$. In order to not obtain transverse momenta $> 8\,\mathrm{a.u.}$, the ions emerging from the Coulomb explosion must have a minimum distance of $170\,a_0$, which is anyway not in our magnetic field region of interest. In Fig. 144 it can be seen from simulation of ion trajectories, that the TOF in dependence of initial transverse momenta between 0 and $2\,\mathrm{a.u.}$ is approximately constant, i.e. varies less than $\pm 5\,\mathrm{ns}$.

The energy transfer from transversal to longitudinal kinetic energy during the trajectory of a $^6\mathrm{Li}_+$ ion emerging from a central magnetic field of $\approx 834\,\mathrm{G}$ with $p_\perp = 1.65\,a.u.$ and being accelerated by a typical extraction field of $0.8\,\frac{V}{cm}$ is illustrated in Fig. 141. However, as can be seen in the second plot from above of Fig. 141, the magnetic moment at the detector is not the same, as when the ion starts from the center and therefore is not adiabatically constant. The quantity $\frac{\mu^{GC}}{\mu^{GC}_{init}}$ is the ratio of the magnetic moment in the GCS, as defined in Eq. 76.

In order to compare the magnitude of the current-independent magnetic gradient force $\sim \frac{\partial_z B_z}{B_z}$, which accelerates the charged fragment, the magnetic gradient force in eV/m is plotted versus the axial distance from the center in Fig. 142, for the same initial conditions

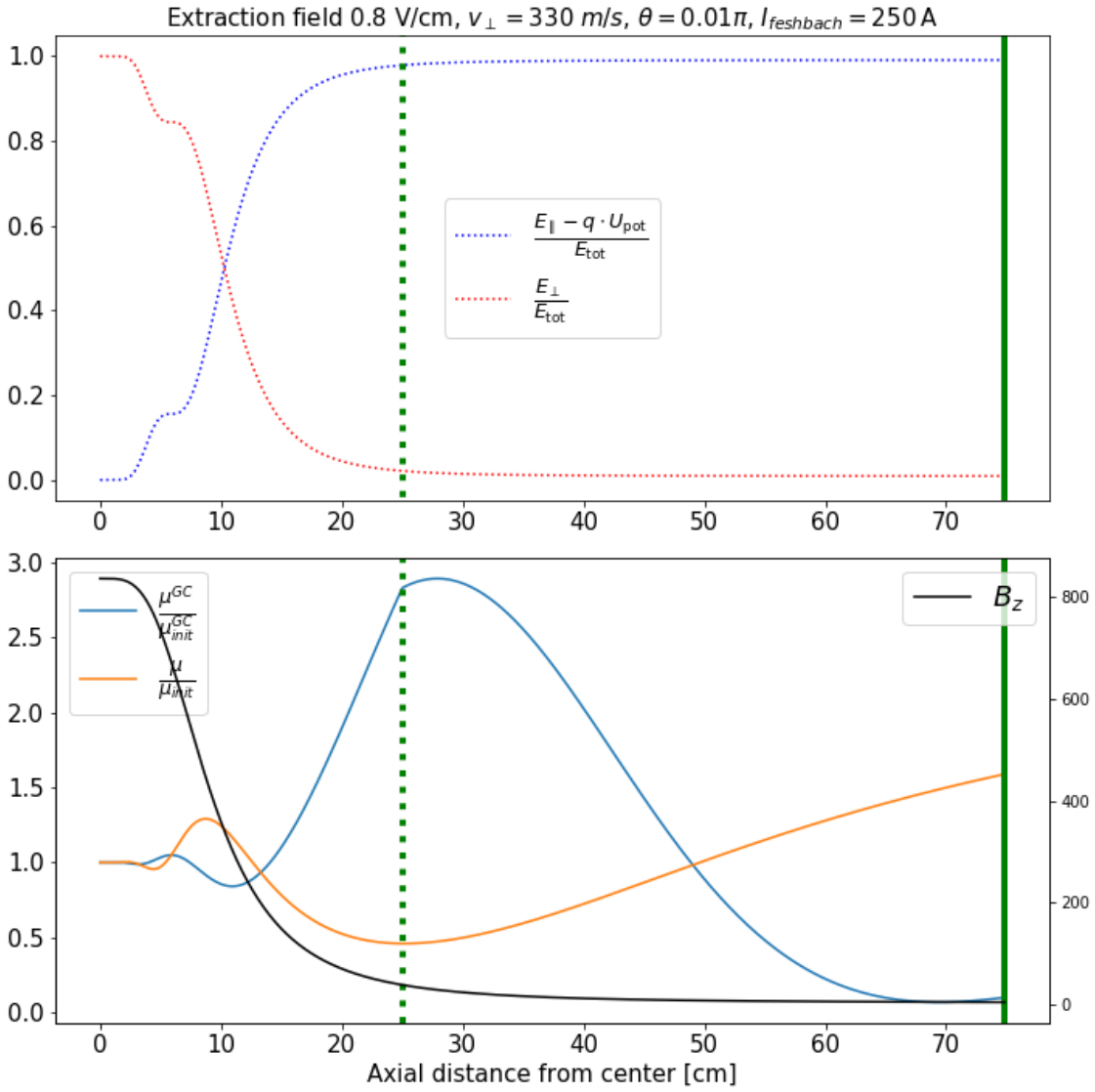

Figure 141: Numerical simulation of energy transfer from perpendicular to longitudinal kinetic energy of a charged $^6Li^+$ particle in an inhomogeneous field created by our Feshbach coil pair for $I = 250\,A$ and typical extraction voltage. The initial condition was $\mathbf{v} = (0, v_\perp \cos\theta, v_\perp \sin\theta)$ with $v_\perp = 330\,m/s$ and $\theta = 0.01\pi$. The vertical green dashed line indicates the end of the acceleration zone. In the upper plot E_{tot} refers to the total initial kinetic energy.

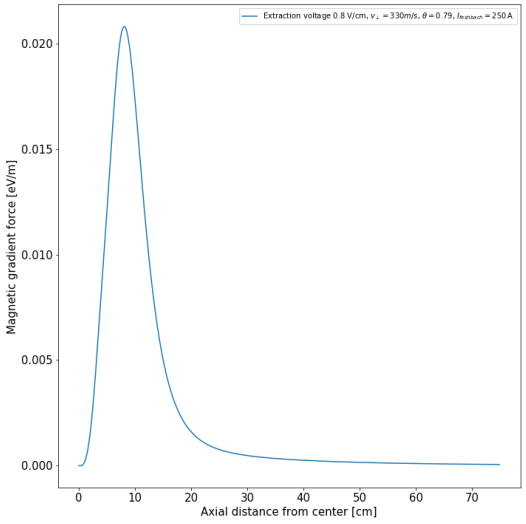

Figure 142: Magnetic gradient force for $^6Li^+$ ion with initial velocity $\mathbf{v} = v_{tot}\,[\cos\theta\mathbf{e}_y + \cos\theta\mathbf{e}_z]$ emerging from central magnetic field $B_z(z = 0, r = 0) = 834\,\mathrm{G}$.

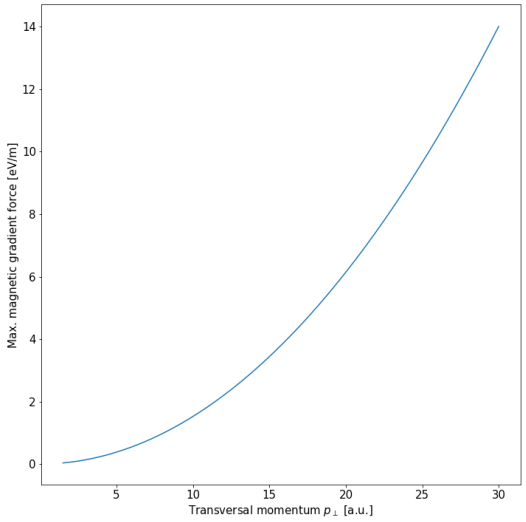

Figure 143: Maximum magnetic field gradient force for ion trajectories with initial transversal momentum $\mathbf{p} = p_\perp\mathbf{e}_y$ with $0 \leq p_\perp \leq 30\,\mathrm{a.u.}$and central magnetic field $B_z(z = 0, r = 0) = 834\,\mathrm{G}$.

as in Fig. 141. The amplitude of the electric extraction field typically ranges from $20 - 200\,\frac{\mathrm{V}}{\mathrm{m}}$ and, as can be seen from Fig. 142, the magnetic field gradient force can in good approximation be considered negligible for a maximum perpendicular momentum of $p_\perp \approx 1.65\,\mathrm{a.u.}$, which would correspond to an ion-ion distance of $\approx 4092\,a_0$ before Coulomb explosion of a dimer.

Therefore, for the maximum transversal momenta which result from Coulomb explosion of weakly-bound dimers the magnetic gradient force can be considered negligible. This is of course also reflected by the TOFs in dependence of the maximum transversal momenta (see Fig. 144), where the green marked region marks maximum transversal momenta between 0.5 a.u. and 1.6 a.u. and the TOF does not shift by more than 3 ns.

For a typical extraction voltage in our experiment of $0.8\,\frac{\mathrm{V}}{\mathrm{cm}}$, the symmetry center of the TOF distribution shifts less than 15 ns and can be considered negligible, because the calculated longitudinal momentum does not shift by more than 0.1 a.u., which is about the resolution we achieved for recoil ions. Therefore, for the case of weakly-bound dimers, the second term in Eq. 81 can be neglected and we can still assume Eq. 4 in order to connect the TOF with the *initial* longitudinal energy $E_{\parallel,init}$. Despite the fact that the ion gets accelerated in longitudinal direction by the magnetic gradient on its way to the detector, the TOF remains approximatively constant for maximum transversal momenta up to 2 a.u.. But even in the case where the magnetic gradient force significantly influences the TOF (= leading to shifts $>$ 15ns), the measured TOF can be compared to a look-up-table calculated by numerically solving Eq. 81 for a specific initial magnetic moment μ_{init}, given that the magnetic moment was adiabatically invariant during the ion trajectory.

The initial magnetic moment can be determined by measuring the transversal kinetic energy $W_{det,\perp}$ at the detector. In case of adiabatic invariance, $W_{det,\perp}$ is connected to the

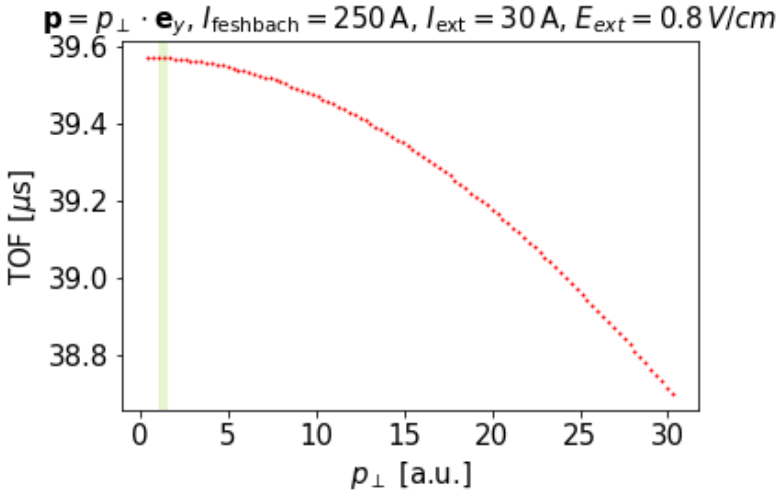

Figure 144: Simulation of ion TOFs for $p_\parallel = 0$ emerging from a Coulomb explosion with $\mathbf{p} = p_\perp \mathbf{e}_y$ and transversal momenta $p_\perp$ in the range of $0 - 30$ a.u. for a typical extraction field of $0.8\,\frac{\text{V}}{\text{cm}}$ in McLaren configuration ($a = 25\,\text{cm}$, $d = 50\,\text{cm}$) and a Feshbach magnetic field in the center of 836 Gauss.

initial transversal kinetic energy $W_{init,det}$ by

$$\begin{aligned} \mu_{det} &= \mu_{init} \\ \frac{W_{det,\perp}}{B_{det}} &= \frac{W_{init,\perp}}{B_{init}} \\ \Leftrightarrow W_{init,\perp} &= \frac{B_{init}}{B_{det}} W_{det,\perp}. \end{aligned} \tag{83}$$

The magnetic field in the center B_{init} is known by calibration or could even be determined in experiment via optical spectroscopy. The magnetic field at the ion detector B_{det} can be approximated by the magnetic field created by the external pair of Helmholtz coils, which as well can be calibrated in experiment by photo-ionization of optically trapped ^6Li and detection of electrons.

The transversal kinetic energy at the detector $W_{det,\perp}$ can be measured, as in the case of a homogeneous magnetic field, via Eq. 10, with the only exception being, that the phase α has to be generalized to

$$\begin{aligned} \alpha &= \int_0^{TOF} \omega_g(r(t), z(t)) dt \\ &= \int_0^{TOF} \frac{qB(r(t), z(t))}{m} dz. \end{aligned}$$

where ω_g is the local gyro frequency in the GCS (Eq. 73). In the approximation $B(r, z) \approx B_z(0, z)$, the phase, as per Eq. 73, can be written as

$$\alpha = \int_0^L \frac{qB_z(0, z)}{m} \frac{dz}{v_\parallel(z)}.$$

In this approximation, the accumulated phase α should in first order only depend on the TOF of the ion, but not on its initial transversal momentum. In Fig. 145, the dependence of the

accumulated phase α on the ion TOF for random initial momenta $\mathbf{p} = p_{tot} \cdot (\cos\theta \mathbf{e}_y + \sin\theta \mathbf{e}_z)$ with p_{tot} in $[1;2]$ a.u.in case of weakly bound dimers and in $[1;30]$ a.u.for the more general case, has been investigated. The uppermost figure shows the linear relation between α and TOF in a conventional reaction microscope with a homogeneous magnetic field. The middle figure shows, that in a momentum range of $[1;2]$ a.u., even in a reaction microscope with inhomogeneous magnetic field, we obtain a linear relationship between α and TOF. The relationship starts to blur out, and a slight error in the sub 10% regime is introduced in the calculation of the transversal momentum at the detector, for transversal momenta in the range of $[1;30]$ a.u..

In summary, given that the magnetic moment is adiabatically conserved, following steps are followed to reconstruct initial longitudinal and initial transversal ion momentum:

1. For a given hit point (x_r, y_r) on the detector, its distance

$$r = \sqrt{(x_r - x_{r,0})^2 + (y_r - y_{r,0})^2}$$

from the center of mass $(x_{r,0}, y_{r,0})$, and its TOF, calculate the cycloton radius R from $R = \frac{r}{2|\sin(\alpha/2)|}$, in which the accumulated phase is replaced by a linear relation $\alpha(TOF) = a \cdot TOF + b$ calculated beforehand for the specific current $I_{feshbach}$, which is *largely independent* of the initial transversal momentum for the momentum range $[0.5;1.6]$ a.u. under consideration. For calculating $\alpha(TOF)$, the magnetic field on the symmetry axis $B_z(r = 0, z)$ has to be known, which can be measured beforehand. The transversal momentum of the ion at the detector then follows analogously to Eq. 10 from $p_{r,\perp} = q \cdot B_{det} \cdot R$, and the initial transversal momentum of the ion is given according to Eq. 83 by

$$\begin{aligned} p_{r,\perp,init} &= \sqrt{\frac{B_{init}}{B_{det}}} \cdot p_{r,\perp,det} \\ &= \sqrt{B_{init} \cdot B_{det}} e \cdot r. \end{aligned}$$

Accordingly, we know the magnetic momentum of the trajectory to be $\mu = \frac{\frac{p_{r,\perp,det}^2}{2m}}{B_{det}}$.

2. In case of $p_{r,\perp} \leq 2$ a.u., we can use directly Eq. 6 to get $p_\parallel$ from the TOF. If $p_{r,\perp} > 2$ a.u., then $p_\parallel$ should be calculated numerically from Eq. 81 for the given magnetic moment μ.

In the special case of the reaction being Coulomb explosion of a $^6Li_2$ dimer, the fragments can be divided into two longitudinal velocity classes, those which are emitted 'forward' in direction of the ion detector and those, which are emitted 'backward' away from the detector. If those two ions are detected *in coincidence*, their initial momenta can be determined via the time difference $\Delta t = TOF_+ - TOF_-$ between the two time-of-flights,

$$p_\parallel = q \cdot \frac{E \cdot \Delta t}{2}.$$

The Larmor radius at the detector of coincidentally detected ions, could be determined from a simple geometrical argument outlined in Fig. 146. When two ions emerge from Coulomb explosion of a $^6Li_2$ dimer, they have opposed transversal momenta $p_\perp$ and both ions moves e.g. counter-clockwise on its helical trajectory when looking in direction of the spectrometer axis onto the ion detector.

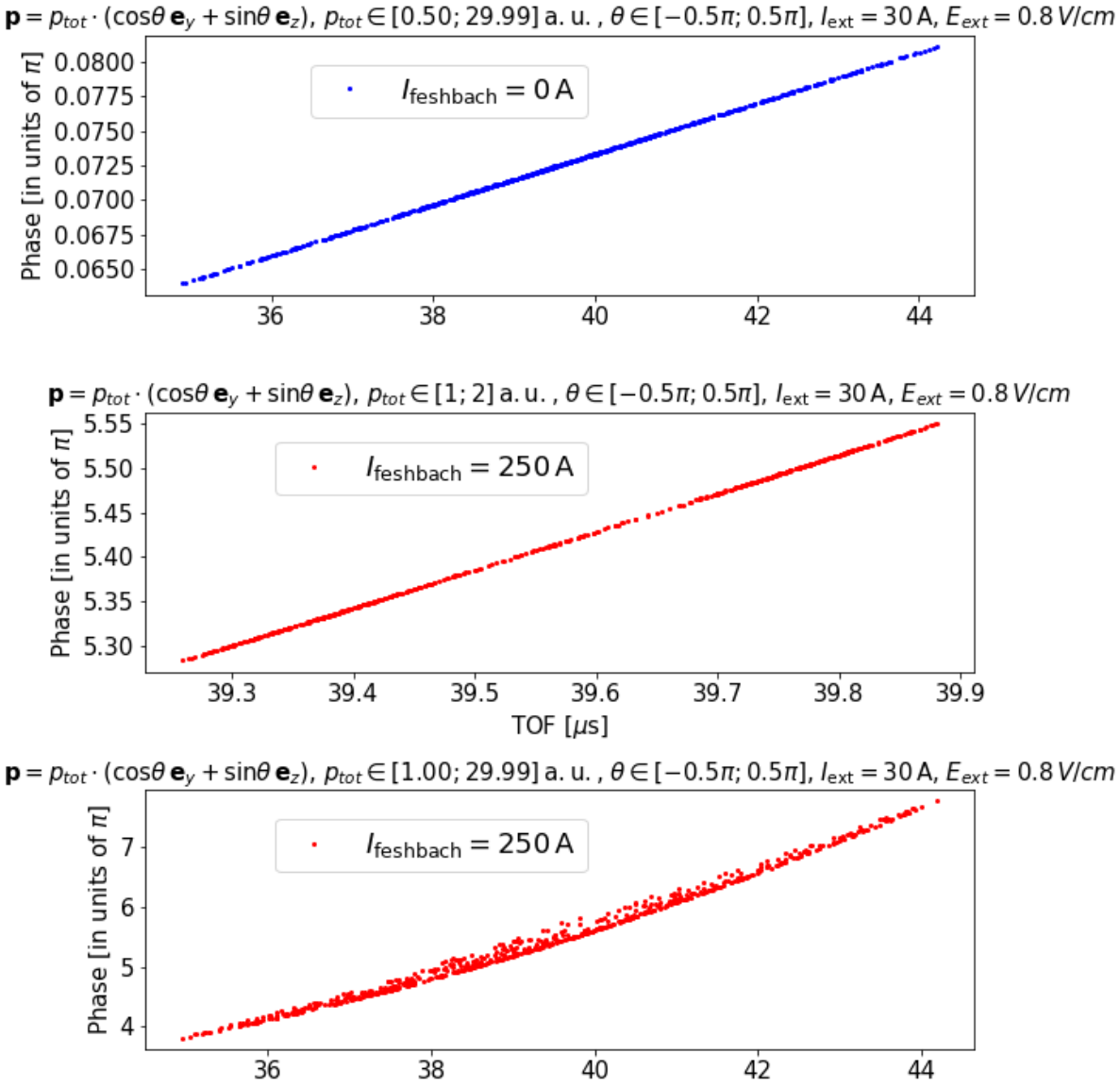

Figure 145: Phase accumulated by $^6Li^+$ until their arrival at the ion detector without and with inhomogeneous Feshbach magnetic field, upper and lower plot respectively for a typical extraction voltage of 0.8 V/cm. Ions emerged with random initial conditions and momenta between 0.5 a.u. and 30 a.u..

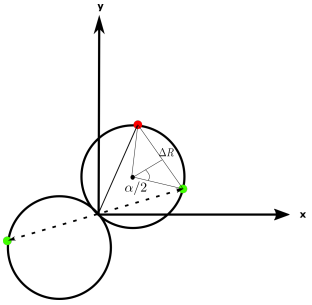

Figure 146: Coincident ions exhibit a phase difference $\alpha \approx \frac{qB_{center}}{m} \cdot \Delta t$ after emerging from a high field region.

The first hit is represented by the red dot. If the second hit, represented by a green dot in Fig. 146, is mirrored with respect to the origin, by virtue of adiabatic invariance

$$B_{det} \cdot r_1^2 = B_{det} \cdot r_2^2$$

the cycloton radius is the same for both ions at the ion detector. If the second hit, green dot in Fig. 146, is inverted at the origin, the cylcoton radius of both ions can be determined via

$$r \cdot \sin(\alpha/2) = \Delta R/2,$$

where, ΔR is the distance between both hit points after inversion of the second hit, $\alpha = \omega(TOF2-TOF1)$ the phase difference and $\omega = \frac{qB_{center}}{m}$ the cycloton frequency in the high-field region in the center. The backward ion is slowed down within the region of field homogeneity below 0.1% of $[-14; +14]$ mm at a low extraction field of 5 V/m for an initial longitudinal kinetic energy up to 70 meV.

Adiabatic invariance of ion and electron trajectories Adiabatic invariance is a concept, widely discussed in the context of plasma physics. It states that in smoothly changing, spatially non-uniform magnetic fields, and slow temporal changes of the total kinetic energy, the magnetic moment in Eq. 75 changes very slowly (or "adiabatically") with respect to the gyroperiod and can be considered a constant of motion. The conditions for adiabatic invariance can be stated more quantitatively as

1. Smoothness of magnetic field: $\frac{B}{|\nabla B|} \gg r_L = \frac{p_\perp}{q \cdot B}$
2. Magnitude of electric extraction field: $\frac{\frac{dE_{kin}}{dt}}{E_{kin}} \ll \omega_g = \frac{qB}{m}$.

The first condition can be restated as

$$p_\perp \ll \frac{qB}{\frac{|\nabla B|}{B}}, \tag{84}$$

and lets anticipate that it is more difficult to achieve adiabatic invariance for high transversal momenta $p_\perp$, low magnetic field B and for high magnetic field gradients $\frac{|\nabla B|}{B}$. The normalized magnetic field gradient $\frac{|\nabla B|}{B}$ should be independent of the actual overall magnetic field amplitude, but rather depend on the gradient of the magnetic field from the high field region, generated in the center by the Feshbach coils, to the low field region at the detector, generated by the external Helmholtz coils. This gradient should be proportional to the magnetic field difference $\Delta B = B_{center} - B_{det}$ between the magnetic field in the reaction volume B_{center} and at the detector B_{det}. It can be influenced by the relative current amplitudes of the magnetic extraction field of the external Helmholtz coils and the magnetic field of the Feshbach coils. Therefore it should be more difficult to achieve adiabaticity for a large difference ΔB_z (see Eq. 82) between those two regions. The second condition lets anticipate, that the electric extraction field should not be too high, in order for the kinetic energy to not change too much within

one gyroperiod. By plugging Eq. 80 into the first condition, we see that $\frac{\dot{E}_{kin}}{E_{kin}} = \frac{qE_{ext}}{m}\frac{v_\parallel}{v_\parallel^2+v_\perp^2}$ which is maximum for $v_\perp = 0$ resulting in a rate of $\frac{qE_{ext}}{p_\parallel}$. Therefore in order for the kinetic energy not to change too rapidly

$$m\frac{E_{ext}}{B} \ll p_\parallel. \tag{85}$$

This condition can be interpreted as an upper limit for the extraction voltage, dependent on the minimum longitudinal momentum, which could occur in the reaction.

Taking these conditions into account, by numerical inspection of solutions of $m_{^6Li}\ddot{\mathbf{r}} = q\cdot\mathbf{E} + q\cdot(\mathbf{v}\times\mathbf{B})$, it can be investigated how adiabaticity of ion trajectories depends on parameters like extraction field E_{ext}, magnetic field at the center B_{center}, initial velocity $\mathbf{v_0} = v_0\,[\cos\theta\sin\varphi, \cos\theta\cos\varphi, \sin\theta]$, being parametrized by the two emission angles θ, φ, see Fig. 147. In all initial conditions, the ions are always supposed to emerge from an idealized point-like reaction volume at $\mathbf{r} = (0,0,0)$.

Since the route to degeneracy prescripes evaporative cooling at a high magnetic field B_{center} in the vincinity of $B_0 = 834\,\mathrm{G}$ and subsequently Coulomb explosion is induced at the same high magnetic field, the magnetic field in the reaction volume B_{center} is not a free parameter and in numerical simulation of charged fragment trajectories, should be chosen to be B_0, in order to determine adiabaticity in the worst case of a high magnetic field gradient $\frac{|\nabla B|}{B}$. By Bio-Savart calculation, the produced magnetic field is symmetric with respect to the spectrometer axis, therefore the emission angle φ (see Fig. 137) of the recoil ion should not matter for the determination of adiabaticity. The initial transversal and longitudinal momentum of ionic fragments emerging from multielectron dissociative ionization of a molecule could be influenced via interaction of the molecule with an intense laser field, as mentioned above, but in the following considerations we will assume arbitrary initial momenta.

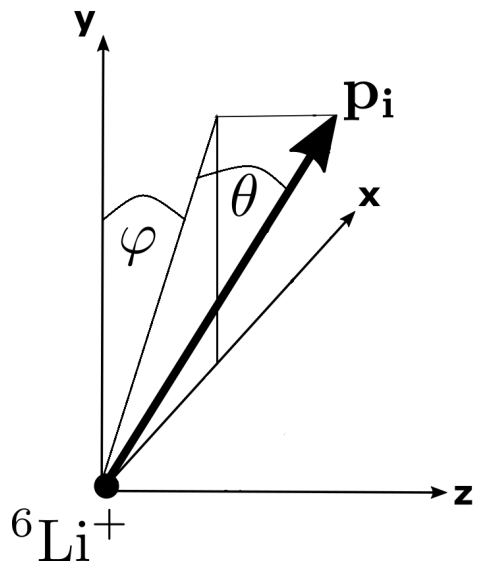

Figure 147: Initial velocities are parametrized through emission angles θ, φ and magnitude of initial velocity $v_0 = \frac{p_0}{m}$.

Adiabaticity for ^{6}Li ions It turns out, that adiabaticity is rather difficult to achieve for $^6Li^+$ trajectories, even with moderately low recoil momenta below 2 a.u.. The ratio of magnetic momenta $\frac{\mu_{det}^{GC}}{\mu_{init}^{GC}}$ for different initial momenta and emission angle have been plotted in Fig. 148 for conventional values of electric and magnetic extraction field strength. As can be seen, the adiabaticity of an ion trajectory strongly depends on its emission angle θ. However there exists a fix point for emission angle $\theta = 0$ for which the adiabaticity is the same for different velocity classes. For the emission angle $\theta = 0$ and an initial momentum of 1.5 a.u., the ratio of magnetic momenta $\frac{\mu_{det}^{GC}}{\mu_{init}^{GC}}$ have been calculated for different extraction field strengths and magnetic field

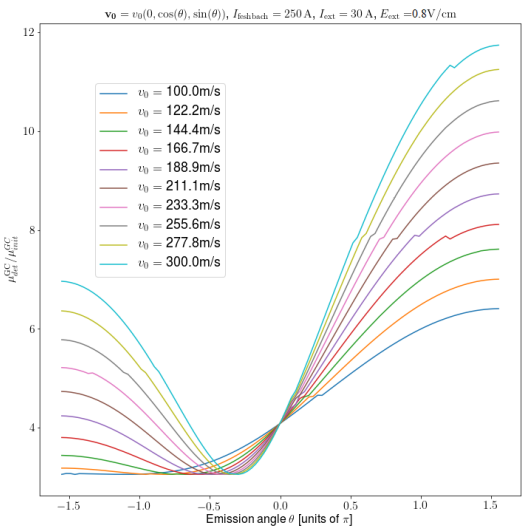

Figure 148: Adiabaticity of ion trajectories in dependence of their emission angle θ for initial momenta between 0.5 a.u. and 1.5 a.u., moderate extraction field of 0.8 V/cm.

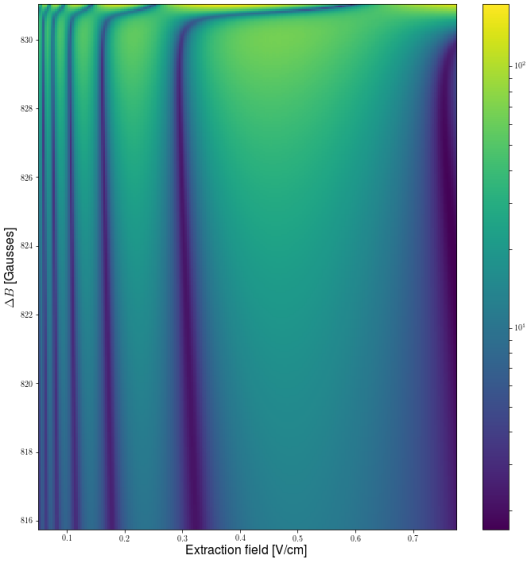

Figure 149: The ratio of magnetic momenta $\frac{\mu_{det}^{GC}}{\mu_{init}^{GC}}$ have been plotted for the specific initial condition $v_0 = (0, v_{tot}, 0)$ with $v_{tot} = 300\,\text{m/s}$ in dependence of the electric extraction field strengths and the magnetic field difference $\Delta B = B_{center} - B_{det}$ between the high and low field region.

gradients (see Fig. 149). As can be seen, the magnetic momentum is not conserved for most combinations, but the general tendency can be seen, that adiabaticity becomes better for lower ΔB and lower electric extraction field strengths.

Indeed for the special case of zero electric extraction field, the magnetic moment seems to be approximately conserved, as can be seen from the numerical solution for initial conditions $\mathbf{r} = (0, 0, 0)$ and $\mathbf{v} = v_\perp(0, \cos(\theta = 0.01\pi), \sin(\theta = 0.01\pi))$ in lower part of Fig. 150 and for a range of initial velocities $v_0 \in [100 : 300]\,\frac{m}{s}$ and angles $\theta \in [0 : 0.5\pi]$ in Fig. 151.

At zero extraction voltage, the ion only is accelerated by the magnetic field gradient and needs $\approx 5.6\,\text{ms}$ to arrive at the ion detector at $z = 0.75\,m$. In the GCS frame, the ratio of magnetic moment at the detector to the magnetic momentum in the center is ≈ 0.989. In order to check to what degree this approximate invariance of the magnetic moment holds for different initial velocities, ion trajectories were simulated for different emission angles θ and velocities v_0 corresponding to atomic ^{6}Li momenta between 0.5 a.u and 1.5 a.u.. As can be seen from Fig. 151 the approximate invariance of adiabaticity for zero extraction field and this momentum range still holds with an error up to 5%.

The two obvious disadvantages of zero extraction voltage are, that (a) only ions emitted in direction of the detector will be detected and (b) the flight time of the ions is greatly increased and multiples higher than the repetition period of our femto laser system. In order to achieve flight times below the repetition period of 250 μs of our fs laser system, the extraction field should be increased to at least 2 V/m for which however the ion trajectories are not adiabatic anymore. There are two possibilities to increase the adiabaticity of the ion trajectories:

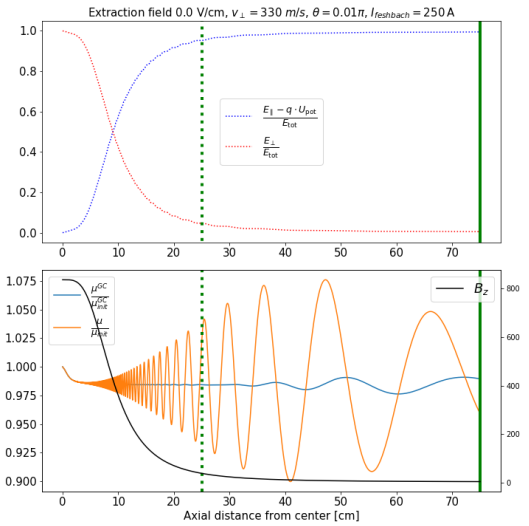

Figure 150: Simulation of ion trajectory with initial momentum 1.65 a.u. and zero extraction field.

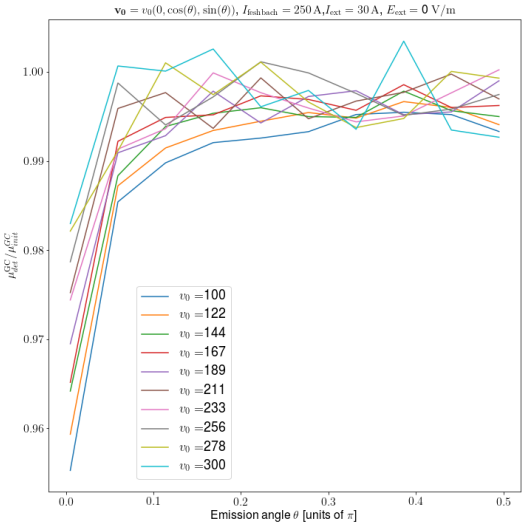

Figure 151: Adiabaticity of ion trajectories with differential initial velocities $\mathbf{v_0} = v_0(0, \cos\theta, \sin\theta)$ for zero extraction voltage. The velocity range $[100; 300]$ m/s corresponds to a range of momenta of $\approx [0.5; 1.5]$ a.u..

1. Restrict the acceleration zone to a small part in the center of the coil pair, where the magnetic field B is high and homogeneous. This way, the second condition Eq. 85 is easier fulfilled and Fig. 152 shows that the relative deviation of $\frac{\mu^{GC}}{\mu^{GC}_{init}}$ from unity is less than 10 % for all initial conditions with momenta between 0.5 and 1.5 a.u.. Still for this low extraction voltage, the arrival times on the ion detector are between 800 μs and 840 μs.

2. Increase the current in the external coils so that the magnetic field gradient $\frac{|\nabla B|}{B}$ decreases and Eq. 84 is easier fulfilled. Numerical checks show, that a magnetic field of about 50 Gausses would be required at the detector in order for the trajectory to be moderately adiabatic. However such a strong homogeneous magnetic bias field will disturb the operation of the MOT, since in a conventional $\sigma^+ - \sigma^-$ configuration, where the pair of counterpropagating beams have the same detuning δ_L and (ideally) the same power, the scattering forces of both beams are in equilibrium at the zero crossing of the magnetic field, and such a strong external magnetic field will shift the zero crossing even out of the diameter of the MOT beams. This could be counter-acted by choosing the same polarization for both beams, in which the equilibrium of the longitudinal scattering force is largely independent of the magnetic field [22].

If one combines all three measures, i.e. for the chosen parameters of

- a moderately low electric extraction field of 0.3 $\frac{\mathrm{V}}{\mathrm{cm}}$,
- a small acceleration region of $s_a = 1$ cm on the ion side,

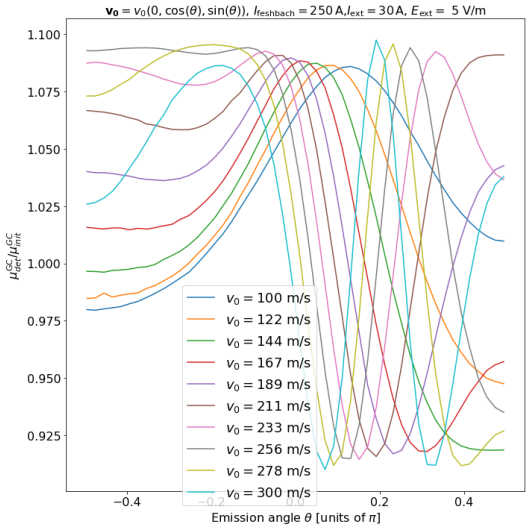

Figure 152: Adiabaticity of ion trajectories with differential initial velocities $\mathbf{v_0} = v_0(0, \cos\theta, \sin\theta)$ for a low extraction voltage of 5 V/m and an acceleration zone that extends only to +0.5 cm on the ion side. The velocity range $[100; 300]$ m/s corresponds to a range of momenta of $\approx [0.5; 1.5]$ a.u.

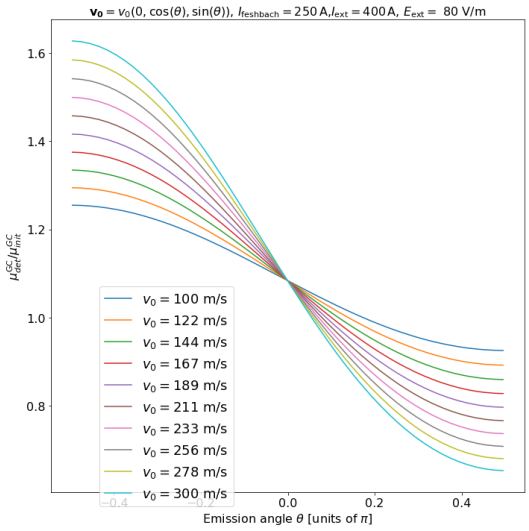

Figure 153: Adiabaticity of ion trajectories with differential initial velocities $\mathbf{v_0} = v_0(0, \cos\theta, \sin\theta)$ for a high magnetic field at the detector of $\approx$ 50 Gausses. The velocity range $[100; 300]$ m/s corresponds to a range of momenta of $\approx [0.5; 1.5]$ a.u.

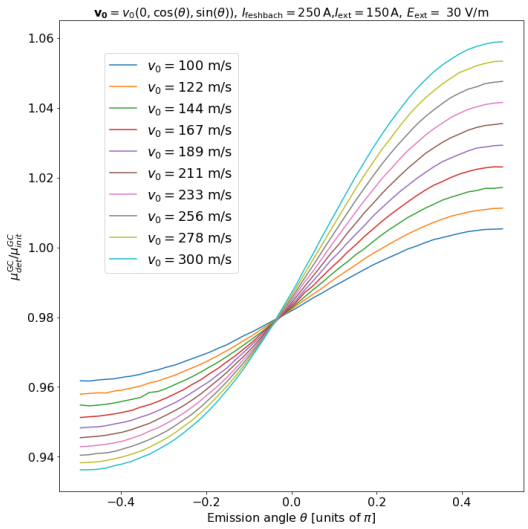

Figure 154: Adiabaticity of ion trajectories with differential initial velocities $\mathbf{v_0} = v_0(0, \cos\theta, \sin\theta)$ for a high magnetic field at the detector of $\approx 50\,\text{Gausses}$, a small acceleration zone on the ion side of $s_a = 1\,\text{cm}$, and a high magnetic field at the detector. The velocity range $[100; 300]\,\text{m/s}$ corresponds to a range of momenta of $\approx [0.5; 1.5]\,\text{a.u.}$

- and a high magnetic field at the detector by applying a current of $I = 150\,\text{A}$ to the external coils

one obtains ion trajectories which are adiabatic within a $10\,\%$ error for all emission angles θ and for momenta between $0.5\,\text{a.u.}$ and $1.5\,\text{a.u.}$ (see Fig. 154).

Adiabaticity for photo-electrons The conditions for adiabaticity Eq. 85 and Eq. 84 are easier fulfilled for electrons. As it can be seen in Fig. 155, the electron trajectories fulfill adiabaticity for a conventional extraction field of $80\,\text{V/m}$ with an error below 1%. The initial velocities tested in Fig. 155 correspond to momenta up to $0.27\,\text{a.u.}$, which could result from multi-photon ionization of ^6Li.

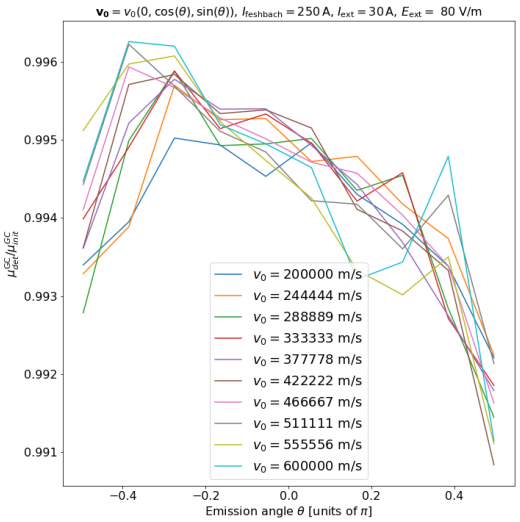

Figure 155: Adiabaticity of electron trajectories with differential initial velocities $\mathbf{v_0} = v_0(0, \cos\theta, \sin\theta)$ for an extraction voltage of $80\,\text{V/m}$. The velocity range $[200000; 600000]\,\text{m/s}$ corresponds to a range of momenta of $\approx [0.09; 0.27]$ a.u., which includes the range of momenta that could result from multi-photon ionization of ^{6}Li atoms.

Part VI
Summary and outlook

In this work, the author combined a well-characterised MOTRIMS momentum spectrometer with a focused beam optical dipole force trap ($\lambda = 1070 \pm 10\,\mathrm{nm}$), into which we could load approximately 10^5 ^{6}Li atoms with $1/e$ lifetimes $> 5\,\mathrm{s}$ and at a temperature of about $400\,\mu\mathrm{K}$. These purely optically trapped atoms were used as a target for multi-photon ionization with spectrally broad and intense femtosecond laser pulses ($\tau = 30\,\mathrm{fs}, E \leq 800\,\mu\mathrm{J}$). For recoil ions and photo electrons we obtained high momentum resolutions of 0.055 a.u. and 0.03 a.u. respectively. Although there exists another MOTRIMS, which implemented a different kind of an all optical trap using resonant trapping lasers [35], our approach has the advantage that not only atoms, but also molecules can be trapped because they have dynamical polarizabilities comparable to that of atoms. In order to demonstrate this point, the author implemented a photoassociation scheme, with which several high-lying vibrational levels of $A^1\Sigma_u^+(\mathrm{Li}_2^*)$ and $1^3\Sigma_g^+(\mathrm{Li}_2^*)$, both connected to the $2s + 2p$ asymptote, were excited in the singlet and triplet system, respectively. The simplest mechanism of ground-state molecule production is to allow for the excited state molecules to spontaneously decay, although for high-lying vibrational levels only a small fraction of the decays leads to ground state molecules. On the other hand, these vibrational levels have the advantage, that if they decay into the electronic ground-state, they predominantly populate the vibrationally highest state of the molecule. The most promising vibrational levels for this ground state molecule production with high specificity of the final vibrational state are discussed in [70]. They are $A^1\Sigma_u^+(\nu = 70)$ and $1^3\Sigma_g^+(\nu = 51)$ in the singlet and triplet system respectively. The binding energies of $1^3\Sigma_g^+(\nu)$ with $\nu < 56$ however have not yet been experimentally determined. With the limitations of the PA setup used, the author chose to excite $A^1\Sigma_u^+(\nu = 65)$ and $1^3\Sigma_g^+(\nu = 57)$ as the next best candidates. When the PA laser was in resonance with $A^1\Sigma_u^+(\nu = 65)$, the author suceeded to detect $1^1\Sigma_g^+(\nu = 38)$ ground-state molecules via 3-photon ionization with broad band femtosecond pulses. In the triplett system however no molecular signal discernible from the background emerged. The author attributes this on one hand to the lower total number of produced ground state molecules and on the other hand to a lower ionization efficiency. This is due to a poorer overlap of wave functions between $1^3\Sigma_g^+(\nu = 57)$ and the accesible vibrational levels in $\mathrm{Li}_2^+ 1^2\Sigma_g$ below the final state energy of $\approx 4.76\,\mathrm{eV}$, i.e. for $\nu \leq 23$. The author measured photoelectron momentum spectra for ionisation of $1^1\Sigma_g^+(\nu = 38)$ ground state molecules in two different setups. The photoelectrons exhibit very small excess energies of $\leq 100\,\mathrm{meV}$, meaning only vibrational states in the range $v = 19-23$ are populated. While the ionization rate due to femtosecond pulse ionization of molecules is rather small with $2-3\,\mathrm{molecules/sec}$, we found a continuous, resonant ionization mechanism, which produces molecular ions in the vibrational states $\nu = 0$ and $\nu = 1$ of the $^6\mathrm{Li}_2^+$ cation potential energy $1^2\Sigma_g$. After photoassociation, the excited state molecules can immediately be promoted via absorption of one IR photon to a bound state of the $3^1\Sigma_g^+$ potential at long range. The nuclei in the molecule then have time to reduce their distance further, until a second IR photon gets absorbed at the condon point $R_C = 9.876\mathrm{a}_0$, which then ionizes the molecule. It is also possible to reach a bound state of Li_2^* $3^1\Sigma_g^+$ by absorption of two femtosecond laser photons, which is why delayed IR ionization of molecules is observed. It might be interesting in the future to ionize the optically trapped molecular sample with a pulsed UV laser, which has sufficient energy to ionize the molecules with one single photon, but not the ^{6}Li atoms, which are trapped in their electronic groundstate $2s$.

Finally, a molecular ion production mechanism was established, which occurs during ionization of the magneto-optically trapped target with broad femtosecond laser pulses. We call this process photo-associative ladder excitation. A fraction of atomic collisions in the MOT occurs between atoms, which are both in their first excited state $2p$. Femtosecond laser photons from the low-energy tail of the spectrum, are able to transfer one of two atoms into the $3s$ state, so that the two atoms proceed to collide on the $2p-3s$ at an energy of 0.166 eV below the dissociation threshold of Li_2^+ $1^2\Sigma_g^+$. They will autoionize into one vibrational level of the molecular ion Li_2^+ $1^2\Sigma_g^+$ due to an avoided crossing with the $2p-3s$ potential energy. It was also noted, that the observation of photoassociative ladder excitation in the experiment is conditional on the density of the MOT being high enough, otherwise atom pairs will radiatively decay before they autoionize. To the knowledge of the author there is no spectroscopic data available for the potential energy curve between atoms in these states. The magnetic field of the MOT did not allow us to measure directly photoelectron energies, but future experiments will aim to study this process in the optical dipole trap by exciting atoms to $2p$ with short Rabi pulses.

This work was part of a bigger project, which has the goal of creating quantum few-particles systems, whose interactions can be controlled, as a target in a reaction microscope. Specifically, a milestone will be the creation a BEC of weakly bound dimers $^6Li_2$ as a target for short and intense laser pulses. In future experiments, the photoassociation technique, implemented in this thesis, however might still play a role, especially in a two-color scheme (see Sec. 12.7). A timed sequence STIRAP scheme will enable to generate $^6Li_2$ ground state molecules in any desired vibrational state with high fidelity, once the quantum degenerate regime is reached. Feshbach resonances complement the photoassociation technique in an ideal way, since the collision rate near a Feshbach resonance is greatly enhanced, thereby also enhancing PA rates. In a BEC of weakly bound $^6Li_2$ dimers a particular reaction of interest to us, is femtolaser pulse induced double ionization of $^6Li_2$ dimers, i.e.

$$^6Li_2 + n\gamma_{fs} \rightarrow ^6Li^+ + ^6Li^+ + e^- + e^-,$$

where n is the necessary number of photons to achieve double ionization of the $^6Li_2$ dimer. In the photoassociation experiments done in this thesis, it was attempted to study this reaction, however in order to be able to observe Coulomb explosion, it is imperative to get rid of the overwhelming atomic signal. Purification of the trapped molecular sample from co-trapped atoms in the macro-trap, by using a resonant pushing-beam, however did not leave a molecular signal. A possible solution to this problem might be the use of a micro-dipole trap as in setup 2 of Sec. 12, which can be loaded with molecules and moved far away from the macro-dipole trap. It was also attempted to enhanced the molecule production rate by exciting deeper lying levels ($\nu = 20-26$ in $1^3\Sigma_g^+$ and $v = 29-35$ in $1^1\Sigma_u^+$) as reported in [66, 65], however in turned out that in a thermal gas of ^6Li, theses s-wave collision resonances cannot be excited.

Appendices

A Atomic units

In atomic and molecular physics, atomic units are the most natural system of units, in which the base units, the most relevant one listed in Tab. 6, refer to properties of the hydrogen atom.

Base unit	Atomic unit	SI unit
Length	Bohr radius a_0	$5.29 \cdot 10^{-11}\,\mathrm{m}$
Mass	Electron mass m_e	$9.11 \cdot 10^{-31}\,\mathrm{kg}$
Charge	Electron charge e	$1.60 \cdot 10^{-19}\,\mathrm{As}$
Energie	Hartree energy $E_h = 2Ry$	$27.211\,\mathrm{eV}$
Time	Atomic time unit $\frac{\hbar}{E_h}$	$1.52 \cdot 10^{-16}\,\mathrm{s}$
Momentum	Atomic unit of momentum	$1.99 \cdot 10^{-24}\,\mathrm{kg \cdot m/s}$
Angular momentum	Planck constant $\hbar$	$6.582 \cdot 10^{-16}\mathrm{eV\,s}$

Table 6: Relevant base units in atomic units and SI units

B Block diagram for high current polarity switch

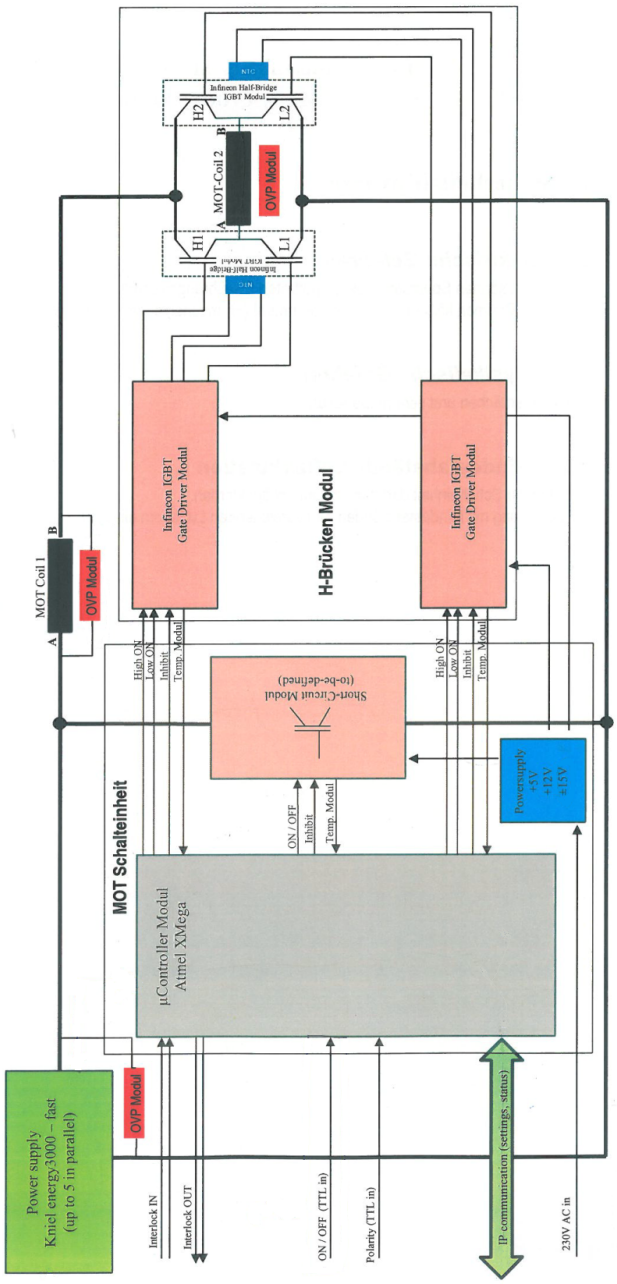

Figure 156: Block diagram of high current switch developed by electronics department of Max-Planck institute of nuclear physics.

References

[1] S Jochim, M Bartenstein, A Altmeyer, G Hendl, S Riedl, C Chin, J Hecker Denschlag, and R Grimm. Bose-Einstein condensation of molecules. *Science (New York, N.Y.)*, 302(5653):2101–3, 2003.

[2] C. H. Schunck, M. W. Zwierlein, C. A. Stan, S. M. F. Raupach, W. Ketterle, A. Simoni, E. Tiesinga, C. J. Williams, and P. S. Julienne. Feshbach resonances in fermionic ^{6}Li. *Phys. Rev. A*, 71:045601, Apr 2005.

[3] M. Bartenstein, A. Altmeyer, S. Riedl, S. Jochim, C. Chin, J. Hecker Denschlag, and R. Grimm. Crossover from a molecular bose-einstein condensate to a degenerate fermi gas. *Phys. Rev. Lett.*, 92:120401, Mar 2004.

[4] Michael Schuricke, Ganjun Zhu, Jochen Steinmann, Konstantinos Simeonidis, Igor Ivanov, Anatoli Kheifets, Alexei N. Grum-Grzhimailo, Klaus Bartschat, Alexander Dorn, and Joachim Ullrich. Strong-field ionization of lithium. *Phys. Rev. A*, 83:023413, Feb 2011.

[5] Michael Schuricke, Klaus Bartschat, Alexei N. Grum-Grzhimailo, Ganjun Zhu, Jochen Steinmann, Robert Moshammer, Joachim Ullrich, and Alexander Dorn. Coherence in multistate resonance-enhanced four-photon ionization of lithium atoms. *Phys. Rev. A*, 88:023427, Aug 2013.

[6] Junyang Yuan, Yixuan Ma, Renyuan Li, Huanyu Ma, Yizhu Zhang, Difa Ye, Zhenjie Shen, Tianmin Yan, Xincheng Wang, Matthias Weidemüller, and Yuhai Jiang. Momentum Spectroscopy for Multiple Ionization of Cold Rubidium in the Elliptically Polarized Laser Field. *Chinese Physics Letters*, 37(5):053201, may 2020.

[7] Philipp Wessels, Bernhard Ruff, Tobias Kroker, Andrey K. Kazansky, Nikolay M. Kabachnik, Klaus Sengstock, Markus Drescher, and Juliette Simonet. Absolute strong-field ionization probabilities of ultracold rubidium atoms. *Communications Physics*, 1(1):32, dec 2018.

[8] D. Ciampini, M. Anderlini, J. H. Müller, F. Fuso, O. Morsch, J. W. Thomsen, and E. Arimondo. Photoionization of ultracold and bose-einstein-condensed rb atoms. *Phys. Rev. A*, 66:043409, Oct 2002.

[9] D. Ciampini, F. Fuso, J. H. Müller, M. Anderlini, O. Morsch, and E. Arimondo. Photoionization of bose-einstein condensates. In N. P. Bigelow, J. H. Eberly, C. R. Stroud, and I. A. Walmsley, editors, *Coherence and Quantum Optics VIII*, pages 309–310, Boston, MA, 2003. Springer US.

[10] Thomas Lompe, Timo B. Ottenstein, Friedhelm Serwane, Andre N. Wenz, Gerhard Zürn, and Selim Jochim. Radio-frequency association of efimov trimers. *Science*, 330(6006):940–944, 2010.

[11] Maksim Kunitski, Stefan Zeller, Jörg Voigtsberger, Anton Kalinin, Lothar Ph. H Schmidt, Markus Schöffler, Achim Czasch, Wieland Schöllkopf, Robert E Grisenti, Till Jahnke, Dörte Blume, and Reinhard Dörner. Observation of the Efimov state of the helium trimer. *Science*, 348(6234):551–555, 2015.

[12] J. Ullrich et al. Ionization collision dynamics in 3.6 mev/u ni^{2}4+ on he encounters. *Nucl. Instr. Meth. B 98*, 1995.

[13] R. Moshammer, M. Unverzagt, W. Schmitt, J. Ulrich, and H. Schmidt-Boecking. A 4π recoil-ion momentum analyzer: a high-resolution "microscope" for the investigation of the dynamics of atomic, molecular and nuclear reactions. *Nuclear Instruments and Methods in Physics Research B*, 1996.

[14] J. Ullrich et al. Recoil-ion momentum spectroscopy. *J. Phys. B: At. Mol. Opt. Phys.*, 30:2917, 1997.

[15] Michael Schuricke. *Two and Three Photon Double Ionization of Lithium.* PhD thesis, 2012.

[16] J. Ullrich. *Many-Particle Quantum Dynamics in Atomic and Molecular Fragmentation.* Springer, 2003.

[17] Steffen Wolf and Hanspeter Helm. Ion-recoil energy measurement in photoionization of laser-cooled rubidium. *Phys. Rev. A*, 56, 1997.

[18] Jochen Steinmann. *Multiphoton Ionization of Laser Cooled Lithium.* PhD thesis, 2007.

[19] J W Turkstra, R Hoekstra, S Knoop, D Meyer, R Morgenstern, and R E Olson. Recoil momentum spectroscopy of highly charged ion collisions on magneto-optically trapped Na. *Physical Review Letters*, 2001.

[20] J Blieck, X Flchard, A Cassimi, H Gilles, S Girard, and D Hennecart. A new magneto-optical trap-target recoil ion momentum spectroscopy apparatus for ion-atom collisions and trapped atom studies. In *Review of Scientific Instruments*, 2008.

[21] G. Zhu, M. Schuricke, J. Steinmann, J. Albrecht, J. Ullrich, I. Ben-Itzhak, T. J. M. Zouros, J. Colgan, M. S. Pindzola, and A. Dorn. Controlling two-electron threshold dynamics in double photoionization of lithium by initial-state preparation. *Phys. Rev. Lett.*, 103(103008), 2009.

[22] R. Hubele, M. Schuricke, J. Goullon, H. Lindenblatt, N. Ferreira, A. Laforge, E. BrÃ$\frac{1}{4}$hl, V. L. B. de Jesus, D. Globig, A. Kelkar, D. Misra, K. Schneider, M. Schulz, M. Sell, Z. Song, X. Wang, S. Zhang, and D. Fischer. Electron and recoil ion momentum imaging with a magneto-optically trapped target. *Review of Scientific Instruments*, 86(3):033105, 2015.

[23] M. Krems, J. Zirbel, M. Thomason, and R. D. DuBois. Channel electron multiplier and channelplate efficiencies for detecting positive ions. *Review of Scientific Instruments*, 76(9):093305, sep 2005.

[24] Joseph L. Wiza. Microchannel plate detectors. *Nuclear Instruments and Methods*, 162:587–601, 1979.

[25] Renate Hubele. *Kinematisch vollständige und zustands-selektive Untersuchung der stossinduzierten Einfachionisation von Lithium.* PhD thesis, 2013.

[26] O. Jagutzki, A. Cerezo, A. Czasch, R. Dorner, M. Hattas, Min Huang, V. Mergel, U. Spillmann, K. Ullmann-Pfleger, T. Weber, H. Schmidt-Bocking, and G.D.W. Smith. Multiple hit readout of a microchannel plate detector with a three-layer delay-line anode. *IEEE Transactions on Nuclear Science*, 49(5):2477–2483, oct 2002.

[27] M. Houbiers, H. T. C. Stoof, W. I. McAlexander, and R. G. Hulet. Elastic and inelastic collisions of ^{6}li atoms in magnetic and optical traps. *Phys. Rev. A, 57(3):R1497*, 1998.

[28] Harold J. Metcalf and Peter van der Straten. *Laser cooling and Trapping.* Springer, 1999.

[29] I.I. Rabi. Space quantization in a gyrating magnetic field. *Phys. Rep. 51*, 652, 1937.

[30] V. S. Letokhov and V. G. Minogin. Laser radiation pressure on free atoms. *Physics Reports*, 73(1):1–65, 1981.

[31] W. I. McAlexander, E. R.I. Abraham, and R. G. Hulet. Radiative lifetime of the [Formula Presented] state of lithium. *Physical Review A - Atomic, Molecular, and Optical Physics*, 54(1):R5–R8, jul 1996.

[32] Paul Hamilton, Geena Kim, Trinity Josi, Biswaroop Mukherjee, Daniel Tiarks, and Holger Mueller. Sisyphus cooling of lithium. *Physical Review A*, 89(023409), 2014.

[33] S. Chu, M.G. Prentiss, A.E. Cable, and J.E. Bjorkholm. Laser cooling and trapping of atoms. In W. Persson and S. Svanberg, editors, *Laser Spectroscopy VIII - Proceedings of the Eigth International Conference*, pages 58–63, 1987.

[34] T. Walker, D. Hoffmann, P. Feng, and R.S. Williamson. A vortex-force atom trap. *Physics Letters A*, 163(4):309–312, mar 1992.

[35] S. Sharma, B. P. Acharya, A. H.N.C. De Silva, N. W. Parris, B. J. Ramsey, K. L. Romans, A. Dorn, V. L.B. De Jesus, and D. Fischer. All-optical atom trap as a target for MOTRIMS-like collision experiments. *Physical Review A*, 2018.

[36] Michael Eric Gehm. *Preparation of an optically-trapped degenerate Fermi gas of ^{6}Li: Finding the route to degeneracy.* PhD thesis, Graduate School of Duke University, 2003.

[37] Craig J. Sansonetti and OTHERS. Absolute transition frequencies and quantum interference in a frequency comb based measurement of the ^{6,7}li d lines. *Physical Review Letters*, 107, 2012.

[38] E. Arimondo, M. Inguscio, and P. Violino. Experimental determinations of the hyperfine structure in the alkali atoms. *Reviews of Modern Physics*, 1977.

[39] Johannes Schindler. Characterization of an erbium atomic beam. Master's thesis, Universität Innsbruck, 2011.

[40] Christoph Bogda. Umbau und Inbetriebnahme eines MOTRemi-Aufbaus fuer zukuenftige Experimente mit ultrakaltem ^{6}Li. Master's thesis, Ruprecht-Karls-Universitaet Heidelberg, 2015.

[41] Michael A. Joffe, Wolfgang Ketterle, Alex Martin, and David E. Pritchard. Transverse cooling and deflection of an atomic beam inside a Zeeman slower. *Journal of the Optical Society of America B*, 1993.

[42] Rudolf Grimm, Matthias Weidemüller, and Yurii B. Ovchinnikov. Optical dipole trap for neutral atoms. 1999.

[43] Steven Chu, J. E. Bjorkholm, A. Ashkin, and A. Cable. Experimental observation of optically trapped atoms. *Physical Review Letters*, 57(3):314–317, jul 1986.

[44] A Mosk, S Jochim, H Moritz, and T Elsässer. Resonator-enhanced optical dipole trap for fermionic lithium atoms. *Optics*, 2001.

[45] J. Fuchs, G.J. Duffy, G. Veeravalli, and P. Dyke. Molecular Bose-Einstein condensation in a versatile low power crossed dipole trap. *Journal of Physics B*, 2007.

[46] Rodney Loudon and Thomas von Foerster. The Quantum Theory of Light. *American Journal of Physics*, 1974.

[47] Li Yan Tang, Zong Chao Yan, Ting Yun Shi, and J. Mitroy. Dynamic dipole polarizabilities of the Li atom and the Be+ ion. *Physical Review A - Atomic, Molecular, and Optical Physics*, 81(4):1–12, 2010.

[48] M. Marinescu, H. R. Sadeghpour, and A. Dalgarno. Dynamic dipole polarizabilities of rubidium. *Physical Review A*, 1994.

[49] Johannes Deiglmayr, Mireille Aymar, Roland Wester, Matthias Weidemüller, and Olivier Dulieu. Calculations of static dipole polarizabilities of alkali dimers: Prospects for alignment of ultracold molecules. *Journal of Chemical Physics*, 129(6):1–36, 2008.

[50] Wolfgang Ketterle and N. J.Van Druten. Evaporative Cooling of Trapped Atoms. *Advances in Atomic, Molecular and Optical Physics*, 1996.

[51] Charles S. Adams, Heun Jin Lee, Nir Davidson, Mark Kasevich, and Steven Chu. Evaporative cooling in a crossed dipole trap. *Physical Review Letters*, 1995.

[52] TA Savard, KM O'hara, and JE Thomas. Laser-noise-induced heating in far-off resonance optical traps. *Physical Review A*, 1997.

[53] ME Gehm, KM O'hara, TA Savard, and JE Thomas. Dynamics of noise-induced heating in atom traps. *Physical Review A*, 1998.

[54] K. M. O'Hara, S. R. Granade, M. E. Gehm, T. A. Savard, S. Bali, C. Freed, and J. E. Thomas. Ultrastable CO 2 Laser Trapping of Lithium Fermions. *Physical Review Letters*, 82(21):4204–4207, may 1999.

[55] Kevin M. Jones, Eite Tiesinga, Paul D. Lett, and Paul S. Julienne. Ultracold photoassociation spectroscopy: Long-range molecules and atomic scattering. *Reviews of Modern Physics*, 78(2):483–535, may 2006.

[56] D. Sesko, T. Walker, C. Monroe, A. Gallagher, and C. Wieman. Collisional losses from a light-force atom trap. *Physical Review Letters*, 1989.

[57] K. M. O'Hara, M. E. Gehm, S. R. Granade, S. Bali, and J. E. Thomas. Stable, strongly attractive, two-state mixture of lithium fermions in an optical trap. *Physical Review Letters*, 85(10):2092–2095, 2000.

[58] Thomas Lompe. *Efimov Physics in a three-component Fermi gas*. PhD thesis, Combined Faculties for the Natural Sciences and Mathematics of the Ruperto-Carola-University of Heidelberg, 2011.

[59] C. J. Joachain, N. J. Kylstra, and R. M. Potvliege. *Atoms in Intense Laser Fields*. Cambridge University Press, 2012.

[60] P. Jasik and J.E. Sienkiewicz. Calculation of adiabatic potentials of Li2. *Chemical Physics*, 323(2-3):563–573, apr 2006.

[61] Boris Minaev. Ab initio study of low-lying triplet states of the lithium dimer. *Spectrochimica Acta - Part A: Molecular and Biomolecular Spectroscopy*, 2005.

[62] Michael Hutchinson and Thomas F George. Laser-induced resonance formation in molecular collisions Application of low-intensity lasers to inelastic scattering and spectroscopy: Application of low-intensity lasers to inelastic scattering and spectroscopy. *MOLECULAR PHYSICS*, 46(1):81–96, 1982.

[63] E. R. I. Abraham, N. W. M. Ritchie, W. I. McAlexander, and R. G. Hulet. Photoassociative spectroscopy of long range states of ultracold $^6Li_2$ and $^7Li_2$. *The Journal of Chemical Physics*, 103(18):7773–7778, nov 1995.

[64] H. R. Thorsheim, J. Weiner, and P. S. Julienne. Laser-induced photoassociation of ultracold sodium atoms. *Physical Review Letters*, 1987.

[65] Mariusz Semczuk, Xuan Li, Will Gunton, Magnus Haw, Nikesh S. Dattani, Julien Witz, Arthur K. Mills, David J. Jones, and Kirk W. Madison. High-resolution photoassociation spectroscopy of the $^6li_2$ $1^3\Sigma_g^+$ state. *Phys. Rev. A*, 87:052505, May 2013.

[66] Will Gunton, Mariusz Semczuk, Nikesh S Dattani, and Kirk W Madison. High-resolution photoassociation spectroscopy of the 6 Li 2 A(1 1 + u) state. *PHYSICAL REVIEW A*, 88:62510, 2013.

[67] R. Côté and A. Dalgarno. Photoassociation intensities and radiative trap loss in lithium. *Phys. Rev. A*, 58:498–508, Jul 1998.

[68] Samoza. Depiction of franck condon principle in absorption and fluorescence.

[69] Attribution-sharealike 3.0 licence, https://creativecommons.org/licenses/by-sa/3.0/legalcode.

[70] R. Côté and A. Dalgarno. Mechanism for the Production of 6Li2 and 7Li2 Ultracold Molecules. *Journal of Molecular Spectroscopy*, 195(2):236–245, jun 1999.

[71] J.T.M. Walraven. Quantum gases lectures. 2018.

[72] A. J. Moerdijk, B. J. Verhaar, and A. Axelsson. Resonances in ultracold collisions of ^{6}Li, ^{7}Li, and ^{23}Na. *Phys. Rev. A*, 51:4852–4861, Jun 1995.

[73] S. Jochim, M. Bartenstein, G. Hendl, J. Hecker Denschlag, and R. Grimm. Magnetic field control of elastic scattering in a cold gas of fermionic lithium atoms. *Physical Review Letters*, 89(27), 2002.

[74] S. Jochim, M. Bartenstein, A. Altmeyer, G. Hendl, S. Riedl, C. Chin, J. Hecker Denschlag, and R. Grimm. Bose-einstein condensation of molecules. *Science*, 302(2101), 2003.

[75] S. Jochim, M. Bartenstein, A. Altmeyer, G. Hendl, C. Chin, J. Hecker Denschlag, and R. Grimm. Pure gas of optically trapped molecules created from fermionic atoms. *Phys. Rev. Lett.*, 91:240402, Dec 2003.

[76] E.R.I. Abraham, W.I. McAlexander, J.M. Gerton, R.G. Hulet, R. Côté, and A. Dalgarno. Triplet s -wave resonance in Li collisions and scattering lengths of 6 Li and 7 Li. *Physical Review A*, 1997.

[77] J Cubizolles, T Bourdel, SJJMF Kokkelmans, GV Shlyapnikov, and C Salomon. Production of Long-Lived Ultracold Li2 Molecules from a Fermi Gas. 91(24):240401, 2003.

[78] U. Schünemann, H. Engler, R. Grimm, M. Weidemüller, and M. Zielonkowski. Simple scheme for tunable frequency offset locking of two lasers. *Review of Scientific Instruments*, 1999.

[79] https://www.toptica.com/products/tunable-diode-lasers/laser-locking-electronics/digilock-110-digital-locking/.

[80] W. Ketterle, D. S. Durfee, and D. M. Stamper-Kurn. Making, probing and understanding bose-einstein condensates, 1999.

[81] Gérard A Mourou, Christopher P J Barty, and Michael D Perry. Ultrahigh-Intensity Lasers: Physics of the Extreme on a Tabletop. *Physics Today*, 51:22, 1998.

[82] Klemens Jesse. *Femtosekundenlaser*. Springer Vieweg, 2016.

[83] Thomas Lompe. An apparatus for the production of molecular bose-einstein condensates. Master's thesis, 2008.

[84] Joji Joykutty, Vaibhav Mathur, V Venkataraman, and Vasant Natarajan. Direct Measurement of the Oscillation Frequency in an Optical-Tweezers Trap by Parametric Excitation. 2005.

[85] Jinwei Wu, Raymond Newell, Marc Hausmann, David J. Vieira, and Xinxin Zhao. Loading dynamics of optical trap and parametric excitation resonances of trapped atoms. *Journal of Applied Physics*, 100(5):054903, sep 2006.

[86] A. Kramida, Yu. Ralchenko, J. Reader, and and NIST ASD Team. NIST Atomic Spectra Database (ver. 5.7.1), [Online]. Available: `https://physics.nist.gov/asd` [2019, October 20]. National Institute of Standards and Technology, Gaithersburg, MD., 2019.

[87] Moritz Weegen. Multiphoton ionisation of lithium from an optical dipole trap. Master's thesis, Department of Physics and Astronomy, University of Heidelberg, 2018.

[88] Constantine E. Theodosiou. Lifetimes of alkali-metal—atom rydberg states. *Phys. Rev. A*, 30:2881–2909, Dec 1984.

[89] T. Takekoshi, B. M. Patterson, and R. J. Knize. Observation of optically trapped cold cesium molecules. *Phys. Rev. Lett.*, 81:5105–5108, Dec 1998.

[90] Wenzel Salzmann. *Photoassociation and coherent control of ultracold molecules by femtosecond pulses*. PhD thesis, Albert-Ludwigs-University Freiburg, 2007.

[91] A. R. L. Caires, V. A. Nascimento, D. C. J. Rezende, V. S. Bagnato, and L. G. Marcassa. Atomic density and light intensity dependences of the Rb 2 molecule formation rate constant in a magneto-optical trap. *Physical Review A*, 71(4):043403, apr 2005.

[92] M. L. Trachy, G. Veshapidze, M. H. Shah, H. U. Jang, and B. D. DePaola. Photoassociation in cold atoms via ladder excitation. *Phys. Rev. Lett.*, 99:043003, Jul 2007.

[93] Pierre Pillet. Formation of ultra-cold cs2molecules through photoassociation. *Physica Scripta*, 68(2):C48–C53, jan 2003.

[94] I. Schmidt-Mink, W. Müller, and W. Meyer. Ground- and excited-state properties of Li2 and Li2+ from ab initio calculations with effective core polarization potentials. *Chemical Physics*, 92(2-3):263–285, jan 1985.

[95] Nicolas Seymour-Smith, Peter Blythe, Matthias Keller, and Wolfgang Lange. Fast scanning cavity offset lock for laser frequency drift stabilization. *Review of Scientific Instruments*, 81(7):075109, jul 2010.

[96] Andrzej Szczepkowicz, Leszek Krzemień, Adam Wojciechowski, Krzysztof Brzozowski, Michael Krüger, Michał Zawada, Marcin Witkowski, Jerzy Zachorowski, and Wojciech Gawlik. Optimal geometry for efficient loading of an optical dipole trap.

[97] U. Schlöder, T. Deuschle, C. Silber, and C. Zimmermann. Autler-townes splitting in two-color photoassociation of ^{6}Li. *Phys. Rev. A*, 68:051403, Nov 2003.

[98] U. Gaubatz, P. Rudecki, S. Schiemann, and K. Bergmann. Population transfer between molecular vibrational levels by stimulated Raman scattering with partially overlapping laserfields. A new concept and experimental results. *The Journal of Chemical Physics*, 92(9):5363–5376, may 1990.

[99] Juha Javanainen and Matt Mackie. Probability of photoassociation from a quasicontinuum approach. *Phys. Rev. A*, 58:R789–R792, Aug 1998.

[100] T. Bergeman, Gidon Erez, and Harold J. Metcalf. Magnetostatic trapping fields for neutral atoms. *Phys. Rev. A*, 35:1535–1546, Feb 1987.

[101] D Normand, L A Lompre, and C Cornaggia. Laser-induced molecular alignment probed by a double-pulse experiment. *Journal of Physics B: Atomic, Molecular and Optical Physics*, 25(20):L497–L503, oct 1992.

[102] Bretislav Friedrich and Dudley Herschbach. Alignment and trapping of molecules in intense laser fields. *Phys. Rev. Lett.*, 74:4623–4626, Jun 1995.